Water Management in Highly Dynamic PEM Fuel Cell System Operation

Von der Fakultät für Maschinenbau
der Gottfried Wilhelm Leibniz Universität Hannover
zur Erlangung des akademischen Grades
Doktor-Ingenieurin / Doktor-Ingenieur
Dr.-Ing.
genehmigte Dissertation

von

M. Sc. Jonas Breitinger

2024

Acknowledgements

Abstract

Polymer Electrolyte Membrane Fuel Cells (PEMFCs) are a promising technology to achieve carbon-free mobility. However, multiple challenges must be overcome for a market breakthrough. In a fuel cell dominant vehicle, where only a small hybridization battery is installed, highly dynamic operation of the Fuel Cell System (FCS) is required: A driver expects power dynamics on a time scale of $1\,\mathrm{s}$, which must be predominantly provided by the FCS. In addition, the system efficiency as well as the lifetime must be kept high.

This work subsequently aims at improving the dynamic capabilities of FCSs, while maintaining high system efficiencies and avoiding lifetime-limiting critical states. Therefore, the understanding of the key processes' dynamics, proceeding on time scales spanning multiple orders of magnitude, is fostered. Special focus lies on the water management as cornerstone of highly dynamic and efficient operation. In contrast to the broad research published, this work features two insufficiently addressed fields. On one hand, highly dynamic operation on the time scale of $1\,\mathrm{s}$ is in focus. On the other hand, the subsystems with their own intrinsic dynamic limitations are also included in the scope of this work. As core contribution of this work, a suite of dynamic experiments is carried out with a sophisticated full-scale automotive fuel cell system.

Four research questions serve as a guidance throughout this work. First, the dominant dynamic processes are identified using targeted dynamic simulations and experiments. Second, the setup and potential pitfalls of dynamic experiments are described, as well as their contribution to advanced modeling. Third, stationary-based control strategies are evaluated, limitations are discussed and improved strategies for highly dynamic operation are developed. Lastly, the impact of two central degrees of freedom on system level, control strategy and system architecture, on efficiency and dynamics is discussed. Overall, the setup of this work follows the logic *from one fuel cell to a fuel cell system to other fuel cell systems.* Cell-internal processes are explained first, then the stack/system interplay is discussed and lastly the results are transferred onto other systems.

Membrane humidification and dry-out dynamics strongly impact the dynamic stack behavior. In addition, liquid water accumulation and drainage plays an important role, as liquid water limits the cross-sectional area available for reactant diffusion. In case of a highly dynamic power increase, too much liquid water quickly results in reactant starvation, while the same amount of liquid water is allowed during low load steady-state operation. As common short stack test rigs fail to resemble the dynamic capabilities of an automotive fuel cell system, the transferability of the results must be checked. The highly dynamic system operation is limited by the Air System (AirS). Changing the AirS architecture or control strategy to achieve higher dynamic capabilities worsens the system efficiency, resulting in a trade-off between the two conflicting goals.

Keywords: Fuel cell systems, dynamic operation, water management

Kurzfassung

Polymerelektrolytmembran-Brennstoffzellen sind eine vielversprechende Technologie, um kohlenstofffreie Mobilität zu erreichen. Allerdings müssen für einen Marktdurchbruch noch mehrere Herausforderungen überwunden werden. Die Anwendung in einem Brennstoffzellen-dominanten Fahrzeug, in dem nur eine kleine Hybridbatterie verbaut ist, erfordert einen hochdynamischen Betrieb des Brennstoffzellensystems: Ein Fahrer erwartet Leistungsdynamiken auf einer Zeitskala von 1 s, welche überwiegend durch das Brennstoffzellensystem bereitgestellt werden muss. Darüber hinaus muss die Systemeffizienz und Lebensdauer auf einem hohen Niveau gehalten werden.

Diese Arbeit zielt folglich auf eine Verbesserung der dynamischen Leistungsfähigkeit von Brennstoffzellensystemen bei gleichzeitiger Erhaltung hoher Systemeffizienzen und Vermeidung Lebensdauer-limitierender, kritischer Zustände ab. Dazu wird das Verständnis der Dynamiken der Kernprozesse, die auf um Größenordnungen variierenden Zeitskalen ablaufen, ausgebaut. Ein besonderer Schwerpunkt liegt auf dem Wassermanagement als Grundstein für hochdynamischen und effizienten Betrieb. Im Gegensatz zur umfangreichen veröffentlichten Forschung beinhaltet diese Arbeit zwei unzureichend beleuchtete Felder. Zum einen ist der hochdynamische Betrieb auf Zeitskalen von 1 s im Fokus. Zum anderen werden die Subsysteme, die eigene dynamische Limitierungen aufweisen, in dieser Arbeit mit berücksichtigt. Kernbeitrag dieser Arbeit sind umfangreiche dynamische Experimente, die mit einem hochentwickelten Automotive-Brennstoffzellensystem durchgeführt werden.

Die Arbeit ist entlang von vier Forschungsfragen aufgebaut. Zuerst werden die dominanten zeitabhängigen Prozesse mittels dynamischen Simulationen und Experimenten identifiziert. Danach werden die Planung und mögliche Schwierigkeiten von dynamischen Experimenten gemeinsam mit deren Beiträgen zur verbesserten Modellierung beschrieben. Nachfolgend werden stationär-basierte Betriebsstrategien bewertet, deren Grenzen beschrieben und verbesserte Betriebsstrategien für den hochdynamischen Betrieb entwickelt. Als Letztes wird der Einfluss von zwei zentralen Freiheitsgraden auf Systemebene, Betriebsstrategie und Systemarchitektur, auf Effizienz und Dynamik diskutiert. Insgesamt folgt der Aufbau dieser Arbeit der Logik *von einer Brennstoffzelle zu einem Brennstoffzellen-System zu anderen Systemen.* Zell-interne Prozesse werden zuerst erklärt, dann das Zusammenspiel von Stack und System diskutiert und abschließend die Ergebnisse auf andere Systeme übertragen.

Membran-Befeuchtung und -Trocknung beeinflussen das dynamische Verhalten des Stacks stark. Darüber hinaus spielt die Ansammlung und der Austrag von Flüssigwasser eine wichtige Rolle, da Flüssigwasser die für die Reaktantendiffusion zur Verfügung stehende Querschnittsfläche limitiert. Bei einer hochdynamische Leistungserhöhung führt zuviel Flüssigwasser schnell zu einer Reaktantenverarmung, während die gleiche Flüssigwassermenge bei Niedriglast zulässig ist. Da verbreitete Short-Stack-Prüfstände die dynamischen Fähigkeiten von Automotive-Brennstoffzellensystemen nicht abbilden können, muss die Übertragbarkeit der Ergebnisse überprüft werden. Der hochdynamische Betrieb wird durch das Luftsystem beschränkt. Ein Wechsel der Luftsystem-Architektur oder der Betriebsstrategie hin zu höheren Dynamik-Fähigkeiten verschlechtert die Systemeffizienz, was eine Abwägung zwischen den widersprüchlichen Zielen notwendig macht.

Stichworte: Brennstoffzellensystem, dynamischer Betrieb, Wassermanagement

Contents

List of Figures

List of Tables

Acronyms & Symbols

Acronyms

ACL Anode Catalyst Layer

AirS Air System

ARB Anode Recirculation Blower

AST Accelerated Stress Test

BC Boundary Condition

BEV Battery Electric Vehicle

BPP Bipolar Plate

CCL Cathode Catalyst Layer

CVM Cell Voltage Monitoring

EAC Electric Air Compressor

ECSA Electrochemical Surface Area

EIS Electrochemical Impedance Spectroscopy

ElecS Electrical System

EOD Electro-Osmotic Drag

FCCU Fuel Cell Control Unit

FCS Fuel Cell System

FCEV Fuel Cell Electric Vehicle

GDL Gas Diffusion Layer

GHG Greenhouse Gas

HOR Hydrogen Oxidation Reaction

HyS Hydrogen System

ICE Internal Combustion Engine

IEA International Energy Agency

IPCC Intergovermental Panel on Climate Change

KPI Key Performance Indicator

LTI Linear Time Invariant

MEA Membrane Electrode Assembly

MPL Micro-porous Layer

ORR Oxygen Reduction Reaction

PEM Polymer Electrolyte Membrane

PEMFC Polymer Electrolyte Membrane Fuel Cell

PFSA Perfluorosulfonic Acid

PTFE Polytetrafluoroethylene

SoC State of Charge

TAC Turbine Air Charger

ThS Thermal System

UN United Nations

USDoE United States Department of Energy

VCU Vehicle Control Unit

WLTC Worldwide harmonized Light-duty vehicles Test Cycle

Symbols

Latin Symbols

a	-	Water activity
A	m^2, -	Area, amplitude
C	-, F	Constant, capacitance
c_p	$J\,kg^{-1}\,K^{-1}$	Specific heat capacity
D	$m^2\,s^{-1}$	Diffusion coefficient
d	m	Diameter
E	$J\,mol^{-1}$	Molar activation energy
f	Hz	Frequency
F	$C\,mol^{-1}$	Faraday constant
g	$J\,mol^{-1}$	Molar Gibbs free energy
h	$W\,m^{-2}\,K^{-1}$	Heat transfer coefficient
HFR	-	High Frequency Resistance
I	A	Current
i	$A\,m^{-2}$	Current density
j	-	Placeholder for species j
J	$kg\,m^{-2}$	Moment of inertia
k	-	Running variable
K	m^2-	Hydraulic permeability, amplification factor

L	m	Reference length
LHV	Jkg^{-1}	Lower Heating Value
M	Nm, $kgmol^{-1}$	Torque, molar mass
$\dot{m}$	kgs^{-1}	Mass flow
m	kg	Mass
$\dot{n}$	$mols^{-1}$	Molar flux
n	min^{-1}, -, mol	Speed, number of cells, amount of substance
p	Pa	Pressure
P	W	Power
r	Ωm^{-2}	Area-specific electrical resistance
R	Ω	Electrical resistance
RH	%	Relative humidity
R_j	$Jkg^{-1}K^{-1}$	Specific gas constant of species j
R_m	$Jmol^{-1}K^{-1}$	Universal gas constant
$RMSD$	-	Root Mean Square Deviation
s	-, $Jmol^{-1}$	Liquid water saturation, specific entropy
t	s	Time
T	K	Temperature
u	ms^{-1}, -	Velocity, input function
U	V	Voltage
V	m^3	Volume
w	-	Weight function
$\dot{Q}$	W	Rate of heat flow
x	-	Molar fraction
y	-	Output function
z	-	Number of electrons involved in electrode reaction

Greek Symbols

α	m^2s^{-1}, -	Thermal diffusivity, charge transfer coefficient
δ	m	Thickness
ϵ	-	Porosity
η	-	Efficiency
γ	-, -	Kinetic reaction order, heat capacity ratio
κ	Sm^{-1}, $Wm^{-1}K^{-1}$	Electronic conductivity, thermal conductivity
λ	-, -	Stoichiometry, membrane water content
ω	$rads^{-1}$	Angular velocity
φ	rad	Phase angle
Π	-	Pressure ratio
Ψ	-	Water vapor factor
ρ	kgm^{-3}	Volumetric density
σ	Sm^{-1}	Ionic conductivity
τ	s, -	Time constant, tortuosity

Indexes

abs	Absolute
accum	Accumulation
act	Activation
an	Anode
amb	Ambient
ca	Cathode
cap	Capillary
comp	Compression
conc	Concentration
cond	Conduction, condensation
cons	Consumed
cont	Contact
cool	Coolant
diss	Dissipative
drain	Drainage
el	Electric
eq	Equivalent
evap	Evaporation
(g)	Gaseous
h	Hydraulic
im	Immobile
in	Inlet
init	Initial
is	Isentropic
(l)	Liquid
lim	Limit
mem	Membrane
ohm	Ohmic
out	Outlet
por	Porous
ref	Reference
rel	Relative
rev	Reversible
(s)	Sorbed
sat	Saturation
sec	Cross-sectional
sorp	Sorption
spec	Specific
tot	Total
tr	Transfer

Chapter 1

Introduction

"All global modelled pathways that limit warming to 1.5°C with no or limited overshoot, and those that limit warming to 2°C, involve rapid and deep and in most cases immediate GHG emission reductions in all sectors."[1]

This conclusion of the latest report of the Intergovermental Panel on Climate Change (IPCC) calls for immediate and decisive action to limit the Greenhouse Gas (GHG) emissions in the near future. Climate action is even one of the *Sustainable Development Goals* set by the United Nations (UN)[2]. Political measures are taken, as e.g. with the Kyoto protocol and Paris agreement, and most countries subsequently implemented more or less ambitious national goals. However, the GHG emissions are still rising globally[1], exacerbating global warming and its consequences. One main contributor is the transport sector with a share of 23% of global energy-related CO_2 emissions, with 70% of the direct transport emissions stemming from road vehicles[3]. Introducing new technologies in the mass market to drastically reduce the carbon footprint of road vehicles is a necessary development. In 2022, a majority of the European Parliament's members voted in favor of a zero-emission target for passenger cars and light duty vehicles to be reached in 2035[4]. However, the technical challenges that must be overcome are demanding, and a combined effort containing governmental restrictions and incentives, academic and industrial research as well as investments in the infrastructure is needed.

In the last years, Battery Electric Vehicles (BEVs) gained market share due to a significant cost reduction[1], national subvention programs[5] and increasing restrictions on Internal Combustion Engine (ICE) vehicles. BEVs especially with higher range require large batteries with capacities of up to 100 kWh, some even above, leading to expensive and heavy vehicles compared to their ICE-driven counterparts. Furthermore, the electricity for charging must be supplied by the grid at the exact moment when the vehicle is charged, a growing challenge due to an increased share of volatile renewable energy sources.

Fuel Cell Electric Vehicles (FCEVs) are promising to complement BEVs. When fueled with green hydrogen produced from renewable sources, FCEVs operate without emission of GHG and are fast to refuel. As renewable energy sources are inherently volatile, large scale energy storage concepts must be implemented. One possible approach is the storage in hydrogen, which can be produced from water via electrolysis. Multiple manufacturers sell FCEVs, but the International Energy Agency (IEA) estimated that only 51,600 FCEVs were in operation in 2021[6]. Refueling stations are still relatively sparse, leading to a chicken and egg problem of vehicles and infrastructure.

In addition to the infrastructural challenges, further development of the fuel cell technology for vehicle application is necessary. Detailed technical targets, formulated in terms of power density, efficiency, cost and durability are published e.g. by the United States Department of Energy (USDoE)[7]. While power densities and efficiencies close to the USDoE's ultimate targets are already achieved, the system cost must be lowered and the durability substantially

increased[7]. In addition to the aforementioned cost and durability targets, Klell, Eichsleder and Trattner present an improvement of dynamic performance as a third major difficulty requiring further research[8].

The automotive application requires challenging dynamic capabilities. If one for example wants to overtake another vehicle, a fast adaption of the electrical power available to the drive-train is expected. It takes a classic turbocharged ICEs between 1 s and 3 s[9,10] to reach 90 % of its maximum torque, the so called time-to-torque. Advanced concepts with electrically assisted turbochargers are capable of time-to-torques between 0.45 s and 0.95 s[9], while BEVs achieve even higher dynamics. A customer therefore expects a FCEV to achieve comparable power dynamics as an ICE vehicle, maybe in the near future even leaning more towards the higher BEV dynamics. As the FCS is hybridized with a battery, the battery's size and therefore its maximum power is limited by cost and volume constraints. Vehicle setups, where the battery is incapable of supplying the full electric power required by the drive-train are called *fuel cell dominant* and they result in the most challenging dynamics requirements for the FCS. If such a highly dynamic operation is mastered, the gained knowledge can be easily transferred onto less dynamically operated systems, while this is certainly invalid the other way round.

For automotive fuel cell systems, stacks of PEMFCs supplied with hydrogen from a tank and oxygen from the ambient air are predominantly used, as they offer high power densities and fast start-up capabilities. Additional components such as an air compressor, valves, radiators, a coolant pump and a recirculation blower are needed to supply the reactants and coolant to the stack, collectively referred to as the FCS. These components feature intrinsic dynamics, interacting with the fuel cell stack and its efficiency. Attention must also be paid to states known to degrade the PEMFC stack, which can occur especially during non-steady-state operation.

The performance of the PEMFCs itself depends on the protonic conductivity of the membrane, which is a function of the membranes' water content. Also, liquid water can hinder the reactant supply to the active sites, reducing the fuel cell's performance. The humidification state must therefore be balanced between too dry conditions with high membrane resistance and too wet conditions, where liquid water blocks the reactant paths. Note that both extremes occur simultaneously within a fuel cell, as the humidification state varies locally. The challenge of controlling the humidification is referred to as water management, and is the centerpiece of this work. In fuel cell systems, a balanced humidification state can be achieved during stationary operation. This is done by an adequate selection of operating conditions, such as pressure, temperature and mass flow of the gases, as well as temperature and mass flow of the coolant. However, the common stationary-based approaches are insufficient during the highly dynamic operation targeted in this work, as the subsystems' and stack's intrinsic dynamics span widely varying time scales. These differences may lead to a mismatch of the required stack supply and the ability of the adjacent subsystems to fulfill them, potentially resulting in critical states with exacerbated aging.

Even though tremendous effort during multiple decades of research went into the understanding of water management in PEMFCs, a substantial gap needs to be bridged towards the application in fuel cell dominant vehicles. Three major points differentiate this work from the research published in literature. First, the time scale of the power dynamics are comparably fast, aiming at the order of 1 s as required by the application. Second, the whole FCS is in scope of this work. The limited subsystem dynamics yield a major influence on the stack

behavior, which cannot be addressed properly with the common, steady-state oriented and stack-focused view. Third, a sophisticated test system is analyzed experimentally. System level research is already less common in literature, but especially experimental research is sparse to non-existent in the open literature. However, it is inevitable to validate empirical simulation models, and the subsystem interactions in a realistic, application-like setting.

To summarize, this work aims at building up knowledge on the central effects during highly dynamic operation and addresses the impact of system level levers such as control strategy and system architecture on efficiency and dynamic capabilities. Understanding the key interactions within the system is the focus of this work, rather than an optimization of a certain architecture or even single components. Also, developing detailed sub-models is not in scope of this work, but established empirical models from fundamental fuel cell research are utilized and checked against experimental results.

Chapter 2

Fundamentals, Challenges and Methodology

This chapter aims at providing the basics of PEMFC operation, challenges of fuel cell systems in the context of the automotive application and the methodology chosen throughout this work. Therefore, a brief discussion of the PEMFC and the whole FCS functionality is presented and the precise terminology definitions are introduced. Subsequently, the key challenges of water management as one central pillar of this work are explained together with strategies to influence it in a favorable manner. The understanding of these interactions is fundamental for the rest of this work. For guidance throughout the whole work, four central research questions are introduced. Also, the scope, methodology and chapter setup which is based on the research questions is explained.

2.1 PEM Fuel Cells

2.1.1 Working principle

Fuel cells harness an electro-chemical reaction to convert chemical energy into electrical energy and heat. In PEMFCs, the fuel is hydrogen stored in a high pressure tank, while the oxidant is oxygen, taken from the ambient air in ground-based applications. Hydrogen and oxygen form water, a non-toxic product.

$$2\,H_2 + O_2 \longrightarrow 2\,H_2O \tag{2.1}$$

Figure 2.1 shows the schematic setup of a modern PEMFC. The two flat electrodes, cathode and anode, form the centerpiece of the Cathode Catalyst Layer (CCL) and the Anode Catalyst Layer (ACL). They are separated by a proton-conductive electrolyte membrane. At each electrode, a sub-reaction of the overall fuel cell reaction takes place. As expressed by Equation 2.2, hydrogen is split into protons and electrons in the Hydrogen Oxidation Reaction (HOR) at the anode. The protons transfer from the anode to the cathode via the PEM, while the electrons are conducted through the other layers of the fuel cell. At the cathode, water forms from oxygen and protons in the Oxygen Reduction Reaction (ORR) shown in Equation 2.3.

$$2\,H_2 \longrightarrow 4\,H^+ + 4\,e^- \tag{2.2}$$

$$O_2 + 4\,e^- + 4\,H^+ \longrightarrow 2\,H_2O \tag{2.3}$$
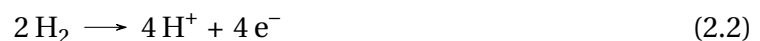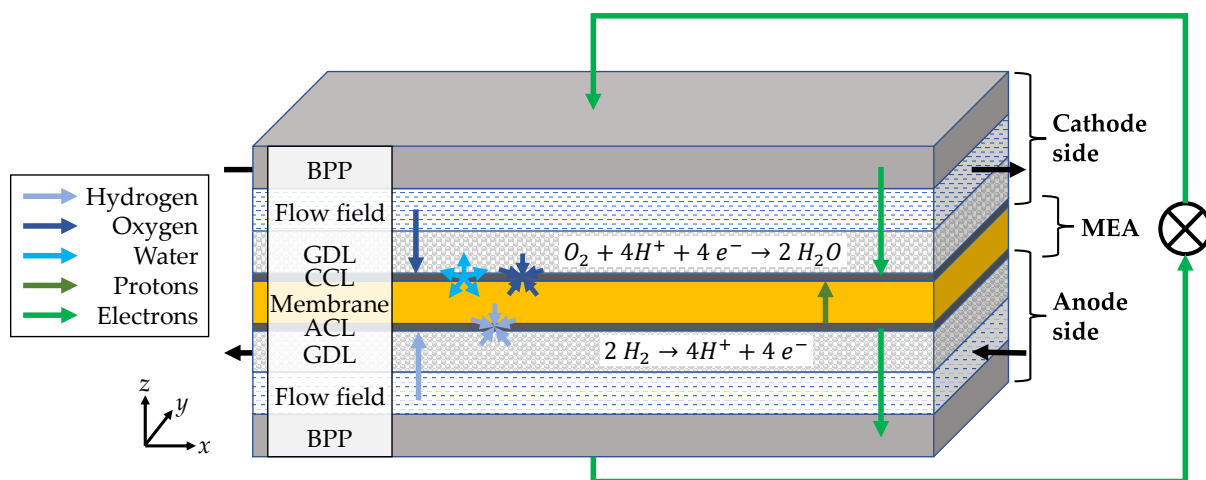
FIG. 2.1 Schematic setup of a PEMFC.

Both reactions proceed at a three-phase boundary, where electrode, electrolyte and reactant are present. To maximize the surface area, the electrodes are made of a conductive porous medium, such as a carbon fiber structure. The electrodes and the membrane are often referred to as Membrane Electrode Assembly (MEA), as the electrodes are attached directly onto the membrane early in the production process. The membrane material predominately used in low temperature PEMFCs is based on Perfluorosulfonic Acid (PFSA), also sold under the brand name Nafion®. To increase the reaction rate, a catalyst is dispersed in small particles on the electrode structure. The most common catalyst in PEMFCs is platinum, although attempts are made to substitute the relatively scarce and expensive material[11].

To distribute the reactants across the whole active area and transport the produced water out of the cell, additional layers are introduced. The GDLs foster reactant diffusion towards the active sites and conduct the electrons and the heat produced by the reaction. They are typically constructed from porous media, such as carbon paper or carbon cloth[12]. A hydrophobic agent such as Polytetrafluoroethylene (PTFE) is often added to reduce the liquid water accumulation within the GDLs at the cost of a reduced porosity, adversely affecting oxygen transport[13]. Sometimes, the GDL is combined with a Micro-porous Layer (MPL), to enhance the liquid water transport and lower the contact resistance occurring at its interface with the catalyst layer[13,14].

The reactants fed into the cell are transported through the flow fields. Most commonly, parallel channel/land flow fields are implemented, although alternative channel geometries remain a research focus[15,16]. The last component of the PEMFC is the Bipolar Plate (BPP). It provides the electrical connection to the current collector or adjacent cells and is either made of carbon-based material such as graphene[17] or metals[18]. Note that the BPP and flow field can be one part or two separate components, depending on the selected cell design.

2.1.2 Performance and loss contributions

If the fuel cell is in operation, multiple loss mechanisms reduce the technically usable cell voltage U_{cell}. Starting from the reversible cell voltage U_{rev}, multiple loss contributions must be subtracted as stated in Equation 2.4. They are usually stated as voltage losses ΔU and

can be divided into three groups: activation losses, ohmic losses and concentration or mass transport losses[19]. Depending on the fuel cell operating point, meaning the selected current and reactant supply conditions, the share of each loss contribution varies.

$$U_{\text{cell}} = U_{\text{rev}} - \Delta U_{\text{act}} - \Delta U_{\text{ohm}} - \Delta U_{\text{conc}} \tag{2.4}$$

The reversible cell voltage for a hydrogen fuel cell is calculated from the change in molar Gibbs free energy Δg of the overall reaction given in Equation 2.1and Faraday's constant F[20]:

$$U_{\text{rev}} = \frac{-\Delta g\left(T, p\right)}{2F} \tag{2.5}$$

The electro-chemical reactions introduced in Equation 2.2 and Equation 2.3 proceed with a limited reaction rate. This limitation causes the activation voltage loss ΔU_{act}, which depends on the drawn current density i. The current density is the area specific density of charged ions transversing the electrolyte membrane. The reaction rate dependence is often described with the Butler-Volmer equation, which derivation and underlying phenomena are explained in detail for example by Newman and Thomas-Alyea[21]. In short, the current density depends on the temperature T, the apparent transfer coefficients of anode and cathode, α_{an} and α_{ca}, the number of electrons per ion involved in the electrode reaction, z, and the exchange current density i_0:

$$i = i_0 \left[\exp\left(\frac{z\alpha_{\text{an}}F\Delta U_{\text{act,an}}}{R_{\text{m}}T} \right) - \exp\left(\frac{z\alpha_{\text{ca}}F\Delta U_{\text{act,ca}}}{R_{\text{m}}T} \right) \right] \tag{2.6}$$

If the exchange current density i_0 is orders of magnitude smaller than the measured current density i, the Butler-Volmer equation can be simplified into the Tafel equation[19]. In PEMFCs, the activation losses caused by the ORR typically outweigh the losses from the HOR by far, simplifying the equation for the activation losses even further[19] to

$$\Delta U_{\text{act}} = \frac{R_{\text{m}}T}{2\alpha F} \ln\left(\frac{i}{i_0} \right). \tag{2.7}$$

In the following, only the cathode reaction as the main loss contributor is considered. Then, the exchange current density is a function of the reference exchange current density $i_{0,\text{ref}}$, the oxygen partial pressure p_{O_2}, the ORR kinetic reaction order γ and the activation energy for the ORR $E_{\text{ca}}^{\text{rev}}$[21]:

$$i_0 = i_{0,\text{ref}} \left(\frac{p_{O_2}}{p_{O_2,ref}} \right)^{\gamma} \exp\left[-\frac{E_{\text{ca}}^{\text{rev}}}{R_{\text{m}}T} \left(1 - \frac{T}{T_{\text{ref}}} \right) \right] \tag{2.8}$$

Next, the group of ohmic loss contributions ΔU_{ohm} is in focus. Ohmic losses are caused by the finite electronic and protonic conductivity of the layers and the non-ideal contact between the layers. For simplification, the ohmic losses are divided into only two contributions, one that is a function of the current only, and one that also depends on the humidification state. First, the area specific contact resistance r_{cont} is assumed to be constant and independent of the humidification state. Within this work, this resistance also accounts for all other constant ohmic contributions, such as the layer's individual resistance. Second, the membrane loss ΔU_{mem} is considered as an ohmic contribution which also depends on the fuel cells humidification state. The membrane's protonic conductivity σ_{mem} is heavily dependent on its water

content λ_{mem}, which is defined later in Equation 2.26 and represents one core impact of water management. This is further elaborated in Section 2.3. In total, the ohmic loss contributions yield a simple linear dependence on the current density:

$$\Delta U_{\text{ohm}} = \Delta U_{\text{cont}} + \Delta U_{\text{mem}} = i \left(r_{\text{cont}} + \frac{1}{\sigma_{\text{mem}}} \right) \tag{2.9}$$

Last, the concentration losses ΔU_{conc}, also referred to as mass transport losses[19], conclude the discussion on the most relevant loss contributions. As reactants are consumed at the electrodes, a continuous supply matching the consumption must be maintained. This mass transport results in a reduction of the reactant concentration available at the electrodes. If the complete supplied flux of reactants is consumed at the electrode, the limiting current density i_{lim} is reached. Subsequently, the concentration losses are calculated as

$$\Delta U_{\text{conc}} = \frac{R_{\text{m}} T}{2F} \ln \left(\frac{i_{\text{lim},H_2}}{i_{\text{lim},H_2} - i} \right) + \frac{R_{\text{m}} T}{4F} \ln \left(\frac{i_{\text{lim},O_2}}{i_{\text{lim},O_2} - i} \right). \tag{2.10}$$

Note that there is an individual limiting current for each electrode, meaning that either the cathode, the anode or both electrodes can lack proper reactant supply causing increased concentration losses. In a simplified model assuming Fickian diffusion, the limiting current density depends on the reactant partial pressure in the flow field p_{FF}, the gas diffusion coefficient D and the GDL thickness δ_{GDL}[22]:

$$i_{\text{lim},O_2} = \frac{4FD_{O_2}}{\delta_{\text{GDL}}} \frac{p_{O_2,\text{FF}}}{R_{O_2} T} \tag{2.11}$$

$$i_{\text{lim},H_2} = \frac{4FD_{H_2}}{\delta_{\text{GDL}}} \frac{p_{H_2,\text{FF}}}{R_{H_2} T} \tag{2.12}$$

If all loss contributions are combined, a polarization curve relating the cell voltage and the area specific current density can be derived. In fuel cell research and application, this is a widespread representation of the fuel cell's performance. An exemplary polarization curve is depicted in Figure 2.2. Three regions can be distinguished based on the dominant voltage loss mechanism. At lower current densities, the activation losses are by far the largest loss contributor. With rising current density, the ohmic loss contributions caused by the non-ideal electric contact between the layers and the membrane's limited protonic resistance grow almost linearly. At high current densities, the concentration losses cause a steep non-linear cell voltage decline. Please note that this polarization curve has been derived for a single PEMFC. The behavior of the overall stack consisting of many cells put in series is analogous, but may differ in some details.
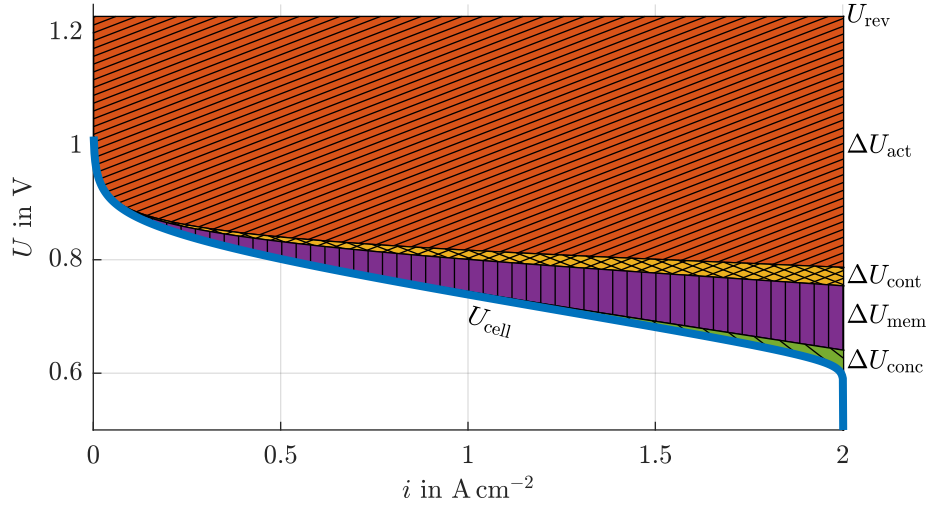
FIG. 2.2 Exemplary polarization curve and voltage loss contributions of a PEMFC.

2.2 PEM Fuel Cell Systems

2.2.1 General structure

The operating voltage of a single cell typically lies between 0.65 V and 0.85 V, multiple orders of magnitude too low for the automotive application. Therefore, several hundred cells are piled to a fuel cell stack. The cells are connected electrically in series by the BPPs and clamped together via end plates combined with bolts or belts[23]. To provide each cell with the reactants and coolant required for operation, the gases and the liquid coolant are distributed between the cells by manifolds. In result, the cells are connected in parallel in the fluidic domain.

Four additional subsystems are required to operate the stack, as shown schematically in Figure 2.3. The Air System (AirS) supplies ambient air to the cathode side of the stack and handles the exhaust gas stream. An Electric Air Compressor (EAC) pressurizes the air, consuming electrical power P_{EAC}. The electric power distribution and the control of the stack current is managed by the Electrical System (ElecS). In a vehicle, the ElecS also controls the charging and discharging of the battery and supplies the drive-train motor with the respective power P_{drive}. Optimizing the energy management between FCS and battery during vehicle operation is a highly relevant adjacent research topic referred to as "power split"[24], but not in scope of this work.

To radiate the heat produced by the stack to the environment, a Thermal System (ThS) is implemented. It mainly consists of a liquid coolant circuit, connecting a radiator with the stack. A pump drives the coolant through the stack and the coolant circuit. The Hydrogen System (HyS) supplies the stack with hydrogen from the tank, where hydrogen is stored under a pressure of up to 700 bar. Typically, the anode exhaust gas is recirculated in an anode loop. As water and nitrogen transported from the cathode to the anode side reduces the share of hydrogen within the loop, it is frequently opened, a state called purging. This decreases the nitrogen and water fraction on the anode side.

Note that the chosen system boundary is closely aligned with the test setup in focus of this work. All subsystems inside the FCS boundary are implemented in hardware at the test rig.

8
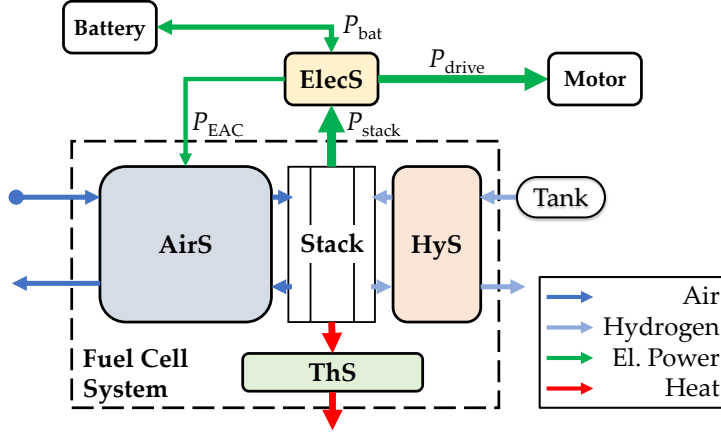
FIG. 2.3 Schematic layout of a FCS with its main subsystems.

While the ElecS is emulated by the test rig, motor and battery are not part of the experimental setup. The hydrogen is supplied from bottles rather than a vehicle tank.

2.2.2 System level equations

An important variable for system operation is the stoichiometry. It represents the proportion between the supplied and consumed reactant molar fluxes. As the reactant consumption is directly proportional to the drawn current[19], two simple equations for the cathode stoichiometry λ_{ca} and anode stoichiometry λ_{an} can be stated as

$$\lambda_{\text{ca}} = \frac{\dot{n}_{\text{O}_2,\text{in}}}{\dot{n}_{\text{O}_2,\text{cons}}} = \dot{n}_{\text{O}_2,\text{in}} \frac{4F}{I} \tag{2.13}$$

and

$$\lambda_{\text{an}} = \frac{\dot{n}_{\text{H}_2,\text{in}}}{\dot{n}_{\text{H}_2,\text{cons}}} = \dot{n}_{\text{H}_2,\text{in}} \frac{2F}{I}. \tag{2.14}$$

Note that four electrons per oxygen molecule, but only two electrons per hydrogen molecule take part in the HOR and ORR described by Equation 2.2 and Equation 2.3, respectively.

Understanding, optimizing and actively shaping the flux of electrical power within the FCS is a central challenge. The electrical power produced by the stack results from the stack voltage and the drawn current I:

$$P_{\text{stack}} = U_{\text{stack}} I \tag{2.15}$$

However, driving the EAC may consume 20 % of the stack power P_{stack}[19], reducing the available net power of the FCS. While the coolant pump in the ThS and, if there is one, an Anode Recirculation Blower (ARB) implemented in the HyS require electrical power as well, their consumption typically is around an order of magnitude lower than the power demand of the EAC in typical passenger car systems. Within this work, only the main contributions of stack and EAC to the net system power P_{net} are considered:

$$P_{\text{net}} = P_{\text{stack}} - P_{\text{EAC}} \tag{2.16}$$

The EAC power P_{EAC} depends on the isentropic compressor efficiency $\eta_{\text{is,comp}}$, the electrical drive efficiency η_{el}, the air mass flow $\dot{m}_{\text{air}}$, the inlet temperature T_{in}, the heat capacity ratio γ

and the pressure ratio Π:

$$P_{\text{EAC}} = \frac{1}{\eta_{\text{is,comp}}\eta_{\text{el}}} \dot{m}_{\text{air}} c_p T_{\text{in}} \left[\Pi^{\frac{\gamma-1}{\gamma}} - 1 \right] \tag{2.17}$$

The hydrogen consumption during a drive cycle is one of the main variables of interest on the vehicle level. If the fuel consumption is decreased, a higher driving range can be achieved with hydrogen tanks of the same size. In addition, a lower consumption reduces the operating cost. In scope of this work, the time-dependent system efficiency is defined via the Lower Heating Value LHV_{H_2} at a constant temperature of 25 °C as[25]

$$\eta_{\text{sys}} = \frac{P_{\text{net}}}{LHV_{\text{H}_2} \dot{m}_{\text{H}_2}}. \tag{2.18}$$

Similarly, the total system efficiency $\eta_{\text{sys}}^{\text{tot}}$ for a whole drive cycle lasting from t_0 to t_1 is calculated by

$$\eta_{\text{sys}}^{\text{tot}} = \frac{\int_{t_0}^{t_1} P_{\text{net}} dt}{LHV_{\text{H}_2} \int_{t_0}^{t_1} \dot{m}_{\text{H}_2} dt}. \tag{2.19}$$

The hydrogen mass flow $\dot{m}_{\text{H}_2}$ supplied to the system can be divided into two shares: the fuel losses and the hydrogen consumed by the fuel cell reaction. The latter can be calculated analytically as stated in Equation 2.14 and depends only on the current. The fuel losses are predominantly caused by the purging of the HyS as well as hydrogen cross-over towards the cathode. In this work, three different quantities will be displayed frequently. The first two quantities target the system's stationary performance, either expressed in terms of net power, as introduced in Equation 2.16, or in terms of the Key Performance Indicator (KPI) system efficiency shown in Equation 2.19. For the latter, the fuel losses are ignored, as they are challenging to track and expected to exhibit only minor variations between the selected comparisons.

The third quantity addressed in this work is the KPI system power dynamics. If a driver wants to accelerate the vehicle, the system should provide the requested electrical power to the motor quickly. What kind of power trajectory the driver perceives as "ideal" is highly subjective. For example, the driver of a sports car expects other power dynamics than the driver of a van. Even between customers of one car manufacturer, the expected power dynamic trajectory might differ. Within this work, a simplified approach is taken. The system power dynamics are calculated based on the time $t_{90,\text{P}_{\text{drive}}}$ it takes the fuel cell system together with the battery to provide a net system power of 90 % of the requested power $P_{\text{drive}}^{\text{req}}$, starting from idle power:

$$P_{\text{drive}}\left(t = t_{90,\text{P}_{\text{drive}}}\right) = 0.9 P_{\text{drive}}^{\text{req}} \tag{2.20}$$

A fuel cell dominant vehicle is selected in this work, which features a rather small battery and results in the most challenging required fuel cell system dynamics. The Toyota Mirai is such a fuel cell dominant vehicle, with a battery capacity of only 1.4 kWh[25]. It can provide a maximum electrical power of 20 kW[25], roughly a fifth of the fuel cell system's power, as the power output of batteries is proportional to their capacity. A lower capacity battery however yields the benefits of reduced cost, volume and mass. Within this work, it is assumed that a small battery is installed, which can provide an electrical power of up to 30 kW. It is paired with an FCS capable of supplying around 100 kW system net power.

Figure 2.4 illustrates possible trajectories of system net power P_{net}, the power available at the drive train P_{drive} and the power gap to be bridged by the battery P_{bat}. With the battery, a faster increase in available drive power is achieved. Note that the battery is only active if the requested power is increased, as the stationary net power shall be provided by the fuel cell system. In such a concept, the energy taken from the battery during the power increase is negligibly small, as its power is only required for a couple of seconds.
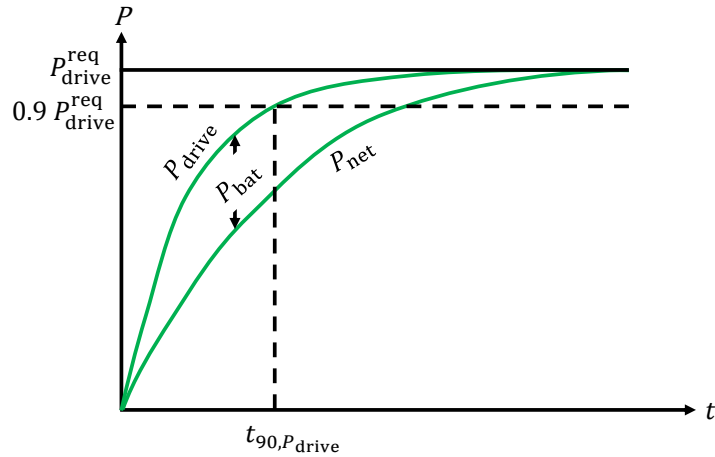
FIG. 2.4   Exemplary dynamic response of the system net power and the battery's contribution to the available driving power.

As dynamic operation is crucial for the vehicle application, a detailed introduction to the central research field limiting the achievable system dynamics is up next: the water management.

2.3   Dynamic Water Management

2.3.1   Definitions

The term "water management" is well established in PEMFC research. However, it is seldom defined precisely and rather applied to a broad range of topics. Depending on the focus of the research, the term might describe different phenomena. For example, the transport of water in dedicated layers, such as the MPL[26] or the GDL and flow field[27]. Such a definition is too narrow for the scope of this work. Therefore, the following definition of water management is chosen:

Water management summarizes the tracking and controlling of supplied and produced water, its storage, distribution and transport within the fuel cells and adjacent subsystems by the means of system level levers in a favorable way.

Tracking and controlling in the FCS context indicates, that the water distribution must be estimated from ex-situ measurements and is actively influenced by *the means of system level levers*. These levers might be the system's architecture, meaning the selection and layout of its components, or the control strategy, referring to the operating conditions of the stack, which are chosen to satisfy a certain power demand. Design changes within the stack, such as adapting the flow field geometry and surface treatment, as well as for example changes

11

in GDL or MEA material selection, are explicitly excluded from the term *system level means*. Water management, as defined in this work, should be an approach generically enough to cope with variations of components within the system.

Water is not only formed by the fuel cell reaction within the stack, but also fed into the cells as vapor carried by the anode and cathode inlet gas streams, as implied by the term *supplied and produced*. Depending on the system architecture, the inlet humidity provided by *adjacent subsystems* might differ substantially, impacting the stack-internal water distribution and transport.

As the key element of this work, dynamic operation is defined as a time-dependent change in one or more stack boundary conditions. An overview of these boundary conditions is given later in Subsection 2.3.4. From a water management point of view, considering transient effects requires to account for *storage* of water in gaseous, liquid and sorbed form. However, common water management research is centered around stationary phenomena, therefore aiming predominantly on the time-independent *distribution and transport. In a favorable way* implies, that system level architecture and operation should be adapted in terms of a threefold top level goal:

1. The system's efficiency shall be increased.
2. The system's dynamic capabilities shall be improved.
3. Critical states shall be avoided.

These goals are discussed later in context of this work's setup shown in Section 2.4. But first, a fundamental understanding of the water management challenges is needed.

2.3.2 Dry-out and flooding

The interaction between the most relevant water management variables is shown in Figure 2.5. Two paths impact the cell voltage, one via the ohmic losses caused by the membrane and another one via the concentration losses. A dry-out of the membrane causes high ohmic losses, as depicted schematically by the red polarization curve in Figure 2.6. Flooding refers to a state, where liquid water hinders the reactant diffusion, resulting in increased concentration losses as shown by the blue curve. Understanding[28], monitoring[29,30] and mitigating[31] the dry-out and flooding phenomena in stationary operation is a field targeted by numerous researchers. A comprehensive review on flooding studies in literature is for example given by Ijaodola et al.[32]. Next, the detailed interaction and variable definitions relevant in scope of this work are discussed in detail.
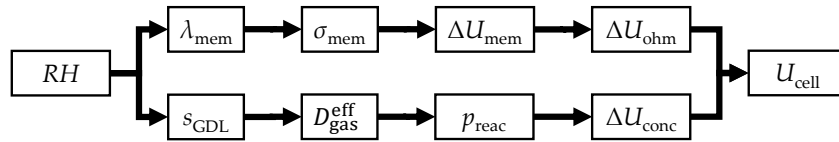
FIG. 2.5 Interaction of the most relevant variables for water management.

First of all, the relative humidity *RH* is defined via the partial pressure of water p_{H_2O} and the saturation pressure $p_{H_2O}^{sat}$ as

$$RH = \frac{p_{H_2O}}{p_{H_2O}^{sat}(T)} \leq 100\,\%.$$

(2.21)
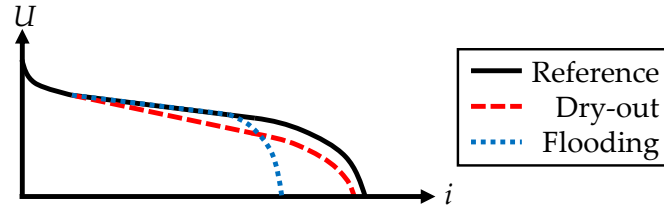
FIG. 2.6 Schematic impact of flooding and dry-out on the polarization curve.

The saturation pressure is exponentially dependent on the temperature, as described for example by Antoine's equation

$$p_{H_2O}^{\text{sat}} = 10^{A - \frac{B}{C+T}} \tag{2.22}$$

with the constants $A = 5.11564$, $B = 687.537\,\text{K}$ and $C = 230.17\,\text{K}$[33]. Note that the saturation pressure calculated with Equation 2.22 and the mentioned constants yields the unit bar.

If RH reaches $100\,\%$, the gas phase is saturated and cannot hold more water vapor. The surplus will condensate, forming liquid water. The amount of liquid water in a multiphase volume is often quantified as liquid water saturation s, the volume fraction occupied by liquid water[34]:

$$s = \frac{V_{H_2O}^{(l)}}{V} \tag{2.23}$$

In porous media, such as the GDLs, the free volume V is the total pore volume. Liquid water decreases the effective diffusion area available for the reactant gas transport and increases the effective path length as shown schematically in Figure 2.7.
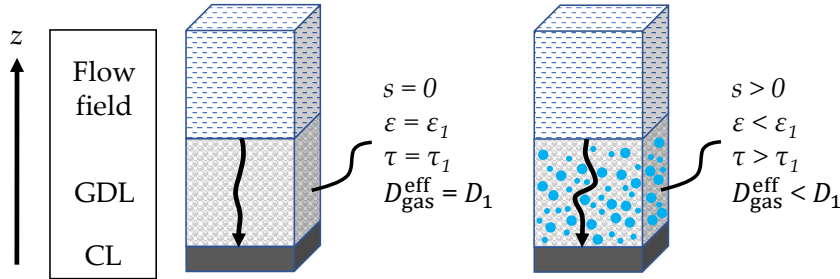
FIG. 2.7 Schematic impact of the liquid water saturation s in the GDL on porosity, tortuosity and effective gas diffusion coefficient.

In general, the impact of the solid structure of porous media on the effective gas diffusion coefficient can be described using Bruggemann's correlation. It relates tortuosity τ and the porosity ϵ, based on Bruggemann's model introduced as early as 1935[35]:

$$D_{\text{gas}}^{\text{eff}} = D_{\text{gas}} \frac{\epsilon}{\tau} \approx D_{\text{gas}} \epsilon^{1.5} \tag{2.24}$$

The impact of liquid water on the diffusion coefficient can be treated similar to a reduction in porosity and increase in tortuosity, as gas diffusion through liquid water is negligibly small[36]:

$$D_{\text{gas}}^{\text{eff}} = D_{\text{gas}} \epsilon^{1.5} (1 - s)^{1.5} \tag{2.25}$$

13

Note that the gas diffusion coefficient D_{gas} in porous GDLs can be modeled as a combined molar and Knudsen diffusion, an approach described in detail by Nonoyama et al.[37]. The reduced effective diffusion coefficient decreases the limiting current introduced in Equation 2.11 and Equation 2.12, resulting in increased concentration losses and therefore lower cell voltages and a decreased maximum achievable electrical power. As the voltage losses caused by the anode are usually smaller than the one on the cathode, flooding occurring on the anode side yields only a small reduction in measured cell voltage, while flooding on the cathode side has a stronger negative performance impact. From an ageing point of view however, anode flooding is more critical, as fuel starvation instantaneously triggers carbon corrosion[38]. Liquid water can affect the whole reactant supply path, as liquid water can limit the gas transport within the flow field, the GDL or the catalyst layer.

For the dry-out phenomenon, the membrane humidification is critical. A well established parameter to quantify this state is the water content λ_{mem}. It describes the number of water molecules sorbed in the membrane per sulfonic acid group as[39]

$$\lambda_{\mathrm{mem}} = \frac{N_{\mathrm{H_2O}}}{N_{\mathrm{SO_3H}}}. \tag{2.26}$$

Numerous empirical literature models describe the vapor sorption isotherms, linking the water content to the water activity a at the membrane interface[40]. The modeling of sorption isotherms and water transport processes is discussed in depth later in context of the simulation model development shown within Chapter 3. The water activity a is defined exactly as the relative humidity introduced in Equation 2.21, but can yield values above 1. If liquid water would occur, it is virtually added to the gas phase to reduce the complexity. Within this work, both formulations are used. For simplified approaches, such as the activity-based water management strategy described later in Subsection 2.3.4, the water activity a is utilized. Detailed analyses of the flooding phenomena with the simulation model require to distinguish between liquid water and water vapor. In this case, the liquid water saturation s in combination with the relative humidity RH are tracked.

The membrane's water content also affects its protonic conductivity σ_{mem}. The drier the membrane, the lower its protonic conductivity and the higher the resulting ohmic losses introduced in Equation 2.9. Again, a wide variety of empirical models for different membrane materials exists in the published literature[40].

An ideal fuel cell operation avoids both extremes of flooding and dry-out. To minimize the ohmic losses, the membrane should be as wet as possible. This requires high water activities at the membrane interface, a state that favors liquid water accumulation. On the other hand, this liquid water accumulation reduces the reactant supply available at the active sites. Balancing a high membrane water content and low liquid water saturation within the GDLs is therefore the central aim of water management. This approach automatically fulfills two of the three top level goals introduced in the previous subsection: Reducing losses increases the efficiency, avoiding dry membrane states and reactant starvation reduces degradation. So how can such an ideally balanced state be achieved? This is the focus of the next but one subsection, as a spatial analysis of the water management-relevant states is needed first.

2.3.3 Spatial distribution

Based on the previous discussion, one could imagine that the challenges of water management mainly revolve around the through-plane direction z. However, across the whole in-plane area xy, strong inhomogeneities in membrane water content, saturation, reactant supply and resulting voltage loss contributions occur. This distribution can be shaped by selecting a certain flow configuration. Most common is a counterflow between anode and cathode, although other flow configurations such as cross- and serpentine-flow are also of scientific interest[41]. Next is a closer look at the basic spacial inhomogeneities during stationary operation.

Figure 2.8 shows the spatial distribution of the most relevant states schematically. The oxygen partial pressure is the highest at the cathode inlet, as indicated by the trapezoid. Along the flow field, oxygen is continuously consumed and water is produced. This results in a decreasing oxygen partial pressure and an increasing relative humidity in x-direction. Within the first segment, the low relative humidity of the air supplied to the cell, causes a rather low membrane water content. The cathode inlet humidity is especially low when air systems without external humidification are installed. However, as the cathode gases' humidity rises towards the second segment, liquid water will occur within the porous GDL, as indicated by the blue dots. The gas diffusion through the GDL is slightly affected by this saturation, as introduced in Equation 2.25. A combination of low oxygen partial pressure in the cathode flow field and high saturation within the cathode GDL occurs in the last segment. This combination leads to the lowest oxygen partial pressure at the CCL.
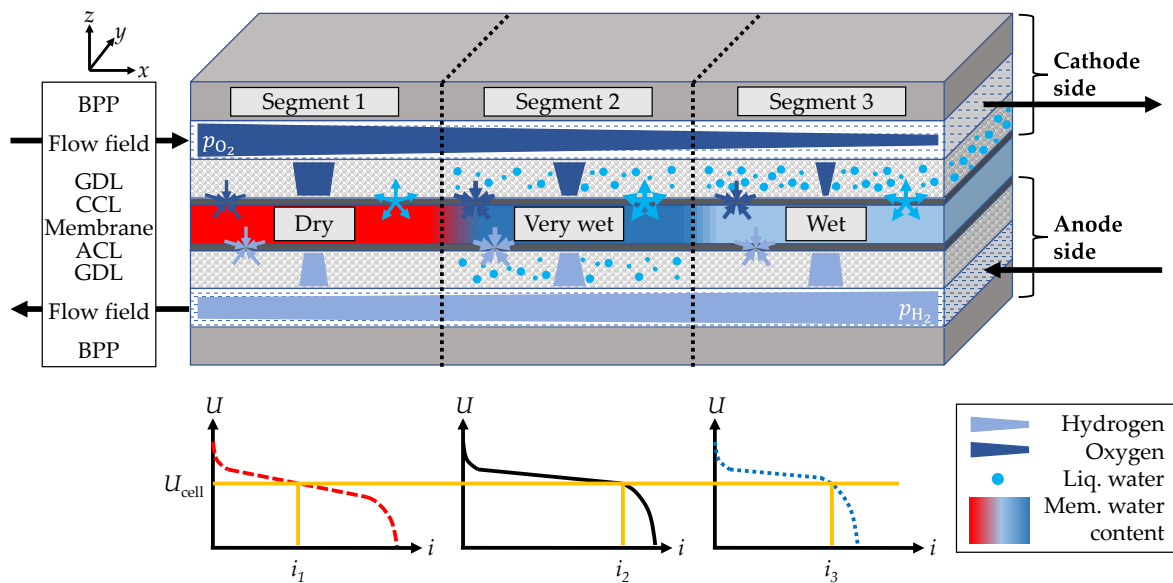
FIG. 2.8 Schematic distribution of reactant partial pressures, liquid water, membrane water content and resulting local polarization curves within a PEM fuel cell.

The anode side displays a similar behavior, although the partial pressure gradients are less pronounced. Usually, the anode is operated at a higher stoichiometry to robustly avoid fuel starvation. When looking at the local polarization curves, one finds similarities with the previously described dry-out and flooding examples. Within the first segment, the dry membrane results in high ohmic losses. In the second segment, an ideal combination of a well humidified membrane and sufficient reactant partial pressure is present. In the last

segment, the lower oxygen partial pressure causes increased concentration losses.

All segments are connected electrically in parallel by the BPPs. If one neglects the ohmic in-plane resistance of the BPP, all segments must share the same voltage. As the polarization curves vary due to the local conditions, the first and the last segment exhibit a lower current density. The total current across all segments is fixed in the galvanostatic operating mode in focus of this work, therefore a higher current density is required in the second segment. The cell voltage is therefore a result of the local conditions including the current density distribution. An increased local current density results in higher reactant demand, but also in increased water production. The water production benefits the membrane water content and causes liquid water to also occur in the anode GDL.

This example demonstrates the fundamental challenge of stationary water management: Drying and flooding might take place at the same time within one cell, as a result of spatial inhomogeneities. One can imagine that a dynamic operation of such a cell becomes even more complex. But first, the levers available in system operation and strategies how to balance the water and reactant distribution in an efficient way need to be addressed.

2.3.4 Water management strategies

In scope of this work, the term *water management strategies* describes a procedure to select the suitable stack operating conditions based on the requested power. As only *system level levers* are in scope of this work, the operation of the stack must be shaped by setting the stack boundary conditions accordingly. A sufficient set to uniquely define the stack operating states is shown in Figure 2.9. Note that depending on the strategy, other redundant variables might be favorable. With the AirS, the stoichiometry, temperature and pressure of the ambient air supplied to the cathode is controlled. If an external humidifier with bypass is implemented, the air's relative humidity can be controlled to a certain extent as well. The gas composition is given by the ambient atmospheric condition.
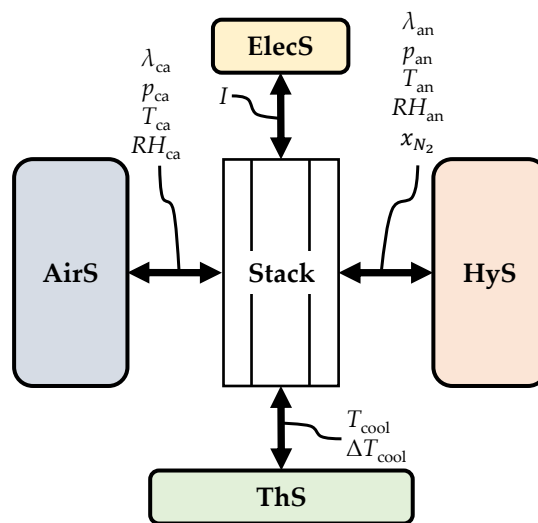
FIG. 2.9   Stack boundary conditions as provided by the respective subsystems.

With the ThS, the coolant inlet temperature and mass flow are set. Via the coolant mass flow, the temperature rise between coolant inlet and outlet ΔT_{cool} can also be manipulated. As the

heat capacity flux of the coolant outweighs the anode and cathode gas heat capacity fluxes, it dominates the stack's temperature. However, the control of the thermal system reacts rather slow, as large heat capacities exist within the radiator, stack and piping. Note that the inlet temperature might be constrained by the ambient conditions. If the ambient temperature is rather high and a large heat flux is produced by the stack, the operating temperature must be raised in order to maintain a sufficient temperature gradient at the radiator.

The anode inlet conditions are controlled by the HyS. As in the AirS, the stoichiometry and pressure are controlled directly. However, the gas composition is subject to complex interactions. In a state-of-the-art HyS, gas is recirculated from the anode outlet to reduce the fuel loss while maintaining sufficient hydrogen partial pressures along the whole length of the cells. In addition, recirculating gas with a high relative humidity from the anode outlet humidifies the anode inlet gas stream. As nitrogen diffusing through the membrane accumulates within the HyS and reduces the hydrogen partial pressure, gas must be removed periodically from the loop by opening the purge valve. All in all, the pressure and mass flow can be controlled directly and the gas composition and humidity indirectly via the purge valve control. The temperature within the loop is not actively controlled and results from the stack operating temperature set by the coolant, the hydrogen supply temperature and the ratio between supplied and recirculated gases.

Lastly, the electrical operating point is set by the ElecS. While it is possible to control either the voltage or the electrical current of a fuel cell, this work will focus on a current controlled operation. This galvanostatic operation allows to exactly calculate the reactant consumption via the fundamental Equations 2.13 and 2.14. A voltage-controlled, potentiostatic operation would result in shifting consumption rates depending on the polarization curve, which can be heavily influenced by the operating state of the fuel cells. Therefore, a galvanostatic operation simplifies the calculation of the required reactant flows to actuate the AirS and HyS accordingly.

In the vehicle application, the whole FCS is controlled by a Fuel Cell Control Unit (FCCU). It features only a limited computational performance and must be able to fulfill real-time requirements during operation. This necessitates a rather simple but robust approach to be implemented, such as load lines, look-up tables or basic equations[42]. In open literature, descriptions of control strategies are sparse. Mostly, one factor at a time variations of e.g. the operating current, pressure, temperature, humidity and/or stoichiometry are carried out, but no closed derivation of optimal variable combinations are presented. When a stack is procured, usually only allowed operating ranges such as a pressure and temperature limit are given. If operating set points are given, often a load line describing e.g. pressure and stoichiometry depending on the current is available. However, the temperature may vary significantly during vehicle operation, with a strong impact on the saturation pressure and subsequently the humidification distribution within the cells. Controller setups are discussed[43], but often lack the inclusion of the full suite of relevant physical effects to determine optimal set points. However, the control strategy greatly influences the system KPIs, as it will be discussed in depth in the remainder of this work. With their high commercial relevance, control strategies typically remain confidential, although every FCS supplier must have developed at least one.

Within this work, the activity-based water management strategy proposed by Hellmann[44] and improved by Grimm as shown in Figure 2.10 is chosen as the baseline strategy. Only the most important boundary conditions yielding a high impact on the humidity distribution within the fuel cell are taken into account to reduce the complexity and computational effort

required in the FCCU. These boundary conditions were found to be the cathode stoichiometry and pressure, temperature and electric current[44]. The current must be selected based on the requested electrical power that the FCS should provide. The operating temperature might change e.g. during start-up or if the cooling capacity limit of the vehicle is reached. Therefore, current and temperature are selected as inputs. Cathode stoichiometry and pressure remain to shape the humidity distribution within the cell for each operating point given by a current/temperature pair. Note that the following formulas contain the cathode outlet temperature. The coolant temperature is used at the system test rig to estimate the cathode outlet temperature, as the measured gas temperature is affected by the heat losses in the cathode exhaust path.
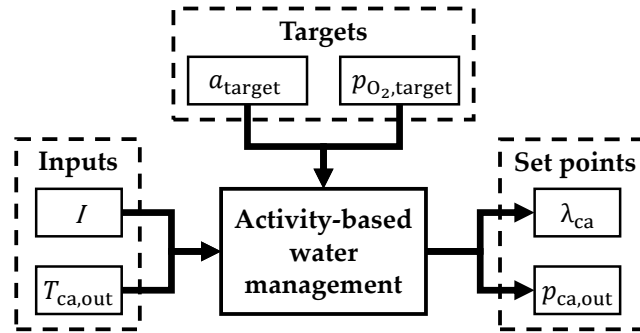
FIG. 2.10 Calculation scheme of the activity-based water management strategy.

To ensure robust operation, Hellmann[44] proposed two targets: One, maintaining sufficient membrane hydration by setting a cathode outlet activity target a_{target} and two, avoiding high concentration losses or even local reactant starvation by setting an oxygen partial pressure target $p_{\text{O}_2,\text{target}}$. The outlet activity is derived from a molar flux balance, as proposed by Dicks and Rand[19], with the molar fractions of oxygen and nitrogen, x_{O_2} and x_{N_2}:

$$a_{\text{out}} = \frac{2 + \Psi \lambda_{\text{ca}} \left(1 + \frac{x_{\text{N}_2}}{x_{\text{O}_2}}\right)}{1 + \lambda_{\text{ca}} \left(1 + \frac{x_{\text{N}_2}}{x_{\text{O}_2}}\right)(1 + \Psi)} \frac{p_{\text{ca,out}}}{p_{\text{ca,out}}^{\text{sat}}} \overset{!}{=} a_{\text{target}} \tag{2.27}$$

Note that the outlet activity is independent of the stack current. The complete derivation is also published[45]. Ψ incorporates the partial pressure of water vapor in the inlet gas stream[19]:

$$\Psi = \frac{p_{\text{H}_2\text{O,in}}}{p_{\text{in}} - p_{\text{H}_2\text{O,in}}} \tag{2.28}$$

As oxygen is consumed continuously along the channel, the oxygen partial pressure is the lowest at the cathode outlet, therefore the partial pressure target is defined here. The partial pressure $p_{\text{O}_2,\text{out}}$ is again based on a molar flux balance, yielding

$$p_{\text{O}_2,\text{out}} = \frac{x_{\text{O}_2}(\lambda_{\text{ca}} - 1)}{(1 + \Psi)\lambda_{\text{ca}} + x_{\text{O}_2}} p_{\text{ca,out}} \overset{!}{=} p_{\text{O}_2,\text{target}}. \tag{2.29}$$

To achieve a certain target partial pressure, the necessary stoichiometry is calculated by

$$\lambda_{\text{ca}} = \frac{x_{\text{O}_2}\left(p_{\text{ca,out}} + p_{\text{O}_2,\text{target}}\right)}{x_{\text{O}_2}p_{\text{ca,out}} - (1 + \Psi)\,p_{\text{O}_2,\text{target}}}. \tag{2.30}$$

For a cathode outlet temperature of 70 °C and an ambient water activity of 0.1, assuming no humidification within the AirS, the targets are displayed as a pressure-stoichiometry-diagram in Figure 2.11. At the intersection of the curves, both targets are fulfilled. This cathode outlet pressure and stoichiometry is then set by the AirS to enable robust fuel cell stack operation.
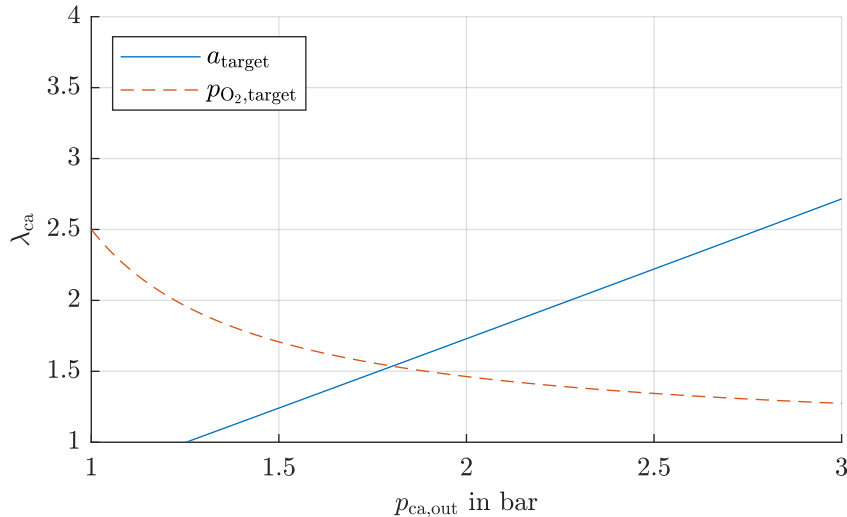
FIG. 2.11 Exemplary plot of outlet water activity target and oxygen partial pressure target in terms of cathode outlet pressure and cathode stoichiometry[46]. ©The Electrochemical Society. Reproduced by permission of IOP Publishing Ltd. All rights reserved.

The approach presented is derived from a water management analysis during stationary operation. However, highly dynamic changes of the requested power are expected in the automotive application. Adding the dimension "time" to the already challenging field of water management complicates it further. Understanding this time-dependent behavior is the focal point of this work. Next, a closer look at the main objectives and selected methodology is given.

2.4 Setup of this Work

2.4.1 Scope

2.4.1.1 Operating range

To narrow down the rather broad topic of dynamic water management, the scope of this work must be restricted further. The operating range chosen within this work is depicted in Figure 2.12 and highlighted in purple. Usually, FCSs are operated around 60 °C. However, a limitation of the vehicles cooling capacity might require a higher coolant temperature of up to 90 °C. Temperatures substantially higher than 90 °C are not yet achieved in application, but fundamental research on PEMFC operation at up to 120 °C with PFSA membranes exists[47,48]. The temperature range below 55 °C is usually omitted during stationary operation, as the low water saturation pressure results in too wet conditions, leading to flooding. However, these temperatures are occurring in a limited time-frame during warm-up and cool-down of the system at the beginning and end of operation. Note that the reduced temperature lowers the

reaction rates and increases the activation losses. Therefore, the full net power cannot be achieved at these temperature levels.
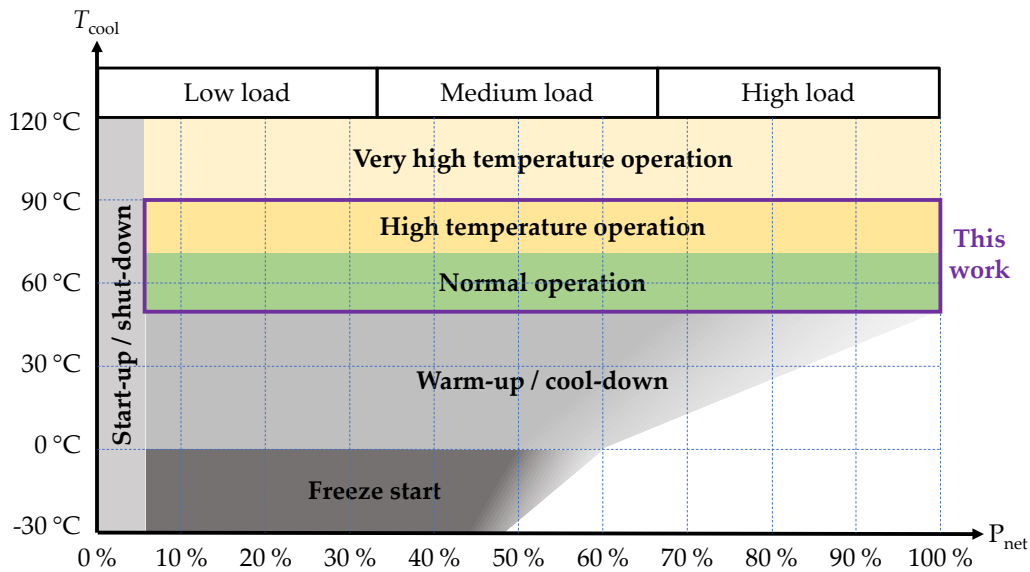
FIG. 2.12 Schematic operating range of a fuel cell system and scope of this work highlighted in purple.

If the vehicle is parked outside in sub-zero temperatures, a freeze start is required to transfer the system into the normal operation state. Water management plays a vital role in controlling the formation of ice during freeze start, which might result in reactant starvation with adverse effects on the fuel cells' lifetime. This topic is not addressed within this work, as the focus lies on operation in a temperature range between 60 °C and 90 °C, where the highest power dynamics are expected. However, a wide variety of research targets the special challenges concerning freeze-start. A comprehensive overview is for example given by Luo and Jiao[49].

The power range is divided into three segments: low, medium and high load. This work addresses almost the full net power range, as the FCS typically faces this whole range of required power during vehicle operation. However, very low loads are omitted during normal operation, as the low currents would result in high cell voltages. These high voltages are known to exacerbate the formation of radicals, which chemically degrade the membrane, and to promote platinum dissolution[38]. By introducing a current limit on the low side, high potentials are avoided during normal operation, an approach called voltage clipping. Only if the fuel cell is started or stopped, this unfavorable voltage regime is allowed for a short period of time.

It is further known that the time scales within a FCS span multiple orders of magnitude. Including all effects and their inherent dynamics would result in unnecessary complexity. Therefore, this work is restricted to a limited time scale range. As the focus lies on highly dynamic operation with changes in electrical power in the order of 1 s, processes advancing slightly faster or slower than this targeted time scale are in focus. Special attention is paid to the dynamic phenomena occurring on time scales between 0.1 s and 100 s. The effect selection process is elaborated in-depth later in this work.

2.4.1.2 Evaluation

The KPIs system efficiency and dynamic capabilities were already discussed in Subsection 2.2.2. The third target aims at avoiding operating states adversely affecting the lifetime of the fuel cells by inducing excessive aging. Understanding aging mechanisms and developing mitigation strategies for fuel cells is a wide and complex research topic especially in context of the automotive application. Comprehensive overviews of this field are given by Ren et al.[38] and Jahnke et al.[50]. Fostering detailed degradation knowledge is not a focal point of this work. However, three of the most relevant known degradation sources shall be included qualitatively within this work.

The first trigger is reactant gas starvation. Local or even global hydrogen starvation causes current reversal, resulting in corrosion of the carbon support carrying the catalyst and reducing the available Electrochemical Surface Area (ECSA)[38]. A decrease in ECSA increases the mass transport losses, as less catalyst surface is available for the fuel cell reaction, limiting the achievable current. Air starvation is less critical regarding aging, but might still cause local hot spots[38]. In addition, the cell voltage and therefore the stack's power output are reduced by a rise in concentration losses, adversely affecting system efficiency and achievable maximum power.

Not only the catalyst support can age, but also the membrane. Dry-wet cycling of the membrane entails shrinking and swelling. This may result in mechanical fatigue, promote the formation of cracks and subsequently increase the unwanted reactant cross-over[51]. In addition, very dry membrane states promote the side chain scission in the widely used material Nafion®, leading to a loss in sulfonic acid groups and reduced protonic conductivity[52].

A suite of further degradation mechanisms is discussed in literature. It is thereby known, that ageing affects the water management and vice-versa. For example, the hydrophobic coating of the GDL can be detached by ice, subsequently deteriorating the liquid water drainage[53]. If carbon corrosion occurs, the surface oxidation decreases the hydrophobicity of the carbon support, resulting in increased mass transport losses within the catalyst layer[54]. On the other hand, poor water management and , for example, liquid water accumulation may result in reactant starvation, leading to carbon corrosion as discussed above. Most of these ageing phenomena occur on rather slow time scales and do therefore not result in fast performance losses. This type of degradation is extremely challenging to track with the experimental setup in focus of this work, which is usually not run for several hundred or even thousand hours without changes in the assembly or control strategy. Therefore, mitigating degradation is only addressed in a scope limited to the three effects of reactant starvation, dry/wet cycling and low membrane water content described in the previous paragraphs.

2.4.1.3 Research level

As this work is focused on the system level, the components comprising the systems remain unchanged during comparisons. In other words, an optimization of individual components including the stack is omitted. However, the control strategy and system architecture as main system level levers are the focal points. An in depth discussion on the experimental levels in fuel cell research is incorporated in the according experimental Chapter 4. For the simulation model, sub-models are picked and adapted from the literature rather than developed completely new.

In conclusion, this work is placed at the intersection between fundamental academic-driven research and the application-oriented industrial research. It aims at utilizing the fundamental understanding for improving the application-relevant performance with an holistic view of the FCS. The core contributions of this work are the high dynamics, the system scope and the sophisticated experimental setup. Now, as the limits and focus of this work are defined, the main research questions, chosen methodology and chapter setup are discussed in the following.

2.4.2   Research questions

As was outlined in the sections before, the direction of this work is based on four central research questions, that are elaborated in the following. From these questions, the scope and methodology of this work are derived.

RQ1. Which water management induced-effects dominate the fuel cell behavior during highly dynamic operation?

RQ2. How can one utilize transient experiments, what are potential pitfalls and how should the experiments be set up to enable an improved modeling of dynamic fuel cell operation?

RQ3. What are the limitations regarding efficiency, dynamic capabilities and critical states of common stationary-based water management strategies and how can they be improved?

RQ4. How do the main system level levers control strategy and architecture impact the expected trade-off between system efficiency and dynamics?

The first research question, RQ1, aims at identifying the relevant processes that shape the dynamic fuel cell response. The open literature provides a great variety of different phenomena that are observed in fuel cell operation[40]. At this point, it is assumed that the decade-long fundamental research covers all relevant effects. In context of this work, the most important aspects regarding the *highly dynamic operation* must be selected. This selection process is part of the simulation model development. To ensure that no relevant process is overlooked and to identify potential mismatches between the available sub-models and the application-like operation, a validation of the model with experimental data is conducted.

RQ2 focuses on the experimental validation of simulation models. In common literature, utilizing stationary experiments is the prevalent method. However, additional information can be derived from transient experiments. In this work, such experiments are carried out to separate the dynamic processes occurring on different time scales. While the common stationary experimental setup is easily described by a limited number of stack boundary conditions, this work showcases *potential pitfalls* in the design of dynamic experiments. Every stack boundary condition, such as for example pressure and mass flow of the reactants, are adapted only with a certain delay caused by the adjacent subsystems' intrinsic dynamics. The system-induced lag interacts with the stack's response to dynamic operation. Predominant stack test rigs however lack the dynamic capabilities of a realistic, application-like system for the automotive application. This yields limitations in the testing scope and promotes misinterpretation of the stack-centered results with respect to the application. From the

experimental analysis, recommendations for designing dynamic experiments allowing for an *improved modeling* shall also be derived.

The three-fold goal of increasing system efficiency, dynamic capabilities and avoiding critical states is the centerpiece of RQ3. The focus lies less on achieving the highest quantitative improvement, but rather on understanding the key effects impacting the goals. Close attention is payed to the *limitations* of common water management strategies. They are typically *stationary-based*, that is they are derived from stationary experiments and developed on stationarity assumptions. If the FCS is only operated with low dynamic load changes on time scales substantially slower than 1 s, these approaches might be sufficient. Even the slow subsystems are then able to provide the stack with the selected boundary conditions at all times. But when the electrical current is switched in a *highly dynamic* fashion, the electric load can in principle outrun e.g. the air mass flow supplied by the AirS. This, for example, may result in the *critical state* of starvation. In this work, the main interactions within the stack, the adjacent subsystems and the electric load during highly dynamic operation are discussed. Finally, an *improved* strategy addressing the subsystems finite dynamic capabilities is presented.

Lastly, RQ4 targets the *main system level levers*. As previously stated, a component optimization is not in scope of this work. In contrast, the system architecture's impact as well as the control strategy adaption is focused on. With knowledge gained from two experimental systems and the simulation model developed in context of the prior research questions, additional insights are generated by simulating multiple other system architectures and comparing control strategies. It is expected that efficiency and dynamics are contrary goals. Therefore, a *trade-off between efficiency and dynamics* must be conducted to choose the control strategy and system architecture for a certain required performance in the targeted application. Finding an optimal solution is not the aim of this work, but rather to built-up an understanding of the *levers'* influence on the trade-off. Note that it is impossible to prove that no ideal architecture and/or control strategy excelling in efficiency and dynamics at the same time exists. However, multiple examples for the conflicting targets are presented within this work. Next is a closer look at the methodology and subsequent chapter setup.

2.4.3   Selected methodology

This work evolves around the application of a fuel cell-dominant vehicle, facing highly dynamic changes in the requested electrical power. In general, the research methodology follows a top-down approach with the philosophy of *as simple as possible, as complex as necessary*. The right level of detail heavily depends on the research question. Therefore, the main research questions and the scope of this work as previously defined have to be kept in mind. It is almost always possible to dive deeper into certain phenomena, but the discussion must be limited to the effects most important in the context of this work. Otherwise, a system level analysis would be narrowed down too strictly and lack the wide field of view.

An overall setup of the chapters within this work is shown in Figure 2.13. In general, three phases are distinguished. First is the motivation of the specific topic, water management in highly dynamic PEM fuel cell system operation. Second comes the detailed analysis of key aspects, and third the synthesis, where the knowledge gain is combined and subsequently examined from a broader perspective.

The first two chapters focused on the motivation and introduced the basic principles and
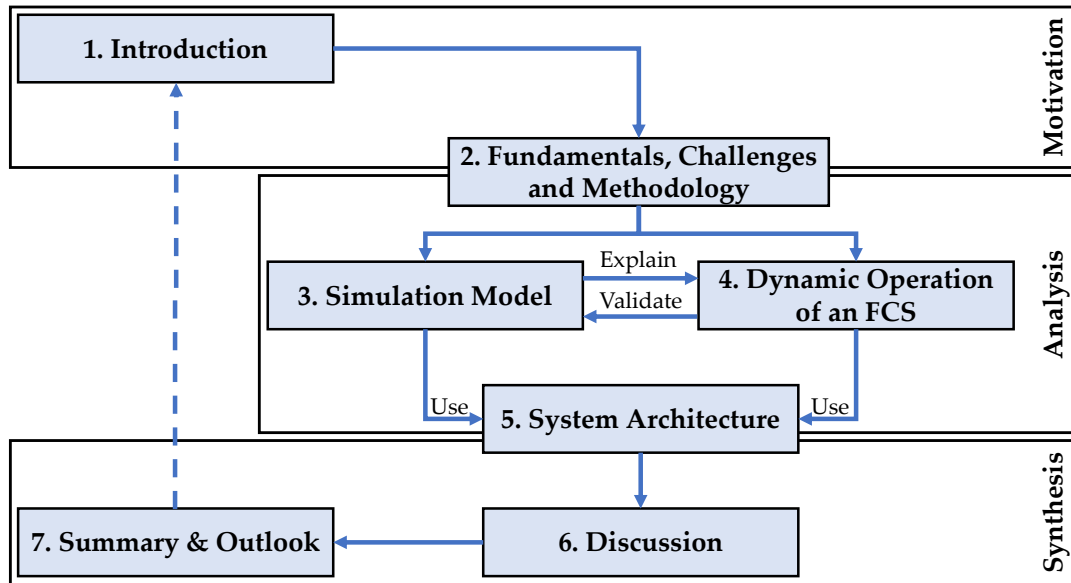
FIG. 2.13 Chapter setup and interaction selected for this work.

definitions. Also a general overview on current PEMFC research was given, providing a first step into the analysis phase. From that, this work now digs deeper into understanding the dynamic water management in fuel cell systems, utilizing two complementary tools: a simulation model including dynamic water transport effects, and a sophisticated fuel cell system test rig, featuring state-of-the-art components. RQ1 is specifically targeted within Chapter 3 and Chapter 4.

In a bottom-up approach, one would start with the fundamental effects by characterizing single layers of the cell and, step-by-step, combining all of them until arriving at the system level. The fuel cell system however constitutes such a complex setup, that addressing all effects within this work is infeasible. Additionally, blindly including all phenomena in e.g. the simulation model, would drastically complicate the implementation and increase the computational effort, even if some of them would not contribute substantially to the KPIs, system efficiency and dynamics. In this work, the simulation model is based on literature correlations for individual phenomena, which in turn are selected so that the model specific requirements are fulfilled. The model development process and main observations during transient operation are explained in the corresponding Chapter 3.

But how can one make sure that no relevant process with respect to RQ1 is overlooked? That is the purpose of the comparison with experimental results obtained on a system test rig, the core element of Chapter 4. In the experiments, all processes that would also occur in real world fuel cell system operation are automatically at work. To foster the detailed understanding, the experimental results are compared to the simulation model. If significant discrepancies are found in this comparison, it shows shortcomings within the simulation model. Following, the simulation model is improved until it represents the crucial aspects of the experimental results. In addition, the experiments carried out in scope of Chapter 4 are also designed to answer RQ2 and RQ3. Note that the research presented in Chapter 3 and Chapter 4 was conducted hand in hand, as shown in Figure 2.13. The chosen chapter setup follows the logic *from cell to system to other systems*.

This work does not stop at understanding the behavior of one specific system. The knowledge

gained during the experiments in combination with the simulation model is utilized in Chapter 5. Here, an extrapolation of the dynamic water management understanding is conducted, extending the findings onto a variety of other system architectures. A detailed analysis of the trade-off between system dynamics and efficiency is carried out, answering RQ4.

Next, the key results are discussed and put into perspective in Chapter 6. The main research questions introduced within this chapter serve as a guidance for the discussion. Additionally, the limitations and potential shortcomings of this work are evaluated. The contributions of this work are summarized in Chapter 7. Finally, possible directions for next steps in the research on dynamic water management in fuel cell systems are included as an outlook.

Note that this work's literature review is split between the chapters. Fundamentals relevant for all chapters were already introduced within this chapter. Specific insights on the PEMFC modeling literature, experimental research and system architectures in vehicles is placed within the respective chapters. In addition, the detailed goals of the chapters are revisited shortly at the beginning. Next, a closer look at the simulation of the centerpiece of every fuel cell system is taken: the fuel cell itself.

Chapter 3

Simulation Model

After the fundamentals and general setup of this work were thoroughly discussed in the last chapter, this chapter revolves around a central tool to answer the research questions RQ1 and RQ3: a dynamic fuel cell simulation model. This model is utilized to gain an in-depth understanding of one fuel cell's internal processes. But what should the model deliver? How precisely must the model represent the experiments? To derive a suited model and guide the development, targets and requirements are formulated first. As extensive research in the field of PEMFC simulation exists, an overview on the existing models, their individual targets and components is given. From that, a new simulation model is developed to fulfill the specific requirements of this work. Sub-models from literature are therefore selected, combined and extended. As core result of this chapter, two exemplary dynamic simulation cases are shown and discussed, highlighting the dry-out phenomenon and the impact of liquid water during a current increase. Understanding these two phenomena is a central building brick for an in-depth explanation of the experimental results in Chapter 4.

The development and implementation of the simulation model presented here was supported by Daniel Seidl's master thesis[55], which was supervised by the author. Additional graphics, an adapted model development description as well as two comprehensive examples and their discussion are added by the author.

3.1 Targets and Requirements

3.1.1 Needs, targets and methodology

Simulation tools are widely used in research and engineering as a cost efficient and fast method to gain additional insight, optimize components and evaluate the impact of selected phenomena. As most simulations are simplifications and contain empirical correlations, a validation of the simulation results with experimental data must be conducted. In this work, the three main needs for a simulation model are: experiment interpretation, process understanding and behavior extrapolation.

During experiments, previously unknown or unexpected behavior may occur. However, the measurement capabilities are often limited by constraints as the lack of appropriate sensors, volume restrictions at the test rig, or a limited number of sensor positions due to costs. For some research questions, an in-depth analysis of the relevant physical parameters, such as local pressure, temperature and humidity, is required with a high resolution in space and/or time. In this case, a simulation model complements the experiment, as local parameters are derived easily. The previously described limitation of experimental research may also complicate effect separation, e.g. the distinction of different transport phenomena. This can be encountered in two ways: 1) a targeted setup of the experiment and/or 2) a simulation

model, where different effects can be switched on and off.

Often, designing the best technical solution requires a sensitivity analysis and/or optimization. With a sensitivity analysis, the impact of various parameters, such as e.g. an operating pressure, can be evaluated for complex setups as fuel cells to gain an in-depth understanding of the challenges and levers to solve those. In a potential next step, an optimization targeting various goals, as efficiency, dynamic capabilities or cost can be set up. The knowledge gained from the sensitivity analysis is utilized in setting up this optimization. Both methods usually require a large set of data, which might be cost- or time-consuming to retrieve experimentally. Here, a simulation model is beneficial, as it easily calculates the needed data sets with very limited additional human effort and no costly experimental hardware.

Lastly, a simulation model is the preferred solution to extrapolate a known system behavior onto other systems or towards new operating ranges. In fuel cell system research, one fundamental question is the choice of the right system architecture for a certain use-case and under multiple constraints, which will be discussed in detail within Chapter 5. Producing hardware for an experimental analysis of each possible architecture choice is infeasible. Based on knowledge gained with one or multiple system architectures, a simulation model allows a modular extension or adaption to new system architectures and drastically reduces the effort to find new suitable solutions.

The primary targets of this work's simulation model are based on the research questions introduced in Subsection 2.4.2. To answer especially the research question RQ4 on the efficiency versus dynamics trade-off in the later Chapter 5, but also identify critical local states as addressed with RQ3, the simulation model needs to be capable of

1. calculating the stack power depending on the operating conditions to quantify the impact of the control strategy and the system architecture and
2. calculating the local current density distribution, membrane humidity, reactant partial pressures and liquid water accumulation to deepen the understanding of dynamic fuel cell operation and to identify critical states such flooding, dry-out or local starvation.

As secondary targets, the model shall further allow for

1. transferability onto new stacks with a limited number of system experiments and
2. computing times sufficiently short for system simulation.

The methodology of the simulation model development is depicted in Figure 3.1 and follows a modified V-shape approach, which is common in software engineering and product development. First, the simulation model specific requirements are defined. Afterwards, literature models are discussed, including their general distinctions, different goals and key phenomena. Subsequently, the general model setup and decomposition into sub-models is derived. Next, the most relevant effects for the sub-models included in this works' model are chosen in order to fulfill the specific requirements, primary and secondary targets. This selection in combination with the later shown experiments also contributes to answering RQ1. The implementation of the model is discussed in the following. As empirical correlations are included in the model, a parametrization of the sub-models based on targeted stationary and dynamic system experiments is conducted. Testing the complete model against a complex load cycle test case concludes the core development tasks. As the model is now ready for deployment, targeted simulation studies can be conducted. Discussing the main findings of the simulation studies utilizing two examples concludes this chapter.
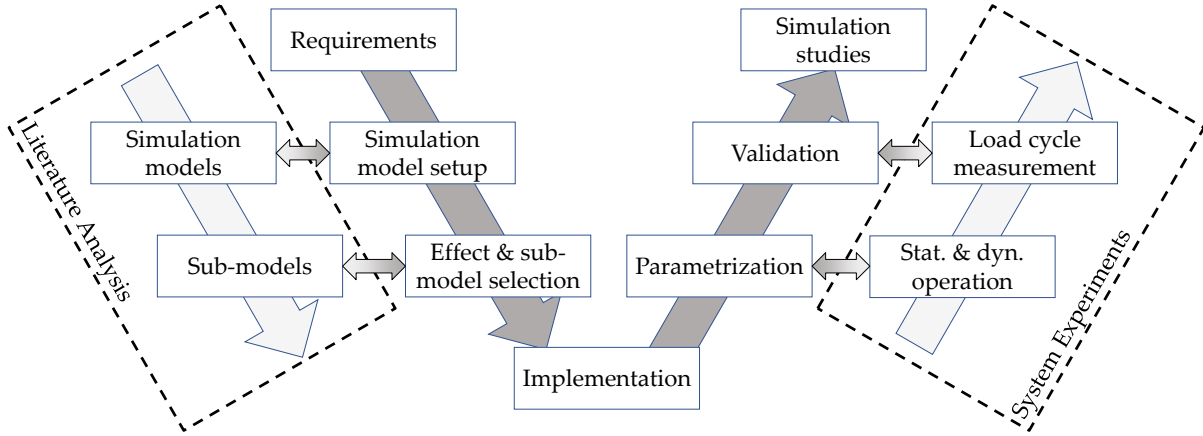
FIG. 3.1   Methodology of the simulation model development.

3.1.2 Model requirements

Based on the primary and secondary targets discussed in Subsection 3.1.1 and the research questions introduced in Subsection 2.4.2, the model specific requirements are defined in Table 3.1. The model shall be able to predict the measured voltage with an accuracy of 5%, which is sufficient to track the dynamic response as well as the stack boundary condition impact. A central contribution to the actual stack voltage are the ohmic losses ΔU_{ohm}. Changes in the ohmic resistance are largely contributed to the membrane, as its conductivity changes heavily depending on the membrane water content. During dry-out, the measured ohmic resistance changes up to a factor of two, as shown later in Subsection 4.4.2. Therefore, a less strict limit of 20% relative error in the simulated ohmic resistance $R_{\text{ohm,sim}}$ is sufficient to monitor such a dry-out state.

Additionally, the model shall include the dynamics of processes with inherent time constants between 0.1 s and 100 s and compute not slower than four times the real time on standard hardware, a laptop with an Intel® XEON® Processor E3-1505M v5. For a simple transfer of the model onto new stacks, the experiments needed for parametrization shall be limited to a maximum of five. Lastly, the boundary conditions of the model shall be system states, which can be measured at the system test rig described in Subsection 4.2.2 to facilitate the model's usage in systems engineering. The next section focuses on the simulation models from literature, which provide the starting point for the model developed within this work.

TABLE 3.1   Simulation model requirements divided in requirement classes.

Class	Requirement
Accuracy	$\lvert U_{\text{sim}} - U_{\text{meas}}\rvert \leq 0.05 U_{\text{meas}}$
Accuracy	$\lvert R_{\text{ohm,sim}} - HFR_{\text{meas}}\rvert \leq 0.2 HFR_{\text{meas}}$
Time-scale	$0.1 \leq \tau_{\text{dyn.processes}} \leq 100\,\text{s}$
Computation time	$t_{\text{sim}} \leq 4\,t_{\text{real}}$
Transferability	≤ 5 experiments for parametrization
Boundary conditions	States measured in system experiment

3.2 Simulation Models in Literature

3.2.1 Goals of literature models

Since Springer, Zawodzinski and Gottesfeld developed the first well-known fuel cell model in 1991[39], numerous additional models have been proposed. But why is there no one-fits-all solution? The main driver for this development are the multi-level characteristics of the fuel cell and its application. Starting from material characterization, extending via the differential cell and cell level towards short stacks and full stacks, finally reaching the fuel cell system level in focus of this work, the specific goals and challenges of each level shape the perfect simulation model for the corresponding task.

Most models focus on predicting the performance of a fuel cell or stack by calculating the electrical power produced. Models of this kind range from reduced, polarization curve approaches[22] to more sophisticated electrochemical models. To develop power split strategies, rather simplistic approaches are chosen[56,57]. Most models include a more or less complex influence of other operating parameters, such as mean pressure and temperature. These models are often limited in scope, as most of them assume stationary conditions. Some models target system operation[58], while other models aim at developing controllers and control techniques for fuel cells[59].

Besides the performance-oriented models, specialized models for certain challenges are developed. Ageing models are trimmed to calculate a performance decline due to various ageing mechanisms, such as reactant starvation, dry-wet cycling of the membrane or high potentials and potential cycling[38,60]. Also, performance models with simplified aging mechanisms were developed to adapt the control strategy of a fuel cell system during its lifetime[56,61]. Other specialized models focus on freeze start, including freezing and thawing of water. Luo and Jiao summarized typical cold start experiments and modeling approaches[49].

Depending on the use-case of each model, they differ greatly in complexity, accuracy and the implementation of specific effects. While most models consist of similar key components, researchers tend to tailor new models suiting their research goals best. This is also done within this work, as no of-the-shelve model fulfills all the requirements and targets formulated in the previous section. The fundamental structure and basic functionality was developed by Grimm et al.[41], but the model is extended substantially as described in the later sections.

3.2.2 Distinction of literature models

Common literature models can be distinguished by multiple criteria. In this section, six fundamental aspects are discussed: the model dimension, the discretization of layers, the phase change of water, the modeling of transport processes, the dynamics included and the validation procedure. In-depth reviews of PEMFC models, transport mechanisms and targeted experiments as well as recent developments in membrane characteristics are found in literature[62–64].

3.2.2.1 Model dimension

The simplest models have no spatial resolution and are therefore referred to as "0D-models". These models[22,56] excel in simplicity and computational effort, but lack many physical phenomena and are therefore often limited in accuracy. As the transport through the fuel cell's layers greatly impacts the cells performance, the first dimension to add for spatial discretization is typically the through-plane direction[59,65–68]. In these cases, any along-the-channel variations in gas composition, temperature and pressure as described in Subsection 2.3.3, are neglected. This limits the scope of the models and subsequently the suitability for certain research questions.

If along-the-channel state gradients should be added to improve accuracy, two general approaches are possible: either 2D-models[69], where all included transport mechanisms affect through-plane and along-the-channel directions equally, or 1D+1D-models, where transport processes in the two directions are decoupled and calculated separately[70]. This second type of modeling approach is especially suited for fuel cell modeling, as the dominating transport mechanism differ in-between the two directions. For example, the gas transport along-the-channel in the flow field is mainly convective, while diffusion dominates in the through-plane direction.

Another reason to separate the two paths are the different length scales. Typical automotive fuel cells have a total thickness of around 1 mm with membrane thicknesses around 20 µm, while the length can span tens of centimeters. This leads to fluxes and process time constants differing by multiple orders of magnitude, as shown later in Subsection 3.3.2.1. Therefore, a 1D+1D separation significantly reduces computational effort. Some flow field geometries require a second in-plane dimension to accurately represent different flow setups such as cross flow or meander flow[41]. Here, 2D+1D models[58,71,72], or full 3D models[73–75] must be implemented.

3.2.2.2 Discretization of layers

Depending on the goal and the trade-off between accuracy and computational effort, researchers reduce the number of layers they discretize. In very simple models, only the flow field and the membrane exist[72] or the GDLs are treated only as a transport resistance[58]. More sophisticated models include the GDLs[66], sometimes also divided into GDL and MPL. Depending on the goal, the electrodes might either be discretized or treated as an infinitely thin interface between GDL and membrane.

3.2.2.3 Phase change

To correctly predict flooding, an interaction between liquid water and gas diffusion must be integrated. Therefore, water vapor needs to condensate into liquid water which in turn must be allowed to evaporate. Simplified models[68,71,73,75] often neglect the liquid phase and virtually add the molar flux to the gas phase, e.g. by utilizing the water activity a[67,76]. This limits accuracy and makes a valid flooding prediction impossible, as the reduction of effective gas diffusion area within the GDLs decreasing the gas transport towards the active sites is neglected. Only a few models include the presence of liquid water[66,72,77]. Especially for freeze start simulation, a freezing and thawing of the water must be implemented. If phase changes

are included, latent heat might also be implemented in the thermal domain, as it impacts the global heat balance of the stack.

3.2.2.4 Transport modeling

Within the fuel cell, a great amount of different transport mechanisms occur, ranging from two-phase convection via diffusion within porous media to charge transport and heat conduction. For most mechanisms, no analytical models exist and an empirical or semi-empirical approach has to be employed. This matter is discussed in more detail within the following Section 3.3.

3.2.2.5 Dynamics

The decision to include dynamic effects yields a significantly more complex model and may demand sophisticated multi-scale numerical methods to solve the resulting equations, as fuel cell processes span multiple orders of magnitude in their characteristic times. The time scales are also discussed in-depth later on in Subsection 3.3.2.1. For simplification, most literature models restrict themselves to stationary conditions[65,73,74]. Only a few models include dynamic effects such as unsteady heat and mass transfer processes[66,71,72].

3.2.2.6 Validation

As all fuel cell models include simplifications or (semi-)empirical formulations, a thorough validation must be conducted to check the models accuracy. Ideally, this is done by realistic experiments. For simpler models, a comparison with a validated, more complex model might also be an option. Ideally, the models' validation should match its setup: For example, a 1D model should be checked via an experiment featuring a spatial resolution along this direction. Transient models should be validated using dynamic experiments. The vast majority of literature models, even the transient ones, are mainly validated via a global, steady-state stack or cell voltage[66,67]. In some cases additional measurements as the High Frequency Resistance *HFR*, water balance or voltage dynamics[71] are also included. An in-depth parametrization and validation of the model developed in this work is discussed in Subsection 3.3.4 and Subsection 3.3.5, respectively.

3.2.3 Key components of literature models

In general, the relevant processes in a fuel cell are divided into three different domains: the media transport domain, the thermal domain and the electrical domain. For each domain, the relevant processes and the main cross-domain couplings are shown in Figure 3.2. After a closer look at the fundamental fields and relevant sub-models, these processes are discussed in depth in context of their respective domain. In common 2D+1D models, the fuel cell is discretized into segments and layers. Along the through-plane direction z, the layers of the fuel cell are discretized. Along the in-plane direction y and along-the-channel direction x, the cell is divided into segments.

The fundamental fields for each domain are stated in Table 3.2. For the gaseous components j, partial pressures p_j or concentrations are commonly used. If liquid water is also addressed,
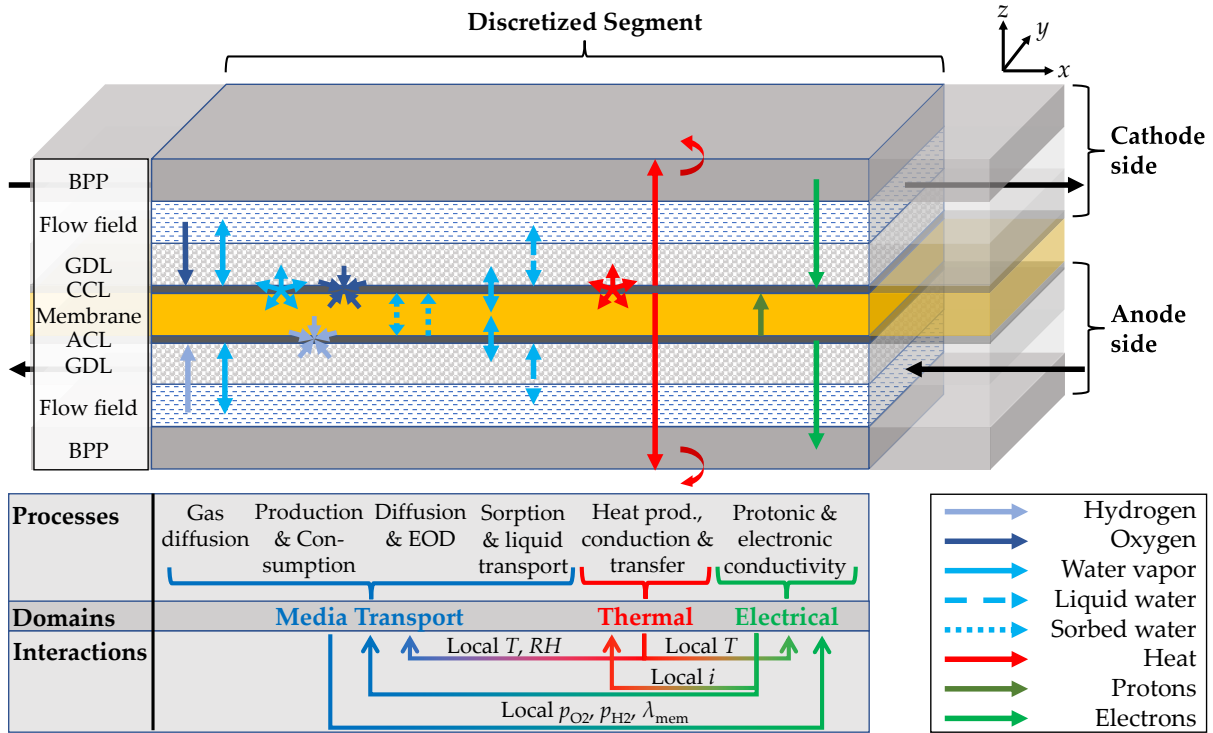
FIG. 3.2 Relevant processes, domains and interactions within one segment of the PEMFC.

the saturation s must be included as an additional field. In the thermal domain, temperatures serve as fundamental fields, allowing to calculate heat fluxes and local saturation pressures. Lastly, the voltage is utilized as fundamental field in the electrical domain. With that selection, spatial discrepancies in reactant distribution, relative humidity, temperature and current density can be calculated with the help of sub-models.

TABLE 3.2 Fundamental fields in simulation models.

Domain	Field	Unit
Media transport	Partial pressures p_j	Pa
Media transport	Liquid water saturation s	-
Thermal	Temperature T	K
Electrical	Voltage U	V

Figure 3.3 displays the central sub-models and their interactions, highlighting the need for (semi-)empirical correlations to determine the most relevant states. In total, seven sub-models are described in detail in the following subsections, divided into their respective domains. The thermal model is necessary to calculate the catalyst layer temperature T_{CL} from the coolant temperature T_{cool} and the dissipative heat flux $\dot{Q}_{diss}$ from the reaction. The catalyst layer temperature is used to derive the relative humidity at the catalyst layer RH_{CL} and a cell voltage U_{cell} via the cell voltage model.

In the media transport domain, the flow field partial pressures $p_{j,FF}$ of the species j, the liquid water saturation of the GDL s_{GDL}, the current density i and the resulting reactant fluxes $\dot{n}_{H_2/O_2}$ are the main inputs for the gas diffusion model, used to calculate the partial pressures

32

$p_{j,\mathrm{CL}}$ at the catalyst layers. Via the local relative humidity RH, the amount of produced liquid water is known and plugged into the liquid water transport model to evaluate the liquid water saturation s_{GDL}. Additionally, the membrane water content λ_{mem} is determined via a sorption model. From that, the net water flux $\dot{n}_{\mathrm{H_2O,net}}$ through the membrane is calculated via an Electro-Osmotic Drag (EOD) model and a diffusion model for the sorbed water.
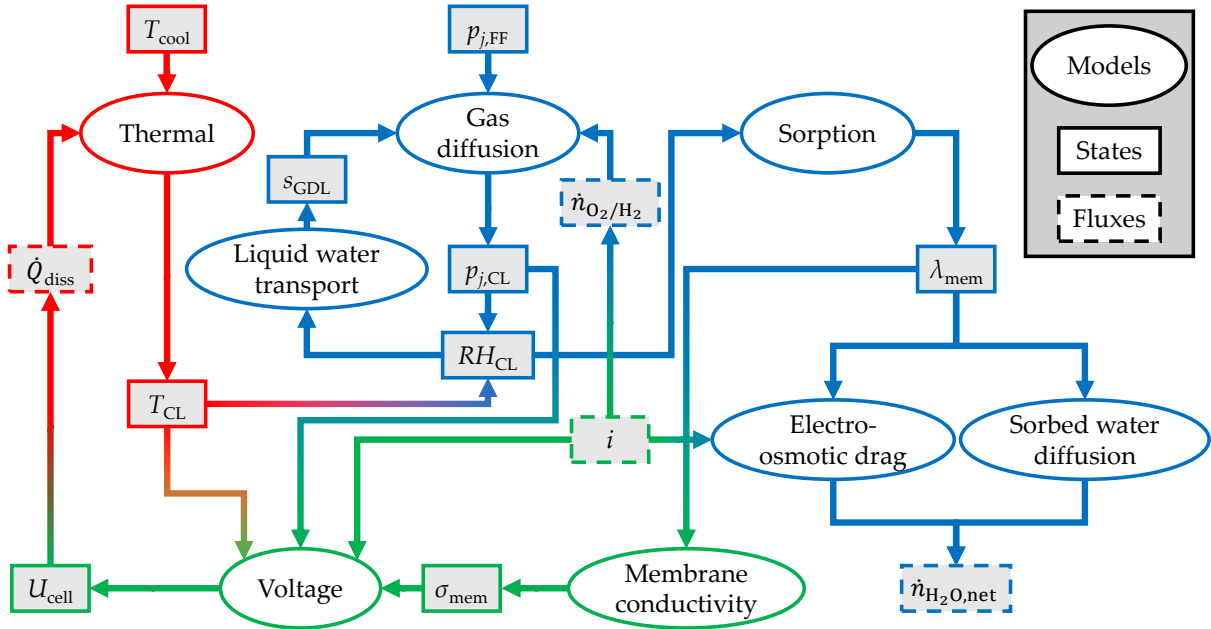
FIG. 3.3 Central sub-models and main couplings in typical PEMFC simulation models. The colors highlight domain-specific processes (blue: media transport, red: thermal, green: electrical).

3.2.3.1 Media transport domain

An overview of the most relevant transport phenomena in fuel cells and the available literature models was presented by Vetter and Schumacher[40]. In a later work, they addressed the uncertainties resulting from the large deviations found in literature models[78], highlighting the need for experimental parametrization and validation, as discussed later in Subsection 3.3.4 and Subsection 3.3.5.

Convection dominates the media transport along the channel. As the channel flow is assumed to be laminar, it represents an incompressible pipe flow of a Newtonian fluid and is therefore often modeled using the Hagen-Poisseuille equation. Assuming constant viscosity of the fluid yields a linear pressure drop along the flow direction.

Through the layers, the gas transport of the reactants and the product water vapor is mainly diffusive, as depicted in Figure 3.2. In the simplest approximation, this process is described as concentration-driven Fick diffusion. Typical GDLs are made from porous media, which impact is described by calculating an effective gas diffusion coefficient as introduced in Equation 2.24. Nonoyama et al. proposed to calculate the effective diffusion coefficient by considering the porosity and tortuosity of the porous media in addition to the baseline diffusion coefficient[37]. In their model, the baseline diffusion coefficient is approximated by using the Bosanquet relation. The diffusion is divided into a Knudsen diffusion and a molec-

ular diffusion contribution, provided by Bird, Stewart and Lightfoot and Perry and Green, respectively[79,80]. The presence of liquid water reduces the effective diffusion coefficient further[36], as introduced in Equation 2.25.

The production of water and consumption of the reactants, also shown in Figure 3.2, are calculated analytically from the current and Faraday's constant[81], as introduced in Equation 2.13 and Equation 2.14. Production and consumption takes place in the catalyst layers of the anode and cathode. At the cathode, oxygen is consumed and water is produced in the ORR displayed in Equation 2.3. At the anode, hydrogen is converted into protons and electrons in the HOR, shown in Equation 2.2.

The sorbed water within the membrane is mainly transported via two mechanisms shown in Figure 3.2: a concentration gradient driven diffusion and the electro-osmotic drag, where protons traveling from anode to cathode pull water molecules with them[81]. Both effects cannot be modeled analytically in a simplified and system adequate degree of detail, as the transport properties depend on the membrane material, the membrane water content and the temperature. Therefore, empirical models must be employed to estimate the diffusion coefficient[39,82–84]. As Vetter and Schumacher pointed out, the reported diffusion coefficients for commonly used Nafion span one to two orders of magnitude[40]. For the electro-osmotic drag, multiple authors proposed their own empirical models based on targeted experiments[39,85–87]. Again, the electro-osmotic drag coefficients derived from experimental data and the proposed models scatter widely[40]. During stationary fuel cell operation, it is impossible to separate both effects from one another, as only the net water transport can be measured.

Depending on the local water activity of the gas phase at the membrane interface, the membrane water content in stationary conditions is typically approximated using vapor sorption isothermes. According empirical relations based on measurement data were proposed by various authors[39,88,89]. The steady-state equilibrium water content resulting from these models yields a rather small scatter[40]. However, if the water transport dynamics should be taken into account, calculating only the steady-state equilibrium is insufficient. The sorption rates must be modeled carefully to allow for transient, non-equilibrium states between the membrane and the adjacent gas phase. While measurements and models were reported in literature[90–93], they result in sorption coefficients spanning more than three orders of magnitude[40] and yield a mismatch with experimental data obtained in this work, as discussed in the following Chapter 4. The high uncertainty of literature models requires a careful parametrization of the sorption sub-model in realistic operation, that is shown later in Subsection 3.3.4.

Most models neglect liquid water to limit the complexity. In operating states close to application, liquid water is however often present towards the cathode outlet, where over-saturated gas conditions occur as explained in Subsection 2.3.3. Note that the interaction between the gaseous phase and the liquid water is crucial: liquid water can partially block the reactant paths, increasing the concentration losses and reducing the operational cell voltage. This effect is often not properly treated, but a key aspect to predict the GDL flooding phenomena with a simulation model. For the scope of this work, liquid water transport therefore cannot be neglected.

To consider the liquid water transport within the GDLs, an approach featuring the saturation gradient Δs_{GDL} as a driving force was for example proposed by Vetter and Schumacher[40]. As shown in Figure 3.4, multiple parameters impact the resulting flux of liquid water $\dot{n}_{\text{H}_2\text{O,GDL}}^{(\text{l})}$ in this model. A capillary pressure saturation model is needed to derive the term $\partial p_{\text{cap}}/\partial s$. Here,

the van Genuchten law with material data from Gostik et al.[94] is implemented. The relative hydraulic permeability K_{rel} is derived from Mualem's model as stated by Zamel et al.[95]. Lastly, the absolute hydraulic permeability K_{abs} is calculated via the Carman-Kozeny equation.
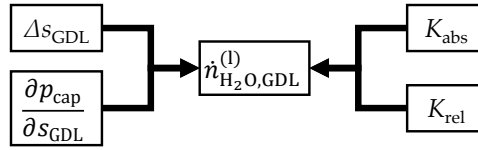
FIG. 3.4 Inputs for the liquid water transport model as proposed by Vetter and Schumacher[40].

In the flow field, two-phase flow might occur. Depending on the flow velocity, different flow regimes may be observed, which in turn limit the liquid water removal[14,27,45,96–98]. The impact of this flow regime transition in experiments is discussed in Section 4.5 and one of the authors publications[45]. These experimental results are also taken into account for the model developed in this work, as described in Section 3.3.

3.2.3.2 Thermal domain

The thermal domain features one main heat source: the fuel cell reaction. Part of the formation enthalpy is utilized as electric power, while the multiple loss mechanisms introduced in Subsection 2.1.2 result in a dissipative heat flux. This heat can be calculated directly if the operational cell voltage, the current and therefore the electrical power is known[19]. The lower the operational cell voltages and the higher the current, the higher the heat flux produced by the reaction. To avoid local hot spots, a sufficient heat conduction from the catalyst layer through the membrane, GDLs, flow fields and BPPs must be ensured. The heat production in the catalyst layer results in a temperature gradient between the active sites and the coolant. Note that the Joule heating within the other layers caused by ohmic losses is often neglected, as it is outweighed by the heat produced from the reaction.

The heat conduction through the layers can be modeled by using Fourier's law. The heat transfer from the BPP to the coolant requires a heat transfer correlation, as well as geometric data such as the surface area[99]. An additional impact on the heat balance might be caused by the phase change of water. Note that isothermal models, which are widely used[59,67,69], neglect two temperature-gradient induced transport mechanisms. The first effect is the thermo-osmosis in the membrane: a temperature gradient drives water sorbed in the hydrophilic Nafion® membranes from the cold to the hot side[100]. Second, if the vapor phase is fully saturated, a temperature gradient induces locally varying saturation pressures as introduced in Equation 2.22. Then, the saturation pressure gradient results in partial pressure gradients, finally yielding a diffusive water vapor transport from hot to cold areas.

3.2.3.3 Electrical domain

The operational cell voltage in PEMFCs is affected by three main loss mechanisms: activation losses, ohmic losses and mass-transport losses, as introduced in Subsection 2.1.2. The activation losses typically dominate the low current region and cannot be influenced directly by improving the water management, as they mainly depend on the catalyst material and its distribution[19]. Note that the activation losses are a function of the operating conditions, especially the temperature and reactant concentration[19].

35

The ohmic losses are linearly dependent on the current and therefore dominant in the mid to high current region of the polarization curve. They consist of several contributions, such as the electronic resistance of the fuel cell layers, the contact resistances between these layers and the protonic conductivity of the membrane. Especially the membrane conductivity is heavily influenced by the water management within the fuel cell, as it strongly depending on the membrane's water content. The membrane conductivity is therefore considered as a key aspect in the simulation model development within this work and displayed as a separate sub-model in Figure 3.3.

As the reactant consumption increases at high currents, a third loss mechanism becomes increasingly important: the mass-transport losses. The cell voltage features a logarithmic dependency on the reactant partial pressures. Therefore, a decrease of these partial pressures yields a strong decrease in cell voltage[19]. The reactant partial pressure at the catalyst layer depends on the gas diffusion from the flow field towards the active site. A high reactant consumption due to high current densities reduces the local partial pressure. Also, liquid water accumulation within the GDL reduces the effective diffusion area for the reactants, highlighting another strong coupling between the water management and the fuel cells performance. This interaction, which is especially relevant for dynamic current increases, is in focus of the second example in Subsection 3.4.2.

3.3 Development of a New Simulation Model

3.3.1 Assumptions

To fulfill the computation time requirement, the complexity of the model must be limited. A first step in simplifying the approach is to introduce multiple assumptions, which are divided into their respective domains:

General

1. Material properties are assumed to be isotropic.
2. The catalyst layer is only an interface and has no spatial extent.
3. Within each segment, only through-plane transport is considered. Interaction between the segments only takes place via the flow field or the BPP.

Media transport domain

1. Oxygen, nitrogen, hydrogen and water vapor are treated as ideal gases and are the only species represented in the model.
2. The phase change of water is considered as instantaneous, therefore the gas and liquid phase are assumed to be always in equilibrium.
3. Ice is neglected, as temperatures well above 0 °C are in focus.
4. The gas flow within the flow fields is assumed to be fully developed and laminar. Changes in viscosity are neglected, resulting in a linear pressure drop.
5. No mass transport occurs orthogonal to the primary transport direction within the flow fields.
6. Convection delay is neglected, as it yields only a small impact on the predicted voltage[55].
7. The membrane is ideally semi-permeable, transporting only water and protons.
8. GDL and MPL are treated as one uniform layer using a combined transport resistance.

9. Water is produced within the membrane at its cathode side interface.

Thermal domain

1. The coolant flow is thermally and hydrodynamically fully developed.
2. The gas temperature reaches the mean value between the adjacent BPP and GDL surface temperatures after 10% of the flow field length, as the coolant flow with its high heat capacity flux is assumed to dominate the temperature distribution within the cell.
3. Heat is only produced in the cathode catalyst layer.
4. The coolant temperature distribution is treated as Dirichlet boundary condition.

Electrical domain

1. Ageing effects impacting the electro-chemical performance and water transport properties are neglected.
2. The in-plane conductivity of the BPP is assumed to be infinite, leading to an equal voltage within all segments of the cell.
3. The cell voltage is determined by superposition of multiple loss contributions, which are assumed to be decoupled.

3.3.2   Process selection

Not all processes known from literature and introduced in Subsection 3.2.3 are modeled in great detail, as the computational effort increases and the transferability deteriorates. Therefore, a systematic methodology on selecting the right processes and their level of detail within the model must be employed. Two main approaches are implemented. In general, processes are selected based on their impact on the voltage prediction and their inherent time scale, as shown in Figure 3.5. As water transport phenomena play a pivotal role in this work, the according transport processes are evaluated separately by estimating their impact on the total water transport, as shown later in Figure 3.8.

Figure 3.5 showcases the two dimensions relevant for the general process selection: the impact on voltage prediction and the inherent time scale. The voltage sensitivity is classified into two regions, low and high impact. As the model complexity should be limited to achieve the computational effort requirement, processes with a low impact are neglected for the model. Along the time scale axis, five regions are differentiated:

1. The "very fast" time scale with time constants below 0.1 s.
2. The "fast" time scale between 0.1 s and 1 s.
3. The "medium" time scale between 1 s and 10 s.
4. The "slow" time scale between 10 s and 100 s.
5. The very slow time scale above 100 s.

Below the x-axis, typical time scale ranges for different challenges are displayed: controlling the fuel cell system usually focuses on the fast to medium time scales, while the power split optimization between FCS and battery tends towards longer relevant time periods. Dynamic water management, as defined in this work, is focused on fast, medium and slow time scales. The duration of typical drive cycles and the vehicle lifetime on the other hand span the very slow time scale. Calculating the time scales of various processes is in focus of the following subsection.
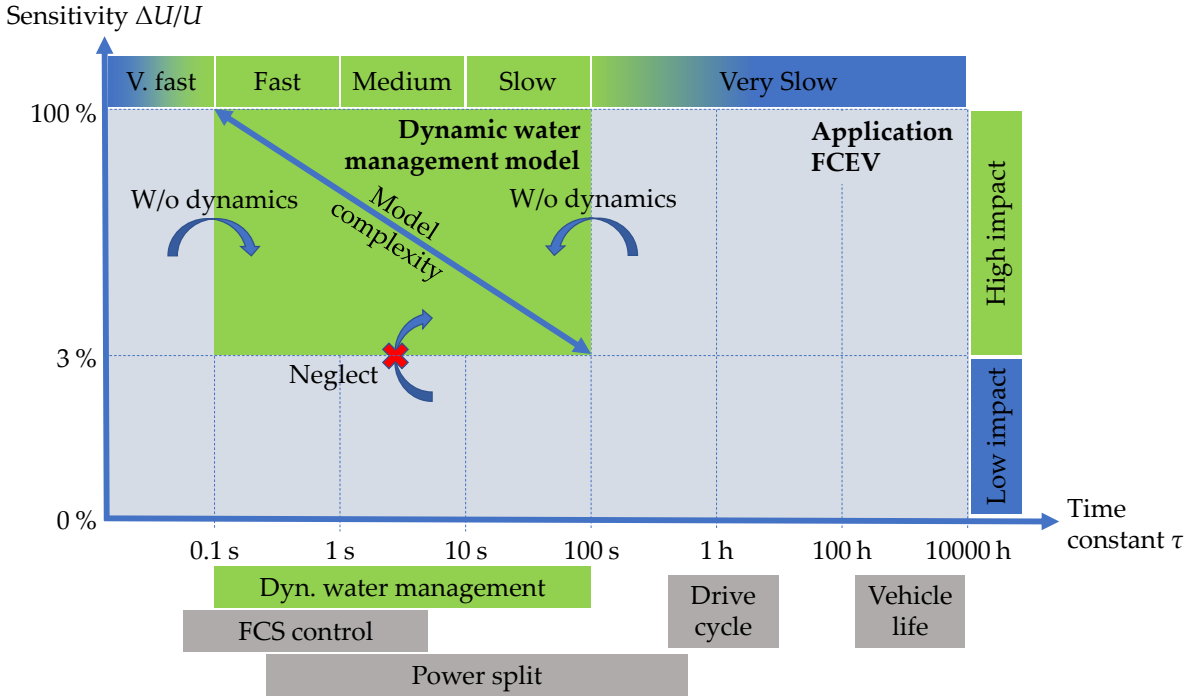
FIG. 3.5 General approach for process selection based on voltage sensitivity and inherent timescale.

3.3.2.1 Time constants

The concept of time constants stems from Linear Time Invariant (LTI) systems analysis and, in this work, is transferred onto various physical processes. A special form of first order LTI system, a PT1-element, is represented by a differential equation containing the time-dependent output function $y(t)$ and input function $u(t)$, the time constant τ and the amplification factor K:

$$\tau \dot{y}(t) + y(t) = K u(t) \tag{3.1}$$

When the Heaviside step function is used as an input function $u(t)$ and the initial condition is defined as $y(t=0) = y_0$, the solution of the differential Equation 3.1 is

$$y_{\text{PT1,step}}(t) = y_0 \exp\left(-t/\tau\right) + K\tau \left[1 - \exp\left(-t/\tau\right)\right] = C_1 \exp\left(-t/\tau\right) + C_2. \tag{3.2}$$

For $t \to \infty$, y approaches $y_\infty = K\tau$. An exemplary plot of a PT1-element step responses for varying time constants τ is shown in Figure 3.6. Generally, $y(\tau) \approx y_0 + 0.632(y_\infty - y_0)$ and $y(5\tau) \approx y_0 + 0.993(y_\infty - y_0)$, meaning that 63% and 99% of the final value are reached after 1τ and 5τ, respectively. Another common metric to describe dynamic behavior is t_{90}, the time to reach 90% of the stationary value after a step input, shown by the vertical dashed lines in Figure 3.6. The time constant τ is converted to t_{90} and vise-versa for a PT1-element via

$$\tau = -\frac{t_{90}}{\ln(0.1)} \approx 0.434\, t_{90}. \tag{3.3}$$

This work focuses on the fast to slow time scales. Very fast processes with time constants lower than 0.1 s are assumed to be in a quasi-stationary state. Very slow processes with time constants above 100 s are only taken into account, if they have significant impact on the cell voltage. Then, these very slow processes are modeled without time-dependent behavior as
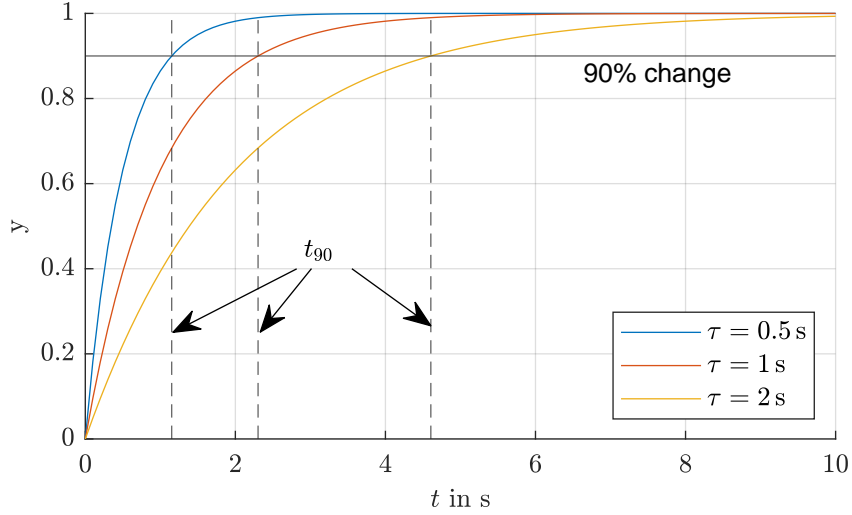
FIG. 3.6 Step response of a PT1 element for $y_0 = 0$, $y_\infty = 1$ and varying time constants τ.

depicted in Figure 3.5. Table 3.3 shows the characteristic time constants of the transport processes introduced in Figure 3.2. Additionally, water condensation and evaporation as well as the charging and discharging of the electrochemical double layer are displayed in Table 3.3

TABLE 3.3 Time constants of the transport processes.

Process	Time constant τ	Source
Gas diffusion	$\frac{L^2}{D^{(g)}}$	Fick's law, Wang & Wang[75]
Production & consumption	τ_I	Own work
Membrane water diffusion	$\frac{L^2}{D^{(s)}}$	Fick's law, Wang & Wang[75]
Electro-osmotic drag	τ_I	Own work
Sorption	$\frac{L}{k_{\text{sorp}}}$	Fick's law, Seidl[55]
Liquid water transport	$\frac{L^2}{D^{(l)}_{H_2O}}$	Fick's law
Condensation	$\frac{1-s}{C_{\text{cond,evap}}}$	Sauter et al.[101]
Evaporation	$\frac{1-s}{C_{\text{cond,evap}}\,s}$	Sauter et al.[101]
Heat production	τ_I	Own work
Heat conduction	$\frac{L^2}{\alpha} = \frac{L^2 \rho c_p}{\kappa}$	Fourier's law
Heat transfer	$\frac{\rho c_p V}{h A}$	Own work
Double-layer charge/discharge	$L^2 A_{\text{spec}} C \left(\frac{1}{\kappa} + \frac{1}{\sigma} \right)$	Ong & Newman[102] from Johnson & Newman[103], Newman[104]

Fick's law of diffusion can be transferred to a first-order differential equation as given by Equation 3.1, if only one spatial dimension is taken into account. From that, the according time constant is derived. This is used for the gas diffusion processes, the sorbed water diffusion through the membrane, as well as the liquid water transport within the GDL. In reality, the latter is a complex capillary diffusion process, which is treated as a simple Fick-

type transport for the process selection within this work. All Fick-type diffusion process time constants include the diffusion length L, e.g. the thickness of the respective layer, and a diffusion constant D. In case of an interfacial mass transfer as the sorption process, the sorption coefficent k_{sorp} is included in the time constant calculation instead.

For condensation and evaporation processes, the time constant is reciprocal to the evaporation and condensation rate $C_{\mathrm{cond,evap}}$. Additionally, the liquid water saturation s introduced in Equation 2.23 is included. Evaporation can only take place as long as gaseous volume remains and liquid water is available ($s > 0$). Note that evaporation only occurs in areas where liquid water is available. Condensation can take place on areas where liquid water is present and on areas where currently no liquid water exists, resulting in faster time constants of the condensation compared to the evaporation process.

The reactant consumption, the water and the heat production, as well as the electro-osmotic drag are directly coupled with the current I drawn from the fuel cell and therefore assumed to feature the same time constant. The heat conduction is treated based on Fourier's law, which is mathematically similar to Fick's law of diffusion when replacing the diffusion coefficient D with the thermal diffusivity $\alpha = \frac{\kappa}{\rho c_p}$. The thermal diffusivity is calculated from the thermal conductivity κ, the volumetric density ρ and the heat capacity c_p of the respective layer. To derive the time constant for the heat transfer process, a solid material with the density ρ, heat capacity c_p and Volume V is assumed. The heat is transferred via a surface area A with a heat transfer coefficient h.

Charging and discharging of the electro-chemical double-layer depends on the layer thickness L, the specific interfacial area A_{spec}, the double-layer capacitance C, as well as the ionic and electronic conductivity σ and κ, respectively.

With material data for a typical fuel cell, the time constants for the processes are computed based on Table 3.3, with the result being shown separately in Figure 3.7. The processes directly coupled with the current variation are not shown in the figure. Due to its very low time constant of $\approx 0.2\,\mu\mathrm{s}$[75], the double-layer charge and discharge are also excluded. Since the length scale along-the-channel is large in comparison, the resulting time constants of e.g. diffusion processes would be several orders of magnitude larger. Therefore only the through-plane direction is considered. *Example: typical layer thickness of a GDL is $\approx 200\,\mu\mathrm{m}$, length of a cell is $\approx 20\,\mathrm{cm}$, leading to a six order of magnitude larger time constant.*

In Figure 3.7, the time constants of three processes lie within the relevant time constant range for dynamic water management as defined in this work: the diffusion of sorbed water through the membrane, the transport of liquid water through the GDL and the sorption of water. The analysis of gas diffusion, condensation and evaporation of water, the heat transport and the current manipulation yield time constants lower than the relevant time scale range. Therefore, these processes are implemented in a quasi-stationary formulation discussed later in Subsection 3.3.2.3. The very low time constants of the condensation and evaporation process support the assumption that gas and liquid phase are always in equilibrium, as introduced in Section 3.3.1.
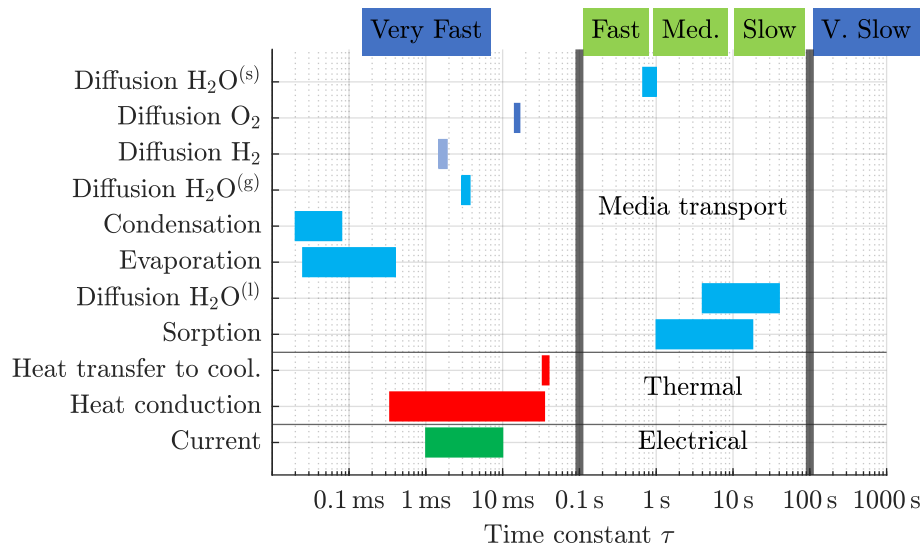
FIG. 3.7 Time scales of processes in the respective domains and relevant time scale range for dynamic water management.

3.3.2.2 Water transport processes

The typical magnitude of water fluxes caused by eight different phenomena is compared in Figure 3.8. Note that the models utilized for this analysis are also displayed in the final model selection in Table 3.4. The hydraulically induced water transport through the membrane is modeled based on Husar et al.[105]. Due to its low resulting molar flux, the hydraulically induced water transport is not included in the final model. In general, the liquid water transport through the GDL yields the largest molar fluxes, which can even outweigh the water production. The other processes, except the hydraulic transport, overlap in their respective water flux range and are therefore all included in the final model.
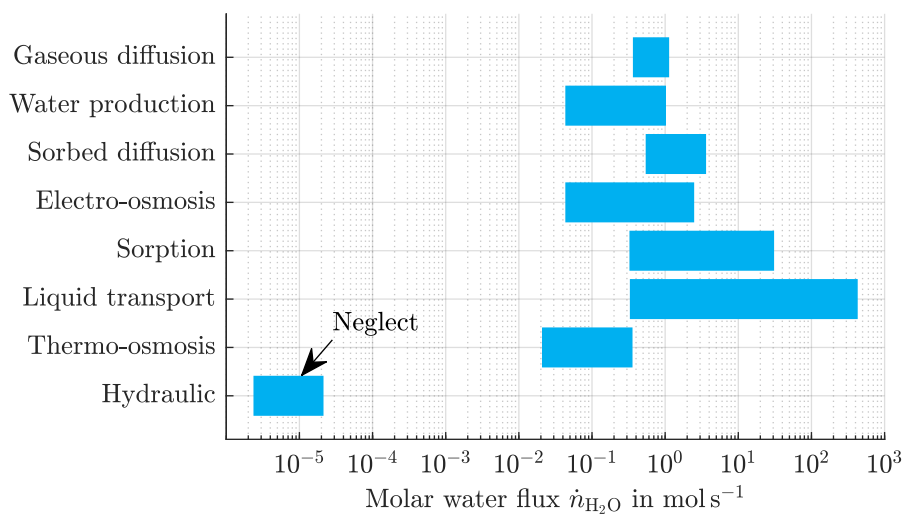
FIG. 3.8 Magnitude of water fluxes caused by different processes in a typical 100 kW automotive PEMFC stack.

3.3.2.3 Final sub-model selection

Based on the analysis in the previous sections, the final process selection is summarized in Table 3.4. As the enhanced model is based on a simulation model developed by Grimm et al.[41], the extensions added within this work are also highlighted. The sub-models are mostly adapted from literature and sometimes extended or modified. In case of the liquid water transport, a limitation of the liquid water flux $\dot{n}_{\mathrm{H_2O,lim}}^{(l)}$ depending on the gas velocity within the flow field is added as shown in Appendix A.1, based on experimental results described in Subsection 4.5.1. In addition, fitting factors are introduced to allow a parametrization of the model based on experimental data.

TABLE 3.4 Final process and model selection, fitting factors and time-dependency sorted with respect to domains.

Model	Source	Fitting factor	Time-dependency	Extension to previous version[41]
Gas diffusion	Nonoyama[37], Zamel et al.[106], Bruggemann[35], Jiao and Li[36]	-	Quasi-stationary	Liquid water interaction
Liquid water transport	Vetter & Schumacher[40], additional limitation	$\dot{n}_{\mathrm{H_2O,lim}}^{(l)}$	Dynamic	Complete sub-model
Sorption	Ferrara et al.[83], modified Ge et al.[55,90]	k_{sorp}	Dynamic	Complete sub-model
Electro-osmotic drag	Weber & Newman[107]	-	Quasi-stationary	Complete sub-model
Thermo-osmosis	Vetter & Schumacher[40]	-	Quasi-stationary	Complete sub-model
Sorbed water diffusion	Modified Ferrara et al.[83]	$f_{\mathrm{diff,mem}}$	Dynamic	No
Thermal	Fourier's law, VDI-Wärmeatlas[99]	-	Quasi-stationary	Complete sub-model
Voltage	Dicks & Rand[19], Kulikovsky[22], Neyerlin et al.[108], Springer et al.[39]	$f_{\mathrm{i,exch}}$, $f_{\mathrm{R,cont}}$, $f_{\mathrm{i,lim}}$, $f_{\mathrm{i,cross}}$	Quasi-stationary	No
Membrane conductivity	Modified Springer et al.[39,109]	$f_{\mathrm{R,mem}}$	Quasi-stationary	No

3.3.3 Implementation

The general structure of the model is taken from a stationary model developed by Grimm et al.[41]. It is extended by various dynamic effects and the time-integration process for dynamic calculations. The model is implemented in Matlab and set up in three functional blocks: the

pre-processing, the processing and the post-processing, as shown in Figure 3.9. For each simulation case, all three blocks are executed consecutively. Multiple simulation cases can be distributed between the processor's cores and evaluated in parallel to reduce the total computation time.
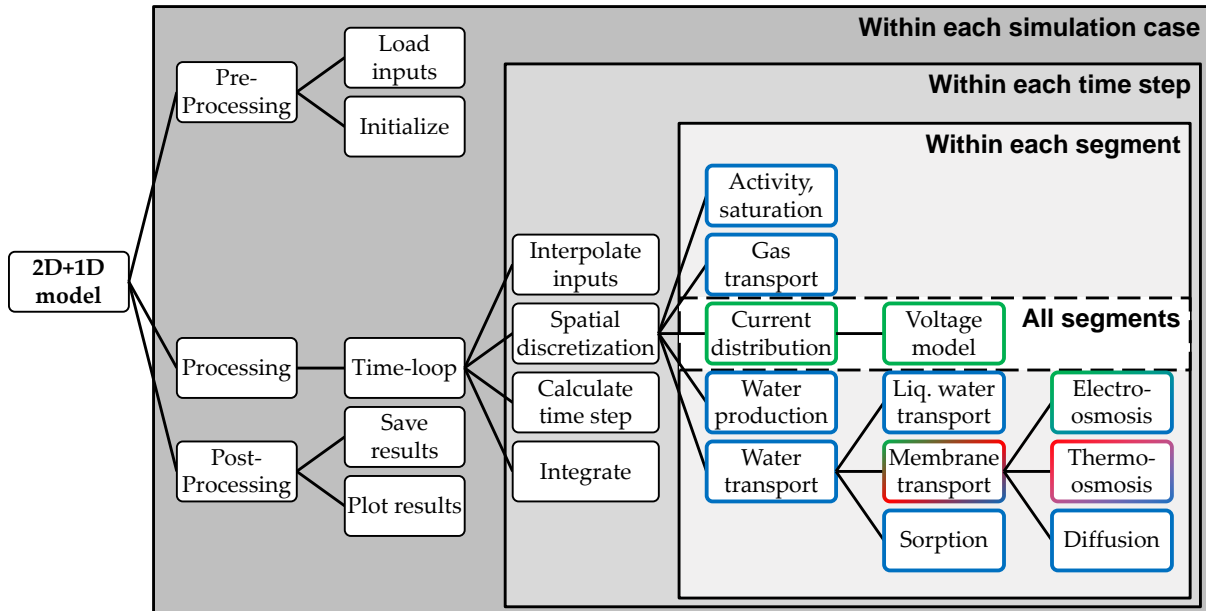
FIG. 3.9 Implemented model structure, colors highlight domain-specific processes (blue: media transport, red: thermal, green: electrical).

In the pre-processing step, the boundary conditions shown in Table 3.5 are imported into the workspace. This might be either synthetic cases or experimental data from the system test rig. Note that the nitrogen molar fraction at the anode inlet $x_{\mathrm{N_2,dry}}$ is given with respect to the dry gas phase excluding water vapor, as this value is directly available from the concentration sensor at the test rig. The interface allows for simulation studies extrapolating known behavior, in-depth analysis of experiments and model validation with experimental data. After the inputs are loaded, the simulation is initialized and the processing step starts. On the top level of the processing step, a time loop is executed, utilizing an explicit time-step adaptive numerical solver to calculate the new states based on the old states and the fluxes.

Within each time step, the boundary conditions from the input are interpolated first. Afterwards, the fluxes within each segment are calculated. To compute also the fluxes between the segments, a computationally efficient vector matrix formulation is implemented[110]. For each segment, the local activity and liquid water saturation as well as the gas diffusion coefficients are evaluated. Next, an iteration is necessary to calculate the current density distribution. As all the segments are connected in parallel by the BPP, the voltage in each segment must be the same. For that, a voltage model is applied and the local current density within the segments is adapted, until all segments' voltages converge towards one global cell voltage.

An exemplary current density iteration process is shown in Figure 3.10. At the beginning of the iteration process, the same current density is applied to all segments. As segment 1 close to the cathode inlet tends towards drier membrane states and therefore higher ohmic losses than segment 2 in the middle of the cell, U_1 will be lower than U_2. Segment 3 on the other hand tends towards wetter membrane states, resulting in lower ohmic losses and a higher segment voltage U_3. As all the segments act electrically in parallel, the iteration process

TABLE 3.5   Boundary conditions for the simulation model.

Description	Variable	Unit
Current	I	A
Cathode stoichiometry	λ_{ca}	-
Cathode inlet pressure	$p_{ca,in}$	Pa
Cathode inlet temperature	$T_{ca,in}$	K
Cathode inlet relative humidity	$RH_{ca,in}$	-
Anode stoichiometry	λ_{an}	-
Anode inlet pressure	$p_{an,in}$	Pa
Anode inlet temperature	$T_{an,in}$	K
Anode inlet relative humidity	$RH_{an,in}$	-
Anode inlet nitrogen fraction	$x_{N_2,dry}$	-
Coolant inlet temperature	$T_{cool,in}$	K
Coolant temperature rise	ΔT_{cool}	K

decreases the current density i_1 and increases i_3, until all segments produce the same voltage.
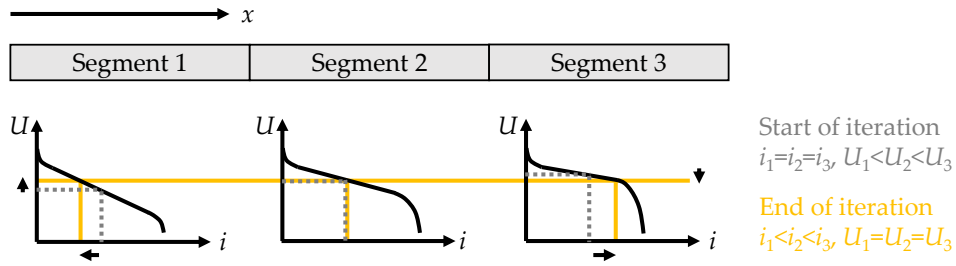
FIG. 3.10   Exemplary current density iteration process within a time step.

As soon as the current density distribution is calculated, the water production and reactant consumption within each segment is known as well. Next, the water transport is evaluated, starting with the liquid water transport in the GDLs and the flow field. The membrane water transport is divided into three transport phenomena, electro-osmosis, thermo-osmosis and diffusion, which add up to a net water transport through the membrane within each segment. Lastly, the sorption at the membrane-GDL interface is evaluated. With that, all fluxes are known and the next time step size is calculated. As an explicit solver is used, the time step size must be limited to ensure numerical stability. Integrating the fluxes yields the new states and the cycle repeats until the end of the simulation case. When the simulation case is complete, the results are saved and plots are created.

3.3.4   Parametrization

To achieve a high accuracy of the model while maintaining simple transferability, a limited set of fitting factors is introduced. This is necessary, as the correlations from literature are only a (semi-)empirical approximation of the real behavior. Deviations from the literature models might be introduced by a variety of reasons, as changing material quality, production processes, cell design, or a different operational setting in the fuel cell compared to simplified

experiments. In total, eight fitting factors are added to the model, as previously displayed in Table 3.4, three of which are impacting the water transport. The other five fitting factors affect the voltage model. As the developed model should accurately predict dynamic and stationary operation, a limited set of stationary and dynamic measurements is utilized for parametrization. As the processes affected by the different fitting factors are coupled, e.g. the water transport affects the membrane conductivity and therefore also the voltage model, the order of the parametrization steps is important. The fitting process is displayed in Figure 3.11.
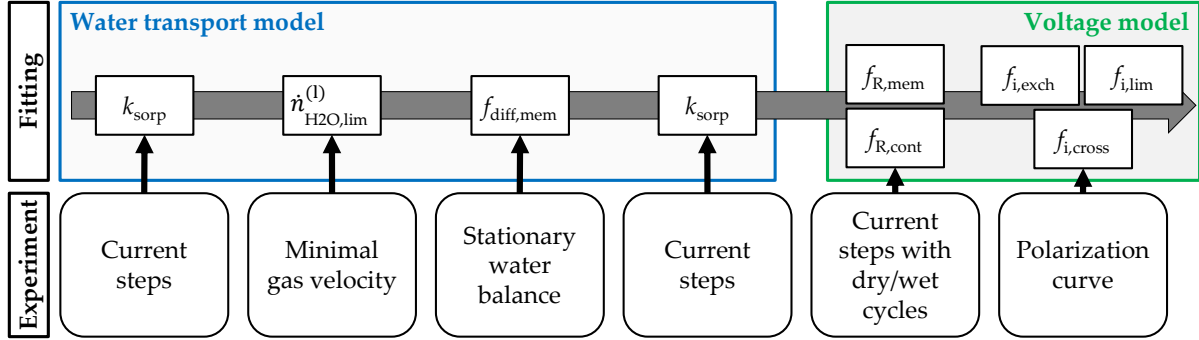
FIG. 3.11 Schematic parametrization process for the simulation model.

First, the sorption fitting factor k_{sorp} is calculated. This process describes the water transfer at the membrane interface. It is derived from the voltage gradient during current steps conducted at the system test rig, described later in Section 4.4. This factor also affects the water balance, meaning the split of water flux between cathode and anode outlet. Second, the liquid water flux $\dot{n}_{\text{H}_2\text{O,lim}}^{(\text{l})}$ from the GDL to the flow field is limited via a bi-linear function on the cathode side, in line with the minimal flow measurements explained later in Subsection 4.5.2 and the condition, that a gas flow of zero yields no liquid water transport out of the cell. The limit function is derived in Appendix A.1. On the anode side, the liquid water drainage limit is not known from the experiments and a linear function is introduced as a placeholder.

Third, the membrane diffusion fitting factor $f_{\text{diff,mem}}$ is calculated based on the water balance measured during stationary operation at various currents. Some of the produced water is neither detected at the anode outlet, nor at the cathode outlet. But as the anode loop is closed, it is likely that the vast majority of this missing liquid water exits through the cathode outlet, but is not separated and measured by the water separator correctly. This hypothesis was also confirmed visually via cameras in the cathode exhaust line downstream of the cathode water separator. Therefore, the missing water flux is attributed to the cathode outlet. As the adaption of the membrane diffusion impacts the dynamic and stationary membrane water content, the sorption factor is updated, using the current step measurements again in a fourth step. With that, the water transport sub-model is fully parametrized.

The last two steps focus on the voltage model. As the *HFR* is measured during experiments and the membrane water balance is already approximated as a result of the previous steps, the ohmic resistance is parametrized. It is divided into two contributions: the membrane resistance, which is dependent on its water content, and the contact resistance, which is assumed to be constant. The contact resistance factor also includes the layers constant ohmic losses, excluding the membrane. To separate the variable and constant contributions, a load step experiment with constant gas supply is conducted. This experiment is described in detail in Subsection 4.4.2 and the simulation results are shown in Section 3.4. The test yields a dry-out and re-humidification cycle of the membrane, resulting in a time-dependent change

45

in membrane resistance. With that, the variable contribution of the membrane factor $f_{R,mem}$ as well as the constant contribution of the contact resistance factor $f_{R,cont}$ are parametrized.

The last step concludes the parametrization process. Here, the three missing fitting factors for the voltage model are calculated: the exchange current factor $f_{i,exch}$, the limiting current factor $f_{i,lim}$, and the cross-over factor $f_{i,cross}$. This is done by fitting the voltage model to a stationary polarization curve, after all water transport processes and the ohmic contributions are known from the previous steps. In theory, additional iterations within the fitting process are possible, but the presented method provides sufficient accuracy to fulfill the model requirements as shown in the following section.

3.3.5 Validation

After the parametrization process, the model is tested regarding the model requirements introduced in Section 3.1.2. A measurement of the Worldwide harmonized Light-duty vehicles Test Cycle (WLTC) from the system test rig described later in Subsection 4.2.2 provides a variety of stationary and dynamic loads typical for the automotive application of fuel cell systems. The stack boundary conditions shown in Table 3.5 are extracted from the measurement data and fed into the simulation model. The calculated mean cell voltage U_{cell} and losses ΔU are displayed in comparison to the measured mean cell voltage U_{meas} in Figure 3.12.
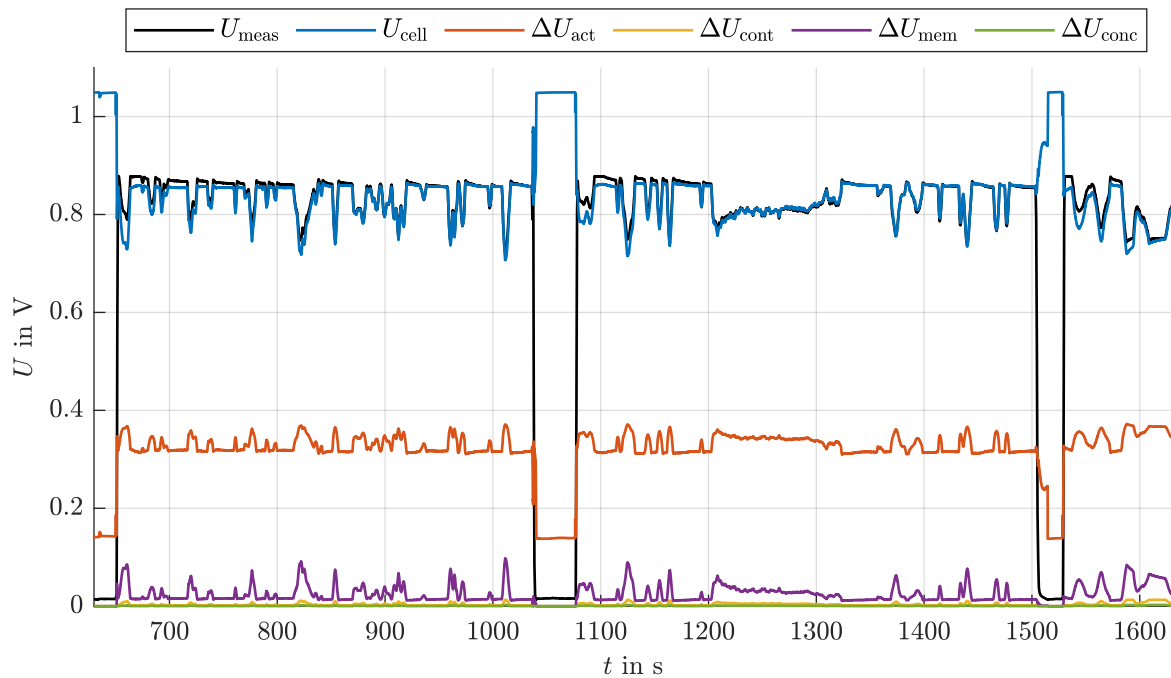
FIG. 3.12 Simulated and measured mean cell voltage and predicted losses during a dynamic load cycle.

Note that during the measurement multiple standstill phases occur, where the model is incapable of computing a valid voltage. After the restart of the system, the predicted cell voltage deviates from the measured voltage for a certain time. About 150 s after the restart, the prediction matches the measurement again with high accuracy. If the start-stop phases are neglected, the mean deviation of the predicted cell voltage is 0.9% and the accuracy requirement of less than 5% relative error is fulfilled during 99% of the time[55].

The ohmic resistance requirement is fulfilled by conducting the respective parametrization shown in the previous section. All dynamic processes with time scales in scope of this work are implemented as described in Section 3.3.2. The computational time needed for simulation t_sim is approximately 1.25 times the physical time t_real[55]. Only five experiments are necessary for a sufficient parametrization: load steps with and without wet/dry cycles (see Subsection 4.4.2), flooding limit measurements (see Subsection 4.5.2), stationary water balance measurements and a polarization curve.

Now, the model is ready to showcase exemplary results for an in-depth understanding of the dominant processes occurring within the stack, as targeted with RQ1. In addition, this model is utilized in scope of Chapter 5, targeting the efficiency and dynamics trade-off when choosing a system architecture and control strategy, as aimed at by RQ4.

3.4 Exemplary Results

3.4.1 Dry-out phases after current decrease

One common way to investigate the dynamic response of a fuel cell is to apply a step change in current. Within this work, such experiments are conducted on a system test rig and described in detail in Section 4.4. In this example, the boundary conditions are measured in the experiment and fed into the simulation model to analyze the underlying processes. The experimental case "fixed boundary conditions" shown in Subsection 4.4.2 is picked, because the constant pressure and mass flow allows to observe a variety of different phenomena. Note that the flow configuration is changed from a serpentine flow in the experiment to a counterflow in the simulation for an easier visualization.

After an equilibration phase, the current is stepped down from 70% to 30% of the rated current, as shown in Figure 3.13. Immediately after the current decrease, the voltage exhibits an overshoot followed by a relaxation towards the new stationary value. This is caused by a complex combination of processes explained in the following. Four distinct points in time are picked for further analysis: (I) at the end of the stationary first phase, (II) 1 s after the current decrease, (III) 10 s after the current decrease and (IV) 50 s after the current decrease.

Figure 3.14 shows the spatial distribution of the most relevant variables at the end of the equilibration phase in cross-sectional views of the fuel cell. From bottom to top, the fuel cell is divided into the anode flow field, anode GDL, membrane, cathode GDL and cathode flow field along the z-axis, as introduced in Figure 3.2. All layers are shown with equal thickness to improve readability. In x-direction, the segmentation in flow direction is represented by the grid lines. The thick white arrows indicate the flow direction within the respective flow fields, in this case a counterflow configuration.

The upper subplot in Figure 3.14 focuses on the water distribution within the cell. The relative humidity RH of the gas phase is displayed in shades of blue within the GDLs and flow fields. As expected, the cathode inlet is the driest spot in the cell, while the relative humidity rises towards the cathode outlet. Due to the higher relative inlet humidity at the anode caused by the recirculation loop, smaller variations in relative humidity occur on the anode side. Within the membrane, the water content λ_mem is depicted according to the right hand color bar. Note that a membrane water content below 5 is considered to harm the membrane and accelerate ageing. Therefore, the color bar is adapted to display a dark red color if this lower limit is

47
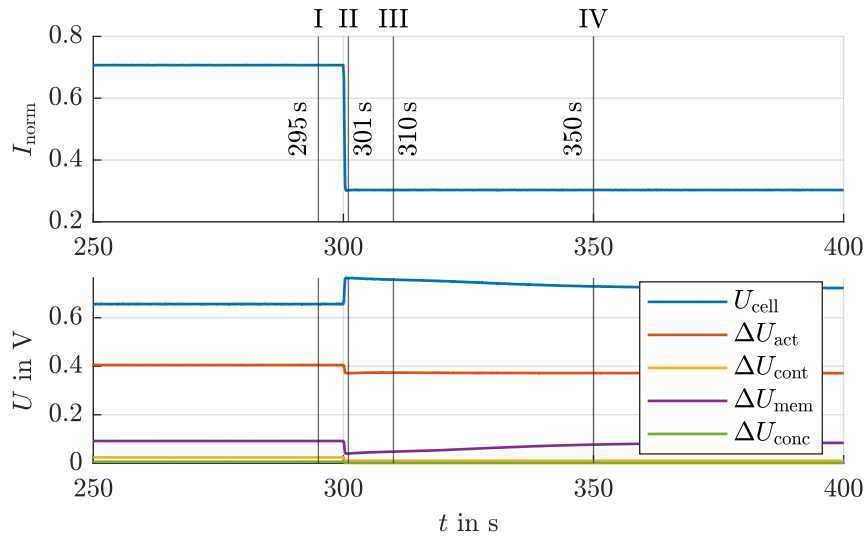
FIG. 3.13 Simulated current, cell voltage and loss contributions in case of a step-wise current decrease. The vertical lines mark the four distinct points in time chosen for further investigation.

violated. In the case displayed, the membrane water content is lowest at the cathode inlet. If liquid water occurs, white points are displayed within the respective layer and segment. The density of these points corresponds to the liquid water saturation. Here, liquid water occurs in the cathode GDL around the middle of the cell, where the water production is the highest.
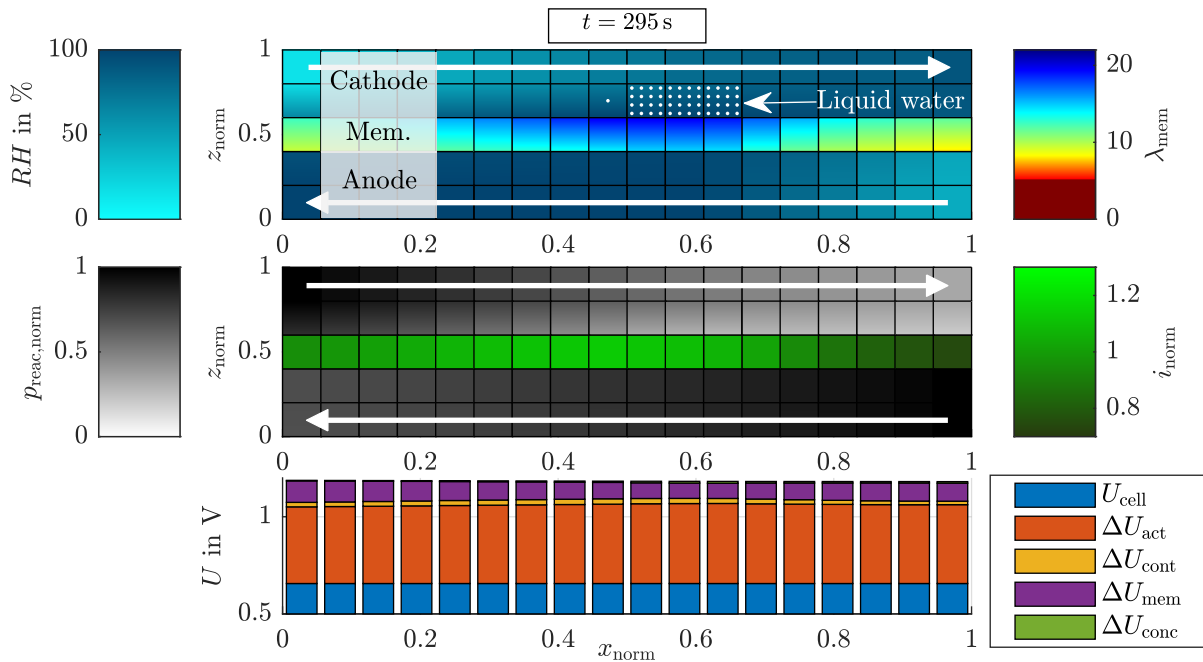
FIG. 3.14 (I) Cross-sectional view of the spatial variations of the most relevant simulated variables at the end of the equilibration phase. **Top:** Relative humidity, membrane water content and saturation (white dots). **Middle:** Normalized reactant partial pressure and normalized current density. **Bottom:** Voltage loss contributions per segment and resulting cell voltage.

The middle subplot displays the partial pressures of the reactant gases p_{reac}, oxygen and

hydrogen for the cathode and anode side, respectively. The partial pressures are normalized to their according maximum value, the inlet partial pressure. Due to the rather high stoichiometry and hydrogen diffusivity on the anode side, the change in hydrogen partial pressure remains rather low. In contrast, a significant reduction of the oxygen partial pressure towards the outlet is observed on the cathode side. Due to the diffusion resistance of the GDL, the available partial pressure at the active sites is also lower than the flow field partial pressure. The current density distribution within the membrane is normalized to its mean value and displayed in shades of green. The highest current density appears where the membrane is sufficiently wet, resulting in low ohmic losses, and the reactant partial pressures are high, reducing activation and mass transport losses. This is the case between 0.4 and 0.7 normalized flow path length x_{norm}.

The lower subplot shows the contribution of the different loss mechanisms within each segment: the activation losses ΔU_{act}, the contact resistance losses ΔU_{cont}, the membrane losses ΔU_{mem} and the concentration losses ΔU_{conc}. As expected, the activation losses are the largest factor within all segments. At the cathode inlet and outlet, the membrane losses are slightly higher due to the drier membrane, compared to the middle of the cell. Concentration losses attribute only a negligible share of the total losses in all segments. As described in Section 3.3.1, the cell voltage is the same in all segments, as the BPP is assumed to be perfectly conductive.

Within the first second after the current is decreased, the fast processes dominate the fuel cell's response, as shown in Figure 3.15. As the consumption is reduced immediately as the current drops, the oxygen partial pressure at the active sites close to the cathode outlet increases due to the very fast gas diffusion, proceeding on time scales well below 0.1 s. The EOD is coupled delay-free with the current, reducing the through-plane gradient in membrane water content. Sorption and liquid water transport are still in non-equilibrium states with the new conditions due to their medium to slow intrinsic time scale, therefore the mean membrane water content and the saturation of the GDL remain roughly same. The cell voltage increases sharply, as all loss contributions are reduced and the current density distribution becomes more homogeneous.

Ten seconds after the current step, the liquid water saturation declines and the membrane starts to dry, beginning at the cathode's and anode's inlets as shown in Figure 3.16. This dry-out is mainly caused by the cathode gas flow. In the experiment, the mass flow and pressure of the air remained the same during, before and after the step, resulting in an air flow too high for the now reduced water production.

Fifty seconds after the current step, the membrane is severely dried, even reaching critically low wetting states at the anode inlet as shown in Figure 3.17. This results in increased membrane losses across all segments. In addition, the feedback via the anode loop in the experiment is at play. As the anode outlet becomes drier, the inlet humidity also declines with a short delay. All liquid water is already drained from the cell. The rather slow sorption process is now dominating the cell's response.

This example demonstrates the interplay of various dynamic processes implemented in the simulation model. In scope of RQ1, the sorption kinetics appear to be the dominant process limiting the dry-out dynamics. This is in line with the results obtained by the dry-out and re-humidification experiments as shown in detail later in Subsection 4.4.2. The knowledge gained with the simulation model therefore helps with interpreting the experimental data obtained at the system test rig, which is discussed in depth in the following chapter.
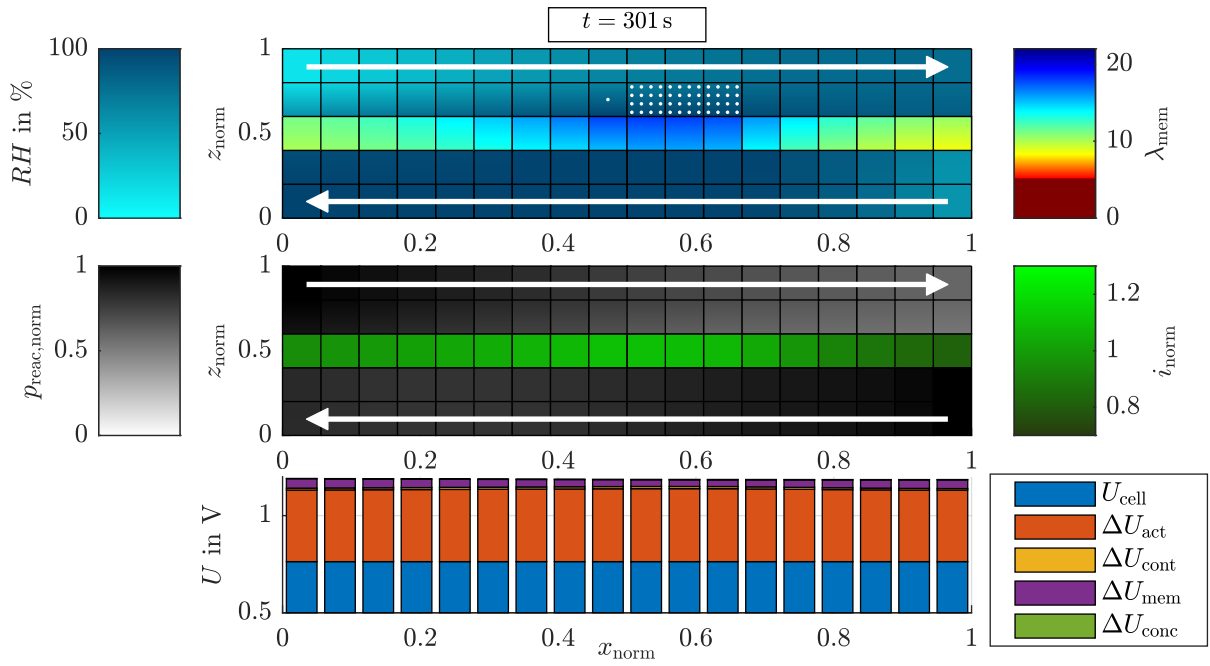
FIG. 3.15 (II) Cross-sectional view of the spatial distribution of various simulated variables 1 s after current reduction.
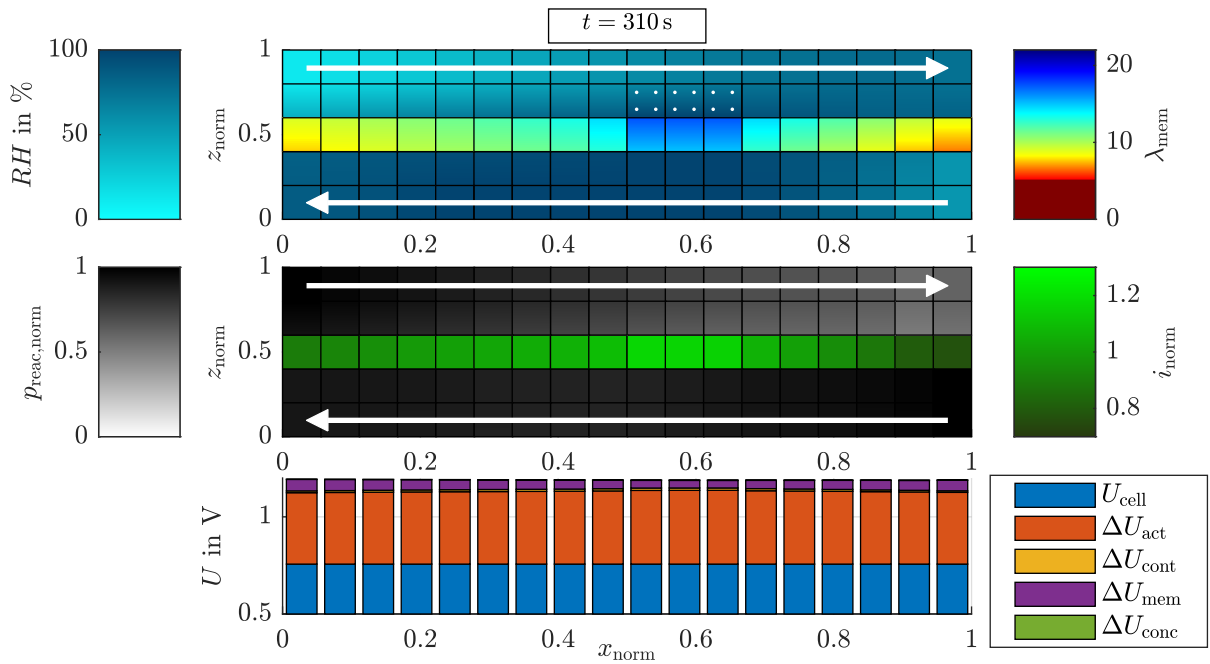
FIG. 3.16 (III) Cross-sectional view of the spatial distribution of various simulated variables 10 s after current reduction.
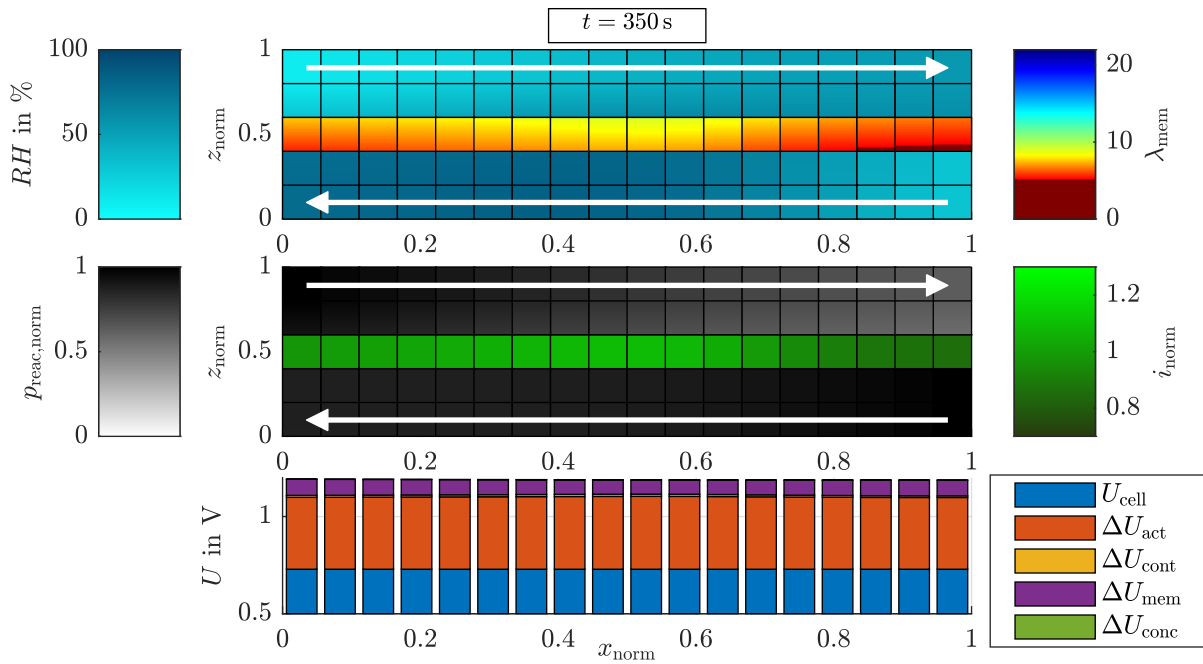
FIG. 3.17 (IV) Cross-sectional view of the spatial distribution of various simulated variables 50 s after current reduction.

3.4.2 Impact of liquid water after current increase

This second example showcases the simulated fuel cell response under the influence of liquid water during a synthetic step-wise current increase, highlighting the main phenomena acting on three distinct time scales. After a stationary phase of 600 s, the current is stepped up from 10% to 90% of the rated current within 0.01 s and the voltage exhibits an undershoot, as displayed in Figure 3.18. Gas flows and pressures are adapted without delay to the new current based on the activity based water management approach introduced in Subsection 2.3.4. Note that this is an idealization to reduce the complexity for a fundamental understanding. In reality, the mass flow and pressure adaption requires a certain response time of the air system in realistic systems, which further amplifies the voltage undershoot analyzed in the following, if the current gradient remains steep. The characteristic behavior of an experimental fuel cell system is discussed in Chapter 4, while the impact of different air system architectures on the fuel cell's response is in focus of Chapter 5.

At the end of the stationary phase, as shown in Figure 3.19, the liquid water saturation within the cathode GDL in the segments between 0.3 and 0.95 of the normalized length is high. Liquid water occurs within the anode GDL as well. However, only small reactant molar fluxes must be maintained to satisfy the rather low consumption at the low current. Therefore, the voltage losses are small and the current density distribution is relatively homogeneous.

Right as the current is increased, the consumption is multiplied, resulting in the states displayed in Figure 3.20. Now, the large amount of liquid water, especially in the cathode GDL, hinders the gas diffusion significantly. This results in a low oxygen partial pressure across large portions of the active area. In turn, a sharp increase of the concentration losses is observed, predominantly in the segments where liquid water saturation is high. The current density in the segments less affected by liquid water, at around 0.3 of the normalized length, rises consequently. Ten seconds after the current increase, liquid water starts to accumulate and

51
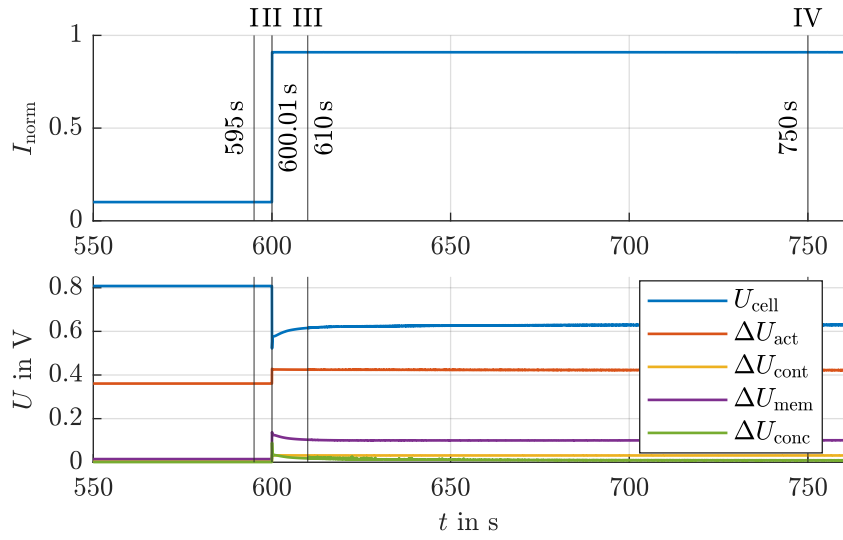
FIG. 3.18 Simulated current, cell voltage and losses in case of a step-wise current increase. The vertical lines mark the four distinct points in time chosen for further investigation.
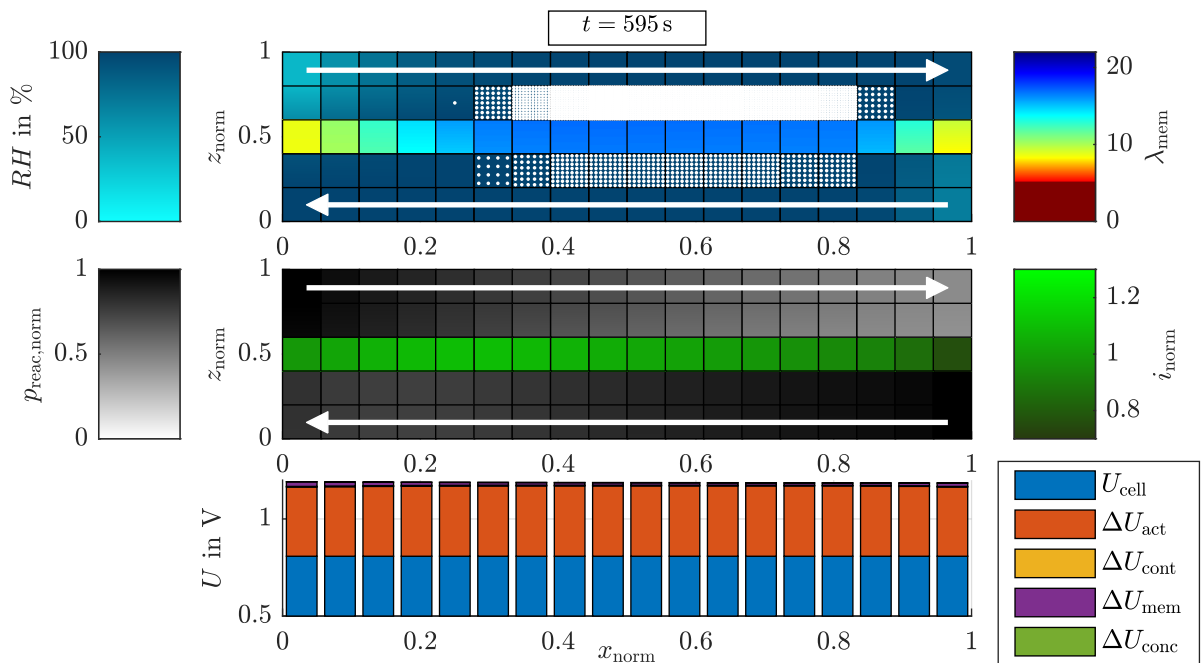
FIG. 3.19 (I) Cross-sectional view of the spatial distribution of various simulated variables at the end of the stationary phase.
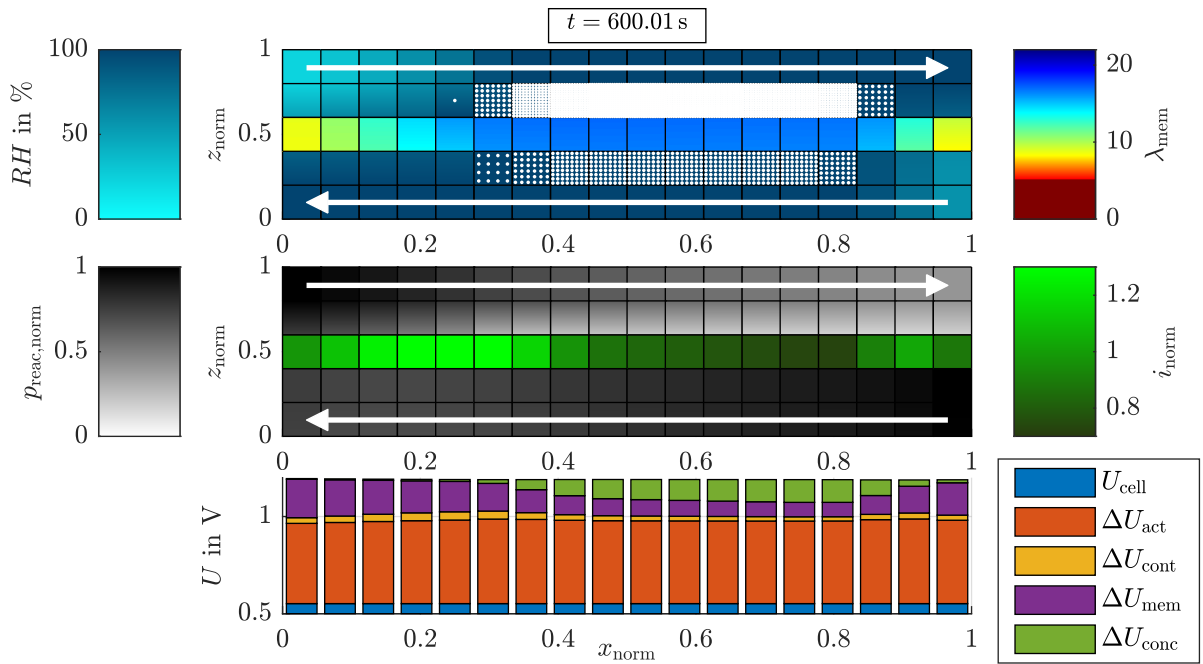
Fig. 3.20 (II) Cross-sectional view of the spatial distribution of various simulated variables right after the current increase.

the membrane water content rises in the segments closer to the cathode inlet as well as in the last segment, pictured in Figure 3.21. This is caused by the water production, which was shifted towards these segments by the step-wise current increase. As the segments become more hydrated, the cell voltage starts rising due to lower total losses.
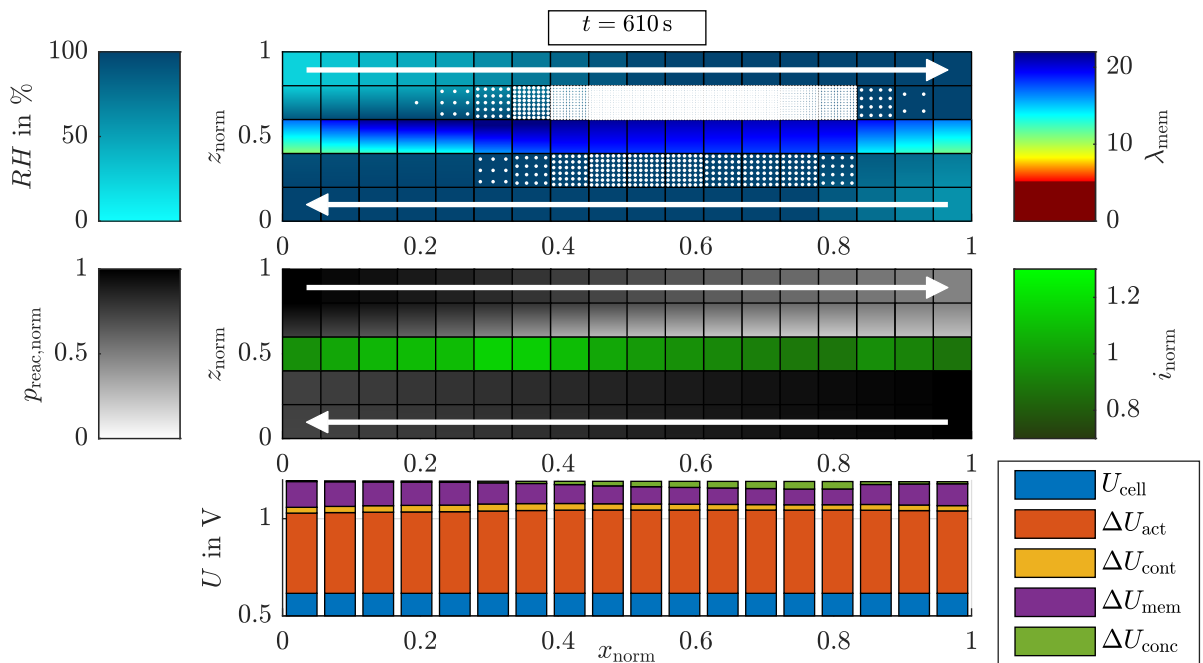
Fig. 3.21 (III) Cross-sectional view of the spatial distribution of various simulated variables 10 s after the current increase.

After 150 s, liquid water is present in the cathode GDL of all segments as shown in Figure 3.22.

Note that the total saturation is significantly reduced, resulting in negligible concentration losses. The current density distribution is almost uniform and the cell voltage has relaxed towards the new stationary value.
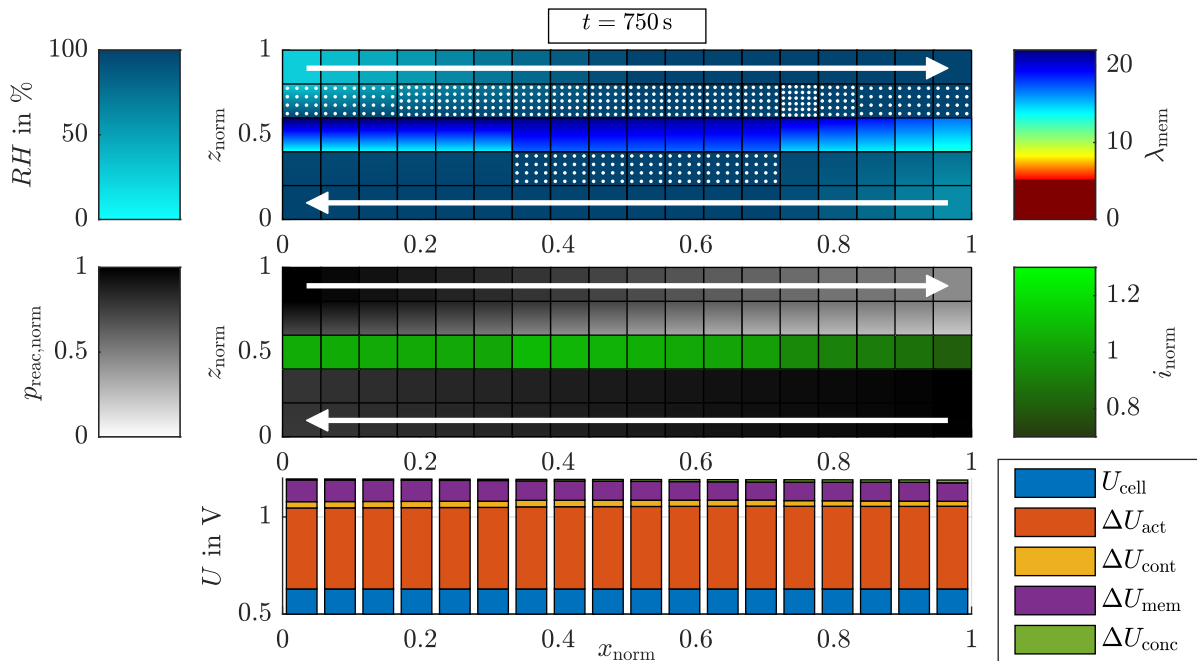
FIG. 3.22 (IV) Cross-sectional view of the spatial distribution of various simulated variables 150 s after the current increase.

This example highlights another central effect for the water management in highly dynamic operation. With respect to RQ1, liquid water built-up and drainage are identified as a second dominant process. Also, first hints towards the stationary-based control strategy limitations in context of RQ3 can be derived: High liquid water saturation in the GDL has no negative impact, as long as the electrical current is relatively low. As soon as the reactant consumption is stepped up, high local concentration losses occur, resulting in a low overall cell voltage. As these step-ups are frequently observed in the automotive application, control strategies must take the present liquid water saturation into account to avoid high concentration losses or even local starvation events. The two examples conclude the simulation chapter, laying the foundation for further analyses. Now, there will be a closer look at the experimental side of this work

Chapter 4

Dynamic Operation of an FCS

To complement the simulation, experiments are central to check the model's precision and find potentially missing effects. This chapter aims at discussing targeted dynamic experiments, some of which are also utilized for the simulation model development presented in the previous Chapter 3. As a special feature, the experiments shown in this chapter are conducted on an application-like system test rig. It incorporates not only the fuel cell stack, but also adjacent subsystems in hardware. Two sophisticated experimental systems are examined in various dynamic scenarios. Diving into the experimental chapter therefore also extends the scope: the step from *one fuel cell to a fuel cell system* is taken.

First of all, the experimental research presented in the open literature is discussed, with a focus on its goals and key areas. Afterwards, measurement techniques and their suitability for certain research areas are explained. Then, the experimental targets of this work corresponding to the research questions are defined, from which the setup and methodology of the whole experimental campaign are derived. As first experiment, a thorough analysis of one fuel cell system's dynamic behavior is carried out, utilizing an oscillating electrical load change and a signal analysis of the system's response. This experiment helps to identify the time scales within the sub-systems, show the contribution of the controller and controlled system and find resonance phenomena. The results of this experiment will later facilitate the selection of the relevant dynamic system dynamics for the comparison of various fuel cell systems in Chapter 5. Additionally, this chapter incorporates multiple step response experiments, which highlight the different phenomena spanning multiple time-scales, each of which can dominate the fuel cell system's dynamic response characteristics. Also a comparison of the system level experiment with a more common short stack experiment is carried out, showing limitations of this widespread test setup regarding realistic highly dynamic operation.

Afterwards, a special periodic dynamic operation of the AirS is presented. It allows for steady-state operation at low electrical loads, where otherwise either flooding or dry-out would occur. But the thorough understanding of the dynamic processes, dry-out and humidification as well as liquid water accumulation and drainage, enables a valuable extension of the operating range. Lastly, the impact of liquid water which was already explained based on simulation results is shown experimentally in order to draw conclusions on how to operate a fuel cell system to allow highly dynamic operation.

4.1 Experimental Research in Literature

4.1.1 Goals and focus areas of literature experiments

Fuel cell research in public literature can be divided into two main branches: simulation research, as discussed in the previous chapter, and experimental research, which is the

centerpiece of this chapter. In general, the goals of experimental fuel cell research condense down to five main targets, as shown in Figure 4.1: increasing the power density, reducing costs, and enhancing the lifetime, efficiency and achievable dynamics. These technical targets and a schedule when certain milestones should be reached are for example formulated by the USDoE[111]. Within this work, the focus lies on improving system efficiency and dynamics.
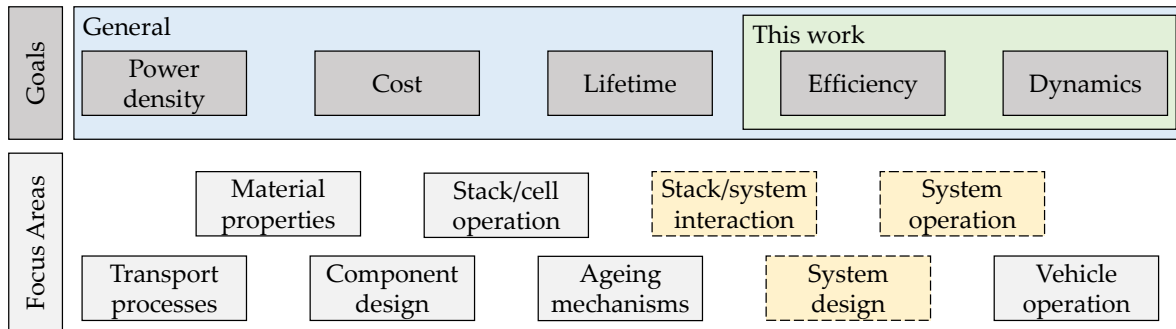
FIG. 4.1 Goals and focus areas of experimental research reported in literature

The experimental research community further addresses different focus areas, some of which are shown in Figure 4.1. Often, these focus areas contribute to more than one general goal and are therefore not strictly ordered. Experimental research in the highlighted focus areas are central in the development process of fuel cell electric vehicles, but are deemed insufficient in currently available literature. The highlighted areas are central for identifying application-relevant processes for research question RQ1, enable improved modeling and determine pitfalls as targeted with RQ2, showcase the limitations and possible improvements of common control strategies in scope of RQ3 and provide examples for the efficiency versus dynamics trade-off implied by RQ4.

Multiple researchers carry out experiments to develop new materials, benchmark them against existing materials and introduce them into new cell designs. Understanding and modeling transport processes within the fuel cell is an adjacent field of research, which is the basis for the development of simulation models and the phenomena separation in fuel cell operation. These processes include for example water diffusion[39,82], water sorption[90,92,112] and gas transport in porous media[37], also discussed in depth previously within Chapter 3. While extensive research exists in this field, there are still high deviations between research groups, as Vetter and Schumacher pointed out[40]. From a system point of view, these deviations add uncertainty to the models and motivate additional, targeted parametrization and validation experiments to adapt the models to the exact experimental setup. This process is described in Subsection 3.3.4 of the previous chapter.

Another field of research is the design of system components, especially the fuel cells themselves. To optimize the cell design, researchers evaluate for example new flow field setups[113–115], GDLs and MPLs[14], as well as MEAs experimentally. The vast majority of these experiments is conducted under stationary conditions, which do not sufficiently represent the real system operation in a vehicle, that includes a high share of dynamic loads. The simulation results presented in the previous chapter already showed the significant impact of transient phenomena acting on different time-scales on the local conditions within the fuel cell in that regard. The dynamic processes influence the KPI efficiency, potentially outweighing the small differences between certain materials typically found in stationary experiments. In the following, the simulation results derived in Chapter 3 are backed up by own experiments,

highlighting the importance of full system testing under realistic dynamic load scenarios.

To tackle the issue of limited lifetime, researchers focus on the underlying ageing processes. As testing the full lifetime is often too time consuming, specialized experiments with a reduced duration called Accelerated Stress Test (AST) are conducted[38]. Developing ASTs in a way that represents the real stress in the later application is especially challenging: The dominant ageing mechanisms may depend heavily on the selected operating conditions, highlighting the importance of realistic testing. Some AST protocols specifically target ageing due to idling[116], dynamic loads[117,118] or start-up and shut-down[119,120]. For the later application, a continuous adaption of the AST protocols, the ideal operating conditions and a realistic stress profile is required. Furthermore, a detailed understanding of the local states is needed to correctly trace back the underlying ageing mechanisms. While this work does not focus on the ageing itself, it shall provide further insights into the time-wise development of various states during realistic, application-like system operation.

Optimizing the operating conditions experimentally, e.g. with respect to efficiency, is common in literature[121,122], but mostly sticks to stack or even cell level. The vast majority of this research is again limited to stationary operation. Only a few researchers addressed the dynamic operation, e.g. by introducing current or voltage step changes[123–127]. The setup and procedure for conducting such dynamic experiments must be selected carefully. As it is shown later in Section 4.4, the stack boundary condition adaption greatly affects the results of these kind of experiments, as the dominant process differs. Stack/system interaction and system design plays an important role in the dynamic behavior of a fuel cell system and can only be addressed at system or even vehicle level as discussed in the following subsection. In common literature, the experimental analysis of stack/system interaction, system design and system operation remains largely untouched, as the appropriate sophisticated test setups are complex, expensive and therefore sparse. The following subsections address this issue by showcasing the complexity of dynamic system operation with an experimental fuel cell system.

Regarding operation of complete fuel cell vehicles, limited research conducted with available series cars exists. Lohse-Busch et al. tested a 2017 Toyota Mirai in various load cycles and reported on the system control and power split between fuel cell system and battery[25]. This approach requires to incorporate the fuel cell system into a vehicle, resulting in the highest costs and difficulties to include measurement equipment.

4.1.2 Experimental levels and capabilities

Depending on the research goals, different experimental setups might be favorable, as depicted in Table 4.1. To characterize new materials and to develop e.g. transport models, research on differential cells or even single layers is appropriate and widely reported in literature[128]. Some researchers even conducted dynamic experiments at this level[124]. However, the differential cell approach is intrinsically unsuited to understand in-plane variations occurring in full size fuel cells. For that, a rather long straight channel cell is a suitable option. With this approach, one is capable of analyzing the along-the-channel distribution of multiple physical variables, such as temperature, pressure and even a current density distribution, if a segmented BPP is utilized as e.g. by Schmitt et al.[28,129]. Single cells still have an advantage in being rather inexpensive, but the complex two-dimensional in-plane transport processes are harder to track, as a high spatial resolution of measurement locations is challenging to

achieve.

Within fuel cell stacks, systematic maldistribution of the gas and coolant flows as well as temperature gradients between the cells occur. This adds to the stochastic electrical, thermal and fluidic performance variations between the cells caused by the production process variance. Such phenomena can only be traced if multiple cells are connected. In short stacks, usually 5-20 cells are stacked, while in full stacks for automotive application typically 250-400 cells are combined. Dynamic control and stack-system interactions can best be evaluated with fuel cell systems, as common stack test rigs lack the dynamic capabilities. This test rig limitation and its impact are also addressed later with a targeted experiment, comparing short stack and system operation in Section 4.4. Lastly, the fuel cell system can be incorporated into a vehicle, where fully realistic environmental conditions such as vibrations, load profiles and changes in ambient temperature occur just as in the final application. Additionally, the whole fuel cell power train must be packed into the tight vehicle volume, resulting in realistic pipe lengths and component arrangement, in contrast to a typical experimental fuel cell test system.

TABLE 4.1   Capabilities and costs of various levels of experimental research.

Experiment	Capabilities								Costs
	Mat. prop.	Transport processes		Stack effects	Stack-system inter-action	System control development		Driving cond. & Package	
		Through-plane	In-plane variations			Stat.	Dyn.		
Vehicle	--	--	--	o	+	+	+	++	
Fuel cell system	--	-	-	+	++	++	++	+	
Full stack	-	-	o	++	-	+	o	o	
Short stack	-	-	o	+	-	+	o	-	Increase
Single cell	o	o	+	--	--	o	-	-	
Straight channel	+	+	++	--	--	o	-	--	
Diff. cell	++	++	--	--	--	-	--	--	

In general, the complexity and costs of the test setup rise with each step towards application. For an in-depth, high precision characterization and evaluation of the fundamental processes and material properties, lower levels within the validation sequence are favorable and less costly. As soon as stack-system interaction effects come into focus, an experimental system is the only possibility to gain further insight. Depending on the task, each experimental level has its benefits and disadvantages, and the experimental setup must match the targets. For this work, understanding stack-system interactions and developing dynamic control strategies is an essential part. Therefore, an application-like, full-scale experimental automotive fuel cell system is chosen as the test bed for the further research activities.

4.1.3   Measurement techniques

Depending on the target variable, a broad variety of different measurement techniques is employed in fuel cell research, as shown in Table 4.2. Common techniques include the direct measurement of pressure, mass flow, temperature, relative humidity and gas composition via appropriate sensors. Liquid water can be separated from the gas phase using a water separator and a fill level sensor in combination with a measurement volume. An alternative is to evaporate the liquid water and measure the relative humidity of the gas phase.

As a special variant, optical fuel cells allow to observe the water distribution within the flow field via a camera[27,96,130–132]. To measure liquid water within the GDL, X-ray diffraction[26,133,134] and neutron scattering techniques are utilized[135,136]. Small angle neutron scattering is even able to differentiate between sorbed water in the membrane and water in adjacent porous media[137]. A review of these and other visualization techniques especially targeting liquid water can be found in the comprehensive work of Bazylak[138].

TABLE 4.2   Measurement techniques depending on the target variable.

Target	Technique	Used?
Pressure	Piezoresistive or capacitive sensors	✔
Mass flow (gas)	Hot film or pitot-based sensors	✔
Mass flow (coolant)	Turbine flow meter	✔
Temperature	Resistance thermometer	✔
Relative humidity	Capacitive thin-film polymer sensors	✔
Gas composition	Electrochemical or catalytic bead sensors, mass spectrometry	✔
Flow pattern and water distribution (flow field)	Optically via camera	✖
Water distribution (GDL & flow field)	X-ray diffraction, neutron imaging	✖
Net water balance	Water separator and fill level sensor, humidity sensors	✔
Current, voltage	Shunts, analog-to-digital converters	✔
Current density distribution	Segmented BPP	✖
Charge transfer, proton & O_2 transport, gas diffusion	EIS	(✔)
Ohmic resistance	*HFR* measurement	✔

To evaluate the electro-chemical performance of a fuel cell, various techniques have been developed and are frequently used complementary to the basic current and stack or cell voltage monitoring. Electrochemical Impedance Spectroscopy (EIS) utilizes an alternating current with various frequencies, which is added onto a constant operating current. From the voltage response, impedance spectra are constructed to separate the underlying processes. These include the charge transfer and proton transport, oxygen transport in the catalyst layer and gas diffusion[139]. An in-depth description of the fundamentals and applications of this technique is given by Yuan et al.[140]. EIS requires stationary conditions and is therefore unsuited to analyze dynamic system operation. The required measurement equipment is implemented at the test rig, but not utilized in this work and consequently marked with (✔) in Table 4.2.

As a variant of the EIS method, the High Frequency Resistance *HFR* is measured by employing a high frequency alternating current, usually in the range of 300 Hz to 1 kHz. With that, the ohmic resistance contribution is found by evaluating the real part of the impedance obtained at the high frequency. It is a common way to track and control the membrane hydration state during experiments[28,129,141] and even in series vehicles[31]. As Schmitt et al. pointed out in their work on a segmented straight channel cell, obtaining only a global *HFR* is not the best option to obtain insights into local humidification processes[129]. But as no segmented BPP is available at the experimental test setup utilized in this work, only a global *HFR* is measured. The local transient humidification states are reconstructed using the simulation model discussed in Chapter 3.

4.2 Experimental Targets, Setup and Methodology

4.2.1 Experimental targets and methodology in this work

In contrast to common literature experiments, a complete application-like fuel cell system assembled on a sophisticated test rig is the centerpiece of the following investigations. To answer the research questions introduced in Subsection 2.4.2, multiple goals must be reached:

1. Understand the key levers and coupling of main effects within the stack and the subsystems (RQ1)
2. Check the simulation model by conducting stationary and dynamic system level experiments and identify additional effects not implemented in the model (RQ1, RQ2)
3. Show the limits and pitfalls of common experimental setups, which neglect subsystem dynamics and interactions (RQ2)
4. Quantify the dynamic capabilities of an application-like fuel cell system and its subsystems (RQ2, RQ3)
5. Develop new control strategies enabled by full system operation to enhance the usable operating range (RQ3)
6. Exemplify the impact of the control strategy and system architecture with respect to the efficiency and dynamics trade-off (RQ4)

The methodology derived from these goals is depicted in Figure 4.2. The experimental results and the knowledge gained are not only utilized within this chapter. They are also transferred to the simulation model described in Chapter 3, to parameterize and validate the model and find potentially missing constraints, such as the drainage limitation. The system dynamics characterization, as a focal point of this chapters investigation, is also utilized as benchmark to evaluate the impact of the system architecture and the resulting trade-off between dynamic capabilities and efficiency of various systems later in Chapter 5.

The system dynamics' characterization itself is based on three pillars: knowledge from public literature as introduced in the previous Section 4.1, the insights into the stack behavior gained with the simulation model described in Chapter 3, and multiple experimental campaigns as part of this chapter. For the dynamic characterization of the system analyzed in this work, two different test cases are introduced.

First, a sine sweep experiment to analyze the subsystem response characteristics is described in Section 4.3. Second, current steps aiming at the system-stack interaction in multiple settings are shown in Section 4.4. The third experimental campaign targets the liquid water

drainage limit to improve the simulation model and is discussed in Subsection 4.5.2. Note that additional stationary measurements of the polarization curve and water balance were carried out to parametrize the model, but are not shown within this chapter. Based on the experimental results, an improved control strategy for an enhanced operating range is developed and described in Section 4.5, as an experiment targeting the liquid water impact concludes this chapter.
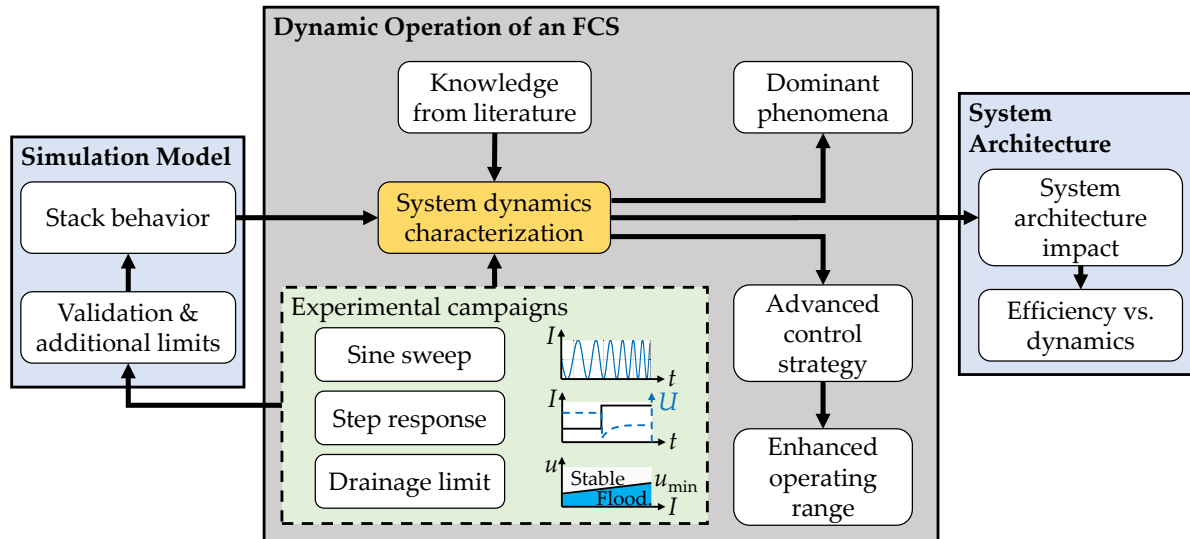
FIG. 4.2 Methodology of the experimental system analysis and interaction with adjacent chapters.

4.2.2 Test rig and fuel cell systems in this work

Two experimental systems contributed to the results in this work. The main subsystems and components of fuel cell system 1, in short System 1, are shown in Figure 4.3. The required system power is communicated to the Fuel Cell Control Unit (FCCU) by a Vehicle Control Unit (VCU). The FCCU then controls the fuel cell system to satisfy the power demand. The FCS itself consists of the stack and three main subsystems, that are in scope of the further analysis. First the AirS featuring a filter, an EAC, a cooler, a bypass valve and a throttle valve. Second the HyS, incorporating a jet pump, an ARB, a purge valve and a water separator. Third the ThS, containing a coolant pump, a cooler and a three-way valve. Note that the ElecS is outside the fuel cell system boundary and emulated by the test rig.

In addition to System 1, a modified System 2 is also analyzed within this work. The key feature of System 2 is a sophisticated AirS with two-stage compression and exhaust enthalpy recuperation via a passive Turbine Air Charger (TAC) as shown in Figure 4.4. Also, a gas-gas heat exchanger between the outlet of the second compression stage and the turbine inlet increases the turbine inlet temperature for a higher turbine power and reduces waste heat to the coolant system. A gas-liquid cooler between the two compression stages reduces the required compressor power of the second stage and protects the downstream components from high temperatures. The other subsystems are not changed compared to System 1.
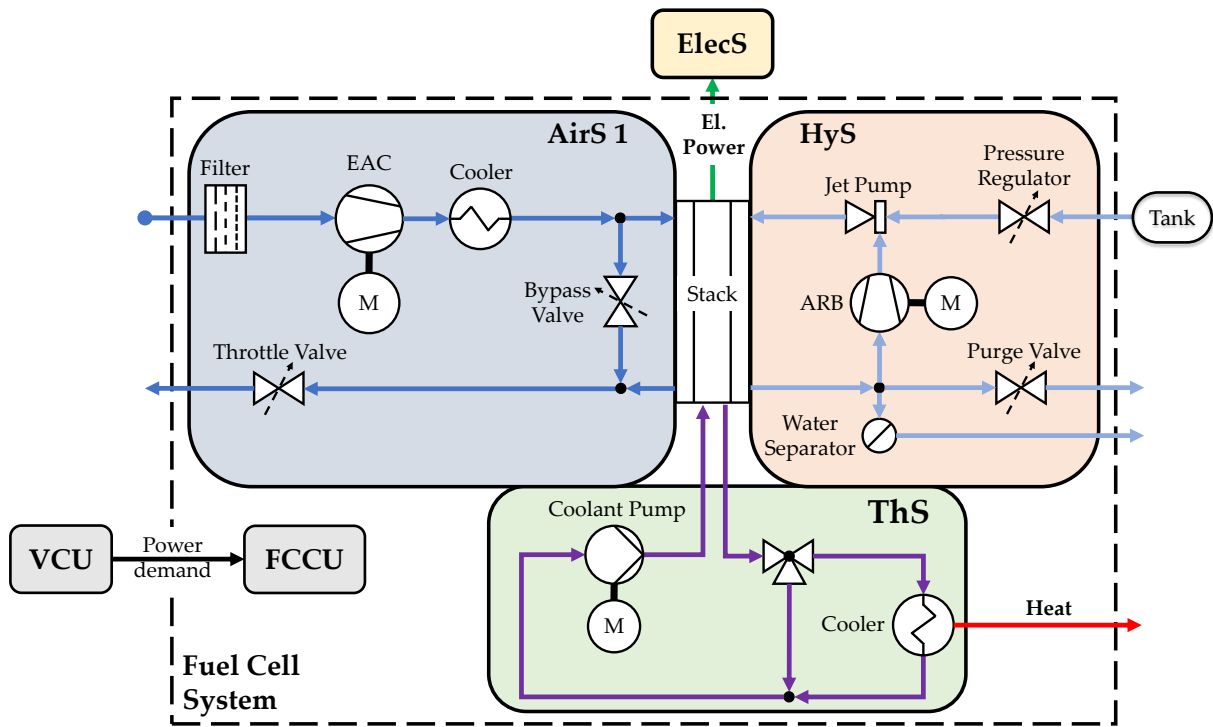
FIG. 4.3 Architecture of the experimental fuel cell system 1, adapted from[46].
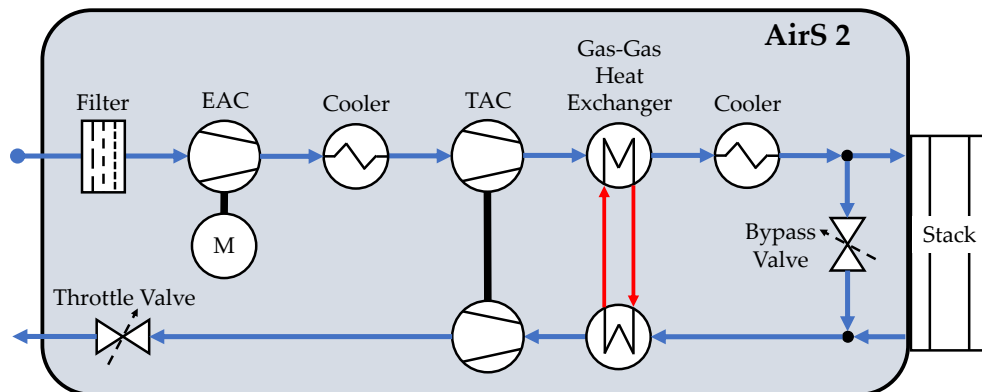
FIG. 4.4 Architecture of the modified AirS of System 2.

The main purpose of the test rig is to supply the system with air and hydrogen at variable pressures and temperatures, emulating changing environmental conditions. In addition, the test rig acts as a sink for electrical power and heat produced by the system, instead of a real vehicle in the later application. The central test chamber of the fuel cell system test rig with an experimental system is shown in Figure 4.5

FIG. 4.5   Test rig chamber with experimental fuel cell system.

The key variables measured during fuel cell system operation and the according sensors are summarized in Table 4.3. Note that a variety of additional sensors are also implemented to monitor other variables at the test rig and within the system. In the following, the focus lies on the ones that are relevant for the upcoming experiments and their evaluation, or serve as inputs for the simulation model. The anode stoichiometry cannot be measured directly in the experimental setup and is derived via a virtual sensor. This approach is based on the pressure gain and speed dependent volume flow map of the ARB in combination with the gas composition sensor.

TABLE 4.3   Key variables and according sensors at the fuel cell system test rig.

Description	Variable	Sensor
Current	I	KS Engineers four quadrant power supply
Stack voltage	U_{stack}	KS Engineers four quadrant power supply
Cell voltage monitoring	U_{cell}	SMART TESTSOLUTIONS CVM-Modules
High frequency resistance	HFR	KS Engineers four quadrant power supply
Cathode inlet mass flow	$\dot{m}_{ca,in}$	Bosch PFM
Cathode inlet pressure	$p_{ca,in}$	WIKA S-20
Cathode inlet temperature	$T_{ca,in}$	Pt100
Cathode inlet relative humidity	$RH_{ca,in}$	Vaisala HMT 317
Anode stoichiometry	λ_{an}	Virtual, map-based from n_{ARB} and Δp_{ARB}
Anode inlet pressure	$p_{an,in}$	WIKA S-20, Bosch LPS5
Anode inlet temperature	$T_{an,in}$	Pt100
Anode inlet relative humidity	$RH_{an,in}$	Vaisala HMT 317
Anode inlet nitrogen fraction	x_{N_2}	Neohysens NEO 985-2
Coolant inlet temperature	$T_{cool,in}$	Pt100
Coolant temperature rise	ΔT_{cool}	Pt100
Coolant mass flow	$\dot{m}_{cool}$	Natec NT-24, Natec NT-8

4.2.3   Key levers and effect coupling

A variety of variables shape the water management and the resulting behavior of a fuel cell stack within a system. To limit the complexity, this work focuses on the most relevant ones as derived by Hellmann[44] and identified in synergy with the simulation model. They are depicted as inputs in Figure 4.6. The subsystems, namely the ElecS, the ThS and the AirS are tasked to deliver the desired Boundary Conditions (BC's) to the stack, which in turn responds by supplying a certain voltage. If the adjacent subsystems are not implemented in the test setup, as it is often the case in literature experiments, the test bench has to approximate the subsystems' behavior to enable system-like results.

The primary variable to control the stack power in this setup is the current I. It is set by the ElecS almost instantaneously with respect to the time scales of interest as defined in Section 3.3.2. This is visualized by black arrows. As already described in Section 3.3, an increase in current directly increases the gas consumption, the water and the heat production. Together with the coolant temperature T_{cool}, which is set by the ThS, the heat production dominates the local temperature at the catalyst layers. While the ThS requires around ten seconds to set a new coolant temperature (blue arrow), the resulting local temperatures within the cell adapt within or even below 0.1 s (yellow arrow). The local temperature then directly impacts the activation losses ΔU_{act}.

Cathode pressure p_{ca} and stoichiometry λ_{ca} are the last two key variables and are controlled by the AirS. In automotive systems, the air supply is typically set within 1 s or less and impacts the local relative humidity RH_{local} as well as the oxygen partial pressure at the catalyst layer $p_{O_2,CL}$. The exact dynamic behavior of the AirS depends heavily on its architecture and the components' dynamic capabilities, which will also be discussed later in Chapter 5. If the local relative humidity reaches 100 %, liquid water occurs within the GDLs or flow fields, hindering
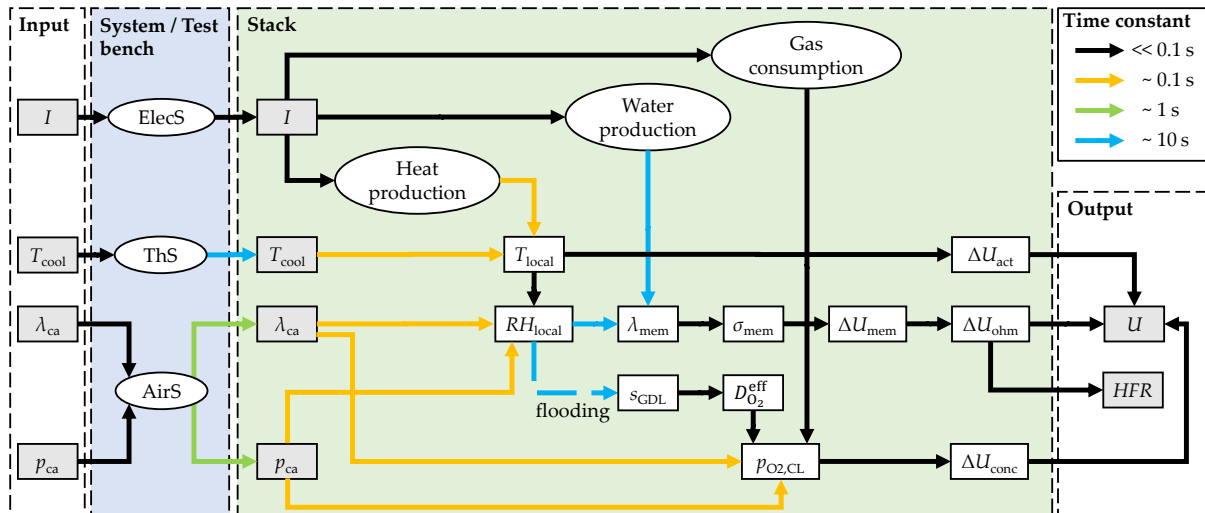
FIG. 4.6 Main interactions between the system inputs, the subsystems' response and the stack response, adapted from[46].

the gas diffusion and reducing the oxygen partial pressure at the catalyst layer, as described in depth in Subsection 3.4.2. This impacts the concentration losses ΔU_{conc} within the stack.

The last main contribution to the stack voltage indirectly influenced by the boundary conditions is the membrane water content λ_{mem}. It depends mainly on the local relative humidity and the water production rate. As shown in Figure 3.7, it changes rather slow, in the order of tens of seconds, as it is mainly limited by the sorption process discussed previously in Chapter 3. Without delay, the membrane water content impacts the protonic conductivity σ_{mem}, which results in changing membrane losses ΔU_{mem} that contribute to the total ohmic losses ΔU_{ohm}. They are distinguishable from other loss contributions by measuring the *HFR*. It is important to note, that only the states in grey boxes shown in Figure 4.6 can be measured directly. The intermediate states in the white boxes cannot be tracked via sensors, but modeled with the simulation model.

4.3 System Dynamics Analysis

Parts of the research displayed in this section were presented by the author at the European Fuel Cell Forum 2023 in Lucerne, Switzerland and consequently published in the transactions[142] under a Creative Commons Attribution License. The content is put into the context of this work and a detailed introductory explanation on the methodology and figures is added.

4.3.1 Phase shift and dampening analysis

The general levers to influence the stack have been introduced. This is not true for the subsystems. Which react fast, which react slowly? Can resonance phenomena occur in the system? To answer these questions, an analysis of the subsystem dynamics is conducted. The concept of system response analysis with a sinusoidal input function is utilized to evaluate the phase shift and dampening behavior of the fuel cell system 2. An example of this approach is given subsequently. Note that the following experiment is one example for the transient

experiments targeted with RQ2, and also allows a model reduction in the next chapter, aiming at RQ4.

In general, if a simple PT1-element as introduced in Subsection 3.3.2.1 is assumed and the time-dependent input $u(t) = \sin(\omega t)$ is added, the stationary output $y(t)$ yields[143]

$$y(t) = A\sin(\omega t + \varphi) = \frac{K}{\sqrt{1 + (\omega\tau)^2}} \sin(\omega t - \arctan(\omega\tau)). \tag{4.1}$$

In Equation 4.1, τ represents the time constant introduced in Equation 3.2, while ω is the angular frequency of the input oscillation. The amplitude A and the phase shift φ characterize the resulting oscillation. Note that the amplification factor K is set to 1 in the following example. Figure 4.7 depicts two exemplary time-dependent responses $y_1(t)$ and $y_2(t)$ of a fast and a slow system with time constants of $\tau_1 = 1\,\text{s}$ and $\tau_2 = 10\,\text{s}$, respectively. In the upper plot, the angular velocity of the input function is set to $0.2\,\text{rad}\,\text{s}^{-1}$, in the lower plot to $1\,\text{rad}\,\text{s}^{-1}$.
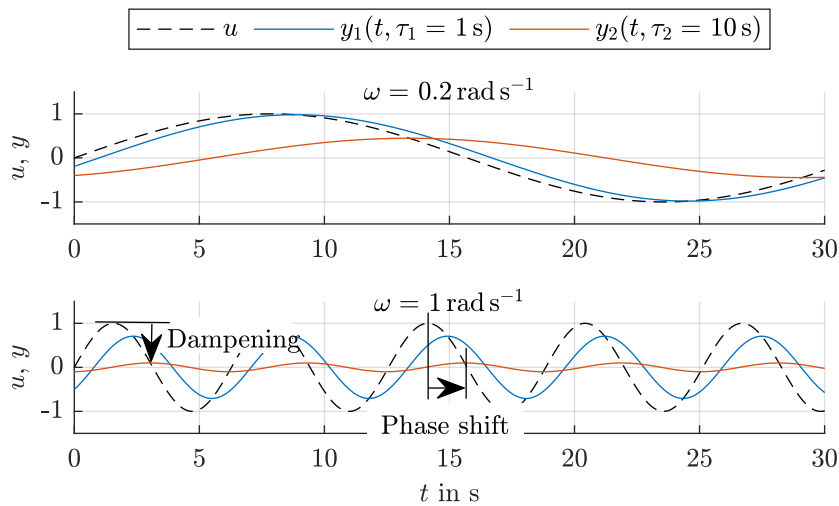
FIG. 4.7 Time-dependent response of a fast and a slow PT1-system to two different input oscillation angular velocities.

The PT1-element dampens the response and a phase shift occurs with respect to the input signal $u(t)$. The faster system with the lower time constant τ_1 exhibits a smaller phase shift φ and less dampening in the magnitude than the slower system. An increased angular velocity ω of the input oscillation results in a higher phase shift and dampening in the response of both systems.

One common way to display the frequency dependent transfer function is a Bode plot, as depicted in Figure 4.8. The upper graph displays the magnitude $A = |G(j\omega)|$ of the output signal. Again, the higher the frequency ω becomes, the stronger the dampening gets, displayed by negative values on the logarithmic scale. The intersection between the dashed tangent and the x-axis corresponds with the time constant τ via $\omega = \frac{2\pi}{\tau}$. In the lower graph, the phase angle φ with respect to the input is shown. The higher the frequency, the larger the phase shift, reaching up to -90°.

With this concept, the subsystem dynamic response characteristics are derived. Faster subsystems result in less dampening and a lower phase shift, while slower systems behave the other way round. As the input frequency is known, the frequency-dependent response behavior is quantified as described in the following.
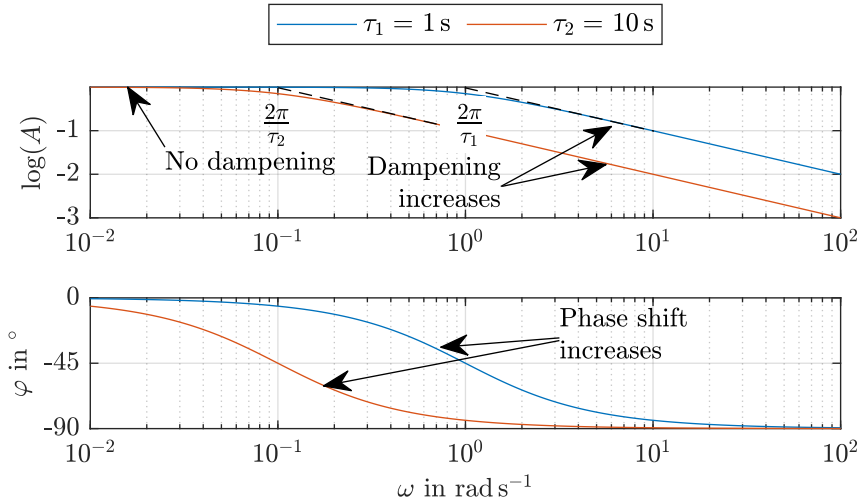
FIG. 4.8 Bode plot of a fast and a slow PT1-system's response.

4.3.2 Sine sweep experiment

4.3.2.1 Evaluation

The theoretical concept is applied to the experimental System 2. To the best of the authors knowledge, this is the first time that such an approach is employed experimentally onto a full scale fuel cell system. San Martin et al. carried out an experiment using current oscillations of varying frequency to validate a simulation model and linked the phase shift between current and voltage to the double-layer capacity[125]. However, it remains unclear whether oscillations in the gas boundary conditions occurred and how they contributed to the observed behavior.

At the test rig, a sinusoidal variation of the current is added to a constant mean current, as shown in Figure 4.9. This appears to be similar to the well-established EIS technique, but there is one key difference: the subsystem set points change according to the current in the following experiment, deliberately resulting in oscillations within the subsystems.
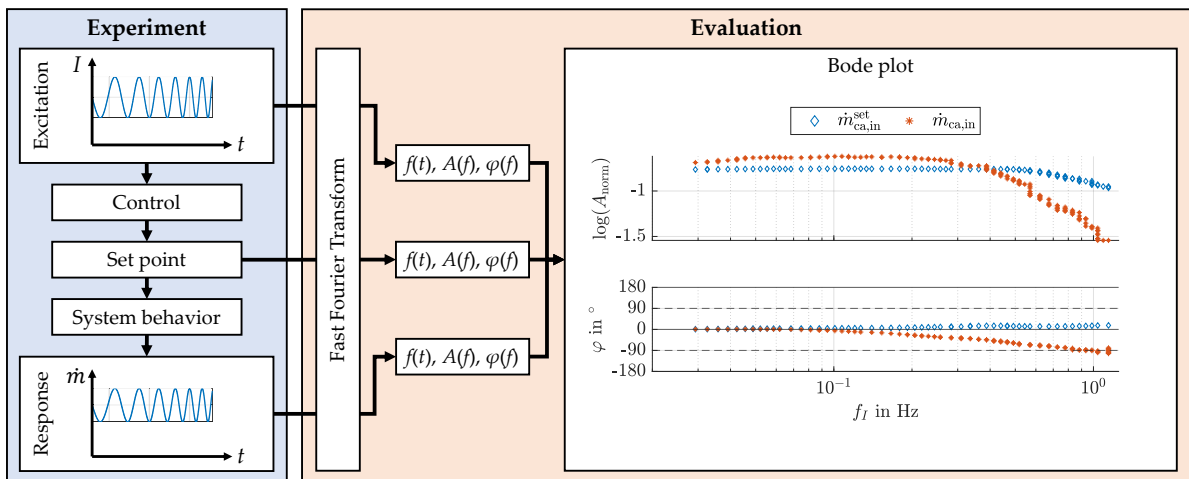
FIG. 4.9 Methodology of the sine sweep experiment at the system test rig, adapted from[142].

The sine sweep experiment evaluation as displayed in Figure 4.9 consists of two main steps. First, a sinusoidal current variation is introduced in the experiment. Multiple variables, such as for example the cathode inlet mass flow $\dot{m}_{\text{ca,in}}$, depend on the current. Via the control strategy, the mass flow set point $\dot{m}_{\text{ca,in}}^{\text{set}}$ is determined in order to control the actuators, in this case mainly the EAC, to achieve an appropriate system response.

Second, the excitation and the response are evaluated. With a Fourier transformation, the power density spectrum is calculated to find the dominant frequency f in the excitation and the response signal. If they match, the response signal analysis yields a valid result and the amplitude A and phase φ are computed as a function of the excitation frequency f_I. A Bode plot displays the amplitude and phase of the mass flow set point and the actual mass flow. In this example, the actual mass flow exhibits a larger magnitude than the set point variation at low to medium frequencies, meaning that the AirS is slightly overshooting. At higher frequencies, a strong dampening is visible. Also, a phase shift of up to $-90°$ is observed in the actual mass flow.

This example showcases the benefit of the sine sweep as one possible transient experiment for improved modeling as targeted with RQ2. It is clearly determined, until which frequency the AirS is able to follow the mass flow set point and, if not, how large the deviations become. Additionally, the impact of the controller setup and the system dynamics can be separated. The approach allows for a systematic subsystem characterization early in the development process, reducing the risk of improper system behavior in later stages. Other findings are now shown in the two following subsections.

4.3.2.2 Comparison of AirS and HyS dynamics

Next is a comparison of the mass flow dynamics at the anode and cathode inlet, which is displayed in Figure 4.10. Note that the anode mass flow is not measured directly in the experiment. Instead, the pressure loss Δp_{an} is displayed, which is approximately proportional to the actual mass flow.
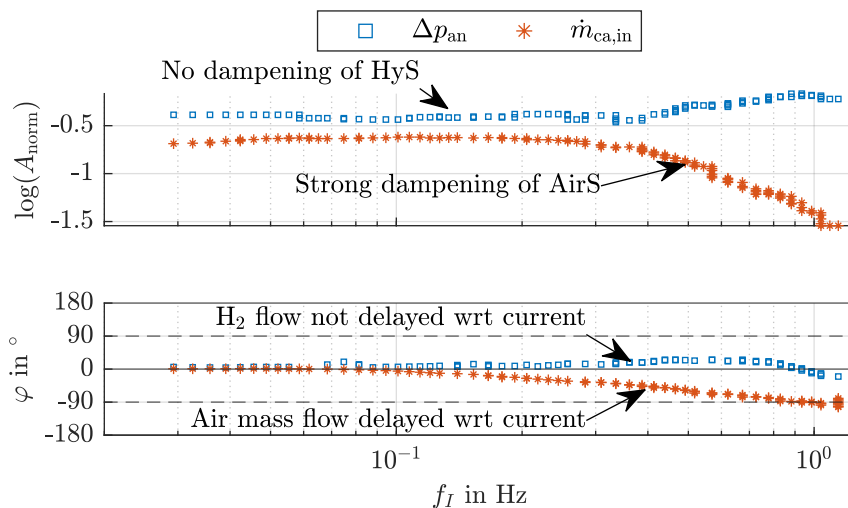
FIG. 4.10   Comparison of the HyS and AirS mass flow dynamics[142].

The cathode mass flow shows a low pass behavior of the AirS. At frequencies below 0.1 Hz, the mass flow follows the current without a phase shift and with almost constant amplitude.

Whenever the current reaches a maximum, the mass flow does as well, resulting in a delay-free subsystem response. As the frequency is increased, the phase shift exhibits negative values, meaning that the subsystem response is substantially delayed with respect to the electrical current. Also, the amplitude is reduced, as the mass flow does no longer reach its maximum and minimum values due to the limited AirS dynamics. In application, a mismatch between the air mass flow and current dynamics may result in increased concentration losses or even local starvation, negatively impacting efficiency and stack lifetime.

The pressure drop dynamics within the anode caused by the HyS behave differently. The amplitude remains almost constant at frequencies below 0.4 Hz. Up to the maximum measured frequency of 1.14 Hz, the phase shift remains below 27°. As expected, the HyS responds significantly faster compared to the AirS, as no relevant inertia is incorporated. An in-depth analysis of the measured signals shows, that the ARB adds no relevant pressure gain. Therefore, the mass flow is driven solely by the jet pump. The positive phase shift is most likely a result of the closed anode loop hydraulic behavior in combination with the cathode-coupled pressure control and the jet pump. In general, the AirS is identified as the limiting subsystem. The cathode mass flow is delayed with respect to the current from lower frequencies on. During highly dynamic operation, a critical mismatch between supply and demand is therefore more likely to occur on the cathode side.

4.3.2.3 AirS resonance phenomenon

Figure 4.11 shows the Bode diagram for the cathode inlet and outlet pressure, the EAC and TAC speeds n_{EAC} and n_{TAC}, and the stack voltage. At higher frequencies, the amplitude of all signals except for the voltage drops. Note that erroneous amplitude values are computed between 0.3 and 0.4 Hz, as the water separator tank in the cathode exhaust path is emptied during this time frame of the experiment.

Analyzing the pressure and compressor phase shifts yields an interesting observation: At a frequency of 0.14 Hz, as marked by the vertical line, the cathode outlet pressure exhibits a phase shift of $\approx -180°$. This is also in line with the phase shift of the TAC speed n_{TAC}. If the current reaches its maximum value, the cathode outlet pressure becomes minimal, which is exactly opposite to the stationary set points. Additionally, the voltage exhibits a positive phase shift with respect to the current, which is discussed later.
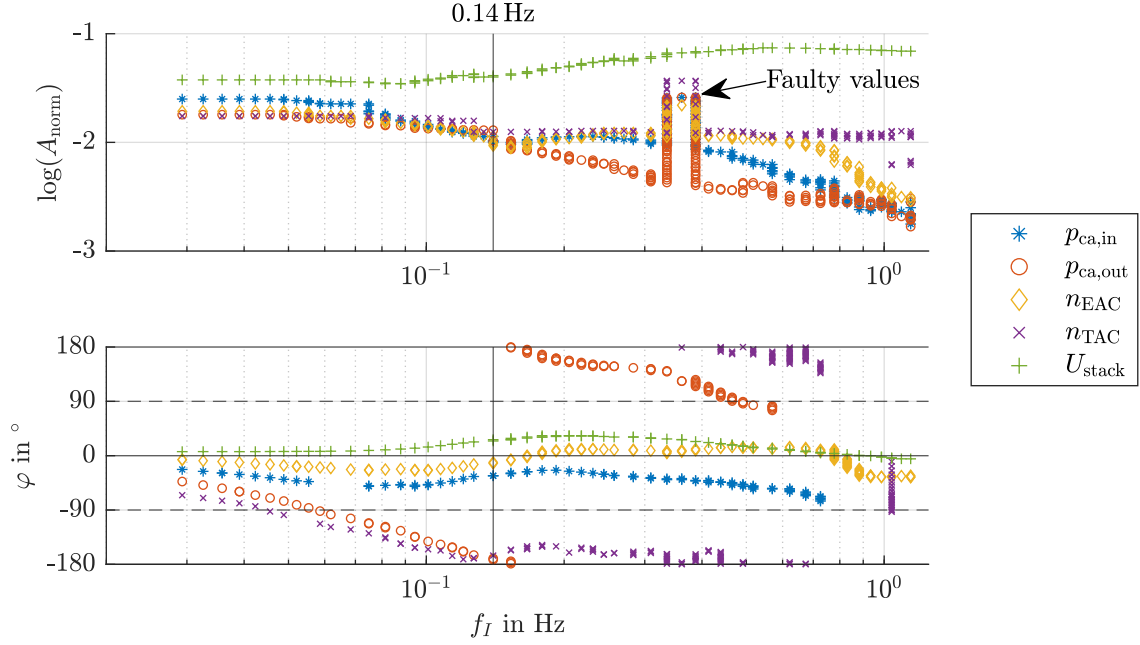
FIG. 4.11 Pressure, compressor and voltage dynamics[142].

Figure 4.12 explains this resonance phenomenon observed at a frequency of 0.14 Hz in the time domain. Along the x-axis, the phase angle of the current φ_I is shown. At a phase angle of 0°, the current increases until reaching its maximum at an angle of 90°. At 180°, the current decreases and reaches a minimum at 270°, before the cycle repeats at 360°. With the phase shifts shown in Figure 4.11, the time-wise sequence within one cycle is derived.
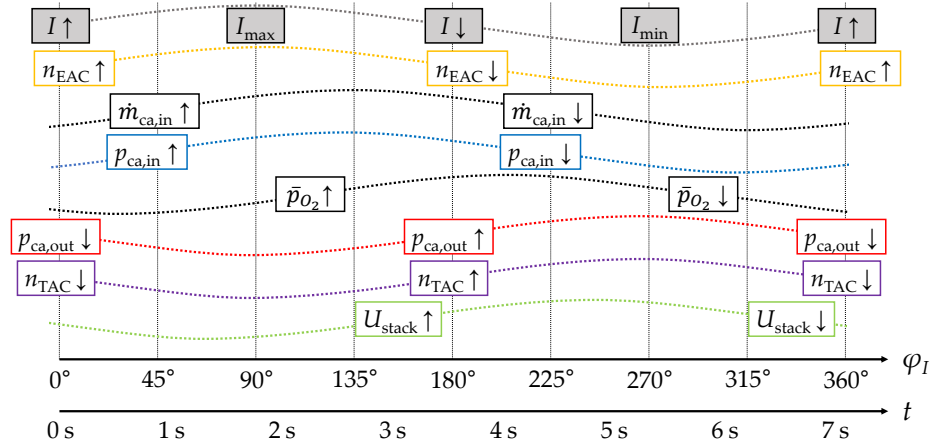
FIG. 4.12 Pressure and compressor dynamics within one oscillation at a frequency of 0.14 Hz[142].

With a small phase shift with respect to the current, the EAC speed n_{EAC} increases. Due to the pipe volume and the TAC inertia, the pressure and mass flow at the cathode inlet start rising with a delay of $\approx -30°$ or around 0.9 s. The TAC speed n_{TAC} is shifted by almost $-180°$, meaning that the TAC accelerates as the current decreases and vice versa. The frequency where this phenomenon occurs is believed to depend mainly on the TAC moment of inertia. An idealized TAC with no inertia would adapt to the new stationary speed immediately if volume effects are ignored. A larger moment of inertia delays the TAC speed-up when the

turbine torque is increased. Similarly, a larger volume between the TAC compressor outlet and TAC turbine inlet should reduce the frequency at which n_{TAC} exhibits the $-180°$ phase shift with respect to the current. The observed behavior is a special feature of the chosen system architecture. It is likely, that other AirS without a TAC exhibit resonance behavior caused by a compressor-volume feedback as well, although the specific TAC-mode observed in this experiment might not occur.

The phase shift of the mean oxygen partial pressure $\bar{p}_{\text{O}_2}$ lies between the ones of the inlet and outlet pressures. As described in Subsection 4.2.3, the oxygen partial pressure directly impacts the stack voltage. If only the current-dependent contributions to the stack voltage would be at play, the voltage would exhibit no phase shift with respect to the current. But as the phase of the oxygen partial pressure is shifted, the measured stack voltage as a result of current- and partial pressure-dependent contributions yields a positive phase shift with respect to the current. However, the low amplitude of the pressure oscillations indicates that other effects must be at play to explain the high voltage amplitude. Here, additional research on the stack internal phenomena is needed.

This case displays one key ability of the sine sweep methodology: finding resonance frequencies within the system. The results of this experiment can be utilized to evaluate the controller setup within a broad frequency range. Also, it allows to further analyze the complex coupling between the passive TAC and the adjacent volumes. If an AirS model would be constructed for an in-depth understanding of this phenomenon, the experiment provides a wide variety of system input and response data to check the respective sub-models implemented. In that regard, it contributes to the improved modeling as targeted with RQ2. From a water management point of view, the coupling between realistic subsystem dynamics and the stacks response is shown over a wide frequency range. The phase shift between voltage and current is partially traced back to phase shifts in the stack boundary conditions, such as the pressure adaption, although more research is needed in this direction.

4.4   Step Response Analysis

Parts of the research displayed in this section were published by the author in the Journal Energies *under a Creative Commons Attribution License CC BY[46]. Another test case targeting the impact of the oxygen partial pressure as well as a net power analysis is added in this work, resulting in broader conclusions.*

4.4.1   Current step experiment overview

As changes in the requested fuel cell system power occur frequently in the fuel cell vehicle application, targeted experiments with changing electrical loads are a known method to separate dynamic phenomena based on their time scale[144]. The step change in load can be performed either by changing the current, the voltage, the resistance or the power, resulting in different behavior[124]. Most common are either voltage or current controlled load steps. In general, a current step up will yield a voltage undershoot, while a step down results in a voltage overshoot, as reported by various researchers based on experimental[125–127,145,146] and simulation results[66,75].

The goal of the following experiments is to showcase the impact of realistic boundary condi-

tion adaption, the steady-state reactant supply, the system architecture and the test rig on the dynamic voltage response of a fuel cell stack to step changes in current. They are designed to identify useful experimental setups and potential pitfalls, as stated in RQ2 and to provide examples for the dynamics versus efficiency trade-off caused by the architecture and control strategy choice as addressed with RQ4. In addition to the current steps, a load profile is also investigated in the system comparison. To evaluate the impact of the test rig, a short stack experiment is conducted as well. Note that at the short stack test rig, only a rather slow current increase could be tested due to the established test protocol aiming at stationary experiments as well as the limited test rig control dynamics. All cases within this experimental campaign are summarized in Table 4.4.

TABLE 4.4   Overview of the test cases.

Case	Description		Load profile
1	Boundary condition adaption	a: Adaptive BC b: Fixed BC	Current steps
2	Reactant supply variation	a: Cushioned Supply b: Standard Supply	Current steps
3	System comparison	a: System 1 b: System 2	Synthetic current profile
4	Test rig comparison	Short stack	Current increase

Before each experiment, the system must be operated under stationary conditions to ensure reproducibility of the experiments, as a varying initial state would adversely affect the results. Therefore, the system is equilibrated for at least 15 minutes, until no more changes in the measured pressures, temperatures, mass flows, relative humidities and voltage are detected. Sometimes, the equilibration phase takes longer than 15 minutes: If the system is started from standstill, the thermal capacity of the components especially in the anode loop, requires a longer warm-up until stationary temperatures are measured. During all experiments, the same type of fuel cells are tested. Systematic deviations introduced by changes in hardware, software and procedure other than the targeted change within each case are omitted as far as possible to allow for unobstructed comparisons. Note that the focus lies on the key variables as defined in Subsection 4.2.3. Additional stack boundary conditions and ambient conditions are displayed in Appendix A.3

4.4.2   Impact of the boundary condition adaption

A significant drawback of the common literature experiments is the unrealistic stack boundary condition adaption. If the current should be stepped-up, the gas flow rates must be adapted to the increased reactant consumption quickly. As underlined by the previous system dynamics experiment, this requires high-performance compressors especially on the cathode side, which are usually not integrated in the prevalent test benches. The inability to step up the gas mass flow as fast as in an application-like system results in two major limitations: one, the mass flow cannot be adapted to one of the two current set points as intended, resulting in at least one state with unrealistic operating conditions and two, the maximum height of the current step is restricted by the one selected air mass flow to avoid oxygen under-supply. It is

72

known from numerical studies conducted by Loo et al.[66], that a delayed cathode stoichiometry adaption impacts the dynamic cell voltage response. Such a system-stack interaction is also be targeted specifically later in Chapter 5.

The first experiment is selected to highlight such an impact of the stack boundary condition adaption on the dynamic cell voltage response. Current steps between medium and low load are conducted, with hold times of 5 min between the upward and downward steps. In the "Adaptive BC" case, the pressure and mass flow are adapted according to the activity-based water management strategy as introduced in Subsection 2.3.4. The "Fixed BC" case on the other hand resembles a typical literature experiment, where the mass flow and pressure are fixed.

Figure 4.13 displays the stack's boundary conditions and its electric response. The current is reduced and increased stepwise between 70 % and 30 % of the rated current. As intended, the cathode inlet pressure $p_{\mathrm{ca,in}}$ is adapted in one case, while it is kept fixed with only minor fluctuations in the other. As the current is adjusted faster than the air mass flow in the "Adaptive BC" case, a higher or lower stoichiometry λ_{ca} occurs for a short period of time after the current steps. If the air mass flow is kept constant, a step change in the cathode stoichiometry is caused by the current change in the "Fixed BC" case. The coolant inlet temperature $T_{\mathrm{cool,in}}$ as the last key variable only exhibits small deviations from the constant set point in both cases.
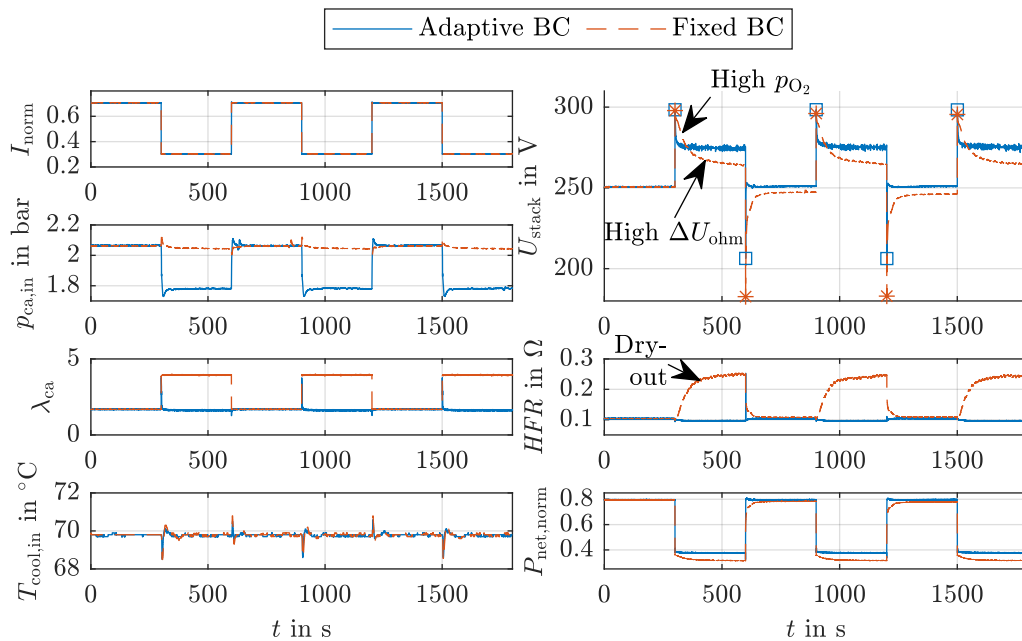
FIG. 4.13 Varying stack boundary condition adaption and resulting step responses, adapted from[46].

The upper right side of Figure 4.13 shows the time-dependent stack voltage response. In both cases, an overshoot of the voltage is observed after a current reduction, while an overshoot occurs after a current increase. The square and star symbols mark the local extrema. This general behavior is in line with the observations reported in literature. Note that the undershoots are less pronounced in the case with adaptive boundary conditions. Also, the two cases result in a significantly different quantitative voltage relaxation: if the boundary conditions are adapted, the voltage relaxes faster to the new stationary level. If the boundary conditions are not adapted, the voltage is higher in the first seconds after the current decrease. This is

mainly caused by the higher oxygen partial pressure, as the air mass flow and pressure are still the same as for the previously higher current.

However, the high air mass flow in combination with the reduced water production rate yields a slow dry-out of the membrane, increasing the ohmic losses and reducing the stack voltage below the one measured with adaptive boundary conditions. This is supported by a doubling of the *HFR* in the "Fixed BC" case. As soon as the current is stepped-up again, a deep voltage undershoot occurs due to the high membrane resistance. With the increased current, the water production returns to the initial level and the membrane is re-humidified. Note that the dry-out process was analyzed in depth with the simulation model previously in Subsection 3.4.1. The dry-out during the low load phase reduces the electrical net power including the two dominant contributions of stack and EAC, as stated in Equation 2.16, by up to 16 %. This translates to an according loss in system efficiency, highlighting how important a dry-out mitigation is for application.

The re-humidification after the current increase is four times faster than the dry-out, suggesting that the sorption process proceeds faster than the desorption process. This contradicts sorption experiments carried out by Didierjean et al.[89], who reported the sorption kinetics to be five times *slower* than the desorption kinetics for Nafion 117. In addition, the time constants of more than 100 s derived in their work are significantly longer than the one measured in this experiment. The mismatch might be caused by the experimental setup, as Didierjean et al. measured the water uptake of the membrane in a controlled environment without an ongoing fuel cell reaction nearby.

4.4.3 Impact of the steady-state reactant supply

When it comes to set point optimization in fuel cell systems, a common goal is to maximize the system efficiency. The electrical power produced by the stack and the required air compressor power are by far the largest contributors to the electrical system net power P_{net} and therefore the system efficiency, as introduced in Equation 2.16 and Equation 2.18, respectively. Again, the cathode pressure and stoichiometry are the two main variables to impact the stack and compressor power. Optimizing the system efficiency by adapting the set points in stationary operation is common in fuel cell system development[8]. But as indicated by RQ4, efficiency is not the only KPI relevant for application. So how does a variation of the steady-state reactant supply impact the dynamic capabilities of a fuel cell system?

In the following experiment, the current steps are repeated. The boundary conditions are adapted to the current, but the set points for pressure and stoichiometry are shifted based on the activity-based water management strategy[44,45] introduced in Subsection 2.3.4. The outlet activity remains the same within both tests, while the targeted partial pressure of the oxygen $p_{\mathrm{O_2}}$ at the cathode outlet is varied. A lower oxygen partial pressure reduces the stack voltage and therefore its power output, but also decreases the required compressor power, as shown in Equation 2.17. As the pressure sensitivity of the stack grows disproportionately towards lower partial pressures, a net power optimum forms for a certain system setup and electrical current. The "Cushioned Supply" is picked conservatively relatively far away from the steep stack voltage decline at the cost of a higher compressor power and slightly reduced net power. The "Standard Supply" lies close to the system's net power maximum. Both supplies are also discussed later in Chapter 5.

The results of the experiments are shown in Figure 4.14. Aiming at a lower oxygen partial

pressure while maintaining a constant outlet activity in case of the standard supply results in lower cathode inlet pressure and cathode stoichiometry. The coolant inlet temperature at the stack is the same in both cases and again exhibits only minor fluctuations. Over- and undershoots are occurring similar to the previous case, but with significantly deeper undershoots in the "Standard Supply" case with a lower p_{O_2}. Note that the stack voltage during the constant current phases is always lower with standard supply. The *HFR* signals are very close, suggesting that the humidification state has, as intended, not changed between the two experiments. The spikes in the *HFR* signal are artifacts of the data acquisition process, which produces faulty values for a very short time period when the current is changed. Reducing the p_{O_2} for the case of the standard supply results in an up to 10 % higher net power during low load operation, as the reduction in compressor power outweighs the stack's power decrease by far.
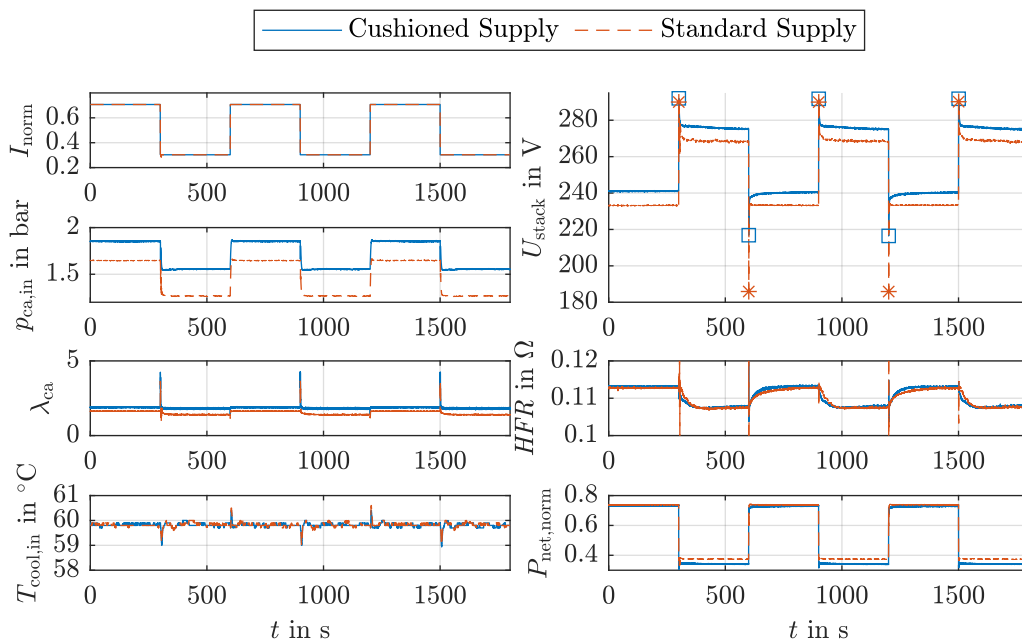
FIG. 4.14 Varying partial pressure set points and resulting step responses.

The experiment showcases the impact of the reactant supply variation on stack and system level, regarding the KPIs efficiency and dynamic capabilities as targeted with RQ4. While the cushioned supply appears to be favorable if only the stack is considered, the standard supply yields a higher system net power due to the significantly decreased compressor power. But as the voltage undershoots detected in the "Standard Supply" case are significantly larger, using the cushioned supply provides a favorable dynamic response characteristic. Deriving the right operating conditions therefore depends on the efficiency versus dynamics trade-off, the stack and AirS architecture, its compressor efficiency and ultimately the partial pressure sensitivity of the system power balance.

4.4.4   Impact of the fuel cell system

The fuel cell system's dynamic characteristics cannot only be influenced by the selected set points but also by the system architecture. To analyze this specific impact experimentally, the two systems introduced in Subsection 4.2.2 are operated according to a synthetic current

profile. Recall that System 1 features only a single stage compressor, while System 2 incorporates a two-stage compression with turbine recuperation and additional heat exchangers. The current profile contains multiple step changes in the current, with constant-current phases in-between. It was developed to investigate the step responses to a variety of step heights in different load regions.

Figure 4.15 depicts the results of these experiments. Note that the current profile is slightly adapted for System 2 to produce comparable steady-state stack voltages. The operating set points for pressure and stoichiometry are also shifted, as the surge line of the EAC limits the achievable pressure-stoichiometry combinations in System 2. During low load stationary phases, the stoichiometry in System 2 is switched periodically to avoid flooding. This control strategy is described detailed in Section 4.5. The coolant temperature is set constant in both experiments and shows only minor fluctuations.
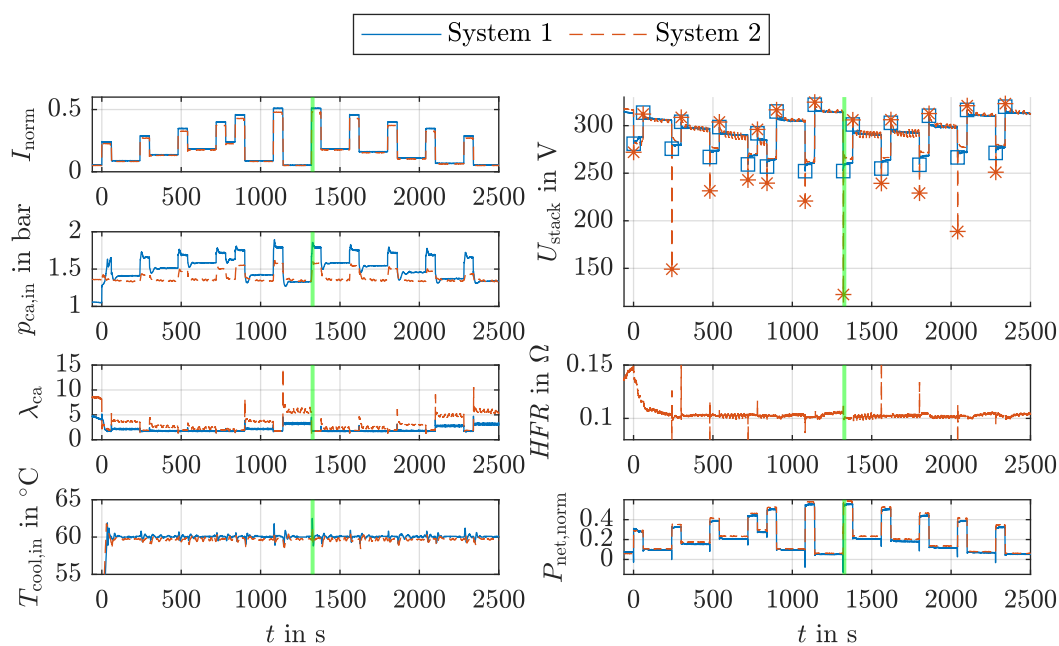
FIG. 4.15 Current profile test with two systems and resulting electrical response, adapted from[46]. The segment highlighted in green is presented as a zoom-in in Figure 4.16.

The stack voltages reveal major differences in the dynamic behavior of the systems, as deeper voltage undershoots occur in System 2. This phenomenon is discussed later in more detail, based on the zoom-in of one undershoot highlighted in green and shown in Figure 4.16. The fluctuations observed in System 2's stack voltage in the low-current phases is caused by the switching of the cathode gas supply. A measurement of the *HFR* is only shown for System 2, as it was not recorded during the operation of its predecessor System 1. The recorded *HFR* signal indicates good membrane humidification during the whole load profile, except for the initial low load operation of System 2. This demonstrates, that with the activity-based water management strategy a sufficiently wet membrane is achieved in a wide operating range, minimizing the ohmic losses caused by the membrane's protonic resistance.

The net power of System 2 lies above the one of System 1 during the stationary phases due to its AirS's recuperation capability. The higher the mass flow and pressure, the more enthalpy is recuperated with the TAC, reducing the required EAC power. At the highest measured currents, the net power of System 2 is around 6 % higher than System 1's net power. System 2 therefore

offers a slight advantage in system efficiency. But what about its dynamic capabilities?

In Figure 4.16, a zoom-in at the largest current increase is displayed. The single stage EAC in System 1 allows for a swift acceleration of the compressor, supplying the required air mass flow and pressure faster than the more complex two-stage AirS of System 2. However, this acceleration results in a high electrical power demand of the EAC for a short period of time, resulting in a short time frame with negative system net power. The strong stack voltage undershoot in System 2 closely correlates with the stoichiometry dropping to almost 1. An under-supply in oxygen is caused by the slower AirS, strongly reducing the stack voltage due to the non-linearly increasing concentration losses. This yields an unwanted temporary net power decrease, instead of the intended steady increase.
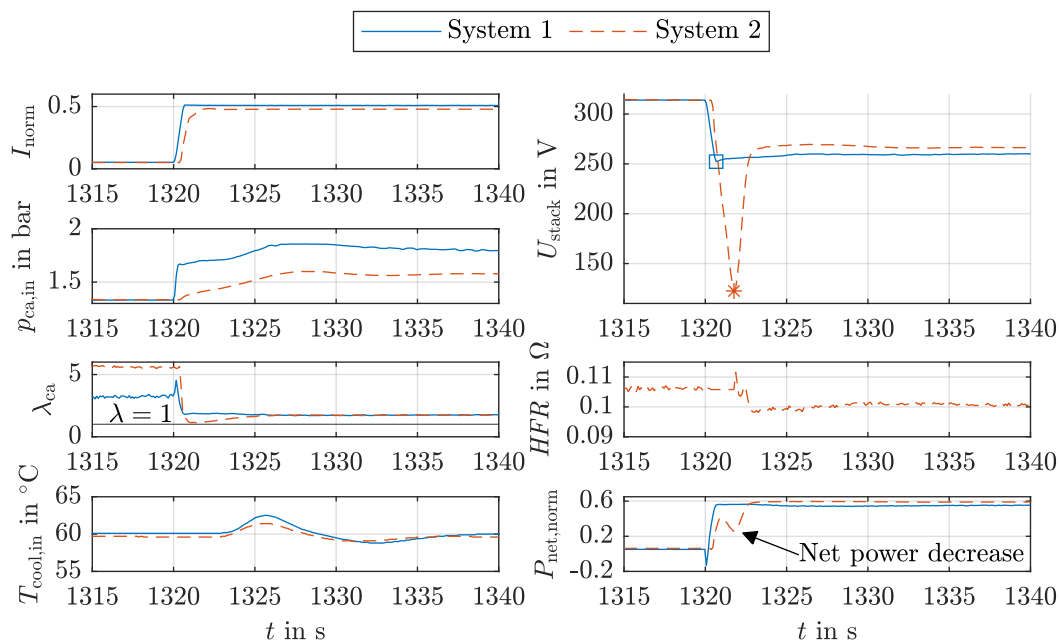
FIG. 4.16   Zoom-in of current increase with two systems, adapted from[46].

Comparing the two realistic experimental fuel cell systems highlights, that the system architecture choice impacts the stationary system efficiency as well as the capability to adapt to dynamic load changes. For the two systems analyzed, these two KPIs conflict with each other: The more efficient System 2 has drawbacks in dynamic performance, resulting in short periods of an oxygen partial pressure deficit. Note that an improvement of the dynamic capabilities of System 2 might be achieved by a turbine bypass or an increase of the steady-state reactant supply. With the reactant-limited current adaption described later in Subsection 5.2.2, the temporary starvation can also be mitigated. A simulation based evaluation of the trade-off between efficiency and dynamics depending on the system architecture is the central topic of Chapter 5 to extrapolate the presented experimental results in scope of RQ4 onto other systems.

4.4.5   Impact of the test rig

So far the system-internal impacts of the BC adaption, the selected set points and the system architecture were shown. But what about the test rig? Does it impact the dynamic behavior

as well? In the next experiment, a state-of-the-art short stack test rig is utilized to compare the dynamic response with the system tests. Therefore, a 15-cell short stack is analyzed with a HORIBA FuelCon Evaluator S5-LT. Between two adjacent stationary operating points, which are held for 15 min, the current is ramped down to zero and ramped up again, with a no-current phase in-between. Each step, the ramp-down, no-current and ramp-up phase, takes 100 s. This procedure was originally developed to conduct stationary experiments. As the short stack test rig adapts the boundary conditions slowly, the current gradients are set significantly slower compared to the system test rig. The following analysis focuses on one current ramp-up event and the subsequent voltage relaxation.

Figure 4.17 displays the measured variables. The current is ramped up linearly, while cathode inlet pressure and mass flow remain constant as intended. The coolant temperature should be constant as well, but exhibits a relaxation behavior caused by the slow test rig control. The resulting voltage response, given as a scaled-up equivalent stack voltage $U_{\text{stack,eq}}$, that a full stack would produce, looks similar to the undershoots in the previous experiments. However, the relaxation process is significantly slower, in the order of 100 s, matching the coolant temperature adaption. Next is a closer look at the underlying phenomena and a comparison with the other test cases.
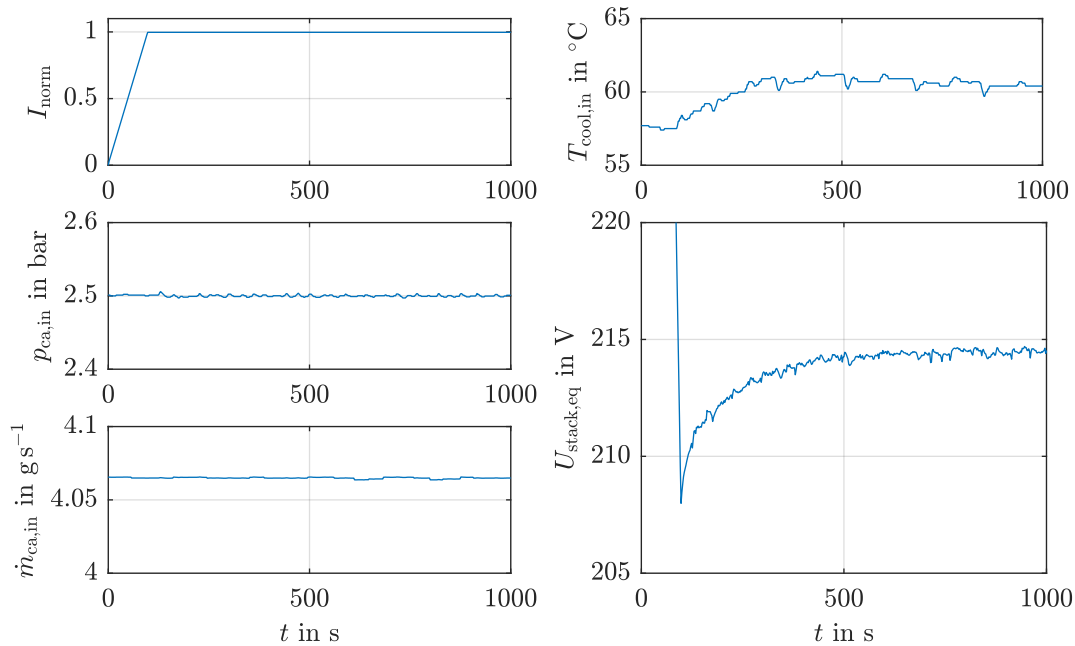
FIG. 4.17 Stack boundary conditions and response in the short stack experiment, adapted from[46].

4.4.6   Comparison using time scale analysis

So what are the dominant effects during dynamic operation in regard of RQ1? With a time scale analysis, the dominant effects shaping the electrical stack behavior become distinguishable. The theoretical concept of time scales was already introduced in the previous Chapter 3. A fitting procedure allows to calculate the time constants τ for the boundary conditions trajectories as well as the voltage response of the stack after a step change in electric current. The step response function of a PT1-element $y_{\text{PT1,step}}$ shown in Equation 3.2 is fitted to the relaxation curve of measured signals y_{meas} towards their next steady-state between two

78

current steps. Note that the fitting interval starts at the local minimum or maximum of the signal if over- or undershoot occur. In this interval, the PT1 response behavior is in good agreement with the measured relaxation curve. The fitting is done by minimizing the function

$$g(\tau, C_1, C_2) = \sum_{i=1}^{N_{\text{sample}}} w_i \left(y_{\text{meas}}(t_i) - y_{\text{PT1,step}}(t_i, \tau, C_1, C_2) \right)^2 \tag{4.2}$$

with the time constant τ and the additional constants C_1 and C_2. This procedure resembles a weighted Least Squares method, where the weights w_i are varied linearly from 1 to 0 to emphasize the initial response characteristic. The shape of the PT1 step response matches the relaxation behavior of selected signals well, when in case of over- and undershoots only the relaxation interval is evaluated. Only the coolant temperature signal in the system experiments deviates from a PT1-like relaxation. In these cases, a settling time with an error band of 0.5 K is calculated instead to evaluate the coolant temperature adaption. An exemplary evaluation is shown in Section A.2.

The fitted time constant ranges for each case divided into current increases and decreases are given in Table 4.5 and Table 4.6, respectively. In the "Fixed BC" case, the mass flow is kept constant with an error below 1.5 %. Therefore, no time constant is given and the respective entry is marked as "const.". The same holds true for the pressure and mass flow in the "Short Stack" case. The *HFR* data is not available in the "System 1" and "Short Stack" cases, therefore the table entry is set to "n.a.". Note that some fits with high errors are neglected for the further analysis. In the load cycle test case "System 2", no sound fitting is achieved for the whole *HFR* signal as the dynamic AirS operation detailed in Section 4.5 causes high periodic fluctuations, making it impossible to track the underlying relaxation with the selected method. The according entry is therefore marked with an "-".

TABLE 4.5 Fitted time constants after current increases in seconds. (*) Settling time instead of time constant is displayed. Adapted from[46].

Case	τ_U	τ_{HFR}	τ_p	τ_λ	τ_T
1a: Adaptive BC	0.2	10.9-11.0	0.9	1.9	5.6-6.4*
1b: Fixed BC	11.1-11.7	10.0-11.0	6.6-6.7	const.	6.7*
2a: Cushioned Supply	2.6-2.7	24.2-27.8	1.7	0.5	5.2-6.0*
2b: Standard Supply	0.7	19.6-28.3	1.6	0.7	6.0-6.4*
3a: System 1	1.8-6.3	n.a.	0.9-2.7	0.1-2.6	7.5-18.3*
3b: System 2	0.3-1.1	-	2.1-4.2	1.3-3.5	6.6-17.0*
4: Short stack	115	n.a.	const.	const.	103

TABLE 4.6 Fitted time constants after current decreases in seconds. (*) Settling time instead of time constant is displayed. Adapted from[46].

Case	τ_U	τ_{HFR}	τ_p	τ_λ	τ_T
1a: Adaptive BC	3.9-4.2	19.1-19.5	1.5	1.5	7.5-7.7*
1b: Fixed BC	40.9-46.0	41.7-48.8	12.5-13.2	const.	9.5-10.0*
2a: Cushioned Supply	3.5	19.5-22.8	3.1	1.5-1.6	8.3-8.9*
2b: Standard Supply	3.8-3.9	30.9-31.0	2.6	1.4	8.1-8.2*
3a: System 1	1.9-5.0	n.a.	0.8-3.9	0.2-0.6	7.5-19.3*
3b: System 2	12.7-30.1	-	7.0-23.8	0.9-8.5	6.7-15.0*

Fixing the BC's drastically prolongs the voltage response during current increases and decreases compared to the experiment with BC adaption. In the "Adaptive BC" case, the voltage time constant τ_U does not clearly match one of the BC's time constants. But as the time constants are rather low, they are most likely correlated with the gas supply dynamics, which yield the lowest characteristic times. In the "Fixed BC" case, where pronounced dry-out and re-humidification cycles are observed, τ_U almost perfectly matches with the *HFR*'s time constant τ_{HFR}. This indicates a *humidification dominated mode* of the voltage response, where the re-humidification takes place around four times faster than the dry-out, contradicting literature data[89] as previously discussed in Subsection 4.4.2.

Reducing the oxygen partial pressure in case of the standard supply impacts τ_U only when the current is increased. A lower partial pressure results in a sharp voltage undershoot, caused by a short period of low oxygen supply as the compressor speeds up, followed by a PT1-like relaxation towards the new steady-state. This behavior results from the non-linear dependency of the voltage on the partial pressure: the lower the partial pressure, the stronger the subsequent voltage drop. A period of critically low oxygen partial pressure causes a sharp and deep voltage undershoot and fast recovery, dominating the time constant of the response. This is supported by τ_U being the same as the stoichiometry time constant τ_λ, as the stoichiometry directly influences the partial pressure. In the following, this behavior is referred to as *gas supply dominated mode*. Note that a higher initial p_{O_2} in case of the cushioned supply reduces the dynamic oxygen decrease during the load increase, resulting in a less pronounced voltage undershoot. However, no clear impact of p_{O_2} on the voltage overshoot time constants following a current decrease is visible.

When comparing the systems' time constants in Table 4.5 and Table 4.6, a wider range of the calculated time constants occurs. This is mainly caused by the various different current steps in the current profile in contrast to the previously discussed constant-height current steps. As expected, the adaption in pressure and stoichiometry takes longer in System 2 due to the inertia of the TAC. However, τ_U of "System 2" is lower than in case of "System 1" when the current increases, which might be counter-intuitive. But a similar phenomenon as discussed previously in the "Standard Supply" case is at play: The slow adaption of the AirS leads to short periods of lower oxygen partial pressures dominating the voltage response, again resulting in a rather sharp and deep voltage undershoot. The voltage responses of both systems after current decreases cannot be directly linked to one specific BC, but appear to be closest to the pressure adaption time constant τ_p.

The short stack test yields an entirely different order of magnitude for τ_U, shown in Table 4.5.

As the gas supply is not changed during the experiment, the temperature adaption remains as the only key BC explaining the voltage undershoot. This is supported by a good match of the time constants τ_U and τ_T. Here, an entirely different third mode in voltage response is observed: the *temperature dominated mode*, caused by the low thermal dynamics of the test rig. In comparison to the application-like ThS integrated in the systems, the short stack test rig takes roughly ten times longer to adapt the coolant inlet temperature, although relating the displayed values directly is complicated by the different calculation approaches for time constant and settling time.

With these observations, the process chain introduced at the beginning of the chapter in Figure 4.6 is broken down into the three dominant modes. Figure 4.18 shows the resulting reduced process chains for each mode. One, the *gas supply dominated mode* with pressure and stoichiometry time constants between 0.9 and 1.9 s. Two, the *humidification dominated mode* with time constants of ≈ 10 s and ≈ 45 s for membrane humidification and dry-out, respectively. Three, the *temperature dominated mode* with a time constant of ≈ 100 s. This comparison clearly demonstrates the pitfalls of the prevalent literature experiments when analyzing dynamic fuel cell operation.
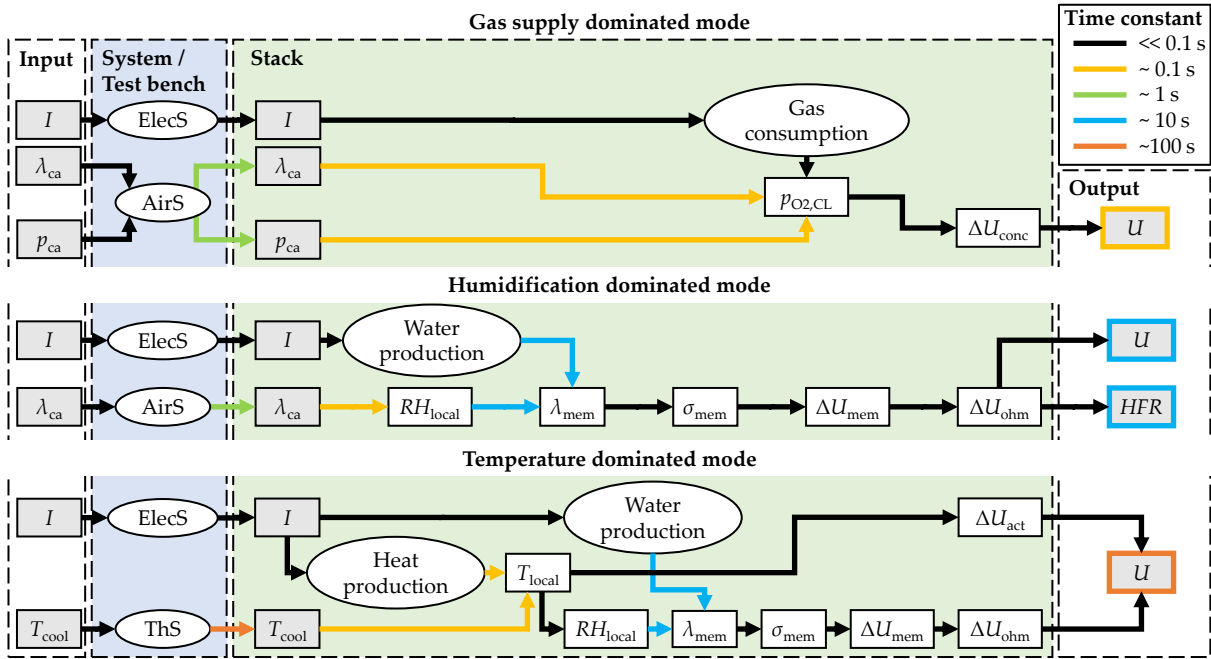
FIG. 4.18 Dominant processes and resulting time scales in the three voltage response modes observed, adapted from[46].

Multiple conclusions are drawn from the experiments conducted in this work, addressing the research questions introduced in Subsection 2.4.2:

RQ1: Coolant temperature, cathode stoichiometry and cathode pressure are the most influential BC's for the electrical stack response in dynamic operation. In line with the simulation model results, the sorption process dominates the dry-out and re-humidification behavior as indicated by the *HFR* measurements.

RQ2: The voltage response might appear to be qualitatively the same, but the time scales differ by almost two orders of magnitude, as different processes dominate. This displays a potential pitfall in the experimental setup. The experiment must be chosen carefully to target a certain response mode. Test rig limitations might restrict the achievable

experimental scope to less realistic scenarios.

RQ3: To be targeted in the following.

RQ4: A trade-off between system net power and dynamic behavior must be carried out in case of the system architecture and the set point selection. System 2 with its sophisticated AirS is more efficient in stationary operation but lacks in terms of pressure and mass flow dynamics, resulting in periods of high concentration losses during highly dynamic current increases. Maintaining a higher oxygen partial pressure during stationary operation, a cushioned supply, requires additional compressor power and reduces the steady-state system net power, but enlarges the margin with respect to local oxygen starvation during fast current increases.

So far, the focus was laid on dynamic changes in the stack current. But if the required system power is constant, can a dynamic operation of subsystems enhance the system's capabilities? To the best of the authors knowledge, research in this direction is sparse to non-existent, as the community lacks appropriate experimental setups. However, the following section addresses such an idea and showcases the benefits of a dynamic AirS operation experimentally, improving common stationary-based water management strategies in scope of RQ3.

4.5   Dynamic Air System Operation

Parts of the research displayed in this section were presented by the author at the 242nd Meeting of the Electrochemical Society in Atlanta, GA and consequently published in the transactions[45]. The content is adapted and put into the context of this work. A permission for reproduction of the figures was obtained from IOP Publishing Ltd. as stated in the figure captions.

4.5.1   Flow regime transition and flooding

During commissioning of System 2, deep cell voltage drops occurred during low load stationary operation. In general, this behavior can be caused by a broad variety of different effects, such as insufficient reactant supply of the electrodes due to e.g. liquid water or nitrogen accumulation, severe dry-out of the membrane or reactant cross-over. The fact, that the voltage declined initially only in a few cells randomly distributed within the stack, lead to the assumption, that a strong non-linear effect such as local reactant starvation might be at play. A dry-out of all cells would result in a slower, continuous voltage reduction in all cells. A systematic distribution of the affected cells would hint towards a stack-induced inhomogeneity of e.g. the cells individual operating temperature or a substantial gas flow maldistribution. In the end, a local lack of reactants was most likely. But what is the underlying cause?

In the flow fields of fuel cells, a complicated two-phase flow of liquid water and gas mixtures of varying composition is expected. At the inlet, relatively dry gas enters the cell. Along the flow path, the relative humidity *RH* rises as the fuel cell reaction produces water and consumes reactants. At some point, *RH* reaches 100 % and liquid water emerges. The interaction of the liquid water and the gas phase in a two-phase flow can be classified into several flow regimes. Multiple researchers analyzed this topic experimentally, focusing on widely used channel-land flow fields.

In a simplified experimental setup consisting only of a GDL and a flow field, Lu et al. injected water from below the GDL and analyzed the resulting flow regime in the flow field with an

optical camera[27]. From these experiments, they derived a flow regime map with three distinct regimes, depending on the gas velocity and liquid water flux. Figure 4.19 shows the flow regimes for varying gas velocities u schematically. First, the water droplets are rather small, being carried by the gas flow detached from the adjacent surfaces, a regime called mist flow. Second, larger droplets compound to a film at the channel surfaces, in a regime referred to as film flow. The liquid film is objected to momentum transfer from the gas flow and therefore exhibits a movement in parallel to the gas stream. This regime is favorable in fuel cell operation, as critical liquid water accumulation is prevented by the continuous drainage of the liquid share. Simultaneously, the gas flow remains largely unaffected, resulting in a sufficient reactant supply for the fuel cell reaction along the whole flow path. Third, if the momentum transferred from the gas flow to the film becomes to small to move the film sufficiently, the liquid water will form larger droplets. This so called slug flow affects the reactant supply adversely in two ways: a) by the reduced or negligible remaining gas flow in the flow field and b) by the hindrance of gas diffusion through the GDLs due to insufficient water drainage, resulting in high liquid water saturation levels.
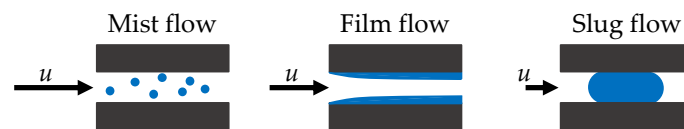
FIG. 4.19   Schematic regimes of the two-phase flow of water and gases in a flow field channel.

Additional experiments support the dependency of the flow regime on the gas velocity and the liquid water flux[96]. Also, the flow field type, channel surface treatment, its geometry and the implementation of an MPL affects the transition velocities[14,97,114,147]. Coeuriot et al. found, that all three flow regime can coexist along the channel of a fuel cell, starting with small droplets at the inlet, followed by droplet growth, and subsequently slug and film flow regimes within the outlet region[132]. Optical fuel cell experiments were carried out by Hussaini and Wang[130] and confiremd the occurence of the flow regimes. Jenssen, Berger and Krewer targeted the anode, defining a critical Reynolds number, below which unstable operation due to insufficient water removal occurs[148].

Based on this literature review, liquid water accumulation due to an unfavorable flow regime in the flow field was the most promising explanation. Next, targeted experiments to identify the flooding limit, its consequences for stationary operation as well as a dynamic flooding mitigation strategy are presented. This research aims at showcasing and overcoming the shortfalls of stationary-based water management strategies in scope of RQ3.

4.5.2   Flooding limit identification

Only limited sensor data is available in the system experiment and e.g. a spatial liquid water distribution cannot be tracked. So how can flooding be detected with the finite ex-situ signals? Monitoring the individual cells' voltages within the stack are an option for this task. If flooding is induced gradually, only a few cells are affected at first. These are cells with e.g. unfavorable geometric deviations, non-ideal coating of the GDLs and/or flow fields, a lower available catalyst surface area or other imperfections induced randomly by the production process. As a local shortage of reactant disproportionately affects the voltage, such an imperfect cell's

voltage diverges substantially from the other cells within the stack, which are not so prone to flooding. Therefore, the root mean square deviation of the CVM signals $RMSD_{CVM}$ is selected to quantify the cell voltage spread. It is calculated from the individual voltages of the cells k, $U_{CVM,k}$, and the mean cell voltage $\bar{U}_{CVM}$ of all the n_{cells} cells in the stack as

$$RMSD_{CVM} = \sqrt{\frac{\sum_{k=1}^{n_{cells}} \left(U_{CVM,k} - \bar{U}_{CVM} \right)^2}{n_{cells}}}. \tag{4.3}$$

An exemplary operation of the fuel cell system including multiple flooding events is displayed in Figure 4.20. As intended, the deviation of a few cells from the mean voltage results in large spikes in the calculated $RMSD_{CVM}$. A threshold of 10 mV is chosen to automatically classify the operating state into either stable conditions, if the deviation is below the threshold, or flooded conditions if it lies in the blue area above the threshold. During normal operation, the $RMSD_{CVM}$ lies around 5 mV, a factor of two below the flooding threshold. Therefore, the deviation is expected to be a highly distinctive feature.
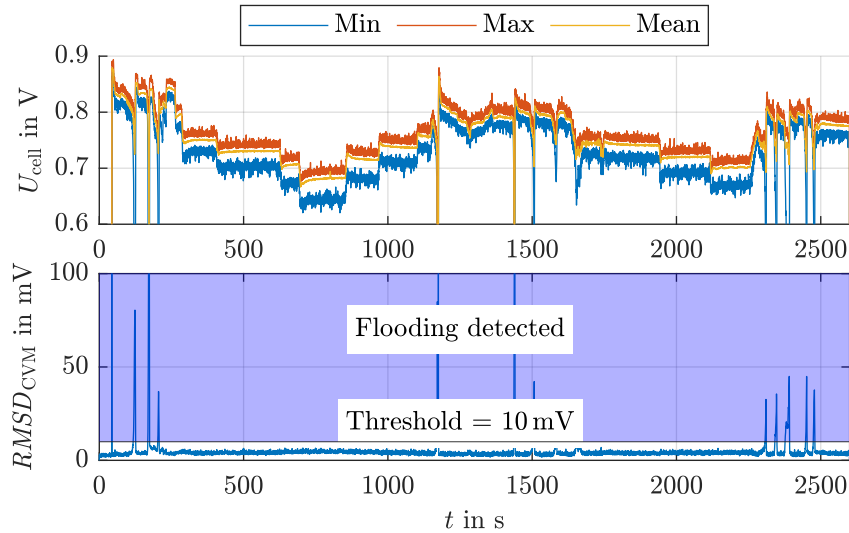
FIG. 4.20 Measured minimum, maximum, and mean cell voltages over time (top) and cell voltage root mean square deviation over time (bottom) for an exemplary test run with several flooding events[46]. ©The Electrochemical Society. Reproduced by permission of IOP Publishing Ltd. All rights reserved.

Now, a series of targeted experiments is conducted to pinpoint the flooding limit and its dependency. Starting from a known stable stationary operating state, the gas velocity is reduced by lowering the cathode mass flow and/or increasing the pressure. To avoid a possible voltage impact of low oxygen partial pressure in the flow field, this adaption of pressure and mass flow is carried out in a wa, that ensures the oxygen partial pressure to be at or above its target value. As soon as flooding is detected, the system is returned to stable operation by raising the gas velocity again. To analyze the impact of temperature and current on the flooding limit, the experiment is repeated for various current and temperature combinations. Note that due to AirS limitations, especially the EAC surge limit, not all temperature-current combinations are tested.

The gas velocity at the cathode inlet $u_{ca,in}$ is calculated from the cathode inlet mass flow

$\dot{m}_{ca,in}$, the gas density $\rho_{ca,in}$ and the cross-sectional area $A_{sec,ca}$ of the cathode flow field by

$$u_{ca,in} = \frac{\dot{m}_{ca,in}}{\rho_{ca,in} A_{sec,ca}}. \tag{4.4}$$

Multiple test runs at various currents and temperatures are combined in Figure 4.21. The unstable, flooded operating states lie almost on a straight line. The higher the current, the higher the minimal gas velocity u_{min} required for stable operation. The temperature variation shows no clear impact on the minimal velocity. Note that some stable operating states lie below the suspected transition velocity. These points are recorded when the system is set to a new temperature-current pair. At low currents, the minimal gas velocity can be reduced below the limit for a short period of time, as the water accumulation takes a couple of seconds until it significantly affects the reactant transport. This observation is critical for the mitigation strategy discussed later.
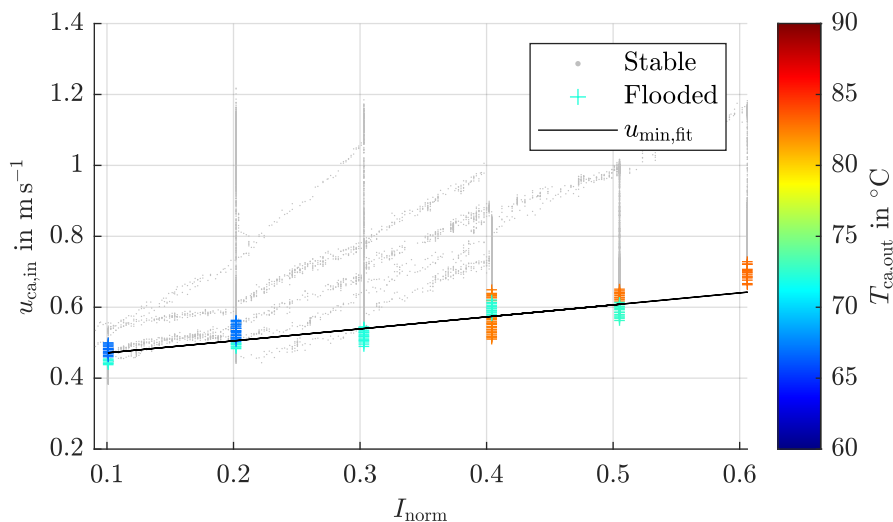
FIG. 4.21 Cathode inlet gas velocity versus normalized current at varying cathode outlet temperatures. Circles mark stable operation; crosses highlight flooded conditions[46]. ©The Electrochemical Society. Reproduced by permission of IOP Publishing Ltd. All rights reserved.

First, the flooding limit is simplified to a simple linear function:

$$u_{min,fit}(I_{norm}) = C_1 + C_2 I_{norm} \tag{4.5}$$

The constants $C_1 = 0.44\,\mathrm{m\,s^{-1}}$ and $C_2 = 0.34\,\mathrm{m\,s^{-1}}$ are obtained by utilizing a Least Squares approach to fit the function to the measured flooded states. Only a current dependency is considered, as the temperature impact is inconclusive. The results of these experiments are incorporated in the liquid water drainage limitation of the simulation model discussed in Chapter 3. The limitation function fit is described in Appendix A.1. In the upcoming subsection, the consequences of the identified velocity limit on the stationary-based operation in context of RQ3 are addressed.

4.5.3 Conflict of stationary limits

The original activity-based water management approach proposed by Hellmann[44] features two limits: a dry-out limit and a flooding limit, defined via a minimum and maximum outlet

activity $a_{\min}$ and $a_{\max}$. The previously shown experiments suggest that the drainage limit, where all liquid water is drained and no flooding occurs, is rather a function of the gas velocity $u_{ca,in}$ than the outlet activity. Therefore, the newly defined drainage limit is called $u_{\min}$ instead of $a_{\max}$. For the example shown in the following, a minimal outlet activity of $a_{\min} = 0.8$ and a target activity of $a_{target} = 1.4$ is selected. The values of the drainage limit are evaluated with equation 4.5.

In Figure 4.22, the drainage and the dry-out limit are added in the stoichiometry-pressure diagram introduced in Figure 2.11. The hatched area indicates, on which side each of the limits is violated. If the stoichiometry is too high and oversteps the $a_{\min}$ limit, the membrane starts to dry-out. If it is too low to comply with the $u_{\min}$ limit, liquid water accumulates, ultimately resulting in a significant voltage decline due to flooding. Note that the drainage limit's position varies depending on the current, while the dry-out limit is independent of the current in the selected coordinate system.
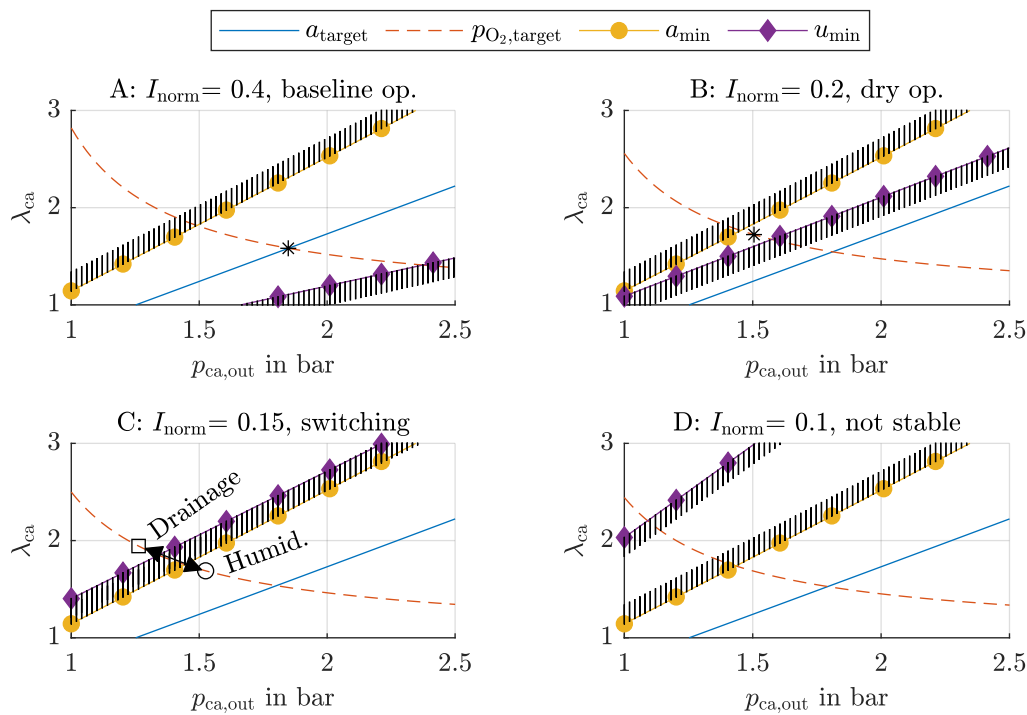
FIG. 4.22 Baseline outlet activity target a_{target}, oxygen partial pressure target $p_{O_2,target}$, dry-out limit $a_{\min}$ and drainage limit $u_{\min}$ at $70\,°C$ cathode outlet temperature in four scenarios (A-D) with varying normalized current I_{norm}[46]. ©The Electrochemical Society. Reproduced by permission of IOP Publishing Ltd. All rights reserved.

Four scenarios are distinguished by plotting the limits for different currents in Figure 4.22. In case A, neither the drainage nor the dry-out limit interfere with the target pressure and stoichiometry combination marked by the star at the intersection of a_{target} and $p_{O_2,target}$. Here, the baseline strategy results in stable operation. If the current is reduced in case B, the drainage limit lies above the set point that would be chosen with the baseline strategy. If the strategy is not adapted, the drainage limit is violated resulting in flooding. One solution would be to abandon the target activity a_{target}, and opt for a stationary operation at lower outlet activity, resulting in a slightly drier membrane as indicated by the star symbol.

Another possibility is the dynamic operation of the AirS. As flooding and dry-out are not

triggered immediately as their respective limit is violated, periodically switching between two operating points, that each fulfill only one of the limits, becomes an option. Therefore, two phases are introduced. During the drainage phase, liquid water is drained from the cell. After several seconds, this would result in a dry-out of the membrane. Now, the pressure and mass flow are switched for the humidification phase, during which the membrane gets re-humidified. Again, a stationary operation at this point would result in unstable cell voltages due to flooding after a while. Following, the AirS set point must be switched back to the dry phase. This *switching operation* is demonstrated experimentally in the upcoming Subsection 4.5.4.

In case C, the current is reduced further. Now, even a drier stationary operation is impossible, as drainage and dry-out limit become incompatible. The previously discussed dynamic switching operation of the AirS is the only option to achieve a stable stack operation without flooding or dry-out. If the current is set to only 10 % of the rated current, case D results. Here, the dry-out and drainage limit lie so far apart, that the achievable dynamics of the AirS are insufficient to switch between the dry phase and the humidification phase fast enough. No stable operation is achievable, neither by a stationary nor the adapted switching strategy.

In Figure 4.23, the temperature dependence of the cases is displayed. As the saturation pressure grows exponentially with increasing temperature, the pressure must be increased drastically if the activity-based water management approach is followed. With that, the air's density is also exponentially increased, resulting in lower gas velocities at the baseline target set point. Therefore, the cases B to D, where no baseline operation is possible, extend up to higher currents as the temperature is increased. Low current operation at high temperature is subsequently most prone to flooding due to too low gas velocities.
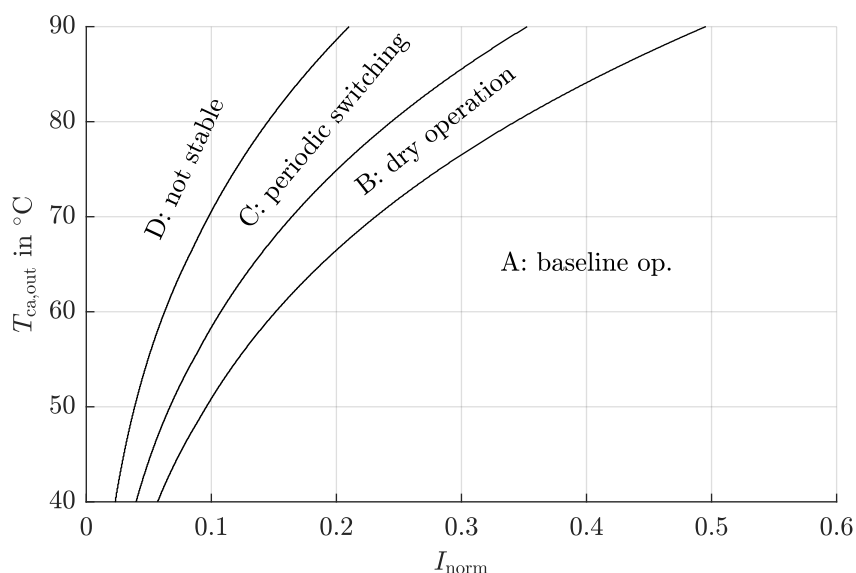
FIG. 4.23 Sections of the operating range (A-D) in terms of cathode outlet temperature and normalized current[46]. ©The Electrochemical Society. Reproduced by permission of IOP Publishing Ltd. All rights reserved.

4.5.4   Flooding mitigation with air system switching operation

The research presented in the literature, previously discussed in Subsection 4.5.1, focuses solely on stationary conditions with respect to gas flow and water production. As a result, the suggested solutions to avoid slug flow and the consequent flooding in fuel cell operation mainly aim at improving the stack design. At system level, these approaches are not applicable as the stack design is fixed and only the operating conditions are adaptable to the stack's fixed requirements. However, system level solutions offer other degrees of freedom, such as changing the stack's BC's either stationary or even dynamically. This playing field is often overlooked in literature and, to the best of the authors knowledge, only Hussaini and Wang[149] proposed such an approach. They switched the external humidification of their single cell on and off in order to avoid flooding while maintaining a sufficient membrane hydration, a technique they called "intermittent *RH* control"[149]. In an automotive system without humidifier as presented in this work, such a procedure is infeasible.

The novel approach developed in this work utilizes the high-performance AirS of the application-like System 2 introduced in Subsection 4.2.2. By switching between a drainage phase and humidification phase, a stable operation with a maximum $RMSD_{CVM}$ of only 6.8 mV, below the flooding limit of 10 mV, is achieved. The measured variables are depicted in Figure 4.24. While the electrical current is set constant, the *HFR* shows the intended humidity cycles of the membrane. During the humidification phase (green), the measured *HFR* drops, but so does the cell voltage, as liquid water accumulates. The pressure is rather high, with the stoichiometry being relatively low during this humidification phase, resulting in a low gas velocity. As the AirS is switched to the drainage phase (orange), the membrane starts to dry as indicated by the rising *HFR*. The cell voltages quickly recover as the liquid water no longer hinders the oxygen diffusion through the cathode GDL. This is achieved by a pressure reduction and stoichiometry increase, leading to a high gas velocity to drain substantial amounts of liquid water from the cell. Afterwards, the cycle repeats.

In conclusion, a conflict between the minimal gas velocity limit u_{min} and the dry-out limit a_{min} arises during low load operation, a phenomenon aggravated by rising operating temperatures. No stationary stable operation can be achieved in these cases, showcasing a shortcoming of common stationary-based strategies as aimed at with RQ3. Targeted experiments allowed to pinpoint the drainage limit u_{min} in the setup in focus, resulting in sections of the operating envelope where the stationary baseline approach fails. For these sections, a two-phase periodic AirS control strategy with switching periods of about 20 s is developed and demonstrated successfully in an application-like experimental FCS, presenting an improvement of the baseline strategy.
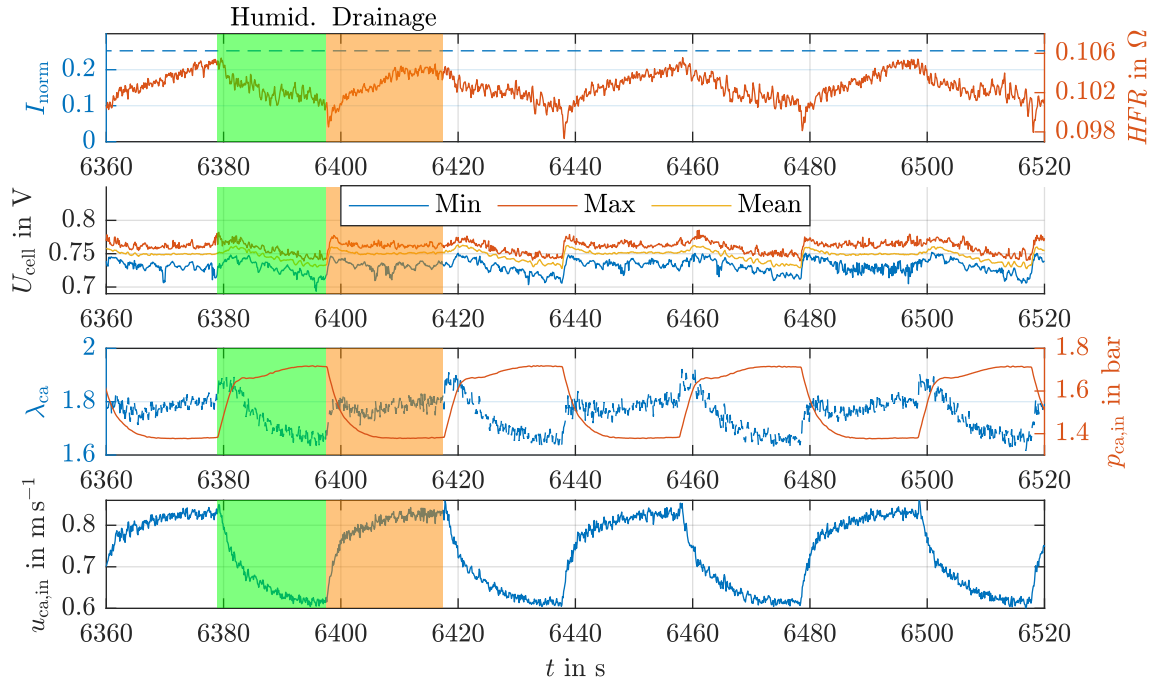
FIG. 4.24 Normalized current, high frequency resistance *HFR*, minimum, mean, and maximum cell voltage, cathode stoichiometry and inlet pressure, and gas velocity at the cathode inlet during dynamic air system operation[46]. ©The Electrochemical Society. Reproduced by permission of IOP Publishing Ltd. All rights reserved.

4.5.5 Benefits for application and outlook on consecutive research topics

With this AirS switching strategy, the achievable operating envelope of the fuel cell system is extended towards lower current and subsequently lower electrical system power while avoiding critical states. A reduced minimum power limit decreases the start/stop cycles a system in vehicle application would face: If no power is requested by the drive-train, the FCS must be switched off as soon as the battery's State of Charge (SoC) reaches its upper limit. If the minimum idle power is reduced, charging the battery can be prolonged over an extended time period, raising the probability of a non-zero power request from the drive train. This reduces the number of start/stop phases required, which is beneficial for the lifetime and efficiency of the system.

The ability to operate the system at increased temperatures yields a twofold benefit. Due to its low typical operating temperature of approximately 60 °C, the driving gradient between the system's and the ambient air's temperature is limited. This results in large required cooler surface areas which are complicated to fit into typical vehicle bodies. If the cooling capacity is insufficient, the heat output and consequently the electrical system power must be reduced to avoid stack damage, a process called thermal derating. Even in hot land hill climb scenarios, a sudden reduction of the required power might occur, e.g. when the vehicle is stopped. As the temperature drops relatively slow, a period of high temperature and low power operation must be bridged. This period can be covered by the proposed AirS switching operation. As a secondary benefit from the increased temperature operation in combination with higher pressure, the system efficiency is increased by reducing activation losses.

It is likely that the exact position of the drainage limit depends on the stack design, especially the coating of GDL and flow field. The coating causes varying contact angles, impacting

the droplet drainage as indicated by literature[98]. In the end, it is necessary to fine-tune the pressure and mass flow during the two phases and their respective durations to the stack and the implemented AirS. Tracking the liquid water accumulation and drainage during dynamic AirS operation with a spatial resolution on the scale of the flow field depth and a time-wise resolution in the order of one second might be a promising approach to foster an in-depth understanding of the underlying phenomena, but is experimentally challenging.

Within this section, the focus lied on the constant-current operation and the implications caused by the flooding limitation. The following section addresses the impact of liquid water on the achievable current steps, as another limitation on stationary-based strategies in the context of RQ3.

4.6 Water-Induced Current Step Limitations

4.6.1 Observation

As shown with the simulation model in Subsection 3.4.2, the presence of liquid water in the GDL might severely increase the concentration losses ΔU_{conc} if the current and subsequently the reactant consumption is increased rapidly, displaying one limitation of stationary-based water management strategies in scope of RQ3. But can this prediction be supported by experimental data? By chance, such a phenomenon is encountered during the flooding limit identification experiment described previously in Subsection 4.5.2. A full EIS measurement carried out during stationary operation very close to the flooding limit is shown in Figure 4.25. The current is deflected sinusoidally with an amplitude of just 7.5 %. However, massive voltage drops of up to 55 % are observed in some cells, displaying a strong non-linearity. Note that all other stack BC's are set constant and only the electrical current is actively manipulated in this experiment.

In the first time frame highlighted in green, the current is increased but the cell voltage spread remains inconspicuous. As the electrical current is raised further and subsequently the reactant consumption keeps increasing, the cell voltages start to diverge significantly. A voltage way below 0.5 V is recorded in one cell. Note that the voltage minimum is shifted with respect to the maximum in consumption and not all cells are affected equally. After the current is decreased again, the cell voltages recover and the spread reduces back to its typical values. A minor fluctuation in stoichiometry is also visible, while the pressure is almost constant and the gas velocity shows no oscillation clearly matching the current. As the stoichiometry is significantly above 1 and the pressure is comparably high, a sufficient oxygen partial pressure should be available in the flow field. But then, why are so deep cell voltage drops observed?
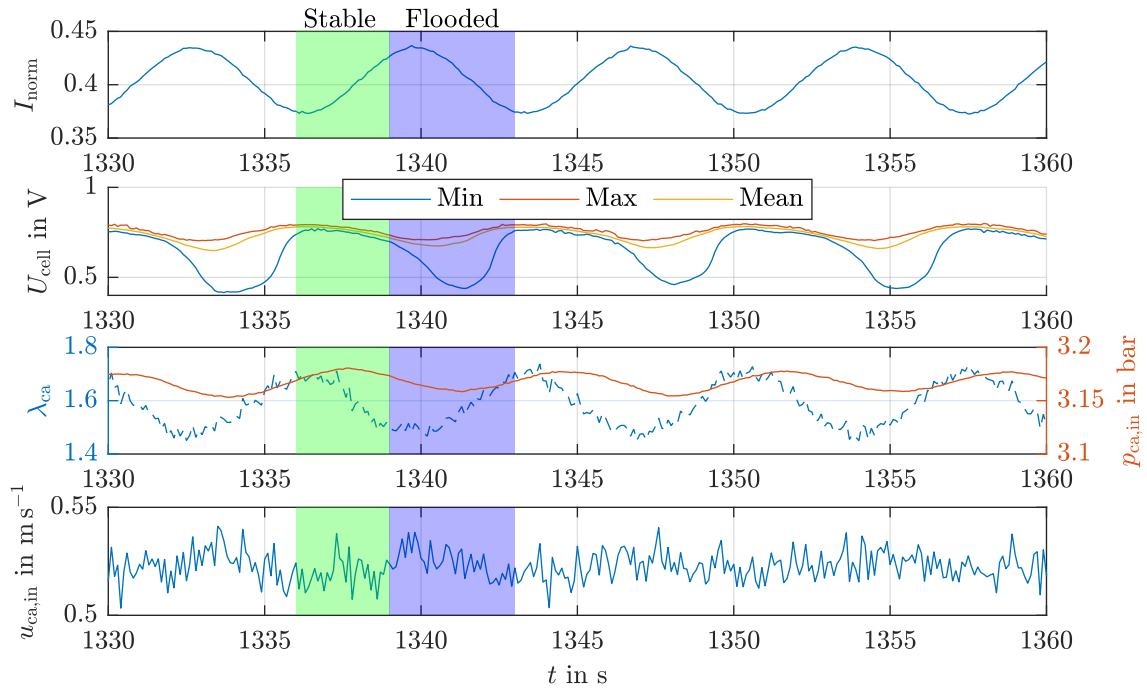
FIG. 4.25 Normalized current, high frequency resistance, minimum, mean, and maximum cell voltage, cathode stoichiometry and inlet pressure, and gas velocity at the cathode inlet during an EIS measurement close to flooding.

4.6.2 Explanation and consequences

The answer lies in the concentration losses, as the observed phenomenon is similar to the example shown in Subsection 3.4.2. Note that the partial pressure of oxygen in the flow field is somewhat irrelevant for the measured cell voltage, as it is only affected by the partial pressure directly at the CCL. But the presence of liquid water within the GDL reduces the partial pressure at the CCL, as with the same partial pressure gradient between CCL and flow field less reactant diffuses due to the reduced available cross-sectional area. In the following, the current density distribution reorganizes towards the segments where sufficient reactant flux is still available, resulting in a drop of the global cell voltage. As a secondary factor, the increased current raises the water production rate. More liquid water flows into the cathode GDL, but the water drained from the GDL into the flow field remains constant due to the constant gas velocity. Following, the liquid water saturation within the GDL rises. This slow accumulation is suspected to cause the delay between the current maximum and voltage minimum. Note that due to the strong non-linearity of mass transport losses observed in the experiment, only minor deviations in e.g. coating quality, available catalyst surface area or other production imperfections between the cells cause greatly diverging cell voltages.

All in all, two major contributors that may cause massive voltage reduction during fast current increases are shown with the experiments. First, a slow AirS resulting in delayed pressure and mass flow adaption as shown in the system comparison in Subsection 4.4.4 can cause temporary starvation. A second important aspect is not a feature of the system, but rather of the stack's state: if the liquid water saturation is rather high, a fast increase in electrical current and therefore reactant consumption results in large concentration losses or even local reactant starvation. The implications of this second aspect are discussed in more detail in the following and present an important contribution to the stationary-based water management

91

strategy limits as targeted with RQ3.

Depending on the reactant consumption, the allowed liquid water saturation s_{max} of the GDL changes, as depicted schematically by the purple dashed line in Figure 4.26. The higher the consumption, the more free volume must be kept available for a sufficient gas diffusion, assuming a constant reactant partial pressure gradient between CCL and flow field. For low electrical currents, more liquid water resulting in a higher saturation level s is acceptable. A certain control strategy, meaning the adaption of the stack boundary conditions such as mass flow or pressure to the current, leads to different load dependent saturation levels. This is indicated by the gray and orange lines. If only stationary or low dynamic operation on a time scale above the one of liquid water drainage is considered, a control strategy resulting in the orange saturation levels is feasible. However, if the electrical current is increased significantly faster than liquid water can be drained, an almost horizontal path in Figure 4.26 results, as shown by the blue arrow. The saturation level that was acceptable at the low load, is too high for the now increased consumption and the s_{max} limit is violated. Consequently, a strong voltage drop as encountered in the experiment occurs.
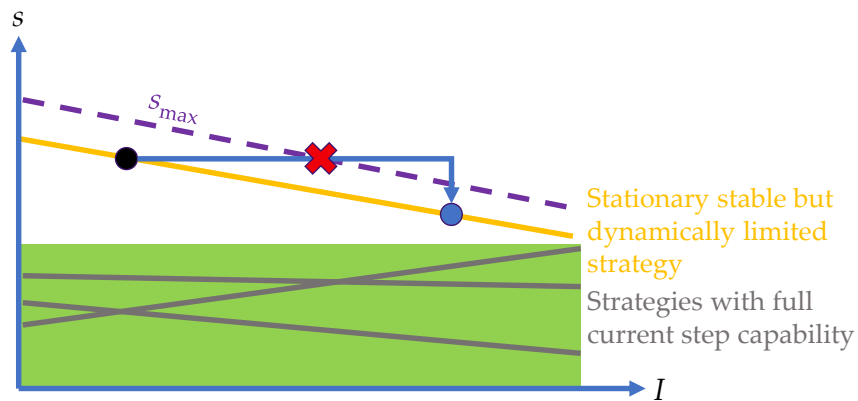
FIG. 4.26 Schematic dependence of the allowed liquid water saturation s_{max} on the current and limitation for fast current increases with various control strategies.

It is possible to find control strategies that aim at maintaining rather low saturation levels, as hinted schematically by the gray lines in the green corridor. This may be achieved by rather high gas velocities or generally drier operating conditions, such as rather low pressure and increased stoichiometry. In these cases, liquid water saturation is sufficiently low to allow for a sudden consumption increase at all times. Maintaining low saturation levels must be balanced with possible dry-outs, that might partially occur within the cell and might also result in an ohmic-dominated voltage undershoot after a current increase. Note that the exact values for s_{max} cannot be quantified from the experiment, as the saturation level is not to be measured directly in the test setup.

Now, as the step from *cell to system* is taken with the previously presented experiments, it is time for the last step in the logic of the setup introduced in Subsection 2.4.3: transferring the knowledge from *this special system to other systems*.

Chapter 5

System Architecture

This chapter aims at broadening the scope of this work even further. Starting from the cell level with the simulation model in Chapter 3, experiments on system level were described in Chapter 4. Now, the gained insights are utilized to foster an understanding of other fuel cell systems in highly dynamic operation. The chapter starts with a description of its goal and scope, before the knowledge gained in previous chapters is combined to allow for a model reduction as well as an improved control strategy for highly dynamic operation. Existing system architectures are analyzed to select three reference architectures, aiming at answering RQ4: evaluating the expected trade-off between efficiency and dynamic capabilities and how it is impacted by the choice of system architecture and control strategy. The cell model is coupled with an AirS model and a dynamics and efficiency analysis is carried out. This chapter concludes with a discussion of a Pareto-frontier, which compactly displays the efficiency versus dynamics trade-off.

The research presented in this chapter was supported by Jannik Schmitt's master thesis[150]. The author supervised this research activity, conducted the foregoing analysis of existing architectures, implemented the reactant-limited current gradient strategy, performed the load cycle analysis and evaluated the efficiency versus dynamics trade-off.

5.1   Goals and Scope

Within this chapter, the knowledge gained from the simulation model and system level experiments is synthesized to extrapolate the behavior of other, virtual systems. The simulation model developed in scope of Chapter 3 provides the capability of tracking local states within the fuel cells during dynamic operation. The impact of the control strategy and the stack boundary conditions on the stack and system behavior were already discussed in depth based on experimental results in the previous Chapter 4. On system level, another degree of freedom heavily impacting the KPIs exists: the choice of the system architecture, meaning the combination and connection of the components within the subsystems. But how do different architectures perform? Which architecture should one choose depending on one's requirements and how should such a system be controlled?

These seemingly simple questions are the focal point of research question RQ4, targeting the impact of the system architecture and control strategy on the efficiency and dynamics trade-off. The multi-step methodology chosen within this chapter is displayed in Figure 5.1. First, knowledge gained from the previous chapters is combined to boil down the relevant time scales within a fuel cell system. In context of RQ3, shortcomings of stationary-based control strategies are discussed and an improved strategy for highly dynamic operation is derived. Following, reference architectures for the subsequent simulation study are selected based on an analysis of architectures implemented in series produced vehicles. Note that the goal is not to find an optimal architecture choice, but to rather showcase the levers via which

the architecture impacts the efficiency and dynamics trade-off. The simulation study then aims at identifying the dynamic capabilities and efficiency of the selected architectures and control strategy adoptions. Finally, the trade-off between dynamics and efficiency as a main contribution of this chapter is discussed.
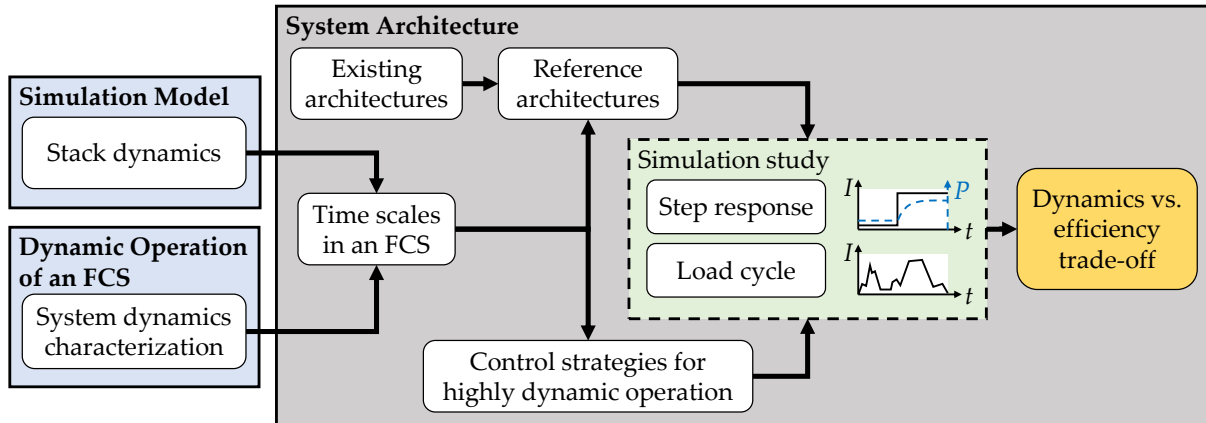
FIG. 5.1 Methodology of the architecture impact analysis and interaction with adjacent chapters.

5.2 Combining Insights of Previous Chapters

5.2.1 Time scales in fuel cell systems

The concept of time scale analysis as introduced in Subsection 3.3.2 cannot only be used to select the relevant cell intrinsic dynamic processes: At the system level, similar derivations are possible. In the following, the main dynamic processes within the stack as well as within the AirS, HyS and ThS are explored, utilizing the experimental results as well as analytic approximations stated in Section A.4. As some processes yield a linear change in the target variable, for example a warm-up of the system with a constant heat flux, the t_{90}-time is selected for quantification. PT1-like processes resulting in a time constant τ as shown in Subsection 3.3.2 are transferred to the t_{90}-notation with Equation 3.3.

Figure 5.2 shows the key stack phenomena and the relevant stack boundary condition dynamics provided by each subsystem in comparison to the required power dynamics. First of all, the targeted time scale for an increase of P_{drive} is displayed. For the highly dynamic operation of a fuel cell dominant vehicle, the targeted dynamics are in the order of 1 s. When analyzing the stack's dynamic behavior with simulations and experiments as done in the previous chapters, five key phenomena can be distinguished: the accumulation and drainage of liquid water, which might hinder the reactant diffusion, a dry-out or humidification of the membrane and the reactant starvation caused by insufficient gas supply.

Accumulating significant amounts of liquid water takes somewhere between tens of seconds to up thousands seconds. This large spread is attributed to the wide span of water production, depending on the electric current drawn from the stack. At very low loads, water accumulation can be endured for much longer, while at high loads water accumulates up to 20 times faster. With respect to the targeted power dynamics, liquid water accumulation proceeds rather slow. Liquid water is drained from the GDL by reaching sufficient gas velocities in the flow field,
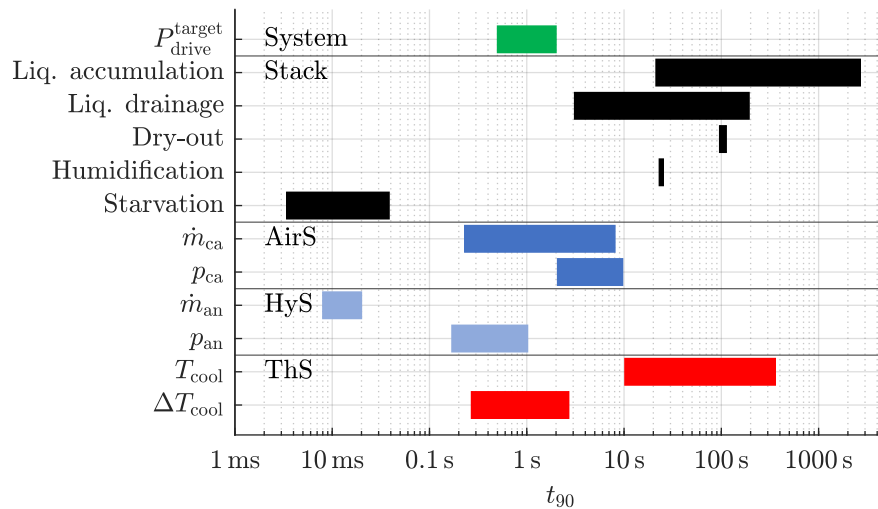
FIG. 5.2 Time scales within the stack and other subsystems in comparison to the targeted power dynamics. For details see Section A.4.

as discussed in-depth in Section 4.5. Draining requires less time compared to accumulation, which is supported by an experiment previously presented in this work: in the AirS switching operation experiment displayed in Figure 4.24, the voltage recovery attributed to drainage is observed to be faster than the decline caused by accumulation. However, even with the fastest achievable drainage, it is impossible to significantly reduce the liquid saturation on the time scale of the targeted power dynamics. This means that the saturation must be kept below the allowed saturation at the highest current $s_{\max}(I_{\max})$ at all times, to enable a highly dynamic current step to full load. The impact of the saturation on the current step capability was discussed in detail within Subsection 3.4.2 and Section 4.6.

As shown with the "Fixed BC" step response experiment described in Subsection 4.4.2, dry-out takes around four times longer than membrane humidification. However, both processes are more than an order of magnitude slower than the targeted power dynamics. A too dry membrane state during low load operation could prevent reaching the full stack power due to high ohmic losses and a correction of the membrane's water content is infeasible on the time scale of the targeted power dynamics. This motivates maintaining a well humidified membrane during low load operation, even though the ohmic loss contribution during this low load operation might seem negligible.

Reactant starvation is a critical state of the stack that can occur rather quickly. If the gas supply in the flow field changes, it impacts the reactant partial pressures at the catalyst layers on the time scale of the reactant diffusion through the GDL as derived in Subsection 3.3.2. The current ramp up therefore must be restricted to the reactant supply dynamics limited by the AirS and HyS. Cathode mass flow dynamics in the order of the targeted power dynamics are achieved with the experimental systems, although the slower System 2 caused a starvation event during a too fast current ramp up as depicted in Figure 4.16. However, the AirS can be switched faster than a dry-out or liquid water accumulation occurs in the stack, enabling the AirS switching operation at constant loads as developed in Section 4.5.

The HyS typically exhibits faster dynamics than the AirS. This is supported by the sine sweep experiment results shown in Figure 4.10, where no relevant phase shift in the anode mass flow occurred within the analyzed frequency range. In comparison, the measured cathode

mass flow supplied by the AirS showed a significant phase shift with respect to its set point, as displayed in Figure 4.9. To maintain a low membrane differential pressure, the anode pressure is controlled to follow the cathode pressure. If this sequence would be inverted, the slow AirS is unable to follow a fast pressure increase in the anode, resulting in high differential pressures. Such high differential pressures might lead to mechanical membrane failure, irreversibly damaging the cells.

Warming up and cooling down the coolant takes rather long, due to the high heat capacity of the stack and the coolant. Substantially changing the temperature on the time scale of the targeted power dynamics is therefore infeasible. If, for example, a low stack temperature during a warm-up phase causes high kinetic losses, full load cannot be achieved. The temperature must be increased first. However, reducing the temperature to counter a dry-out and humidify the membrane might be a viable approach, as the time scales of the phenomena match. The coolant temperature gain ΔT_{cool} between inlet an outlet is controlled by the coolant pump, which can change the coolant mass flow in the order of 1 s. However, manipulating this temperature gain cannot mitigate a starvation which is the fastest stack phenomenon.

5.2.2 Control strategies for highly dynamic operation

From the previous discussion, the following four key points for the control strategy are derived:

1. Starvation occurs orders of magnitude faster than the targeted power dynamics. If the consumption should be increased, the supply must meet the demand at all times. The AirS is the limiting subsystem for this case.
2. Liquid water cannot be drained fast enough to adapt the saturation level to the increased gas diffusion cross-section demand. Therefore, low saturation levels must be ensured during low current operation to avoid drastic concentration losses during a highly dynamic electric current step.
3. Humidifying a too dry membrane just as a load step is requested is infeasible, because the humidification takes an order of magnitude longer than the load step. Therefore, sufficient membrane hydration must be maintained at all times.
4. The coolant temperature must be high enough to allow full load capability at all times, since a temperature increase would be too slow for achieving the targeted power dynamics.

The ability to control the liquid water saturation via the gas flow was demonstrated in Subsection 4.5.4. It is therefore deemed possible to keep the liquid water saturation below the saturation limit of the maximum current at all times, as suggested in Section 4.6. Also, the membrane can be kept well humidified with the original activity-based water management strategy throughout a wide operating range, as shown by the experimental analysis in Subsection 4.4.4. Typical operating conditions between 60 and 90 °C do not prevent the system from reaching its rated current.

However, the first point regarding starvation mitigation is not addressed at all with the original activity-based control strategy introduced in Figure 2.10. The set points for mass flow and pressure are directly adapted to a change in current, but the delayed response of the AirS in combination with a constant current gradient can cause temporary starvation, as shown experimentally in Figure 4.16 and schematically in Figure 5.3. The higher the current, the more partial pressure must be held available within the flow field to enable the higher required reactant flux through the GDL. This is described by the partial pressure limit, shown as

hatched area in Figure 5.3: below the limit, starvation at the catalyst layer occurs.

In principle, two approaches to mitigate the starvation risk are possible: The first option is to maintain a reactant supply cushion resulting in an increased steady-state partial pressure, as demonstrated experimentally in Subsection 4.4.3. While the increased EAC power demand worsens the steady-state system efficiency compared to the standard supply, a limited but theoretically instantaneous current increase becomes feasible. Without a current gradient limitation, starvation might still occur, as shown in the center tile of Figure 5.3. The second option is to limit the current gradient depending on the actually available reactant flows. Then, mitigating starvation becomes possible even without raising the steady-state supply. Both approaches can also be combined to further improve the dynamic capabilities. With a supply cushion, a larger immediate current increase becomes feasible, while the current gradient is then limited according to the available reactant supply.
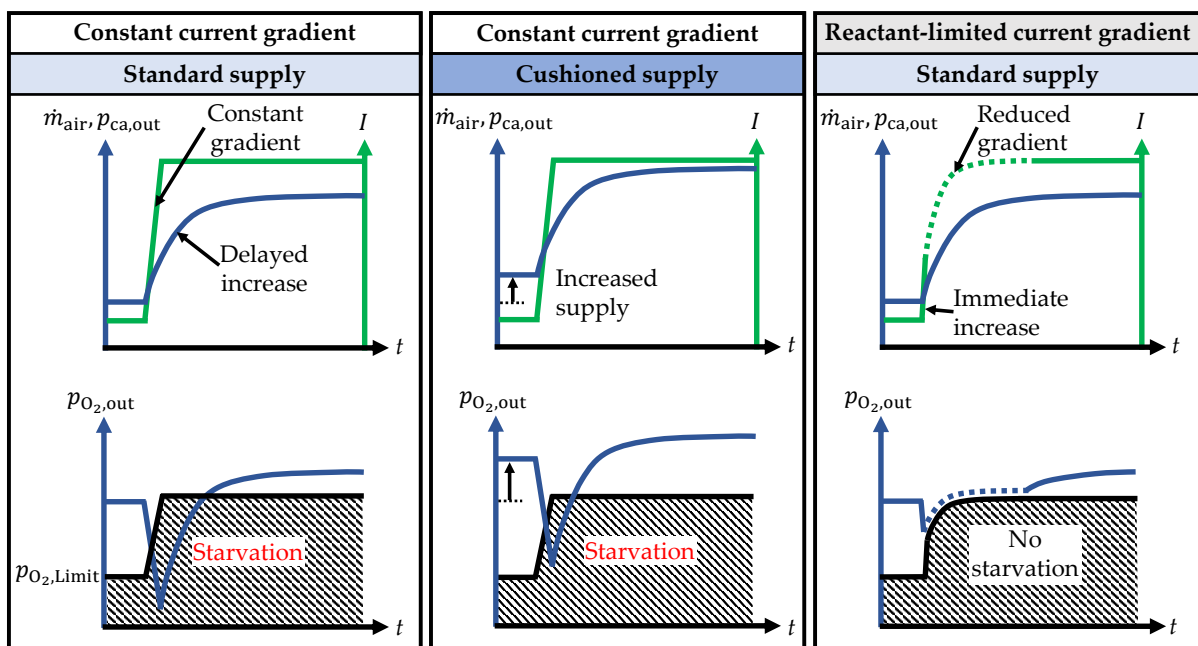
FIG. 5.3   Comparison of the original control strategy, a p_{O_2}-cushion strategy and the reactant-limited current gradient strategy.

For the reactant-limited current gradient strategy, the calculation scheme of the activity-based water management as introduced in Figure 2.10 is reversed. Instead of aiming for a set point of pressure and stoichiometry, the allowed current is calculated based on the actually available air mass flow and pressure so that the oxygen partial pressure remains above a certain limit $p_{O_2,\text{limit}}$. This results in a fast initial current increase, followed by a slower further increase, as shown in the right tile of Figure 5.3. The according calculation procedure is depicted in Figure 5.4. Note that the humidification target a_{target} can be neglected for a couple of seconds, as a dry-out or liquid water accumulation would require a humidification target violation for tens of seconds.

Now that the control strategy is improved for the highly dynamic operation, multiple architectures are selected. As previously discussed, starvation is the critical phenomenon and the limiting subsystem is the AirS. Therefore, the following analyses are focused on the AirS, starting with existing architectures. Afterwards, several architectures are selected and compared with respect to their dynamic capabilities and efficiency.
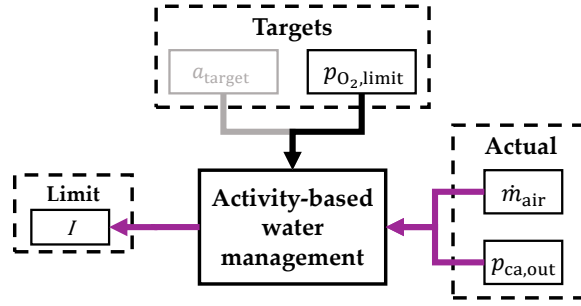
FIG. 5.4 Reactant-limited current gradient strategy to restrict the current increase in highly dynamic operation.

5.3 Architecture Selection

5.3.1 Analysis of Existing Architectures

A variety of FCEV models from different manufacturers is available on the market, although the total produced number of these vehicles is still rather low. Two of the latest models in the passenger car segment are Toyota's second generation Mirai released in 2020[151] and Hyundai's Nexo introduced in 2018[152]. Their predecessors, the first generation Toyota Mirai and the Hyundai ix35 Fuel Cell date back to 2014[153] and 2013[154], respectively. Mercedes-Benz introduced their plugin-hybrid FCEV GLC F-CELL in 2019[155]. Honda produced the FCX Clarity from 2008[156] on, and the later model Honda Clarity was first delivered in 2017[157]. Most recently, the pilot fleet of BMW's iX5 Hydrogen entered operation[158].

Table 5.1 displays the main features of six FCEVs that entered series production. As the AirS is the limiting factor for the dynamic operation and its compressor's power demand dominates over the other balance-of-plant components, the analyses in this work is focused on the AirS. In addition, the flow configuration of the cells integrated in the vehicles is shown, as it is known to affect the cell-internal humidity distribution[41].

TABLE 5.1 Architecture features for ● Vehicle 1, ● Vehicle 2, ● Vehicle 3, ● Vehicle 4, ● Vehicle 5 and ● Vehicle 6

Design choice		Selection			
Compression	Stages	1 ●●●●●	2 ●		
	Type	Centrifugal ●●●●●	Displacement ●		
Expansion	Turbine	None ●●●●●	Yes ●		
	Throttle valve	None ●●	Yes ●●●●		
Conditioning	Cooler	None ●	Air/coolant ●●●●●	Air/air ●	
	Humidification	None ●●	Membrane ●●●●		
Flow conf.	Anode/cath.	Co-flow	Counter-flow ●●●	Cross-fl. ●	Serp. ●
	Coolant/cath.	Co-flow ●●●	Counter-flow	Cross-fl. ●●	Serp.

First of all, the number of compressor stages must be selected. If the stack should be operated at high pressures above ≈3 bar, a single stage compression is most likely insufficient and a second stage must be added. Such high operating pressures are key to enable high temperature operation above 80 °C, as the saturation partial pressure exponentially increases and the

relative humidity is significantly reduced. To prevent a membrane dry-out, raising the total pressure is an adequate solution especially for systems without external humidification. The temperature-pressure dependency is incorporated in the activity-based water management strategy introduced in Subsection 2.3.4.

Two types of compressors are integrated in the known systems: radial centrifugal compressors and Roots-type displacement compressors. Centrifugal compressors are limited towards low mass flows and high pressure ratios by the surge line and towards high mass flows and low pressure ratios by the choke limit. If the surge limits is violated, the compressor operation becomes unstable, possibly resulting in component damage. The choke limit does not result in unstable operation, but restricts the achievable pressure and mass flow combinations. In contrast, displacement compressors such as the common Roots-type are not exhibiting these operating limits and are therefore preferred if low mass flows and medium to high pressure ratios should be delivered. In the analyzed vehicle architectures, single stage centrifugal compressors are predominant.

The compressed exhaust gas carries a certain enthalpy flow, that can be recuperated with a turbine. The higher the stack operating pressure becomes, the more turbine power can be harnessed to decrease the electric power demand for the compression. With such an architecture, high pressure operation of a stack becomes more efficient. A throttle valve in the exhaust path might be utilized to set stack operating pressures well above ambient. In addition, a stack bypass further increases the achievable mass flow and pressure combinations at the stack. As shown in Table 5.1, the throttle valve is omitted only in ●Vehicle 3, that operates the stack close to ambient pressure. It is also avoided in ●Vehicle 6, where a turbine is installed to recuperate exhaust enthalpy.

If the inlet air is compressed, its temperature rises. This might result in an air temperature too high to be directly fed into the stack. Then, a cooler needs to be added. Cooling the cathode inlet air is almost always required due to the selected stack operating pressure in the vehicles and is usually achieved with an efficient, low-volume gas-liquid cooler. Depending on the selected temperature levels, a low-temperature coolant circuit in addition to the stacks high-temperature coolant circuit might be necessary. This is one example of the interdependency of subsystem architecture choice.

Low membrane humidity occurs when the air's relative humidity and/or the produced water flux is rather low. Dry-out not only reduces the protonic conductivity and therefore the cell voltage, but also exposes the membrane to increased mechanical stress caused by possible shrinking/swelling cycles. To mitigate these risks, the inlet air can be humidified upstream of the stack. Different concepts are employed for that task, the most common one being membrane humidifiers, which recirculate water from the wet exhaust gas stream using a semi-permeable membrane. Membrane humidifiers are not only adding volume and cost but might also age significantly, sometimes even faster than the stack, as they are facing the challenging dry operating conditions. The vehicle comparison in Table 5.1 shows that humidification of the cathode inlet air is mostly done with a membrane humidifier. Two vehicles feature no humidification at all, resulting in a cheaper, less bulky system.

When it comes to the cell design, various flow configurations of the coolant, anode and cathode paths might be selected. A co-flow of anode and cathode is not relevant in application, especially in systems without external humidification. In non-humidified systems, the internal water recirculation of the wet anode outlet humidifying the dry cathode inlet is a key for homogeneous humidification. A co-flow setup may however be chosen for research

purposes[28] to reduce the water transports' complexity. The anode gas can also be set to flow against the cathode flow direction, the predominant setup in series vehicles, as displayed in Table 5.1. From a water management centered point of view, this concept is beneficial to achieve a homogeneous humidity distribution, even with a low or no stack-external humidification of the cathode gas feed. The relatively dry cathode inlet region lies opposite to the wet anode outlet, while the wet cathode outlet region is opposite to the drier anode inlet region. An internal circulation of water results from the humidity gradients, effectively sustaining high membrane water content levels across the whole cell[44], as also shown with the simulation model in Section 3.4. Other, less common flow configurations are a cross-flow or serpentine flow of the anode.

For the coolant flow direction, the co-flow configuration with respect to the cathode is most common, as shown in Table 5.1. While product water is added into the cathode gas stream and oxygen is consumed, the relative humidity rises from inlet to outlet. To achieve a relative humidity close to saturation for an ideally wet membrane without large amounts of liquid water occurring in the GDLs across substantial regions of the cell, a rising temperature along-the-channel is preferable. This is achievable with a co-flow setup between coolant and cathode, the dominant approach in the analyzed systems. Other flow configurations might be a result of optimizing the stack volume by distributing the ports around the whole cell, resulting e.g. in cross-flow configurations. Note that no information on the flow configuration in ⬤Vehicle 6 is available to the author.

A similar analysis was conducted for the other subsystems, namely HyS and ThS, but is described only briefly due to this work's focus on the AirS-stack interaction. The HyS in state-of-art FCSs always features an anode loop, where unreacted hydrogen and water is recirculated. This allows for an over-stoichiometric operation of the anode, mitigating the risk of local fuel starvation and reducing losses of precious fuel, while humidifying the anode inlet gas stream. Two components are predominantly implemented to achieve the recirculation: a jet pump, a passive device utilizing the high tank pressure, and an active ARB. As the jet pump operation is restricted by sub-critical flow towards low flow rates[159], it is sometimes complemented with an ARB for these operating conditions. In other approaches, only one of the two devices is implemented to limit complexity and cost. To purge nitrogen gas diffusing through the membrane and accumulating in the loop, valves are implemented to periodically expel too nitrogen-rich recirculate gas. Possibly occurring liquid water may be drained via a separate valve or together with the gas phase in a combined purge/drain valve. The analysis showed no clear trend towards a favorable solution, suggesting that additional effort needs to be spend on finding an optimal HyS for the vehicle application.

A typical ThS in series vehicles consists of more than one coolant circuit, operating at different temperature levels. They are connected with multiple radiators to transfer the heat to the environment and avoid too high temperatures within the system. Especially during low speed driving at high loads, as for example in a hill climb scenario, fans might be needed to increase the heat transfer to the ambient air. Especially for a freeze start of the system, external heaters are sometimes included in the stack's coolant circuit to heat-up the stack in a so called assisted freeze start. However, if the freeze start is achieved solely by utilizing the stack's heat output, the external heater is omitted to save system cost and volume.

5.3.2 Definition of reference architectures

Based on the previous analysis of existing architectures in series vehicles, three reference architectures are now defined for further insights. Recall that this work's goal is not to find an optimal architecture but rather to showcase the impact of architecture choice on the dynamics and efficiency trade-off in scope of RQ4. Therefore, one architecture with a focus on dynamics and another one aiming at high efficiency are selected in addition to a state-of-art architecture. The "Baseline" architecture is close to the existing systems, featuring a single stage radial compressor, a stack bypass, a cooler and a throttle valve as shown in Figure 5.5. Instead of the radial compressor, a Roots-type displacement compressor is utilized in the second, dynamic-oriented architecture. Although the Roots compressor exhibits a higher moment of inertia, it requires lower speeds for a given pressure and mass flow. As the rotational energy grows linearly with the moment of inertia but quadratic with rotational speed, utilizing a Roots compressor typically results in faster air supply dynamics[160]. All other components remain the same compared to the "Baseline" architecture.
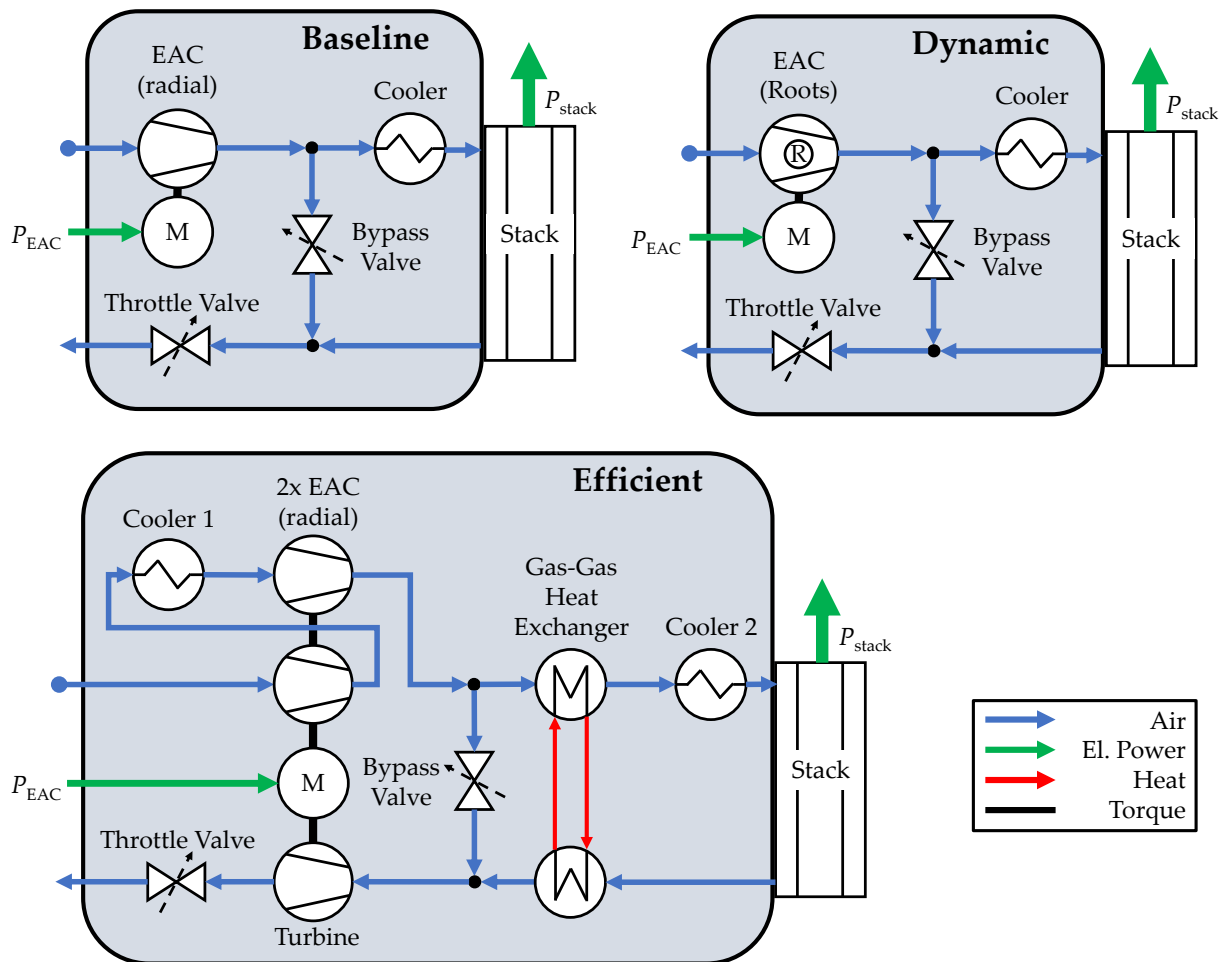
FIG. 5.5 Setup of the three selected AirS reference architectures.

The third architecture aims at achieving a higher system efficiency. Subsequently, a two-stage compression with an intermediate cooler is implemented. The cooler reduces the compressor inlet temperature of the second stage, decreasing the compressor's power demand for a given pressure ratio. A turbine is attached to the same shaft as the two compressor stages and the

electric motor. It partially utilizes the exhaust enthalpy flow to reduce the electric power demand for compression. In addition, a gas-gas heat exchanger transfers heat from the compressed inlet air into the exhaust gas stream. As the turbine inlet temperature is raised, its shaft power increases. Such a heat exchanger is not integrated into one of the existing systems, but a previous work showed potential system efficiency gains of up to 2.2 %[161]. To avoid too high cathode inlet temperatures, a second cooler is integrated as in the other architectures.

Note that none of the architectures feature a humidification component. Omitting the common membrane humidifier reduces volume and cost and is therefore beneficial for the automotive application. Experimental results acquired with the non-humidified systems presented in this work as well as the performance of ● Vehicle 2 and ● Vehicle 5 prove the feasibility of such an approach. For dynamic operation, a humidifier is expected to have negative impact: the additional volume delays the mass flow and pressure increase observed at the stack inlet. Also, the humidification of the inlet air by the exhaust gas is delayed. Assuming a similar dynamic behavior as for the membrane humidification process in the stack, it takes tens of seconds until the beneficial effect of a humidified inlet air kicks in. This is at least one order of magnitude too slow to significantly impact the dynamic response towards a highly dynamic load increase. The stack flow configuration is selected to be the same for all architectures. A counter-flow between anode and cathode as well as a co-flow between coolant and cathode is chosen. Now that the reference architectures are defined, it follows a closer look at the simulation study as the centerpiece of this chapter.

5.4 Simulation Study

5.4.1 Test cases

First of all, the test cases are introduced starting with the electric load profile. It is rather complex to derive the stack current trajectory from widely used drive cycles as displayed in Figure 5.6. Drive cycles are usually stated as a velocity versus time trajectory of the vehicle. A vehicle model is necessary to estimate the required drive-train power to overcome the friction and air resistance at the given velocity. Then, a power split model balancing the electric power share supplied to the drive-train by the FCS and/or the battery must be integrated. Finally, the appropriate current is selected for example by employing a polarization curve model. As vehicle and power split modeling are out of scope of this work, the focus lies on a variation of the current trajectories. This approach results in the same hydrogen consumption, but different system net powers between the test cases. However, it allows to avoid a costly and complex iteration between the current trajectory and FCS power.
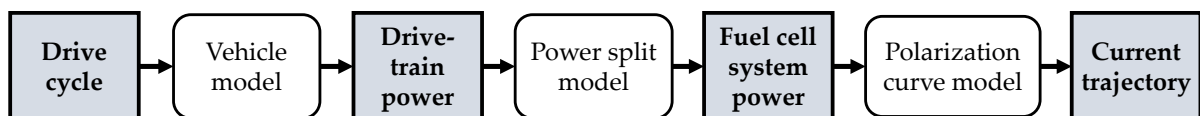
FIG. 5.6 Required power flow down from drive cycle to fuel cell stack level.

Two scenarios are analyzed in the following, one targeting the dynamic behavior and the other one aiming at the system efficiency. An overview of the test cases is displayed in Figure 5.7.

To quantify the dynamic capabilities, a step-like increase in current is simulated with the different architectures. The maximum current increase achievable with each architecture is selected, starting from 10 % rated current to up to 90 % rated current. Currents below the lower or above the upper limit could not be accomplished with all architectures due to component restrictions, especially the surge line of the turbo compressor. With the short duration of the load step and the minor impact on the overall energy consumption, this test case is however insufficient to quantify the system efficiency.

Therefore, a load cycle is simulated to calculate the efficiency. Note that load cycles on the other hand are chosen in a way that a human driver can reproduce it with sufficient accuracy at a vehicle test rig. Because of that, a load cycle requires only limited dynamics and is not suitable to evaluate the achievable dynamic response. The current trajectory resulting from the drive cycle was derived by colleagues based on a vehicle model, a power split model and a polarization curve model as shown in Figure 5.6.
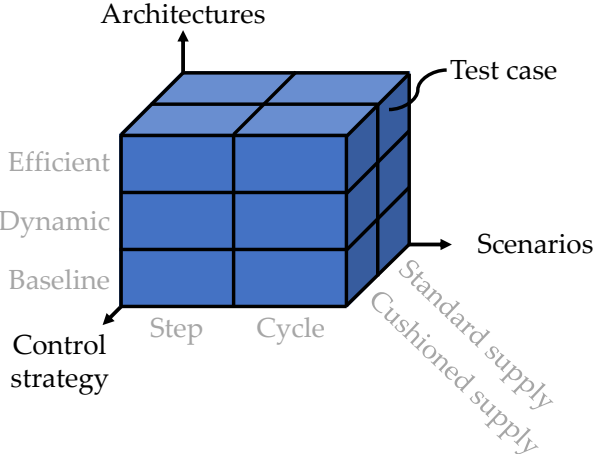
FIG. 5.7   Three dimensional variations of the selected test cases.

For each of the three reference architectures introduced in the previous section, the impact of the control strategy is also analyzed, as shown in Figure 5.7. Because the original activity-based water management strategy might cause starvation, the reactant-limited current gradient strategy derived in Subsection 5.2.2 is coupled with the p_{O_2}-cushion approach: In one supply variant, the oxygen partial pressure is picked close to the steady-state system efficiency optimum, a selection referred to as standard supply. In the second, dynamic-oriented variant, a partial pressure cushion is added. Note that increased currents require generally higher flow field partial pressures to avoid starvation, as an increased diffusive reactant flux across the GDL is required. The resulting partial pressure targets for both variants are displayed in Figure 5.8. In addition, an exemplary starvation limit is displayed, below which reactant shortage at the catalyst layer is expected.

Note that the exact position of the limit is not only current-dependent, but also heavily impacted by the liquid water saturation. As demonstrated experimentally and discussed in-depth in Section 4.6, a higher liquid water saturation within the GDLs is allowed during low current operation. But as the current is increased quickly and the liquid water is being drained with a certain delay, it might potentially cause reactant starvation. It is possible, that the partial pressure limit derived from the actual saturation state in an allowed steady-state low electric current operating point lies above the partial pressure limit derived at a lower saturation for higher current steady-state operation. Such a scenario would prevent highly
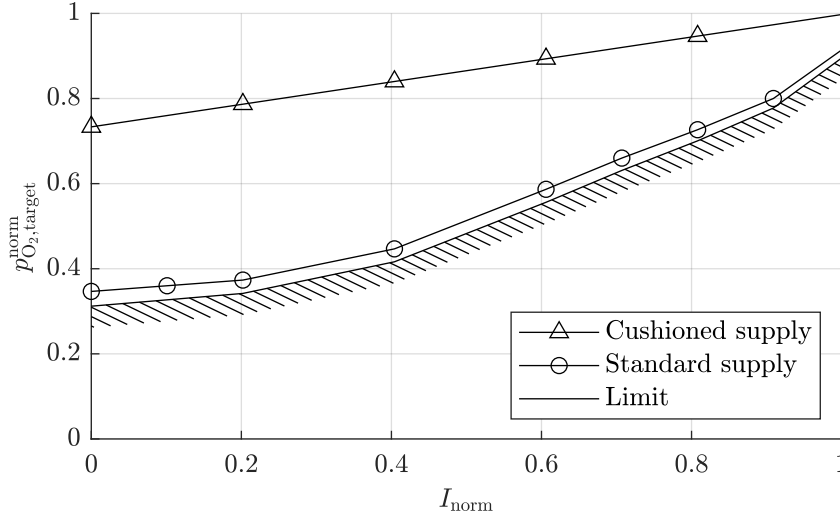
FIG. 5.8 Normalized cathode outlet oxygen partial pressure target for the efficiency-oriented standard supply, the dynamic-oriented supply with cushion and an exemplary starvation limit depending on current.

dynamic operation, or require the flow field partial pressure to be raised above the steady-state target of the high current operating point to compensate the lower cross-sectional area available for diffusion.

5.4.2 Modeling setup

Two simulation models need to be coupled to answer RQ4, targeting the architecture and control strategy dependent efficiency and dynamics trade-off. As shown in Figure 5.9, multiple other building bricks from previous analyses are also combined. Because the AirS is the limiting subsystem for the highly dynamic operation, its time-dependent stack boundary conditions must be modeled. In case of the step response, the mass flow and pressure set points at the stack are calculated based on the original activity-based water management. A step-wise increase of the electric current yields an instantaneous rise of the pressure and mass flow set point, which are then fed into the AirS model. Utilizing a simplified stack model representing only the pneumatic characteristics of the stack, the actually achieved mass flow and pressure dynamics at the stack boundary are computed. The reactant-limited current gradient strategy for highly dynamic operation, as introduced in Subsection 5.2.2, yields the allowed current trajectory based on the actual mass flow and pressure.

The stack's dynamic response is calculated via the dynamic 2D+1D dynamic cell model developed in Chapter 3. Note that a single cell is assumed as representative for the whole stack. As previously discussed, the HyS is able to adapt the anode inlet conditions an order of magnitude faster than the targeted power dynamics and is therefore not modeled in detail. Instead, it is assumed that the anode mass flow is adapted lag-free to the electric current, while the pressure follows the cathode's pressure trajectory. In the experiments reported in Chapter 4, the well controlled ThS provides a constant coolant temperature with a maximum deviation of only 2.5 K. It is therefore assumed, that the ThS is able to provide a constant coolant inlet and outlet temperature to the stack. In conclusion, only the AirS must be modeled in detail, while the HyS and ThS dynamics are of negligible relevance to answer RQ4.
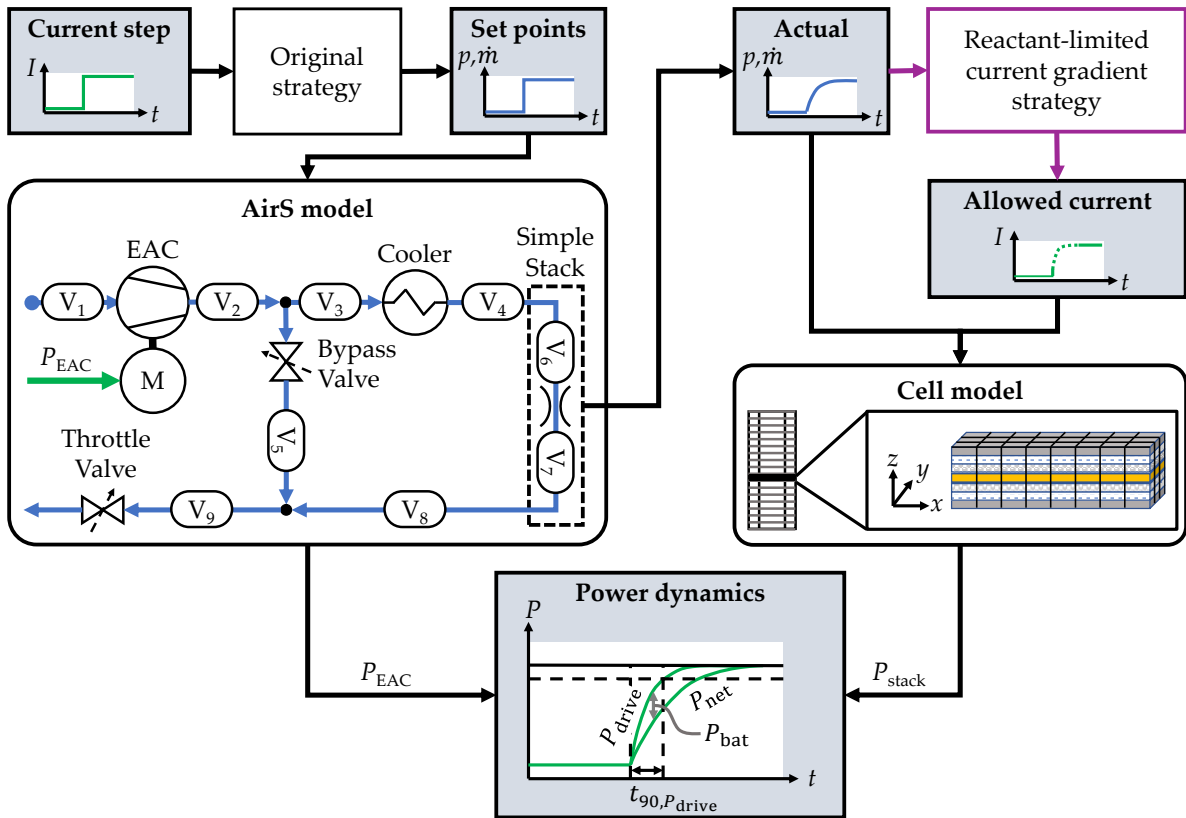
FIG. 5.9 Schematic coupling of the simulation models.

The power dynamics at system and drive-train level are then calculated by using the stack power P_{stack} and the compressor power P_{EAC}. The battery capable of supplying up to 30 kW provides power only during the transient. It is controlled in a way, that a PT1-like drive-train power P_{drive} trajectory is achieved, as discussed in Subsection 2.2.2. Then, the dynamics criterion $t_{90,P_{drive}}$ is evaluated. The efficiency calculation based on a drive cycle simulation does not require the strategy for highly dynamic operation limiting the current. However, the rest of the modeling setup remains the same as in the step simulations aiming at the dynamics quantification. As the general setup is defined, the following subsection explains the relevant details of the AirS model. The dynamic 2D+1D cell model was already discussed in Chapter 3.

5.4.3   Air system model

The AirS model shown in the according box in Figure 5.9 is implemented in GT-Suite, a multi-physics system simulation software developed by Gamma Technologies, LLC. EAC and turbine sub-model include a compressor and turbine map, respectively. These maps feature the isentropic efficiency depending on the operating condition as well as choke and surge limits. In addition, the rotor's moment of inertia is incorporated to delay the speed up realistically. The motor driving the EAC is assumed to provide a constant moment across the whole rotational speed envelope utilized in the step with a constant electric efficiency of 90 %. As the Roots compressor requires lower rotational speeds, the motor is adapted to achieve comparability: The maximum moment M_{max} is scaled, so that the same power P_{max} is required at the maximum respective rotational speed n_{max} as depicted schematically in Figure 5.10. For both motors it is assumed that the maximum electric power is 30 kW, resulting

in shaft powers of 27 kW.
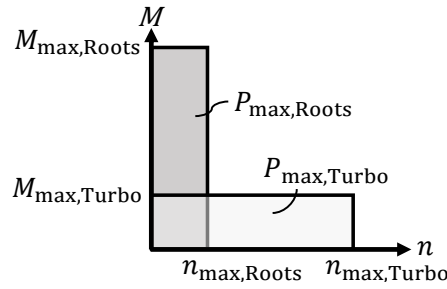
FIG. 5.10   Electric motor scaling for the Roots and turbo compressor.

The coolers are simplified to a volume and a pressure loss. It is further assumed that the liquid side is controlled in a way that results in nearly constant gas temperatures. For the gas-gas heat exchanger implemented in the efficiency-oriented architecture, an detailed offset strip fin heat exchanger model from a previous master thesis is integrated[161]. The stack's pneumatic behavior is resembled in a simplified way via two volumes, V_6 and V_7, with a throttle in-between. To adapt the stack boundary conditions to the set points, the moment provided to the EAC by the motor and the opening of the stack bypass and throttle valve is controlled. Note that the stack bypass is especially needed to avoid a surge at the turbo-compressor: bypassing the stack reduces the downstream pressure loss and mitigates the surge. To reduce the computational effort of the 2D+1D dynamic cell model, a grid convergence study was carried out, resulting in a selected spatial discretization of the cell into 16 segments[150]. With the coupled modeling setup, the simulation study is conducted and the results are discussed next.

5.5   Results

5.5.1   Dynamics comparison

So how do the three architectures perform in terms of dynamics? The simulated pressure and mass flow trajectory provided by the three system architectures is displayed in Figure 5.11. With the standard supply, lower pressures and mass flows in both stationary operating points are set. Note that especially the desired pressure change Δp between the initial low current point and the final high current point is larger in the standard supply cases. This results in longer t_{90}-times with the standard supply for all architectures, as marked by the symbols on the x-axis. As expected, the three architectures yield a different dynamic response. The "Dynamic" architecture provides the fastest pressure and mass flow rise, followed by the "Baseline" architecture. The "Efficient" architecture yields the longest t_{90}-times. This ranking is independent of the supply choice.

Controlling the architectures is challenging, as compressor, bypass valve and throttle valve must be actuated simultaneously. Also, all actors impact both controlled variables, mass flow and pressure. The oscillations in the mass flow trajectories depicted in Figure 5.11 are caused by a non-optimal controller setup. With a further optimized controller setup, the compressor speed t_{90}-times could be reduced further by approximately 8 to 18 %[150]. A similar improvement is expected for the pressure and mass flow dynamics, which are mainly limited by the compressor speed-up. However, even with the non-optimal controllers, all
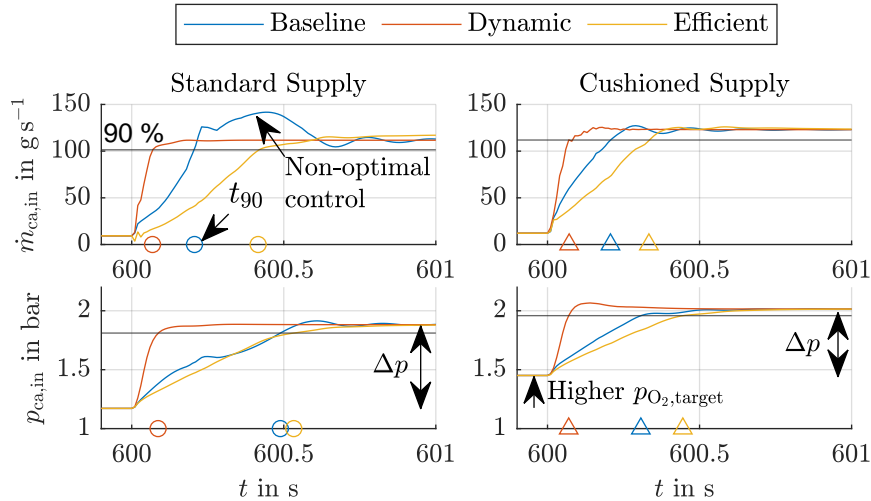
FIG. 5.11 Pressure (top) and mass flow (bottom) trajectories and t_{90}-times of the three architectures with standard supply (left) and cushioned supply (right).

architectures yield a pressure and mass flow adaptation around or below 0.5 s. It should therefore be possible to ramp-up the current in under 1 s without starvation in all dynamic cases.

The reactant-limited current gradient strategy, which is based on the available oxygen partial pressure as introduced in Figure 5.3, results in a two-step increase of the current. An exemplary case, the "Baseline" architecture with cushioned supply, is displayed in Figure 5.12. In the first time step, the current is ramped-up quickly until the partial pressure limit is reached. Then, the current gradient is chosen so that the actual oxygen partial pressure calculated with Equation 2.29 never falls below the limit. Note that the limit changes depending on the current as shown in Figure 5.8. As the new stationary current is reached, the AirS is still transitioning towards its new steady-state supply, resulting in the actual partial pressure rising above the lower limit.
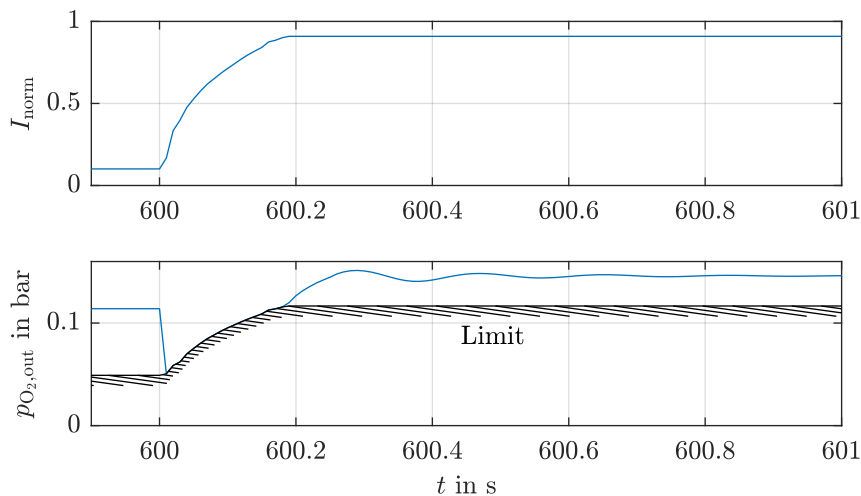
FIG. 5.12 Example of the reactant-limited current gradient strategy for the "Baseline" architecture with cushioned supply

Now the trajectories for pressure, mass flow and current are known. But how does the stack respond? Figure 5.13 displays the time-dependent electric current as well as the resulting cell voltage and loss contributions. The transient spatially resolved phenomena inside the cell during a current step with immediate supply adaptation were discussed in detail within Subsection 3.4.2. In contrast to the case with lag-free reactant supply adaptation shown as dashed lines in Figure 5.13, the delayed air supply adaptation affects only the short-term cell voltage dynamics below 1 s. As expected, the concentration loss contribution during the current increase amplified by the higher initial liquid water saturation is shifted in time due to the delayed current adaptation, and subsequently the resulting cell voltage undershoot is also shifted.

Compared to the starvation event identified at the test rig, the voltage undershoot magnitude is relatively small, similar to the lag-free case. The reactant-limited current gradient strategy therefore successfully ensures that no pronounced voltage undershoot is caused by the delayed AirS's supply. After the undershoot, the membrane's water content increases and liquid water is drained, resulting in a slow relaxation towards the new stationary voltage. One second after the current increase started, the stack voltages in the lag-free and delayed supply cases are identical, as the AirS reached its steady-state supply. A comparable behavior is observed for the other test cases, although the current adaptations and resulting power gradients differ.
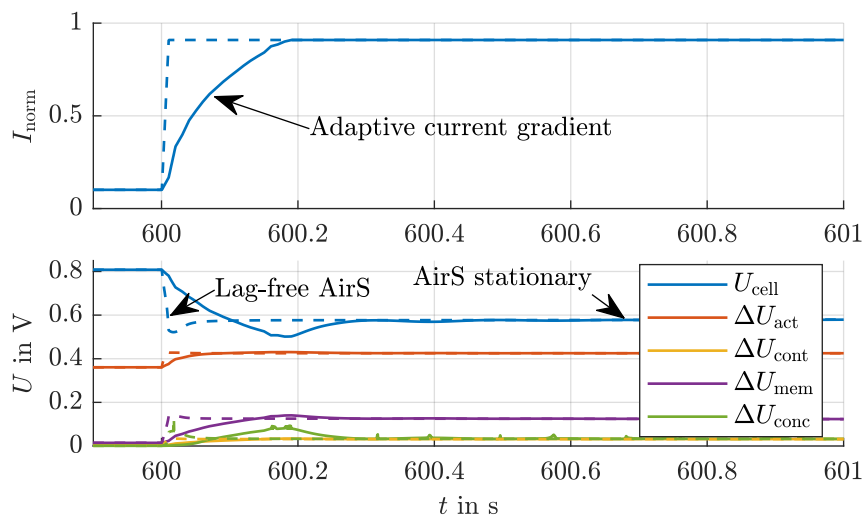
FIG. 5.13 Example of the resulting cell voltage and loss contributions for the "Baseline" architecture with cushioned supply (solid) compared to the lag-free AirS example (dashed) as discussed in Subsection 3.4.2.

To later derive the electric power available to the drive-train, the stack power and the system net power for the three architectures and two supplies are calculated and displayed in Figure 5.14. As expected, the current ramp-up is the fastest for the "Dynamic" architecture, as the mass flow and pressure dynamics provided by this AirS are the highest. Utilizing the cushioned supply instead of the standard supply with the "Efficient" architecture yields a 35 % improvement in the t_{90}-time of the electric current, the highest improvement observed in all architectures. The non-ideal control of the "Efficient" architecture causes a temporary reduction in available oxygen partial pressure in the standard supply case. This behavior was displayed earlier in the according mass flow trajectory in Figure 5.11. Subsequently, the current is slightly reduced in the first time step by the reactant-limited current gradient

strategy.
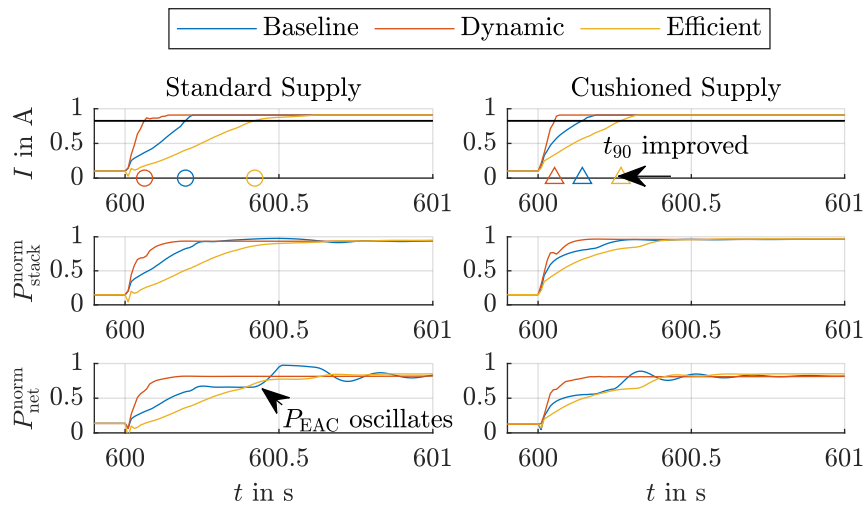
FIG. 5.14 Current increase (top), resulting stack power (middle) and system net power (bottom) of the three architectures with standard supply (left) and cushioned supply (right).

Comparing the stack power trajectories fits the previous observations: The faster the current can be increased without risking starvation, the faster the stack power rises. As intended, the stack produces the same steady-state power independent of the architectures. As shown in Figure 5.15 the cushioned supply results in higher stack powers due to the increased oxygen partial pressure. But this advantage is overcompensated by the higher required EAC power, leading to slightly lower stationary system net powers. At the final point, the turbine in the "Efficient" architecture provides additional power, raising the system net power by 3.3 % compared to the "Baseline" architecture when using cushioned supply. A further discussion on the system efficiency comparison is focus of the next Subsection 5.5.2.
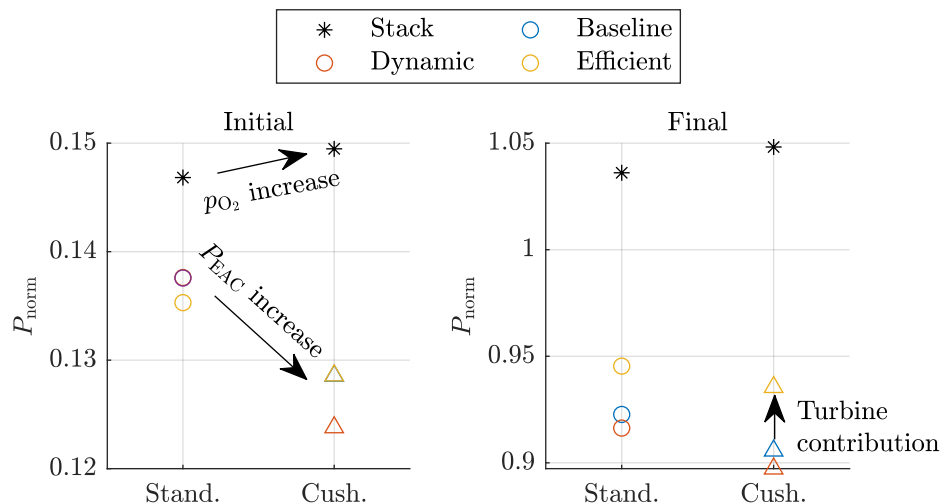
FIG. 5.15 Comparison of the stationary stack and system net power before (left) and after (right) the current increase. The blue and red circle as well as the blue and yellow triangle overlay in the left diagram.

Note that only the dynamics in the order of 1 s are depicted in Figure 5.14. After the displayed

time frame, the stack voltage relaxes significantly slower, on the time scale of tens of seconds, towards its new stationary value. This process is unaffected by the different AirS, which have already reached their mass flow and pressure steady-state below 1 s. Unfortunately, the slow stack-limited voltage relaxation delays achieving 90 % of the stationary stack power especially in the "Dynamic" case. But as the "Baseline" and "Efficient" architectures exhibit a stack power overshoot due to oscillations caused by the non-ideal AirS control, no meaningful t_{90}-times can be derived for stack and net system power. The net power trajectory is also influenced by the oscillating EAC power, most notably in the "Baseline" architecture with standard supply.

Now, the fuel cell net power is combined with the battery's power. The battery can provide a maximum electric power of 30 kW and is controlled so that a smooth PT1-like drive-train power is available. Figure 5.16 showcases the trajectories of the system net power and the drive-train power, exemplary again for the "Baseline" case with cushioned supply. The marker at the x-axis depicts the t_{90}-time of the drive-train power. As expected, the battery helps to further reduce the t_{90}-time, while smoothing the power available to the drive-train and perceptible by the driver. In both steady-states, the battery is not active. For the final operating point, the moment where system net power equals drive-train power is out of the displayed time frame, as the stack voltage relaxes slowly. As high power from the battery is only required for some seconds, even a low capacity battery is able to provide the energy required in this scenario.
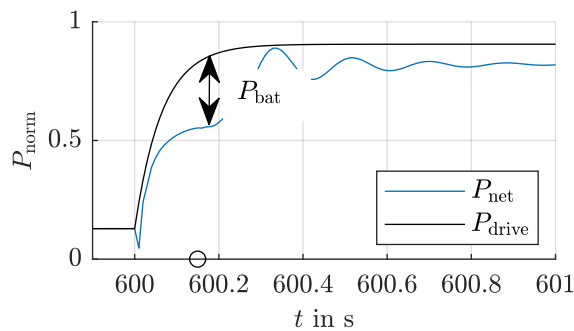
FIG. 5.16 System net power and drive-train power trajectories.

Lastly, the t_{90}-times of the central variables in the different cases are summarized in Figure 5.17. Note that all test cases yield faster drive-train power dynamics than common ICEs, which exhibit time-to-torques between 1 s and 3 s[9,10]. The fuel cell systems' dynamics in the selected cases are comparable to the dynamics of advanced ICE concepts with an electrically assisted turbocharger, that achieve time-to-torques between 0.45 s and 0.95 s[9].

As discussed earlier, the "Dynamic" architecture provides the fastest mass flow and pressure dynamics, allowing for the highest current dynamics. Utilizing a cushioned supply allows to increase the current dynamics even further, most notably for the slowest "Efficient" architecture. A cushioned supply enables the "Efficient" architecture to achieve drive-train power dynamics comparable to the "Baseline" architecture with the standard supply. However, as shown in Figure 5.15, the "Efficient" architecture provides a higher net power compared to the "Baseline" architecture with standard supply at high electric currents. Within the upcoming subsection, a detailed analysis of the system efficiencies depending on architecture and control strategy is conducted to complete the dynamics versus efficiency trade-off.
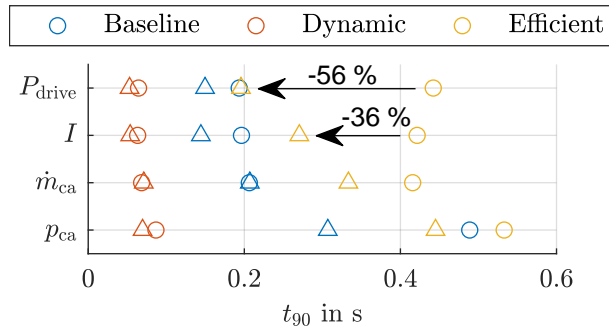
FIG. 5.17 Comparison of t_{90}-times for the three architectures and standard supply ($\circ$) or cushioned supply ($\triangle$).

5.5.2 Efficiency comparison and trade-off with dynamics

The second goal of this chapter is to analyze the system efficiencies. To evaluate these for the three architectures, operating with standard or cushioned supply, a load cycle is utilized. As discussed in Subsection 5.4.1, it is a complex task to derive the current trajectory of the fuel cell stack from a given load cycle defined in terms of vehicle velocity. In this work, a simplified approach is implemented. A fixed current trajectory is used for all architectures. This results in the same hydrogen consumption in all cases, but in varying system net powers and subsequently system efficiencies. This method does not require an iteration of the current trajectory to achieve the same system net power, but is also capable of displaying the discrepancies between each simulation case. The current trajectory shown in Figure 5.18 is derived from a well-known passenger car cycle, the WLTC. Note that this cycle mainly features low load operation and the maximum electric current occurring is only about 40 % of the rated current. The cycle shown in Figure 5.18 is also slightly shorter than the full WLTC, as multiple standstill phases are neglected for the further analysis. The standstill phases are assumed to yield no impact on system efficiency, as the system is idling with negligible hydrogen consumption.
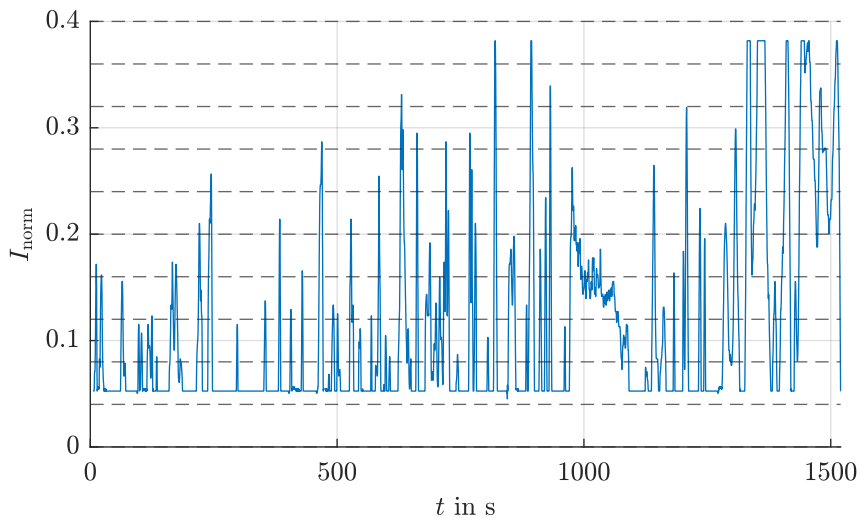
FIG. 5.18 Current trajectory of the drive cycle. The dashed lines bound the ten current regions for further analysis.

111

Next, the coupled AirS and stack model are run. In case of this rather low dynamic load cycle, the reactant-limited current gradient strategy is not necessary to avoid starvation states. In Figure 5.19, the mean system efficiencies in ten current regions are shown for the three architectures and two supplies. Generally, higher currents cause increased activation and ohmic losses, resulting in decreasing stack and subsequently system efficiency. At the lowest currents, the EAC's power demand share can sometimes increase substantially leading to a declining system efficiency. This behavior is observed in case of the "Baseline" and "Dynamic" architectures with cushioned supply. The "Efficient" architecture operating with cushioned supply on the other hand exhibits its maximum efficiency within the lowest analyzed current region. Note that no data is available in the lowermost current region, as it is not included in the current trajectory displayed in Figure 5.18.
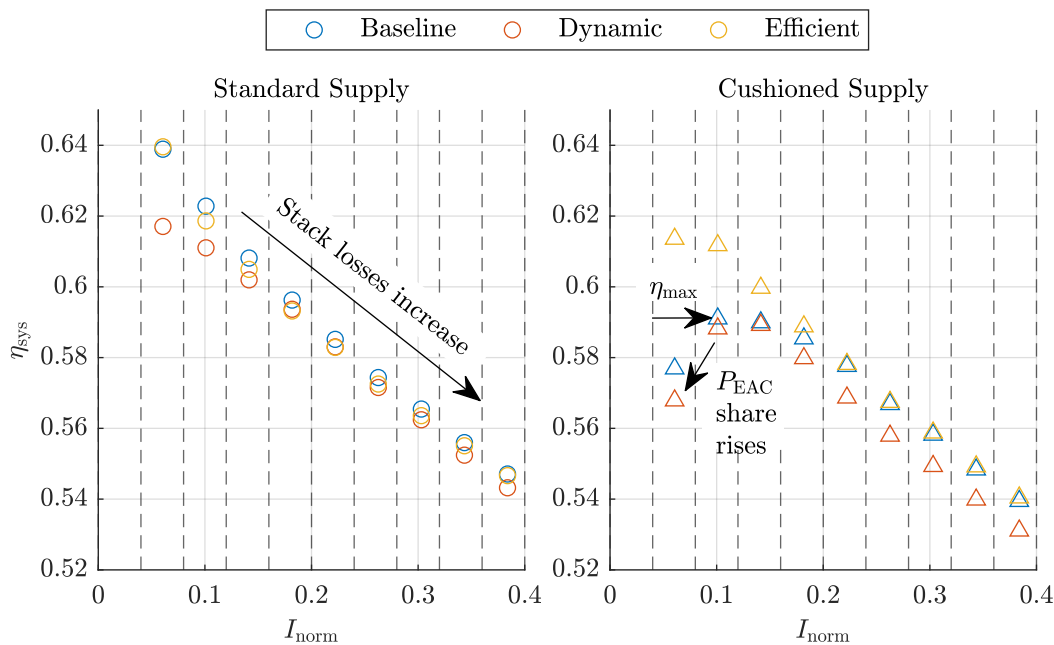
FIG. 5.19 Comparison of mean system efficiency in ten current regions for the three architectures and standard supply or cushioned supply.

The highest overall efficiency is achieved in almost all current regions with the "Baseline" architecture operating at standard supply. Only within the lowest current region analyzed, the "Efficient" architecture exhibits a marginally higher efficiency. However, it is expected that at high currents not included in the load cycle, the "Efficient" architecture yields higher efficiency gains. The stationary load comparison discussed within the context of Figure 5.15 showcased a net power and efficiency gain by 2.5 to 3.3 % of the "Efficient" architecture compared to the "Baseline" architecture, when operated at 90 % of the rated electric current.

Finally, the full cycle efficiency $\eta_{\text{sys}}^{\text{tot}}$ is calculated via Equation 2.19. Now the trade-off between the KPIs drive power dynamics and full cycle efficiency becomes visible in Figure 5.20. As the two KPIs are conflicting targets, no single optimal solution is found. Depending on the weighting of the targets, multiple Pareto-optimal solutions exist. A theoretical but infeasible solution featuring the highest achieved efficiency in combination with the highest dynamics is depicted as utopia point. With the exemplary cases simulated and analyzed previously, three of the six cases fulfill the Pareto-optimality criterion, defining the Pareto frontier. If the dynamics target is weighted stronger than the efficiency target, the "Dynamic" architecture

with cushioned supply is favorable. An intermediate optimal solution, addressing efficiency as well as dynamics would be to operate the "Dynamic" architecture with standard supply. If the system efficiency is in focus, the "Baseline" architecture utilizing standard supply should be selected. The other combinations are unfavorable, as superior solutions exist.
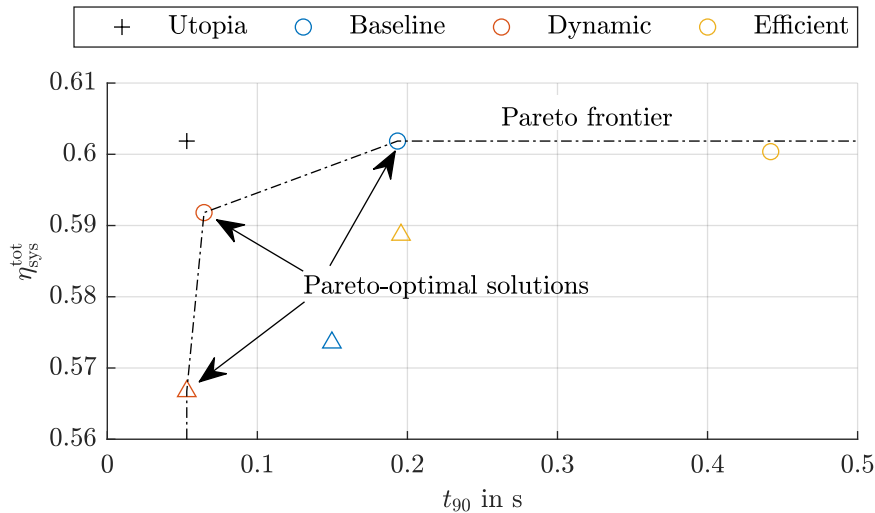
FIG. 5.20 Trade-off between achievable drive-train power dynamics and system efficiency for the three architectures and standard supply ($\circ$) or cushioned supply ($\triangle$).

Note that this outcome depends on the defined simulation cases. If one would change the use-case and subsequently the load cycle for efficiency computation, the position of the solutions in the graph will shift. It is for example expected, that a load cycle featuring a significant share of increased currents favors the "Efficient" architecture. Also, architectures or supply strategies with higher efficiency and dynamics might be found. Finally, the system designer must decide between one of the Pareto-optimal solutions by balancing the conflicting targets. The depiction in Figure 5.20 helps during this decision process, as it answers important questions in the field of RQ4: how much system efficiency must be sacrificed to improve the power dynamics? Which solution should be picked for a certain use-case and target weighting? How far is each solution's performance from utopia?

This analysis concludes the last research chapter, showcasing the importance of the *system level levers* control strategy and system architecture for the trade-off between the KPIs efficiency and dynamics. In the following, the central findings from all three research chapters are cross-linked and put into the context of research available in literature, before a summary and outlook on possible future research topics completes this work.

Chapter 6

Discussion

Throughout Chapter 3, Chapter 4 and Chapter 5, simulation-based and experimental research was presented. Now the three-fold top level goal for *dynamic water management* in the system context is revisited: increasing the system's efficiency and its dynamic capabilities while avoiding critical states. Four research questions were introduced in Subsection 2.4.2 to approach different aspects of the challenging task and pride guidance throughout the work. The following discussion is centered around these research questions, aiming at combining and connecting the insights of the previous chapters. Each research question is therefore answered separately based on the results of this work, while also providing a comparison with literature results highlighting contradictions and potential causes for these mismatches.

6.1 Which water management induced-effects dominate the fuel cell behavior during highly dynamic operation?

In general, the requirements for maintaining a high stack voltage condense down to only two points: keep up the reactant partial pressure at the catalyst layer to avoid concentration losses and sufficiently humidify the membrane for low ohmic losses. However, these targets are competing from a water management point-of-view. A well humidified membrane is achieved by maintaining a high relative humidity within the contacting gas phase. This promotes the accumulation of liquid water in the GDLs, hindering the reactant diffusion towards the catalyst layer. During highly dynamic operation, a steady-state assumption falls short of reality. Two dominant processes are found to shape the fuel cells behavior during the transient states.

The first dominating effect is the sorption, meaning the transfer of water into the sorbed membrane phase, and its counterpart, the desorption. This process is found to be the time limiting phenomenon for changes in the membrane humidity. Although the limitation was identified in the literature and transport models were developed subsequently, the published data scatters over more than three orders of magnitude[40]. The large uncertainty is one reason why a thorough model validation must be conducted. In scope of this work, targeted experiments unveiled the sorption process to be faster than the desorption process, an observation conflicting with literature results[89]. An explanation for these discrepancies might be the experimental setup commonly used for sorption experiments. There, the membrane water uptake is measured in a controlled environment, but without a water producing fuel cell reaction close to the interface. For such simplified setups, the transferability towards cells with ongoing fuel cell operation is shown to be questionable.

The t_{90}-times of the sorption and desorption process found by experiments conducted in scope of this work lie around 25 s and 100 s, respectively. With that, these processes are orders of magnitude slower than the targeted fuel cell system power dynamics around 1 s. The rather

slow dynamics can be taken advantage of by a sophisticated switching operation of the AirS: For a short period, a relative gas humidity too dry for stationary operation can be endured by the membrane, as the dry-out process is slowed by the limited desorption kinetics. On the other hand, a membrane dry-out cannot be corrected within a short period of time, as the water uptake of the membrane is limited by the sorption process. Therefore, a sufficient membrane humidification also during low load operation is a key to enable highly dynamic load increases without large membrane losses.

The second important process is the transport of the liquid water into and out of the porous layers. It is undisputed in the literature that the liquid water saturation interacts with the gas diffusion and potentially causes concentration losses. However, a large portion of fuel cell models neglect not only the dynamic accumulation and drainage of liquid water, but also the existence of liquid water in the porous layers as a whole[67,71,162]. This is often done to reduce the models' complexity and might be acceptable for some research questions. In the context of highly dynamic operation however, this simplification is insufficient. Liquid water is present within the fuel cell during normal operation at nearly all loads. While its presence might not have a measurable impact on the cell voltage especially at low currents, it must not be ignored in case of a highly dynamic operation

As shown experimentally in this work, high liquid water saturation levels can be endured at low loads. If the current is increased fast and the water saturation level is too high, the present liquid water causes an immediate non-linear drop of the measured cell voltage. In such a case, the cell is incapable of a current step. In an extreme scenario analyzed in this work, the saturation level could be set so that a current increase of only 7.5 % starting from a stable operating point triggered a massive voltage drop of 55 % in single cells induced by local starvation.

In general, the commonly-used term of flooding, referring to a liquid water built-up and blocking of the constant reactant supply should be refined. High concentration losses as the key outcome of flooding can also be induced dynamically by a rapid increase of the reactant consumption, even if the liquid water saturation remains the same. The concentration loss dominated voltage undershoot is then observed on a much smaller time scale in the order of the current dynamics, which can be way below 1 s. In contrast, accumulating liquid water takes typically tens to thousands of seconds depending on the water production rate. It is therefore proposed to generalize the term flooding as a state where the liquid water saturation yields significant concentration losses. This broader terminology does explicitly not only indicate that only the saturation levels are rising while the consumption remains constant, but also that the saturation state limits a highly dynamic increase in consumption. Another possible distinction might be to use the term "flooding" for water accumulation dominated voltage drops and "dynamic flooding" for voltage drops caused by dynamically increasing reactant consumption.

Draining liquid water from the GDLs via the flow fields is critical to control the liquid water saturation. A two-phase flow of gas and liquid water occurs within the flow fields. As several researchers showed, the flow regime and the resulting liquid water drainage depends mainly on the gas velocity[27,130,132]. In an application-like operation assessed in this work, liquid water drainage becomes insufficient especially at low electrical loads, which yield too low gas velocities. The rather slow process of water accumulation allows to drain the water only periodically and endure a certain, non-critical built-up. This is the second enabling factor for the low load AirS switching operation presented in this work.

Reflecting on the methodology, several limitations must be addressed. The simulation model fulfilled the requirements of this work, but the validation procedure could be improved. Ideally, local states such as the current density distribution within the cell should be measured experimentally to compare the results with the models prediction on the redistribution processes during load changes. The dynamic cell behavior observed ex-situ matches the model's prediction well, although uncertainties due to the unavailable spatially resolved data remain. A special challenge poses the liquid water saturation. Unlike the membrane resistance, which can be tracked with high temporal resolution through the *HFR*[129], liquid water saturation cannot be measured easily. Optical fuel cells, X-ray diffraction and neutron imaging are in principle established techniques, but an application onto a full-scale system test rig seems unlikely. Instead, the liquid water saturation is probably best to be measured indirectly via a current variation and an analysis of the voltage signal to derive the limiting current. This has to be done an order of magnitude faster than a potential change in saturation level, ideally below 1 s. Measuring the ex-situ water balance is likely too imprecise, as the errors adding up over time are expected to mask the small changes in saturation. Note that the selected voltage-based approach is unable to resolve where the gas diffusion is hindered by liquid water, be it in the catalyst layer, MPL or GDL of the examined cells.

6.2 How can one utilize transient experiments, what are potential pitfalls and how should the experiments be set up to enable an improved modeling of dynamic fuel cell operation?

Multiple water transport processes, like water diffusion, electro-osmotic drag, sorption and liquid water transport, can only be measured as a whole in a typical ex-situ experimental fuel cell setup. Multiple approaches to separate the individual contributions were described in literature. For example, a specialized setup consisting of a membrane in contact with water and dry nitrogen on each side is used to calculate the diffusion coefficient[82]. Also, step changes in current or voltage were employed by several researchers[124,125,145]. This technique is also utilized in this work to separate the various transport phenomena based on their time-scale. Even with limited spatial resolution, the time dimension carries valuable information.

Phenomena such as the dry-out and re-humidification can be deliberately targeted with specifically designed experiments. Close attention must be paid to the exact experimental setup, as shown by multiple experiments in scope of this work. Depending on the procedure, different modes with similar qualitative response behavior but vastly diverging time constants are observed. These are either dominated by dynamic changes in membrane humidity, gas supply or operating temperature[46]. For application, the gas supply dominated mode is the most important one, as membrane humidity and temperature can be controlled with only minor deviations in automotive fuel cell system operation. Analyzing this gas supply dominant mode requires high-performance, application-like air supply capabilities reacting within seconds. The common short stack test rigs are incapable of providing such dynamic changes in the gas supply. While current steps with constant gas supply yield insights into the dry-out and re-humidification dynamics valuable for simulation model parametrization, they are not easily transferable towards the application. The gap towards application must be bridged by application-like, high-performance fuel cell system test rigs.

Pin-pointing the gas velocity and current dependent liquid water drainage limit is also achieved via targeted experiments. While the exact spatial distribution and flow pattern is not identified directly, as in specialized setups[96,130], a water saturation built-up is identified via voltage drops of some of the cells within the stack. The dynamic 2D+1D model is parametrized with a limited set of five experiments: dry-out and humidification cycles, stationary water balance and polarization curve measurements, current steps with gas supply adaption and the drainage limit experiment. It is expected that the model developed in this work can be easily transferred to other stacks, simply by re-parameterizing it with data from such experiments.

A novel experiment, previously not presented in literature to the best of the authors knowledge, is also introduced in this work: a sine sweep of the electric current in an application-like experimental fuel cell system. In contrast to the established EIS-technique[140], the subsystems implemented in hardware at the system test rig are actuated to adapt to the changing current. This enables a frequency-domain analysis of various signals, such as pressures and mass flows of air and hydrogen, enabling a precise quantification of the phase shift and dampening behavior. Potentially critical mismatches in time scale as well as resonances and insufficient controller behavior can be identified early on. Although the interaction of the complex dynamically changing boundary conditions on the stacks internal behavior is not fully understood yet, the presented approach showed several benefits for future system development: Identifying the system characteristics early in the development process helps to reduce the time-to-market, mitigating the risk of unwanted resonances occurring later in the development and providing valuable data to parametrize and validate dynamic system models.

As already touched on in the discussion of the previous research question, some improvements in the measurement setup could be done. Especially measuring the current density distribution within the stack operated in the experimental system is expected to yield additional insights into the dynamic humidification state evolution, as specialized stand-alone experiments suggest[28]. For the gas velocity limit identification, a higher resolution in the individual cell voltages would be beneficial. In the presented setup, every cell close to the top and bottom of the stack is probed separately, but the middle cells are monitored in pairs of two. With a completely individual cell voltage monitoring, voltage drops within single cells could be detected early on also in the middle cells, without noise added by the neighboring cells performance.

If one aims at expanding the operating range in scope of this work and outlined in Figure 2.12, several approaches are expected to yield valuable further insights. To improve the freeze start, controlling the liquid water saturation within the GDLs and the membrane is key. Liquid water remaining in the cells during cool-down freezes, subsequently reducing the ice capacity available for the actual freeze start[49]. Therefore, the so called drying procedure, preparing the system for a future freeze start, must be optimized. As this process is intrinsically dynamic, it is expected that the desorption kinetics and liquid water drainage analyzed within this work provide a valuable basis, which should be extended via targeted drying experiments. On the other side of the temperature envelope, dry-out prevention is expected to be increasingly challenging for high temperature operation. Especially if the AirS is incapable of reaching pressures above approximately 3 bar, a slow temperature-induced dry-out is likely inevitable at operating temperatures around or even above 90 °C without an external humidifier. However, a targeted experimental campaign might be worthwhile to answer the question of how long such a mismatch between pressure and temperature can be endured

before unacceptably dry states occur.

6.3 What are the limitations regarding efficiency, dynamic capabilities and critical states of common stationary-based water management strategies and how can they be improved?

To avoid the critical states of dry-out and liquid water-induced starvation, the operating conditions of the stack must be selected carefully. The cathode pressure and stoichiometry depending on the current and therefore the water production are the most influential variables for the stack's humidification state, sometimes the coolant temperature is also included[44]. The typical process to choose the operating conditions of the stack is based on stationary design-of-experiment studies, which are conducted experimentally and/or via simulation. From that, the optimal combination of e.g. pressure and stoichiometry are derived[8,121], so that for example the efficiency is maximized. Attention must be paid to the system interaction: maximizing the stack's efficiency without including the EAC power demand will certainly not result in the highest possible system efficiency. Therefore, the EAC must be included in the set point derivation process. One way to systematically obtain the steady-state operating points is a coordinate transformation onto outlet activity and oxygen partial pressure[44,45].

These approaches focus on efficiency and avoidance of critical steady-states. However, the automotive application, especially a fuel cell dominant passenger car, almost never results in true steady-state operation. A fixed look-up table might become insufficient, as the stack's state differs from equilibrium. More sophisticated control strategies incorporate a feedback control, which assesses the actual fuel cells' operating state, to mitigate this shortcoming. If an efficiency-wise non-ideal or even critical operating state is identified, the system is tasked to counteract for example a potential dry-out or flooding. To detect a dry membrane state, the *HFR* signal can be interpreted: if the ohmic resistance is rather high, the system is controlled to humidify the membrane. This strategy was already published back in 2010 and is probably implemented in Toyota's Mirai[31]. While such an approach works well for avoiding dry-outs, the *HFR*'s sensitivity towards flooding is probably insufficient. Liquid water accumulation in the GDLs, a prerequisite for flooding, does not increase the membrane humidity significantly. In addition, the resistance decrease caused by a further humidification of an already wet membrane is rather weak. An improvement of this feedback strategy includes monitoring the cell voltage[163], sometimes in combination with the cells' position in the stack[164]. If flooding occurs, a steep voltage decline is detected and the system reacts accordingly.

The previously discussed strategies allow for an efficient steady-state or even low-dynamic operation, but two major drawbacks remain. First, critical states, especially flooding, are detected as they occur and can therefore not safely be prevented. Second, the strategies fail to predictively include the history of the stack's state. A discrepancy between the expected steady-state and the actual state of the stack caused by dynamic operation might also become critical. For example, if the saturation levels within the GDL are high during low load operation and the current is increased faster than the water is drained, it results in the critical state of starvation. As a rule of thumb, steady-state based water management strategies are sufficient as long as the targeted current dynamics are slower than the key processes of membrane

humidification and liquid water drainage. As they proceed on the scale of tens of seconds, a highly dynamic operation of the fuel cell system with power dynamics around and below 1 s remains unreachable with the common strategies.

If highly dynamic operation should be achieved, multiple extensions need to be added to the established strategies. First, a thorough understanding of the relevant stack internal processes during fast load changes must be established to later predict and prevent critical states rather than just react. The dry-out is easy to mitigate, as it is easily traceable via the *HFR*. Too dry conditions of the gas phase can further be endured for tens of seconds, until critical dry-out occurs. It is far more challenging to avoid reactant starvation, as it becomes critical within tens of milliseconds, if the electrical current is ramped dynamically. Two root causes can result in such a state: either a high liquid water saturation within the GDLs or a too low reactant partial pressure in the flow field. The liquid water saturation cannot be measured ex-situ and must therefore be predicted based on models or via a suite of limiting current experiments. As the AirS reacts slower than the electric current could theoretically be ramped, too low reactant partial pressures in the flow field can also occur. Therefore, this work proposes to reverse the calculation direction of common approaches: Instead of calculating the stoichiometry and pressure set point based on the current, the current gradient is adapted to the actually available reactant partial pressure. This methodology avoids a possible mismatch between demand and supply. Such an approach must be implemented, if the current should be changed in the order of or faster than the AirS's dynamics, which lie around or below 1 s for application-like systems. Note that the membrane humidification requirement as part of the activity-based water management strategy[44,45] is ignorable on this short time scale.

This work demonstrates the feasibility of the adaptive current gradient strategy as one solution to avoid starvation during highly dynamic operation. The partial pressure limit utilized in this approach is selected as a steady-state current-dependent function, which does not reflect the impact of time-wise changes in liquid water saturation. In an improved version, the actual saturation level should be estimated and the partial pressure limit adapted accordingly. If the actual saturation is higher, the limit must be placed at higher partial pressures to avoid starvation, while it can be lowered if the GDLs are rather dry. This requires an real-time estimation of the actual liquid water saturation, which is challenging as previously discussed. However, the simulation model and validation measurements might serve as a first step towards such an implementation. Note that the experiments conducted in this work are incapable of distinguishing liquid water in the catalyst layers from liquid water in the GDLs. Although the ex-situ behavior is well represented by the simulation model, an in-depth experimental analysis of the liquid water distribution in-between catalyst layer and GDL is expected to foster a deepened understanding.

So far only the drawbacks of stationary-based operating strategies in dynamic operation and possible improvements were discussed. But, as shown in this work, the steady-state approaches might also fail in steady-state cases: Drainage and humidification targets become incompatible, especially in non-humidified systems. During low load operation, a steady-state supply of air causes either a dry-out or flooding due to insufficient liquid water drainage. With a dynamic AirS operation, such a low load operation is enabled: by switching between two operating points, one for liquid water drainage and one for membrane humidification, the targets are fulfilled alternately. This is another example of potential benefits offered by dynamic system operation: an improved operating range.

6.4 How do the main system level levers control strategy and architecture impact the expected trade-off between system efficiency and dynamics?

On system level, two factors impact the overall system performance, quantified in terms of dynamic capability and efficiency. The first option is a change in the control software: when should which operating conditions be set? The set points for pressure and stoichiometry supplied by the AirS are again the most important ones, as they not only impact the stack's efficiency but also the system net power heavily. Usually, efficiency-oriented set points for pressure and stoichiometry are derived. In the activity-based water management strategy[44,46], this means that the oxygen partial pressure is reduced until the stack voltage drops disproportionally, overcompensating the reduction in EAC power demand. At this point, the system efficiency optimum for stationary operation is found. However, such a selection leaves little room for highly dynamic operation. In contrast, an increased steady-state partial pressure, to ensure a cushioned supply, slightly reduces the efficiency. On the other hand, the increase in current is faster and subsequently higher power dynamics are achieved. In the first time frame of a current step, where the EAC is still speeding up to the new stationary operating point, the current can be increased instantaneously to the partial pressure limit. Especially in case of a slowly reacting AirS, the t_{90}-time of the available drive-train power is reduced by up to 56 %.

This work offers explanations and analyses of the key dynamic phenomena within the fuel cell stack interacting with the adjacent subsystems. It is shown that incorporating the improved control strategies discussed in the previous paragraph, safely avoids critical states and yields benefits for efficiency and dynamic capabilities. However, these targets are incompatible. A trade-off must be conducted to derive the best solution for each application case: an efficiency-focused approach might aim at rather low reactant partial pressure, while the supply cushion enables higher achievable dynamics at the cost of an increased compressor power demand and therefore a lower system efficiency. The efficiency drawback of using the cushioned supply lies between 1.2 % and 2.8 % in the analyzed load cycle, depending on the system architecture.

In literature, control strategies for highly dynamic operation are an active research topic. Effort is spent on developing fast and robust controller schemes, with some even incorporating inherent limitations of PEM fuel cells such as reactant starvation[43]. However, a controller must fulfill real-time requirements, resulting in rather simplified physical foundations. These concepts therefore often neglect a major contributor: liquid water[61,162]. Without this building brick, derived control strategies are likely too conservative, leaving a possible further optimization regarding efficiency and dynamic capabilities inaccessible. For example, a higher partial pressure might be picked to account for possible liquid water saturation unknown to the controller. Or, the allowed current gradient might be limited to a constant value to avoid dynamic phenomena such as starvation at all times, which is also apart from the theoretically achievable dynamics. This is a direct result of the underlying models' uncertainties. The more room for error must be accounted for, the further away from the "real" limit lies the solution found with these approaches. Transferring in-depth understanding of the fuel cell's internal processes during dynamic operation into the control structure is one core contribution to achieve further improvements.

As second *system level lever*, the architecture is addressed in this work. Here, the selection of the components and their setup are varied. Special attention must be paid to the AirS, dominating the balance of plant component power demand and also limiting the achievable system dynamics. In contrast to the HyS, which adapts the gas mass flow within tens of milliseconds, the AirS operates on a time scale around or below 1 s. The AirS therefore restricts the achievable current gradient via the oxygen partial pressure available to the fuel cell reaction, and subsequently the achievable stack power dynamics. However, publicly available research on system architecture impact is sparse in the fuel cell community, and only a few publications exist[160]. This is likely caused by three factors. One, the architecture selection, that every developer must take during the system design process, is at the core of the companies intellectual property. Publishing the results or even the design philosophy and central decisions within such a selection process is therefore viewed to be economically unwise, as it might benefit competitors. Two, the whole selection process requires a deep understanding at system level, as complex interactions and various limiting use-cases impact the feasibility of the concepts. This knowledge is only sparsely available at the system designing companies, as central elements to built-up this knowledge, such as system test rigs, exist only in very limited numbers. Three, there are so many possible combinations and resulting variants, that great effort must be spent to find an Pareto-optimal solution. Different application cases result in different requirements and KPI weighting, and following varying selected architectures. Therefore, the whole chain from use-case definition to system design must be mastered.

In this work, the architectures' impact is evaluated on a narrowed scope. Rather than finding optimal solutions with an ideal balance between the KPIs, three different architectures aiming either at high dynamic capabilities or efficiency as well as a baseline architecture are analyzed. As expected, no single best solution is identified. Only Pareto-optimal architecture and control strategy combinations, exhibiting either higher efficiencies or dynamics, are found. While the results are by far not giving the full picture of possible architecture and control strategy combinations as well as use-cases, they strongly endorse the system level approach. The analyzed solutions span drive-train power dynamics from 0.05 s to 0.44 s with total system efficiencies ranging from 56.7 % to 60.2 %. The effort devoted to this field is therefore not spent in vain: substantial improvements in the fuel cell system's performance can be achieved, critical for a market break-through of fuel cell electric vehicles. The highly dynamic fuel cell system operation enables to build fuel cell dominant FCEVs featuring only small batteries, while achieving drive-train power dynamics surpassing their classic ICE counterparts. However, in-depth understanding of the main processes inside the fuel cells and the adjacent subsystems, closely linked to the water management, is needed.

Chapter 7

Summary & Outlook

While FCEVs are a promising technical solution to achieve carbon-free mobility such that decade-long research was invested in this field, multiple challenges for market break-through remain. This work aimed at a three-fold goal of improving the dynamic capabilities and efficiency of an automotive FCS while avoiding critical states within the cells. A fuel cell dominant passenger car with a battery able to provide only one third of the steady-state FCS power was selected as a use-case. It requires highly dynamic FCS power variations on the time scale of 1 s. Here, the water management dynamics within the fuel cells as well as the subsystems' intrinsic dynamics are of utmost importance. Four research questions were introduced to derive a holistic methodology, synergically harnessing tailored simulation models and system level experiments. The research questions target the dynamic effects dominant in highly dynamic operation, the design of proper experiments, the limitations and possible improvements of stationary-based water management strategies as well as the impact of control strategy and system architecture on efficiency and dynamic capabilities.

One core contribution of this work is a spatially resolved, time-dependent fuel cell model including liquid water dynamics. In contrast to common literature models, it was parametrized and validated with application-like system level experiments. Second, improvements of the highly dynamic operation as well as potential pitfalls in widely-used experimental setups were analyzed with targeted dynamic experiments. These experiments also included a novel approach for a dynamic system analysis of a sophisticated FCS. Third, the knowledge gained with the cell model and system experiments was combined for a rare system level dynamics and efficiency trade-off for different system architectures and control strategies, following the overall setup of this work: *from cell to system to other systems.*

Liquid water drainage as well as sorption were found to be the key processes in the highly dynamic operation. A simulation model must incorporate these aspects. Furthermore, attention should be paid to the transferability of experimental results, as voltage response modes with widely varying time scales are triggered. Widespread short stack setups fail to produce the gas supply dominated response mode most critical for the application, as they lack the required gas supply dynamics in the order of 1 s. Steady-state based control strategies neglect the intrinsic subsystem dynamics and are therefore limited to low dynamic operation in the range of tens of seconds. In highly dynamic operation, the AirS bounds the reactant supply dynamics and the current ramp-up must be delayed accordingly to avoid starvation. Then, drive-train power dynamics between 0.05 s and 0.44 s are achievable with FCSs, outperforming their ICE counterparts' dynamics of 1 s to 3 s[9,10].

Further research is needed to prove the adapted current gradient strategy for highly dynamic operation experimentally. Additionally, the simulation model should be checked against spatially resolved dynamic experimental data. Uncertainties in sub-models, especially regarding sorption and drainage, should be reduced by targeted application-like experiments. Potential game-changers in the near future might be the operation at even higher temperatures of up to 120 °C, as well as a ban of the predominant PFSA-based membranes.

Bibliography

[1]   IPCC. "Summary for Policymakers". In: *Climate Change 2022: Mitigation of Climate Change. Contribution of Working Group III to the Sixth Assessment Report of the Intergovernmental Panel on Climate Change*. Ed. by P.R. Shukla et al. Cambridge, UK and New York, NY, USA: Cambridge University Press, 2022.

[2]   United Nations. *Take Action for the Sustainable Development Goals*. URL: https://www.un.org/sustainabledevelopment/sustainable-development-goals/ (visited on 01/25/2023).

[3]   M. Pathak et al. "Technical Summary". In: *Climate Change 2022: Mitigation of Climate Change. Contribution of Working Group III to the Sixth Assessment Report of the Intergovernmental Panel on Climate Change*. Ed. by P.R. Shukla et al. Cambridge, UK and New York, NY, USA: Cambridge University Press, 2022.

[4]   Directorate General for Communication and European Parliament. *Fit for 55: MEPs back objective of zero emissions for cars and vans in 2035*. June 2022. URL: https://www.europarl.europa.eu/news/en/press-room/20220603IPR32129/ (visited on 03/02/2023).

[5]   Bundesamt für Wirtschaft und Ausfuhrkontrolle. *Erhöhter Umweltbonus für E-Autos*. June 2020. URL: https://www.bafa.de/SharedDocs/Kurzmeldungen/DE/Energie/Elektromobilitaet/20200610_erhoehter_umweltbonus.html (visited on 03/02/2023).

[6]   IEA. *Global EV Outlook 2022*. May 2022. URL: ttps://www.iea.org/reports/global-ev-outlook-2022 (visited on 02/03/2023).

[7]   Elliot Padget and Gregory Kleen. *Automotive Fuel Cell Targets and Status*. Oct. 2020. URL: https://www.hydrogen.energy.gov/pdfs/20005-automotive-fuel-cell-targets-status.pdf#:~:text=To%20ensure%20the%20competitiveness%20of%20fuel%20cells%20for,work%20with%20industry%20to%20update%20targets%20as%20needed. (visited on 02/03/2023).

[8]   Manfred Klell, Helmut Eichlseder, and Alexander Trattner. *Wasserstoff in der Fahrzeugtechnik*. Wiesbaden: Springer Fachmedien Wiesbaden, 2018. ISBN: 978-3-658-20446-4.

[9]   Jamal Dabbabi et al. "Elektrisch unterstützter Turbolader für das 48-V-Bordnetz". In: *MTZ-Motortechnische Zeitschrift* 78.10 (2017).

[10] Jan Linsel and Stephan Wanner. "Zweistufige Aufladung mit Spirallader und Abgasturbolader". In: *MTZ-Motortechnische Zeitschrift* 76.11 (2015).

[11] Jiayao Cui et al. "Recent advances in non-precious metal electrocatalysts for oxygen reduction in acidic media and PEMFCs: an activity, stability and mechanism study". In: *Green Chemistry* 23.18 (2021). DOI: 10.1039/D1GC01040A.

[12] Paul C. Okonkwo and Clement Otor. "A review of gas diffusion layer properties and water management in proton exchange membrane fuel cell system". In: *International Journal of Energy Research* 45.3 (Mar. 2021). DOI: 10.1002/er.6227.

[13] Reza Omrani and Bahman Shabani. "Gas diffusion layer modifications and treatments for improving the performance of proton exchange membrane fuel cells and electrolysers: A review". In: *International Journal of Hydrogen Energy* 42.47 (Nov. 2017). DOI: 10.1016/j.ijhydene.2017.09.132.

[14] Zijie Lu et al. "Water management studies in PEM fuel cells, part III: Dynamic breakthrough and intermittent drainage characteristics from GDLs with and without MPLs". In: *International Journal of Hydrogen Energy* 35.9 (May 2010). DOI: 10.1016/j.ijhydene.2010.01.012.

[15] B. H. Lim et al. "Effects of flow field design on water management and reactant distribution in PEMFC: a review". In: *Ionics* 22.3 (Mar. 2016). DOI: 10.1007/s11581-016-1644-y.

[16] Marco Sauermoser et al. "Flow Field Patterns for Proton Exchange Membrane Fuel Cells". In: *Frontiers in Energy Research* 8 (Feb. 2020). DOI: 10.3389/fenrg.2020.00013.

[17] Ram Sevak Singh, Anurag Gautam, and Varun Rai. "Graphene-based bipolar plates for polymer electrolyte membrane fuel cells". In: *Frontiers of Materials Science* 13.3 (Sept. 2019). DOI: 10.1007/s11706-019-0465-0.

[18] Zhutian Xu et al. "Towards mass applications: A review on the challenges and developments in metallic bipolar plates for PEMFC". In: *Progress in Natural Science: Materials International* 30.6 (Dec. 2020). DOI: 10.1016/j.pnsc.2020.10.015.

[19] Andrew Dicks and D. A. J. Rand. *Fuel cell systems explained.* Third edition. Vol. 113. Topics in Applied Physics. Hoboken, NJ, USA: Wiley, 2018. ISBN: 978-1-118-70696-1 978-1-118-70697-8.

[20] Xianguo Li. *Principles of fuel cells.* New York: Taylor & Francis, 2006. ISBN: 978-1-59169-022-1.

[21] John S. Newman and Karen E. Thomas-Alyea. *Electrochemical systems.* 3rd ed. Hoboken, N.J: J. Wiley, Nov. 2012. ISBN: 978-0-471-47756-3.

[22] A. A. Kulikovsky. "A Physically–Based Analytical Polarization Curve of a PEM Fuel Cell". In: *Journal of The Electrochemical Society* 161.3 (2014). DOI: 10.1149/2.028403jes.

[23] C.W. Wu et al. "A systematic review for structure optimization and clamping load design of large proton exchange membrane fuel cell stack". In: *Journal of Power Sources* 476 (Nov. 2020). DOI: 10.1016/j.jpowsour.2020.228724.

[24] Meiling Yue et al. "Review on health-conscious energy management strategies for fuel cell hybrid electric vehicles: Degradation models and strategies". In: *International Journal of Hydrogen Energy* 44.13 (Mar. 2019). DOI: 10.1016/j.ijhydene.2019.01.190.

[25] Henning Lohse-Busch et al. *Technology Assessment of a Fuel Cell Vehicle: 2017 Toyota Mirai.* June 2018.

[26] Yasutaka Nagai et al. "Improving water management in fuel cells through microporous layer modifications: Fast operando tomographic imaging of liquid water". In: *Journal of Power Sources* 435 (Sept. 2019). DOI: 10.1016/j.jpowsour.2019.226809.

[27] Z. Lu et al. "Water management studies in PEM fuel cells, Part II: Ex situ investigation of flow maldistribution, pressure drop and two-phase flow pattern in gas channels". In: *International Journal of Hydrogen Energy* 34.8 (May 2009). DOI: 10.1016/j.ijhydene.2008.12.025.

[28] Tobias Schmitt et al. "An Experimental Study of Humidity Distribution Dynamics in a Segmented PEM Fuel Cell". In: *Journal of The Electrochemical Society* 169.12 (Dec. 2022). DOI: 10.1149/1945-7111/aca720.

[29] Nicolas Fouquet. "Real time model-based monitoring of a pem fuel cell flooding and drying out". In: *2010 IEEE Vehicle Power and Propulsion Conference.* IEEE, 2010.

[30] Dong-Hoon Shin, Seung-Ryeol Yoo, and Young-Hyun Lee. "Real Time Water Contents Measurement Based on Step Response for PEM Fuel Cell". In: *International Journal of Precision Engineering and Manufacturing-Green Technology* 6.5 (Oct. 2019). DOI: 10.1007/s40684-019-00099-0.

[31] Nobuyuki Kitamura et al. "Development of Water Content Control System for Fuel Cell Hybrid Vehicles Based on AC Impedance". In: Apr. 2010. DOI: 10.4271/2010-01-1088.

[32] O.S. Ijaodola et al. "Energy efficiency improvements by investigating the water flooding management on proton exchange membrane fuel cell (PEMFC)". In: *Energy* 179 (July 2019). DOI: 10.1016/j.energy.2019.04.074.

[33] Bruce E. Poling, J. M. Prausnitz, and John P. O'Connell. *The properties of gases and liquids*. 5th ed. New York: McGraw-Hill, 2001. ISBN: 978-0-07-011682-5.

[34] Jeff T. Gostick et al. "Direct measurement of the capillary pressure characteristics of water–air–gas diffusion layer systems for PEM fuel cells". In: *Electrochemistry Communications* 10.10 (Oct. 2008). DOI: 10.1016/j.elecom.2008.08.008.

[35] D. A. G. Bruggeman. "Berechnung verschiedener physikalischer Konstanten von heterogenen Substanzen. I. Dielektrizitätskonstanten und Leitfähigkeiten der Mischkörper aus isotropen Substanzen". In: *Annalen der Physik* 416.7 (1935). DOI: 10.1002/andp.19354160705.

[36] Kui Jiao and Xianguo Li. "Water transport in polymer electrolyte membrane fuel cells". In: *Progress in Energy and Combustion Science* 37.3 (June 2011). DOI: 10.1016/j.pecs.2010.06.002.

[37] Nobuaki Nonoyama et al. "Analysis of oxygen-transport diffusion resistance in proton-exchange-membrane fuel cells". In: *Journal of The Electrochemical Society* 158.4 (2011).

[38] Peng Ren et al. "Degradation mechanisms of proton exchange membrane fuel cell under typical automotive operating conditions". In: *Progress in Energy and Combustion Science* 80 (Sept. 2020). DOI: 10.1016/j.pecs.2020.100859.

[39] Thomas E. Springer, T. A. Zawodzinski, and Shimshon Gottesfeld. "Polymer electrolyte fuel cell model". In: *Journal of the electrochemical society* 138.8 (1991).

[40] Roman Vetter and Jürgen O. Schumacher. "Experimental parameter uncertainty in proton exchange membrane fuel cell modeling. Part I: Scatter in material parameterization". In: *Journal of Power Sources* 438 (Oct. 2019). DOI: 10.1016/j.jpowsour.2019.227018.

[41] Mirjam Grimm et al. "Interaction of cell flow directions and performance in PEM fuel cell systems following an anode based water management approach". In: *Journal of Power Sources* 580 (Oct. 2023). DOI: 10.1016/j.jpowsour.2023.233270.

[42] Sergei Hahn. "Modellbasierte Betriebsstrategie für PEM-Brennstoffzellensysteme". PhD Thesis. Stuttgart: Universität Stuttgart, Mar. 2023.

[43] W.R.W. Daud et al. "PEM fuel cell system control: A review". In: *Renewable Energy* 113 (Dec. 2017). DOI: 10.1016/j.renene.2017.06.027.

[44] Mark Hellmann. *Robuste Auslegung von mobilen Brennstoffzellensystemen*. Berichte aus dem IDS 2014,2. Garbsen: TEWISS - Techn. und Wissen GmbH, 2014. ISBN: 978-3-944586-73-1.

[45] Jonas Breitinger et al. "Flooding Characteristics and Countermeasures in a PEM Fuel Cell System". In: *ECS Transactions* 109.9 (Sept. 2022). DOI: 10.1149/10909.0227ecst.

[46] Jonas Breitinger et al. "Automotive Fuel Cell Systems: Testing Highly Dynamic Scenarios". In: *Energies* 16.2 (Jan. 2023). DOI: 10.3390/en16020664.

[47] Katsuyoshi Kakinuma et al. "The Possibility of Intermediate–Temperature (120° C)–Operated Polymer Electrolyte Fuel Cells using Perfluorosulfonic Acid Polymer Membranes". In: *Journal of The Electrochemical Society* 169.4 (2022).

[48] Sho Kobayashi et al. "Operando X-Ray Absorption Spectroscopy of Pt Catalyst in Polymer Electrolyte Fuel Cell Under High Temperature and Low Humidification". In: *ECS Meeting Abstracts* MA2022-02.42 (Oct. 2022). DOI: 10.1149/MA2022-02421589mtgabs.

[49] Yueqi Luo and Kui Jiao. "Cold start of proton exchange membrane fuel cell". In: *Progress in Energy and Combustion Science* 64 (Jan. 2018). DOI: 10.1016/j.pecs.2017.10.003.

[50] T. Jahnke et al. "Performance and degradation of Proton Exchange Membrane Fuel Cells: State of the art in modeling from atomistic to system scale". In: *Journal of Power Sources* 304 (Feb. 2016). DOI: 10.1016/j.jpowsour.2015.11.041.

[51] Diankai Qiu et al. "Mechanical failure and mitigation strategies for the membrane in a proton exchange membrane fuel cell". In: *Renewable and Sustainable Energy Reviews* 113 (Oct. 2019). DOI: 10.1016/j.rser.2019.109289.

[52] Cheng Chen and Thomas F. Fuller. "The effect of humidity on the degradation of Nafion® membrane". In: *Polymer Degradation and Stability* 94.9 (Sept. 2009). DOI: 10.1016/j.polymdegradstab.2009.05.016.

[53] Kah-Young Song and Hee-Tak Kim. "Effect of air purging and dry operation on durability of PEMFC under freeze/thaw cycles". In: *International Journal of Hydrogen Energy* 36.19 (Sept. 2011). DOI: 10.1016/j.ijhydene.2011.06.095.

[54] Xu Zhang et al. "Effects of carbon corrosion on mass transfer losses in proton exchange membrane fuel cells". In: *International Journal of Hydrogen Energy* 42.7 (Feb. 2017). DOI: 10.1016/j.ijhydene.2016.08.223.

[55] Daniel Seidl. "Development of a Dynamic Water Management Model for Mobile PEM Fuel Cell Systems". Master Thesis. Stuttgart: Universität Stuttgart, Apr. 2022.

[56] Sergei Hahn et al. "Optimization of the efficiency and degradation rate of an automotive fuel cell system". In: *International Journal of Hydrogen Energy* (Jan. 2021). DOI: 10.1016/j.ijhydene.2020.12.084.

[57] Sara Luciani and Andrea Tonoli. "Control Strategy Assessment for Improving PEM Fuel Cell System Efficiency in Fuel Cell Hybrid Vehicles". In: *Energies* 15.6 (Mar. 2022). DOI: 10.3390/en15062004.

[58] Sönke Gößling, Niklas Nickig, and Matthias Bahr. "2-D + 1-D PEM fuel cell model for fuel cell system simulations". In: *International Journal of Hydrogen Energy* 46.70 (Oct. 2021). DOI: 10.1016/j.ijhydene.2021.08.044.

[59] Verica Radisavljević-Gajić, Miloš Milanović, and Patrick Rose. "Modeling and System Analysis of PEM Fuel Cells". In: *Multi-Stage and Multi-Time Scale Feedback Control of Linear Systems with Applications to Fuel Cells*. DOI: 10.1007/978-3-030-10389-7_7. Cham: Springer International Publishing, 2019. ISBN: 978-3-030-10388-0 978-3-030-10389-7.

[60] Alexander Kneer and Nadja Wagner. "A semi-empirical catalyst degradation model based on voltage cycling under automotive operating conditions in PEM fuel cells". In: *Journal of The Electrochemical Society* 166.2 (2019).

[61] Sergei Hahn et al. "Adaptive operation strategy of a polymer electrolyte membrane fuel cell air system based on model predictive control". In: *International Journal of Hydrogen Energy* 46.33 (May 2021). DOI: 10.1016/j.ijhydene.2021.02.135.

[62] Wei Dai et al. "A review on water balance in the membrane electrode assembly of proton exchange membrane fuel cells". In: *International Journal of Hydrogen Energy* 34.23 (Dec. 2009). DOI: 10.1016/j.ijhydene.2009.09.017.

[63] Horng-Wen Wu. "A review of recent development: Transport and performance modeling of PEM fuel cells". In: *Applied Energy* 165 (Mar. 2016). DOI: 10.1016/j.apenergy.2015.12.075.

[64] Mingzhang Pan et al. "A review of membranes in proton exchange membrane fuel cells: Transport phenomena, performance and durability". In: *Renewable and Sustainable Energy Reviews* 141 (May 2021). DOI: 10.1016/j.rser.2021.110771.

[65] D.S. Falcão et al. "Water transport through a PEM fuel cell: A one-dimensional model with heat transfer effects". In: *Chemical Engineering Science* 64.9 (May 2009). DOI: 10.1016/j.ces.2009.01.049.

[66] K.H. Loo et al. "Characterization of the dynamic response of proton exchange membrane fuel cells – A numerical study". In: *International Journal of Hydrogen Energy* 35.21 (Nov. 2010). DOI: 10.1016/j.ijhydene.2010.08.071.

[67] Xiaolong Li, Kai Han, and Yu Song. "Dynamic behaviors of PEM fuel cells under load changes". In: *International Journal of Hydrogen Energy* 45.39 (Aug. 2020). DOI: 10.1016/j.ijhydene.2019.12.034.

[68] P. Noiying et al. "Using electrical analogy to describe mass and charge transport in PEM fuel cell". In: *Renewable Energy* 44 (Aug. 2012). DOI: 10.1016/j.renene.2012.01.081.

[69] A. Verma and R. Pitchumani. "Influence of membrane properties on the transient behavior of polymer electrolyte fuel cells". In: *Journal of Power Sources* 268 (Dec. 2014). DOI: 10.1016/j.jpowsour.2014.06.065.

[70] A.A. Kulikovsky. "Semi-analytical 1D+1D model of a polymer electrolyte fuel cell". In: *Electrochemistry Communications* 6.10 (Oct. 2004). DOI: 10.1016/j.elecom.2004.07.009.

[71] Daming Zhou et al. "Global parameters sensitivity analysis and development of a two-dimensional real-time model of proton-exchange-membrane fuel cells". In: *Energy Conversion and Management* 162 (Apr. 2018). DOI: 10.1016/j.enconman.2018.02.036.

[72] Jian Chen et al. "A dynamic scalable segmented model of PEM fuel cell systems with two-phase water flow". In: *Mathematics and Computers in Simulation* 167 (Jan. 2020). DOI: 10.1016/j.matcom.2018.05.006.

[73] Hyunchul Ju, Hua Meng, and Chao-Yang Wang. "A single-phase, non-isothermal model for PEM fuel cells". In: *International Journal of Heat and Mass Transfer* 48.7 (Mar. 2005). DOI: 10.1016/j.ijheatmasstransfer.2004.10.004.

[74] J.M. Sierra, J. Moreira, and P.J. Sebastian. "Numerical analysis of the effect of different gas feeding modes in a proton exchange membrane fuel cell with serpentine flow-field". In: *Journal of Power Sources* 196.11 (June 2011). DOI: 10.1016/j.jpowsour.2011.01.079.

[75] Yun Wang and Chao-Yang Wang. "Transient analysis of polymer electrolyte fuel cells". In: *Electrochimica Acta* 50.6 (Jan. 2005). DOI: 10.1016/j.electacta.2004.08.022.

[76] M. Grimm et al. "Water Management of PEM Fuel Cell Systems Based on the Humidity Distribution in the Anode Gas Channels". In: *Fuel Cells* 20.4 (Aug. 2020). DOI: 10.1002/fuce.202000070.

[77] Xiao-Dong Wang et al. "Transient response of PEM fuel cells with parallel and interdigitated flow field designs". In: *International Journal of Heat and Mass Transfer* 54.11-12 (May 2011). DOI: 10.1016/j.ijheatmasstransfer.2011.02.024.

[78] Roman Vetter and Jürgen O. Schumacher. "Experimental parameter uncertainty in proton exchange membrane fuel cell modeling. Part II: Sensitivity analysis and importance ranking". In: *Journal of Power Sources* 439 (Nov. 2019). DOI: 10.1016/j.jpowsour.2019.04.057.

[79] R. B. Bird, W. E. Stewart, and E. N. Lightfoot. *Transport phenomena*. New York, NY: John Wiley & Sons, Inc., 2002.

[80] Robert H. Perry and Don W. Green, eds. *Perry's chemical engineers' handbook*. 7th Edition. OCLC: 833624525. New York, NY: McGraw-Hill, 1997.

[81] James Larminie and Andrew Dicks. *Fuel cell systems explained*. 2nd ed. Chichester, West Sussex: J. Wiley, 2003. ISBN: 978-0-470-84857-9.

[82] Sathya Motupally, Aaron J. Becker, and John W. Weidner. "Diffusion of water in Nafion 115 membranes". In: *Journal of the Electrochemical Society* 147.9 (2000).

[83] Alessandro Ferrara, Pierpaolo Polverino, and Cesare Pianese. "Analytical calculation of electrolyte water content of a Proton Exchange Membrane Fuel Cell for on-board modelling applications". In: *Journal of Power Sources* 390 (June 2018). DOI: 10.1016/j.jpowsour.2018.04.005.

[84]   Xinhuai Ye and Chao-Yang Wang. "Measurement of Water Transport Properties Through Membrane-Electrode Assemblies". In: *Journal of The Electrochemical Society* 154.7 (2007). DOI: 10.1149/1.2737379.

[85]   Adam Z. Weber and John Newman. "Transport in Polymer-Electrolyte Membranes". In: *Journal of The Electrochemical Society* 151.2 (2004). DOI: 10.1149/1.1639157.

[86]   Thomas F. Fuller and John Newman. "Experimental Determination of the Transport Number of Water in Nafion 117 Membrane". In: *Journal of The Electrochemical Society* 139.5 (May 1992). DOI: 10.1149/1.2069407.

[87]   Shanhai Ge, Baolian Yi, and Pingwen Ming. "Experimental Determination of Electro-Osmotic Drag Coefficient in Nafion Membrane for Fuel Cells". In: *Journal of The Electrochemical Society* 153.8 (2006). DOI: 10.1149/1.2203934.

[88]   James T. Hinatsu, Minoru Mizuhata, and Hiroyasu Takenaka. "Water Uptake of Perfluorosulfonic Acid Membranes from Liquid Water and Water Vapor". In: *The Electrochemical Society* 141.6 (June 1994). DOI: 10.1149/1.2054951.

[89]   S. Didierjean et al. "Theoretical evidence of the difference in kinetics of water sorption and desorption in Nafion® membrane and experimental validation". In: *Journal of Power Sources* 300 (Dec. 2015). DOI: 10.1016/j.jpowsour.2015.09.053.

[90]   Shanhai Ge et al. "Absorption, Desorption, and Transport of Water in Polymer Electrolyte Membranes for Fuel Cells". In: *Journal of The Electrochemical Society* 152.6 (2005). DOI: 10.1149/1.1899263.

[91]   Qinggang He et al. "Correlating Humidity-Dependent Ionically Conductive Surface Area with Transport Phenomena in Proton-Exchange Membranes". In: *The Journal of Physical Chemistry B* 115.40 (Oct. 2011). DOI: 10.1021/jp206154y.

[92]   Anusorn Kongkanand. "Interfacial Water Transport Measurements in Nafion Thin Films Using a Quartz-Crystal Microbalance". In: *The Journal of Physical Chemistry C* 115.22 (June 2011). DOI: 10.1021/jp2028214.

[93]   Ahmet Kusoglu et al. "Water Uptake of Fuel-Cell Catalyst Layers". In: *Journal of The Electrochemical Society* 159.9 (2012). DOI: 10.1149/2.031209jes.

[94]   Jeff T. Gostick et al. "Wettability and capillary behavior of fibrous gas diffusion media for polymer electrolyte membrane fuel cells". In: *Journal of Power Sources* 194.1 (Oct. 2009). DOI: 10.1016/j.jpowsour.2009.04.052.

[95]   Nada Zamel et al. "Effect of liquid water on transport properties of the gas diffusion layer of polymer electrolyte membrane fuel cells". In: *International Journal of Hydrogen Energy* 36.9 (May 2011). DOI: 10.1016/j.ijhydene.2011.01.146.

[96]   Michael Grimm, Evan J. See, and Satish G. Kandlikar. "Modeling gas flow in PEMFC channels: Part I – Flow pattern transitions and pressure drop in a simulated ex situ channel with uniform water injection through the GDL". In: *International Journal of Hydrogen Energy* 37.17 (Sept. 2012). DOI: 10.1016/j.ijhydene.2012.06.001.

[97]   Zijie Lu et al. "Water management studies in PEM fuel cells, part IV: Effects of channel surface wettability, geometry and orientation on the two-phase flow in parallel gas channels". In: *International Journal of Hydrogen Energy* 36.16 (Aug. 2011). DOI: 10.1016/j.ijhydene.2011.04.226.

[98]   F. Y. Zhang, X. G. Yang, and C. Y. Wang. "Liquid Water Removal from a Polymer Electrolyte Fuel Cell". In: *Journal of The Electrochemical Society* 153.2 (2006). DOI: 10.1149/1.2138675.

[99]   VDI e. V., ed. *VDI-Wärmeatlas*. DOI: 10.1007/978-3-642-19981-3. Berlin, Heidelberg: Springer Berlin Heidelberg, 2013. ISBN: 978-3-642-19980-6 978-3-642-19981-3.

[100] V. María Barragán and Signe Kjelstrup. "Thermo-osmosis in Membrane Systems: A Review". In: *Journal of Non-Equilibrium Thermodynamics* 42.3 (Jan. 2017). DOI: 10.1515/jnet-2016-0088.

[101] Ulrich Sauter et al. *The Coarse Stack Model Release 'Robin' - Equations and Implementation Details (Internal note)*. Nov. 2020.

[102] Irene J. Ong and John Newman. "Double-Layer Capacitance in a Dual Lithium Ion Insertion Cell". In: *Journal of The Electrochemical Society* 146.12 (Dec. 1999). DOI: 10.1149/1.1392643.

[103] A. M. Johnson and John Newman. "Desalting by Means of Porous Carbon Electrodes". In: *Journal of The Electrochemical Society* 118.3 (Mar. 1971). DOI: 10.1149/1.2408094.

[104] John S. Newman. *Electrochemical systems*. 2nd ed. Prentice Hall international series in the physical and chemical engineering sciences. Englewood Cliffs, N.J: Prentice Hall, 1991. ISBN: 978-0-13-248758-0.

[105] Attila Husar, Andrew Higier, and Hongtan Liu. "In situ measurements of water transfer due to different mechanisms in a proton exchange membrane fuel cell". In: *Journal of Power Sources* 183.1 (Aug. 2008). DOI: 10.1016/j.jpowsour.2008.04.042.

[106] Nada Zamel, Xianguo Li, and Jun Shen. "Correlation for the Effective Gas Diffusion Coefficient in Carbon Paper Diffusion Media". In: *Energy & Fuels* 23.12 (Dec. 2009). DOI: 10.1021/ef900653x.

[107] Adam Z. Weber and John Newman. "Transport in Polymer-Electrolyte Membranes". In: *Journal of The Electrochemical Society* 150.7 (2003). DOI: 10.1149/1.1580822.

[108] K. C. Neyerlin et al. "Determination of Catalyst Unique Parameters for the Oxygen Reduction Reaction in a PEMFC". In: *Journal of The Electrochemical Society* 153.10 (2006). DOI: 10.1149/1.2266294.

[109] Nicolas Meßner. "Entwicklung eines Simulationsmodells für das Wassermanagement von PEM-Brennstoffzellen". Master Thesis. Offenburg: Hochschule Offenburg, Oct. 2019.

[110] Victoria Scheuer. "Erstellung eines Simulationsmodells für das Wassermanagement von Brennstoffzellen für mobile Anwendungen". Master Thesis. Berlin: Technische Universität Berlin, Nov. 2018.

[111] U. S. Department of Energy. *DOE Technical Targets for Fuel Cell Systems and Stacks for Transportation Applications*. URL: https://www.energy.gov/eere/fuelcells/doe-technical-targets-fuel-cell-systems-and-stacks-transportation-applications (visited on 06/30/2022).

[112] M. Barclay Satterfield and J. B. Benziger. "Non-Fickian Water Vapor Sorption Dynamics by Nafion Membranes". In: *The Journal of Physical Chemistry B* 112.12 (Mar. 2008). DOI: 10.1021/jp7103243.

[113] Tomoo Yoshizumi, Hideki Kubo, and Masao Okumura. "Development of High-Performance FC Stack for the New MIRAI". In: Apr. 2021. DOI: 10.4271/2021-01-0740.

[114] Chung-Jen Tseng et al. "A PEM fuel cell with metal foam as flow distributor". In: *Energy Conversion and Management* 62 (Oct. 2012). DOI: 10.1016/j.enconman.2012.03.018.

[115] Marco Sauermoser. *Non-equilibrium thermodynamics and nature-inspired chemical engineering applied to PEM fuel cells*. Jan. 2021.

[116] P Pei, Q Chang, and T Tang. "A quick evaluating method for automotive fuel cell lifetime". In: *International Journal of Hydrogen Energy* 33.14 (July 2008). DOI: 10.1016/j.ijhydene.2008.04.048.

[117] Yeh-Hung Lai and Gerald W. Fly. "In-situ diagnostics and degradation mapping of a mixed-mode accelerated stress test for proton exchange membranes". In: *Journal of Power Sources* 274 (Jan. 2015). DOI: 10.1016/j.jpowsour.2014.10.116.

[118] Guangjin Wang et al. "Degradation behavior of a proton exchange membrane fuel cell stack under dynamic cycles between idling and rated condition". In: *International Journal of Hydrogen Energy* 43.9 (Mar. 2018). DOI: 10.1016/j.ijhydene.2018.01.020.

[119] KwangSup Eom et al. "Effects of Pt loading in the anode on the durability of a membrane–electrode assembly for polymer electrolyte membrane fuel cells during startup/shutdown cycling". In: *International Journal of Hydrogen Energy* 37.23 (Dec. 2012). DOI: 10.1016/j.ijhydene.2012.09.077.

[120] Jae Hong Kim et al. "Development of a Durable PEMFC Startup Process by Applying a Dummy Load". In: *Journal of The Electrochemical Society* 156.8 (2009). DOI: 10.1149/1.3148222.

[121] Hui-Wen Ku and Horng-Wen Wu. "Influences of operational factors on proton exchange membrane fuel cell performance with modified interdigitated flow field design". In: *Journal of Power Sources* 232 (June 2013). DOI: 10.1016/j.jpowsour.2013.01.020.

[122] Roberto C. Dante et al. "Fractional factorial design of experiments for PEM fuel cell performances improvement". In: *International Journal of Hydrogen Energy* 28.3 (2003).

[123] Sunhoe Kim, S. Shimpalee, and J.W. Van Zee. "The effect of stoichiometry on dynamic behavior of a proton exchange membrane fuel cell (PEMFC) during load change". In: *Journal of Power Sources* 135.1-2 (Sept. 2004). DOI: 10.1016/j.jpowsour.2004.03.060.

[124] Ivonne Karina Peña Arias et al. "Understanding PEM fuel cell dynamics: The reversal curve". In: *International Journal of Hydrogen Energy* 42.24 (June 2017). DOI: 10.1016/j.ijhydene.2017.05.087.

[125] Idoia San Martín, Alfredo Ursúa, and Pablo Sanchis. "Modelling of PEM Fuel Cell Performance: Steady-State and Dynamic Experimental Validation". In: *Energies* 7.2 (Feb. 2014). DOI: 10.3390/en7020670.

[126] Yong Tang et al. "Experimental investigation of dynamic performance and transient responses of a kW-class PEM fuel cell stack under various load changes". In: *Applied Energy* 87.4 (Apr. 2010). DOI: 10.1016/j.apenergy.2009.08.047.

[127] Junhyun Cho, Han-Sang Kim, and Kyoungdoug Min. "Transient response of a unit proton-exchange membrane fuel cell under various operating conditions". In: *Journal of Power Sources* 185.1 (Oct. 2008). DOI: 10.1016/j.jpowsour.2008.06.073.

[128] Christophe Gerling et al. "Full Factorial In Situ Characterization of Ionomer Properties in Differential PEM Fuel Cells". In: *Journal of The Electrochemical Society* 168.8 (Aug. 2021). DOI: 10.1149/1945-7111/ac1812.

[129] Tobias Schmitt et al. "Rapid and Local EIS on a Segmented Fuel Cell: A New Method for Spatial and Temporal Resolution". In: *Journal of The Electrochemical Society* 169.9 (Sept. 2022). DOI: 10.1149/1945-7111/ac9089.

[130] Irfan S. Hussaini and Chao-Yang Wang. "Visualization and quantification of cathode channel flooding in PEM fuel cells". In: *Journal of Power Sources* 187.2 (Feb. 2009). DOI: 10.1016/j.jpowsour.2008.11.030.

[131] R.M. Aslam et al. "Simultaneous thermal and visual imaging of liquid water of the PEM fuel cell flow channels". In: *Journal of the Energy Institute* 92.2 (Apr. 2019). DOI: 10.1016/j.joei.2018.01.005.

[132]   Vincent Coeuriot et al. "An ex-situ experiment to study the two-phase flow induced by water condensation into the channels of proton exchange membrane fuel cells (PEMFC)". In: *International Journal of Hydrogen Energy* 40.22 (June 2015). DOI: 10.1016/j.ijhydene.2015.04.008.

[133]   Yen-Chun Chen et al. "A Method for Spatial Quantification of Water in Microporous Layers of Polymer Electrolyte Fuel Cells by X-ray Tomographic Microscopy". In: *ACS Applied Materials & Interfaces* 13.14 (Apr. 2021). DOI: 10.1021/acsami.0c22358.

[134]   Hong Xu et al. "Effects of gas diffusion layer substrates on PEFC water management: Part I. Operando liquid water saturation and gas diffusion properties". In: *Journal of The Electrochemical Society* 168.7 (2021).

[135]   R. Satija et al. "In situ neutron imaging technique for evaluation of water management systems in operating PEM fuel cells". In: *Journal of Power Sources* 129.2 (Apr. 2004). DOI: 10.1016/j.jpowsour.2003.11.068.

[136]   Kavi Chintam et al. *Water Imaging in Mirai Short-Stack provided by USCAR*. Tech. rep. LA-UR–19-22972, 1505950. DOI: 10.2172/1505950. Apr. 2019.

[137]   N. Martinez et al. "Real time monitoring of water distribution in an operando fuel cell during transient states". In: *Journal of Power Sources* 365 (Oct. 2017). DOI: 10.1016/j.jpowsour.2017.08.067.

[138]   A. Bazylak. "Liquid water visualization in PEM fuel cells: A review". In: *International Journal of Hydrogen Energy* 34.9 (May 2009). DOI: 10.1016/j.ijhydene.2009.02.084.

[139]   Andrei Kulikovsky. "A fast low-current model for impedance of a PEM fuel cell cathode at low air stoichiometry". In: *Journal of The Electrochemical Society* 164.9 (2017). DOI: 10.1149/2.0561709jes.

[140]   Xiao-Zi Yuan et al. *Electrochemical Impedance Spectroscopy in PEM Fuel Cells*. DOI: 10.1007/978-1-84882-846-9. London: Springer London, 2010. ISBN: 978-1-84882-845-2 978-1-84882-846-9.

[141]   N. Fouquet et al. "Model based PEM fuel cell state-of-health monitoring via ac impedance measurements". In: *Journal of Power Sources* 159.2 (Sept. 2006). DOI: 10.1016/j.jpowsour.2005.11.035.

[142]   Jonas Breitinger et al. "Experimental Dynamics Analysis of a Full-Scale Automotive PEM Fuel Cell System". In: *European Fuel Cell Forum 2023 (submitted)*.

[143]   Ekbert Hering, Julian Endres, and Jürgen Gutekunst, eds. *Elektronik für Ingenieure und Naturwissenschaftler*. Berlin, Heidelberg: Springer Berlin Heidelberg, 2021. DOI: 10.1007/978-3-662-62698-6.

[144]   Russell L. Edwards and Ayodeji Demuren. "Regression analysis of PEM fuel cell transient response". In: *International Journal of Energy and Environmental Engineering* 7.3 (Sept. 2016). DOI: 10.1007/s40095-016-0209-1.

[145]   Alexey Loskutov et al. "Investigation of PEM Fuel Cell Characteristics in Steady and Dynamic Operation Modes". In: *Energies* 15.19 (Sept. 2022). DOI: 10.3390/en15196863.

[146]   Helge Weydahl, Steffen Møller-Holst, and Børre Børresen. "Effect of gas composition and gas utilisation on the dynamic response of a proton exchange membrane fuel cell". In: *Journal of Power Sources* 180.2 (June 2008). DOI: 10.1016/j.jpowsour.2008.01.037.

[147]   Xuan Liu, Hang Guo, and Chongfang Ma. "Water flooding and two-phase flow in cathode channels of proton exchange membrane fuel cells". In: *Journal of Power Sources* 156.2 (June 2006). DOI: 10.1016/j.jpowsour.2005.06.027.

[148] Dirk Jenssen, Oliver Berger, and Ulrike Krewer. "Anode flooding characteristics as design boundary for a hydrogen supply system for automotive polymer electrolyte membrane fuel cells". In: *Journal of Power Sources* 298 (Dec. 2015). DOI: 10.1016/j.jpowsour.2015.08.005.

[149] I.S. Hussaini and C.Y. Wang. "Dynamic water management of polymer electrolyte membrane fuel cells using intermittent RH control". In: *Journal of Power Sources* 195.12 (June 2010). DOI: 10.1016/j.jpowsour.2009.12.112.

[150] Jannik Schmitt. "Analyse von Systemarchitekturen dynamisch betriebener mobiler PEM-Brennstoffzellensysteme". Master Thesis. Stuttgart: Universität Stuttgart, May 2023.

[151] Toyota Motor Corporation. *Toyota Launches the New Mirai.* Dec. 2020. URL: https://global.toyota/en/newsroom/toyota/33558148.html#.ZF4fgWVM--c.link (visited on 01/27/2023).

[152] Hyundai Motor Company. *NEXO: The next-generation Fuel Cell Vehicle from Hyundai.* Jan. 2018. URL: https://www.hyundai.news/eu/articles/press-releases/nexo-the-next-generation-fuel-cell-vehicle-from-hyundai.html (visited on 01/27/2023).

[153] Toyota Motor Corporation. *Toyota Ushers in the Future with Launch of 'Mirai' Fuel Cell Sedan.* Nov. 2014. URL: https://global.toyota/en/detail/4198334 (visited on 06/30/2022).

[154] Hyundai Motor Co. *Release Hyundai ix35 Fuel Cell.* Mar. 2013. URL: https://www.hyundai.com/worldwide/en/company/newsroom/hyundai-ix35-fuel-cell-0000001596 (visited on 08/02/2022).

[155] Mercedes-Benz Group AG. *Mercedes-Benz GLC F-CELL: Market launch of the world's first electric vehicle featuring fuel cell and plug-in hybrid technology.* Nov. 2018. URL: https://group-media.mercedes-benz.com/marsMediaSite/ko/en/41813012 (visited on 01/27/2023).

[156] American Honda Motor Co. *Honda Announces First FCX Clarity Customers and World's First Fuel Cell Vehicle Dealership Network as Clarity Production Begins in Japan.* June 2008. URL: https://hondanews.com/en-US/honda-automobiles/releases/release-54f66820c49d2fb6c8596f004c34bcf6 (visited on 01/27/2023).

[157] American Honda Motor Co. *Honda Delivers First Clarity Fuel Cell in Northern California.* Feb. 2017. URL: https://hondanews.com/en-US/honda-automobiles/releases/release-0d89e659830543278019d3c199e9b6b9 (visited on 01/27/2023).

[158] BMW Group. *Launch of the BMW iX5 Hydrogen Pilot Fleet.* Feb. 2023. URL: https://www.bmwgroup.com/en/news/general/2023/BMWiX5Hydrogen.html (visited on 02/28/2023).

[159] Christophe Gerling. "Wasserstoff-Rezirkulation von Next-Genertaion-Brennstoffzellensystemen". Master Thesis. Offenburg: Hochschule Offenburg, Feb. 2018.

[160] David Koppius. "Variantenanalyse eines Brennstoffzellenluftsystems". Master Thesis. Aachen: RWTH Aachen, Apr. 2019.

[161] Jonas Breitinger. "Optimization of Charge Air Cooling with Energy Recovery for Mobile Fuel Cell". Master Thesis. Robert Bosch Corporate Research, May 2020.

[162] Milos Milanovic and Verica Radisavljevic-Gajic. "Multi-Timescale-Based Partial Optimal Control of a Proton-Exchange Membrane Fuel Cell". In: *Energies* 13.1 (Dec. 2019). DOI: 10.3390/en13010166.

[163] Po Hong. *Water Content Estimation and Control of PEM Fuel Cell Stack and the Individual Cell in Vehicle.* Springer Theses. DOI: 10.1007/978-981-16-8814-0. Singapore: Springer Nature Singapore, 2022. ISBN: 9789811688133 9789811688140.

[164] Baitao Zhang et al. "Experimental Investigation of Control Strategies on Voltage Inconsistency for Proton Exchange Membrane Fuel Cells". In: Apr. 2021. DOI: 10.4271/2021-01-0736.

[165]   Neil Tandon. *Hatchfill*. 2011. URL: https : / / www . mathworks . com / matlabcentral / fileexchange/30733-hatchfill.

Publications

Journal and Conference Papers

Jonas Breitinger, Mark Hellmann, Helerson Kemmer and Stephan Kabelac. "Flooding Characteristics and Countermeasures in a PEM Fuel Cell System". In: *ECS Transactions* 109.9 (Sept. 2022). DOI: 10.1149/10909.0227ecst.

Jonas Breitinger, Mark Hellmann, Helerson Kemmer and Stephan Kabelac. "Automotive Fuel Cell Systems: Testing Highly Dynamic Scenarios". In: *Energies* 16.2 (Jan. 2023). DOI: 10.3390/en16020664.

Jonas Breitinger, Mark Hellmann, Helerson Kemmer and Stephan Kabelac. "Experimental Dynamics Analysis of a Full-Scale Automotive PEM Fuel Cell System". In: *European Fuel Cell Forum 2023* (submitted).

Patent Applications

Mark Hellmann, Helerson Kemmer, Matthias Rink and Jonas Breitinger. "Brennstoffzellensystem und Betriebsverfahren für ein Brennstoffzellensystem". DE102021206204 B4 and WO2022/263392 A1.

Jonas Breitinger, Mark Hellmann and Helerson Kemmer. "Verfahren zum Trocknen einer Brennstoffzelle sowie Brennstoffzellensystem". DE102021210110 A1 and WO23041287 A1.

Jonas Breitinger and Matthias Rink. "Verfahren zum Betreiben eines Brennstoffzellensystems". DE102021207908 A1 and WO23001568 A1.

Mark Hellmann and Jonas Breitinger. "Verfahren zum Kühlen eines Brennstoffzellensystems und ein Brennstoffzellensystem". 102022200134.6 and EP2022/087771.

Jonas Breitinger, Mark Hellmann, Helerson Kemmer and Matthias Rink. "Verfahren zur Trocknung eines elektrochemischen Energiewandlers". 102021214749.6.

Mark Hellmann and Jonas Breitinger. "Brennstoffzellensystem und Trocknungsverfahren für ein Brennstoffzellensystem". 102022204523.8.

Jonas Breitinger and Helerson Kemmer. "Brennstoffzellensystem und Betriebsverfahren für ein Brennstoffzellensystem im Dynamikbetrieb". 102022203321.3 and EP2023/058499.

Jonas Breitinger, Mark Hellmann, Matthias Rink and Fabian Straub. "Brennstoffzellensystem und Betriebsverfahren für ein Brennstoffzellensystem im intermittierenden Betrieb". 102022203319.1 and EP2023/052837.

Mark Hellmann et al. "Brennstoffzellensystem, Betriebsverfahren und Bipolarplatte für ein Brennstoffzellensystem". 102022207544.7.

Mark Hellmann and Jonas Breitinger. "Verfahren zum Betreiben eines Brennstoffzellensystems". 102022208491.8.

Mark Hellmann and Jonas Breitinger. "Herstellungsverfahren für einen Brennstoffzellenstapel". 102022206784.3.

Jonas Breitinger and Mark Hellmann. "Verfahren zum Betreiben eines Antriebssystems für ein Kraftfahrzeug". 102022207452.1.

Jonas Breitinger and Mark Hellmann. "Verfahren zum Betrieb eines Brennstoffzellensystems". 102022206485.2.

Jonas Breitinger. "Verfahren zum Betreiben eines Brennstoffzellensystems". 102022207460.2.

Matthias Rink, Jonas Breitinger and Mark Hellmann. "Brennstoffzellensystem und Betriebsverfahren für ein Brennstoffzellensystem". 102022207204.9.

Jonas Breitinger and Mark Hellmann. "Separatorplattenhälfte, Separatorplatte, Brennstoffzellensystem sowie Verfahren". 102022209317.8.

Jonas Breitinger, Mark Hellmann and Daniel Seidl. "Lastreduktionsbegrenzung im Hochtemperaturbetrieb". 102022207195.6.

Mark Hellmann and Jonas Breitinger. "Brennstoffzellensystem zum Versorgen eines Verbrauchers mit elektrischer Energie und Betriebsverfahren für ein Brennstoffzellensystem". 102022209595.2.

Jonas Breitinger. "Brennstoffzellensystem und Betriebsverfahren für ein Brennstoffzellensystem". 102023202922.7.

Jonas Breitinger and Mark Hellmann. "Brennstoffzellensystem und Verfahren zum Betreiben eines Brennstoffzellensystems". 102022209566.9.

Jonas Breitinger, Matthias Rink and Daniel Deifel. "Brennstoffzellensystem und Betriebsverfahren für ein Brennstoffzellensystem". 102022210735.7.

Jonas Breitinger and Mark Hellmann. "Brennstoffzellensystem und Betriebsverfahren für ein Brennstoffzellensystem". 102023202925.1.

Jonas Breitinger. " Verfahren zum Trocknen eines Brennstoffzellenstapels, Brennstoffzellensystem, Fahrzeug, Computerprogrammprodukt, computerlesbares Medium sowie Datenträgersignal". 102023201279.0.

Jonas Breitinger. "Verfahren zum Betreiben eines Brennstoffzellensystems in einem dynamischen Betrieb". 102023201326.6.

Jonas Breitinger, Mark Hellmann, Matthias Rink and Leonie Möller. "Brennstoffzellensystem und Verfahren zum Betreiben eines Brennstoffzellensystems". 102022213476.1.

Jonas Breitinger, Jürgen Marquart and Erhard Hirth. "Verfahren zur eigenschaftsbezogenen Anordnung von Brennstoffzellen innerhalb eines Brennstoffzellenstapels". 102022214236.5.

Mark Hellmann and Jonas Breitinger. "Betriebsverfahren zum Vermeiden einer Anodenverarmung beim Betrieb eines Brennstoffzellensystems". 102023204074.3.

Jonas Breitinger and Mark Hellmann. "Verfahren zum Betreiben eines Brennstoffzellensystems, Brennstoffzellensystem für ein Kraftfahrzeug, Rechnereinheit, Computerprogrammprodukt sowie computerlesbares Medium". 102023203983.4.

Jonas Breitinger, Mark Hellmann and Leonie Möller. "Betriebsverfahren zum Betreiben eines Brennstoffzellensystems". 102023203250.3.

Appendix

A.1 Liquid Water Transport Limitation

The maximum molar flux of liquid water drained from the cathode GDL $\dot{n}_{H_2O,lim}^{(l)}$ is determined from the minimal gas velocity experiment discussed in Subsection 4.5.2. At this point, the gas flow is able to drain exactly the liquid water flux present at the cathode side. If more liquid water enters the GDL than the gas flow can drain, the limiter becomes active and accumulation starts. A bi-linear function shown in Figure A.1 is chosen for $\dot{n}_{H_2O,lim}^{(l)} = f(u_{ca,in})$, to implement the condition that a gas velocity of zero results in no drained water. A linear dependence between the drained liquid water and the stoichiometry was also proposed by Zhang et al.[98]. As they measured at constant pressure and temperature, the stoichiometry variation can be linearly translated to the gas velocity selected in this work.
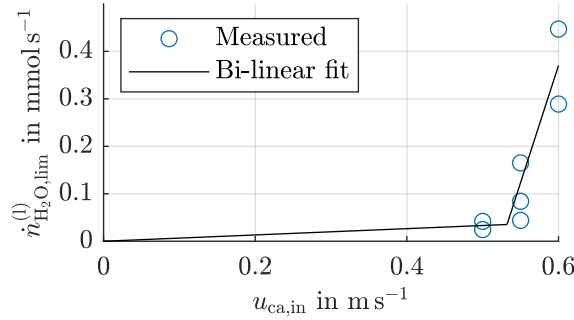

**FIG. A.1**   Measured and fitted liquid water flux limit depending on the gas velocity.

With that, the following bi-linear function is implemented in the model:

$$\dot{n}_{H_2O,lim}^{(l)} = \begin{cases} 6.63E-5\ u_{ca,in}\ \mathrm{mol\,m^{-1}} & \text{if } u_{ca,in} \leq 0.532\,\mathrm{m\,s^{-1}} \\ 4.93E-3\ u_{ca,in}\ \mathrm{mol\,m^{-1}} - 2.59E-3\,\mathrm{mol\,s^{-1}} & \text{if } u_{ca,in} > 0.532\,\mathrm{m\,s^{-1}} \end{cases} \tag{A.1}$$

A.2 Fitting of Time Constants

The time scale analysis outlined in Subsection 4.4.6 focuses on quantifying the relaxation behavior of various signals by fitting a PT1 step response function. Such fits are shown in Figure A.2 for the fixed BC case 1b discussed in Subsection 4.4.2. The fit interval starts at the end of the electrical current ramp, and ends with the beginning of the next current ramp. The overshoot in stack voltage occurs at the end of the current ramp, from where on the PT1-like relaxation process begins. In case of the coolant temperature a settling time is utilized as alternative formulation, since the signal shape does not correspond with a PT1-like behavior.

The settling time is measured from the end of the current ramp to the point in time, from which the measured signal remains within the 0.5 K error band displayed as dashed horizontal lines.
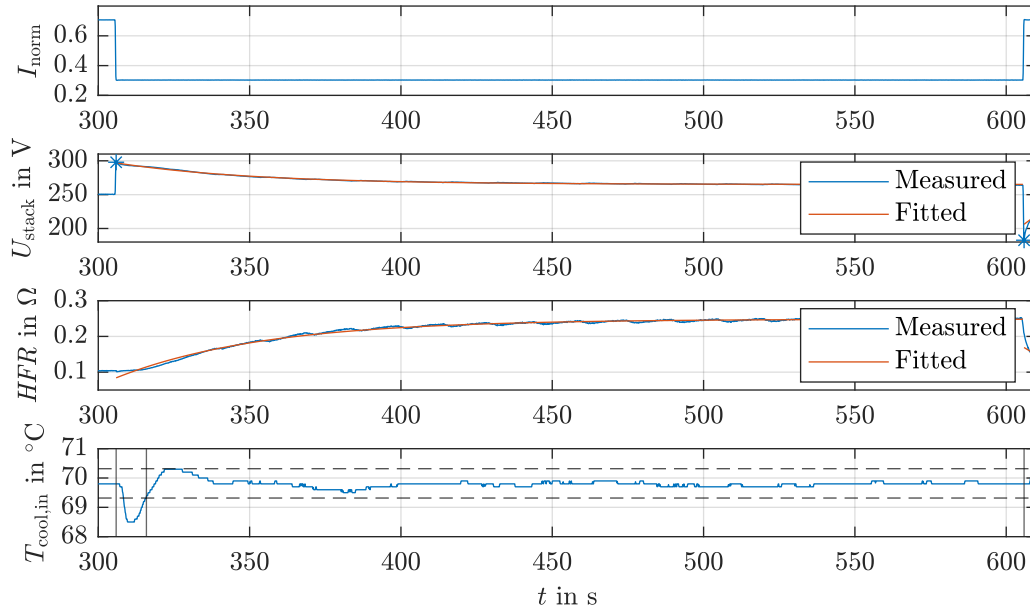
FIG. A.2 Exemplary fit of the PT1-like relaxation behavior of stack voltage and *HFR*. For the coolant temperature, the settling time is displayed.

A.3 Additional Experimental Boundary Conditions

The additional boundary conditions selected for the test cases are typical for automotive operation and shown in Table A.1, Table A.2, Table A.3, Table A.4. The measured mean value and standard deviation for each variable is given. Note that in the cases 1, 2 and 3, where a fuel cell system is used, not all stack inlet conditions are controlled directly and may change over time during dynamic operation.

TABLE A.1 Boundary conditions for test case 1[46]

Parameter	Value		Unit
	Case 1a	Case 1b	
I_{norm}	See Figure 4.13		-
p_{amb}	0.9800 ± 0.0001	0.9800 ± 0.0001	bar
T_{amb}	20.83 ± 1.57	20.99 ± 0.28	°C
RH_{amb}	40.74 ± 3.96	40.06 ± 1.43	%
$p_{ca,in}$	See Figure 4.13		bar
λ_{ca}	See Figure 4.13		$g\,s^{-1}$
$p_{an,in} - p_{ca,in}$	0.247 ± 0.029	0.252 ± 0.029	bar
$T_{cool,in}$	See Figure 4.13		°C
ΔT_{cool}	5.30 ± 0.48	5.26 ± 0.71	K

TABLE A.2 Boundary conditions for test case 2

Parameter	Value		Unit
	Case 2a	Case 2b	
I_{norm}	See Figure 4.14		-
p_{amb}	0.9800 ± 0.0001	0.9800 ± 0.0001	bar
T_{amb}	21.00 ± 0.37	21.08 ± 0.38	°C
RH_{amb}	40.20 ± 1.50	40.15 ± 1.82	%
$p_{\text{ca,in}}$	See Figure 4.14		bar
λ_{ca}	See Figure 4.14		g s^{-1}
$p_{\text{an,in}} - p_{\text{ca,in}}$	0.201 ± 0.049	0.213 ± 0.037	bar
$T_{\text{cool,in}}$	See Figure 4.14		°C
ΔT_{cool}	5.38 ± 0.72	5.41 ± 0.73	K

TABLE A.3 Boundary conditions for test case 3[46]

Parameter	Value		Unit
	Case 3a	Case 3b	
I_{norm}	See Figure 4.15		-
p_{amb}	0.9800 ± 0.0002	0.9800 ± 0.0001	bar
T_{amb}	20.96 ± 0.77	20.99 ± 0.59	°C
RH_{amb}	42.21 ± 6.16	40.65 ± 2.67	%
$p_{\text{ca,in}}$	See Figure 4.15		bar
λ_{ca}	See Figure 4.15		g s^{-1}
$p_{\text{an,in}} - p_{\text{ca,in}}$	0.141 ± 0.035	0.175 ± 0.048	bar
$T_{\text{cool,in}}$	See Figure 4.15		°C
ΔT_{cool}	3.89 ± 2.21	3.65 ± 1.65	K

TABLE A.4 Boundary conditions for test case 4[46]

Parameter	Value	Unit
I_{norm}	See Figure 4.17	-
$p_{\text{ca,in}}$	See Figure 4.17	bar
$T_{\text{ca,in}}$	59.99 ± 0.05	°C
$RH_{\text{ca,in}}$	16.15 ± 0.07	%
$\dot{m}_{\text{air}}$	See Figure 4.17	g s^{-1}
$p_{\text{an,in}}$	2.500 ± 0.004	bar
$T_{\text{an,in}}$	59.94 ± 0.05	°C
$RH_{\text{an,in}}$	87.57 ± 0.20	%
$\dot{m}_{\text{H}_2}$	0.122 ± 0.000	g s^{-1}
$T_{\text{cool,in}}$	See Figure 4.17	°C
ΔT_{cool}	11.80 ± 2.73	K

A.4 Time Scale Estimation in Fuel Cell Systems

A.4.1 Liquid water accumulation

In this case, it is assumed that no liquid water is removed from the GDL into the flow field. The liquid water flux into the cathode GDL is approximated to be 25 % of the produced water, based on water balance measurement evaluations carried out by Seidl[55]. With a pore volume V_{pore} of $2.76 \times 10^{-6}\,\text{m}^3$ for a cell used in the experiments and currents ranging from 25 to 500 A, the time it takes to change the saturation by 90 % of Δs is calculated by

$$t_{90,\text{accum}} = 0.9\Delta s \frac{V_{\text{pore}}}{\dot{V}_{\text{H}_2\text{O,ca}}^{(l)}} = 0.9\Delta s V_{\text{pore}} \frac{2F}{0.25I} \frac{\rho_{\text{H}_2\text{O}}^{(l)}}{M_{\text{H}_2\text{O}}} = 21.3 - 2684\,\text{s} \tag{A.2}$$

Note that a saturation change of $\Delta s = 0.1$ and the maximum current is assumed in the fast case, while a larger change of $\Delta s = 0.7$ is assumed in the slow case. This is motivated by the allowed saturation discussion in Section 4.6: at low currents, a higher saturation is allowed, while only a lower saturation is acceptable at increased currents.

A.4.2 Liquid water drainage

Liquid water drainage is limited by the gas flow in the adjacent flow field. Depending on the velocity, liquid water molar fluxes $\dot{n}_{\text{H}_2\text{O,lim}}^{(l)}$ between 0.5×10^{-6} and $4.5 \times 10^{-6}\,\text{mol}\,\text{s}^{-1}$ were observed experimentally, as shown in Figure A.1. Assuming that the cell is not producing liquid water, the time to reduce the saturation by $\Delta s = 0.1$ with the maximum liquid water flux and $\Delta s = 0.7$ with the minimal water flux in the fast and slow case respectively, yield

$$t_{90,\text{drain}} = 0.9\Delta s \frac{n_{\text{H}_2\text{O}}^{(l)}}{\dot{n}_{\text{H}_2\text{O}}^{(l)}} = 0.9\Delta s \frac{V_{\text{pore}}\rho_{\text{H}_2\text{O}}^{(l)}}{\dot{n}_{\text{H}_2\text{O,lim}}^{(l)} M_{\text{H}_2\text{O}}} = 3.1 - 193\,\text{s} \tag{A.3}$$

A.4.3 Anode mass flow

If a jet pump is implemented, the mass flow ramp-up at the anode inlet is limited by the opening dynamics of the adjacent hydrogen gas injector valve. Typical opening times of magnetic switch valves lie between 8 and 20 ms. The volume between the jet pump and the stack baseplate is minimized in current constructions and assumed to add only a negligible delay in the mass flow ramp-up.

A.4.4 Anode pressure

Assuming an anode loop volume including the stack of $V_{\text{an}} = 3\,\text{L}$, a maximum hydrogen mass flow $\dot{m}_{\text{H}_2}$ of 120 % of the maximum consumption, raising the pressure within the loop by

$\Delta p = 2$ bar at a typical operating temperature of $T = 60\,°C$ leads to the following t_{90}-time:

$$t_{90,p_{an}} = 0.9\Delta p \frac{V_{an}}{R_{H_2} T \dot{m}_{H_2}} = 0.17 - 1.02\,s \tag{A.4}$$

Note that in the fast case, no hydrogen consumption is assumed, while the maximum consumption is taken into account for the slow case.

A.4.5   Coolant temperature

For the warm-up of the system, a stack heat flux $\dot{Q}_{stack}$ of 3.4 kW is assumed in the slow case during idling operation, while a heat flux of 120 kW is considered for the fastest possible warm-up at full load. A warm-up of the stack and the coolant with a combined heat capacity of $mc_p = 45\,kJ\,K^{-1}$ from 60 °C to 90 °C yields a t_{90}-time of

$$t_{90,T_{cool}} = 0.9\Delta T \frac{\dot{Q}_{stack}}{mc_p} = 10.2 - 359\,s \tag{A.5}$$

The cool-down is driven by the radiator, with a typical heat transfer coefficient of $hA = 700 - 3500\,W\,K^{-1}$ depending on the passenger car class and driving speed[44]. Utilizing a heat capacity of $mc_p = 53\,kJ\,K^{-1}$ for stack, coolant and radiator, the time constant τ_{cool} and subsequently the t_{90} is derived as

$$t_{90,T_{cool}} = -\ln 0.1\,\tau_{cool} = -\ln 0.1 \frac{mc_p}{hA} = 35 - 175\,s \tag{A.6}$$

The warm-up therefore represents the lower limit and upper limit for the coolant temperature dynamics.

A.4.6   Coolant temperature rise

The coolant temperature rise from stack inlet to outlet ΔT_{cool} is controlled via the coolant mass flow, which depends on the coolant pump speed. A run up of the coolant pump from zero to full speed takes around 3 s, resulting in a maximum t_{90} of 2.7 s. In the fast scenario, a reduced speed variation of only ten percent of the full range subsequently results in a t_{90} of 0.27 s, assuming a constant rotational speed gradient.

A.5   Plot functions

The hatched areas in the Figures 2.2, 5.8 and 5.12 are plotted using a Matlab function by Tandon[165].

Curriculum Vitae: Jonas Breitinger

Education

10/2020 – 11/2023	**Ph.D. Studies, Mechanical Engineering** Leibniz University Hannover	
04/2017 – 05/2020	**M. Sc. Studies, Aerospace Engineering** University of Stuttgart	
08/2018 – 12/2018	**Study abroad, Aerospace Engineering** Purdue University, West Lafayette, IN, USA	
10/2013 – 03/2017	**B. Sc. Studies, Aerospace Engineering** University of Stuttgart	

Work Experience

Since 05/2023	**Research engineer, Robert Bosch GmbH, Renningen** Fuel cell system simulation and system interaction analysis
10/2020 – 04/2023	**Ph.D. candidate, Robert Bosch GmbH, Renningen** "Water Management in Highly Dynamic PEM Fuel Cell System Operation"
10/2019 – 04/2020	**Master thesis, Robert Bosch GmbH, Renningen** "Optimization of Charge Air Cooling with Energy Recovery for Mobile Fuel Cell Systems"
02/2019 – 08/2019	**Working student, Daimler AG, Sindelfingen** Method development aerodynamic simulations
04/2018 – 08/2018	**Teaching assistant "Numerical Simulation", University of Stuttgart**
11/2016 – 03/2017	**Bachelor thesis, DLR, Lampoldshausen** "Development and Test of an Experimental Hybrid Rocket Engine for Orbital Application"
04/2016 – 07/2016	**Internship, Airbus Defence & Space, Immenstaad** Satellite project JUpiter ICy moons Explorer (JUICE)